University of Potsdam

Cumulative Dissertation

LEARNING MORE TO PREDICT LANDSLIDES

Author:
Ugur Öztürk

Supervisor:
Prof. Oliver Korup, Ph.D.
Prof. Dr. Jürgen Kurths

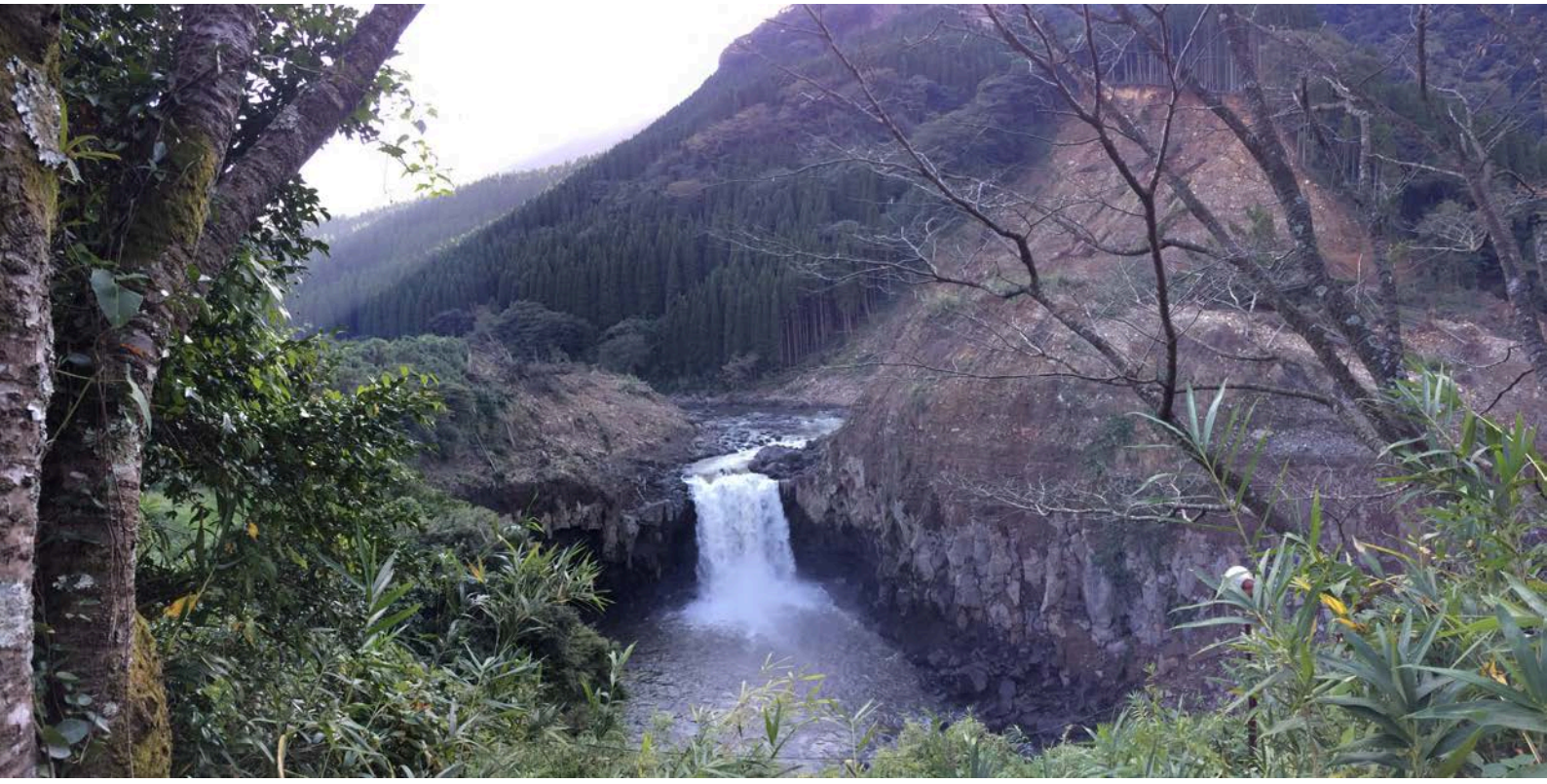

Publication-based dissertation submitted in fulfilment of the requirements for the degree of Doctor of Engineering (Doktor der Ingenieurwissenschaften, Dr.-Ing.) under the discipline of
Geohazards
Institute of Earth and Environmental Sciences
Faculty of Science

March 21, 2019

Published online at the
Institutional Repository of the University of Potsdam:
https://doi.org/10.25932/publishup-42643
https://nbn-resolving.org/urn:nbn:de:kobv:517-opus4-426439

Learning More to Predict Landslides

by Ugur Öztürk

Supervisor:	*Affiliation:*
Prof. Oliver Korup, Ph.D.	*University of Potsdam*
Prof. Dr. Dr. h.c. mult. Jürgen Kurths *(Reviewer)*	*Humboldt-Universität zu Berlin* *Potsdam Institute for Climate Impact Research (PIK)* *University of Potsdam*
Co-Supervisor:	
Dr. rer. nat. Norbert Marwan	*Potsdam Institute for Climate Impact Research (PIK)*
Assoc. Prof. Hitoshi Saito, Ph.D.	*Kanto Gakuin University*
Mentor:	
Prof. Dr.-Ing Jürgen Jensen	*University of Siegen*

Assessment Committee:	
Prof. Dr. Fabrice Cotton *(Chair)*	*German Research Centre for Geosciences (GFZ)* *University of Potsdam*
Prof. Dr.-Ing Axel Bronstert *(Reviewer)*	*University of Potsdam*
Prof. Eva Nora Paton, Ph.D. *(Reviewer)*	*Technische Universität Berlin*
Prof. Dr.-Ing Bruno Merz	*German Research Centre for Geosciences (GFZ)* *University of Potsdam*

Publication-based dissertation submitted in fulfilment of the requirements for the degree of Doctor of Engineering (Doktor der Ingenieurwissenschaften, Dr.-Ing.) within the DFG - Research Training Group "NatRiskChange" under the discipline of Geohazards at the Institute of Earth and Environmental Sciences, Faculty of Science, University of Potsdam.

Declaration of Authorship

I, Ugur Öztürk, declare that this thesis titled, "Learning More to Predict Landslides" and the work presented in it are my own. I confirm that:

- This work was done wholly or mainly while in candidature for a research degree at the University of Potsdam.
- Where any part of this dissertation has previously been submitted for a degree or any other qualification at the University of Potsdam, or any other institution, this has been clearly stated.
- Where I have consulted the published work of others, this is always clearly attributed.
- Where I have quoted from the work of others, the source is always given. With the exception of such quotations, this thesis is entirely my own work.
- I have acknowledged all main sources of help.
- Where the thesis is based on work done by myself jointly with others, I have made clear exactly what was done by others and what I have contributed myself.

Signature:

Date:

"*Raise your words, not voice. It is rain that grows flowers, not thunder.*"

Rumi

Abstract

Landslides are frequent natural hazards in rugged terrain, when the resisting frictional force of the surface of rupture yields to the gravitational force. These forces are functions of geological and morphological factors, such as angle of internal friction, local slope gradient or curvature, which remain static over hundreds of years; whereas more dynamic triggering events, such as rainfall and earthquakes, compromise the force balance by temporarily reducing resisting forces or adding transient loads. This thesis investigates landslide distribution and orientation due to landslide triggers (e.g. rainfall) at different scales (6–4·10^5 km^2); and aims to link rainfall movement with the landslide distribution. It additionally explores the local impacts of the extreme rainstorms on landsliding and the role of precursory stability conditions that could be induced by an earlier trigger, such as an earthquake.

Extreme rainfall is a common landslide trigger. Although several studies assessed rainfall intensity and duration to study the distribution of thus triggered landslides, only a few case studies quantified spatial rainfall patterns (i.e. orographic effect). Quantifying the regional trajectories of extreme rainfall could aid predicting landslide prone regions in Japan. To this end, I combined a non-linear correlation metric, namely event synchronization, and radial statistics to assess the general pattern of extreme rainfall tracks over distances of hundreds of kilometers using satellite based rainfall estimates. Results showed that, although the increase in rainfall intensity and duration positively correlates with landslide occurrence, the trajectories of typhoons and frontal storms were insufficient to explain landslide distribution in Japan. Extreme rainfall trajectories inclined northwestwards and were concentrated along some certain locations, such as coastlines of southern Japan, which was unnoticed in the landslide distribution of about 5000 rainfall-triggered landslides. These landslides seemed to respond to the mean annual rainfall rates.

Above mentioned findings suggest further investigation on a more local scale to better understand the mechanistic response of landscape to extreme rainfall in terms of landslides. On May 2016 intense rainfall struck southern Germany triggering high waters and landslides. The highest damage was reported at the Braunsbach, which is located on the tributary-mouth fan formed by the Orlacher Bach. Orlacher Bach is a ∼3 km long creek that drains a catchment of about ∼6 km^2. I visited this catchment in June 2016 and mapped 48 landslides along the creek. Such high landslide activity was not reported in the nearby catchments within ∼3300 km^2, despite similar rainfall intensity and duration based on weather radar estimates. My hypothesis was that several landslides were triggered by rainfall-triggered flash floods that undercut hillslope toes along the Orlacher Bach. I found that morphometric features such as slope and curvature play an important role in landslide distribution on this micro scale study site (<10 km^2). In addition, the high number of landslides along the Orlacher Bach could also be boosted by accumulated damages on hillslopes due karst weathering over longer time scales.

Precursory damages on hillslopes could also be induced by past triggering events that effect landscape evolution, but this interaction is hard to assess independently from the latest trigger. For example, an earthquake might influence the evolution of a landscape decades long, besides its direct impacts, such as landslides that follow the earthquake. Here I studied the consequences of the 2016 Kumamoto Earthquake (M_W 7.1) that triggered some 1500 landslides in an area of ∼4000 km^2 in central Kyushu, Japan. Topography, i.e. local slope and curvature, both amplified and attenuated seismic waves, thus controlling the failure mechanism of those landslides (e.g. progressive). I found that topography fails in explaining the distribution and the preferred orientation of the landslides after the earthquake; instead the landslides were concentrated around the northeast of the rupture area and faced mostly normal to the rupture plane. This preferred location of the landslides was dominated mainly by the directivity effect of the strike-slip earthquake, which is the propagation of wave energy along the fault in the rupture direction; whereas amplitude variations of the seismic radiation altered the preferred orientation. I suspect that the earthquake directivity and the asymmetry of seismic radiation damaged hillslopes at those preferred locations increasing landslide susceptibility. Hence a future weak triggering event, e.g. scattered rainfall, could further trigger landslides at those damaged hillslopes.

Zusammenfassung

Hangrutschungen treten häufig in steilem Gelände auf, wenn die Erdanziehungskraft die Scherkräfte an der Oberfläche übersteigt. Diese Kräfte beinhalten geologische und geomorphologische Faktoren wie den Reibungswinkel oder die Neigung und Krümmung von Hängen, die über Jahrhunderte statisch bleiben können. Dynamische Ereignisse wie Regenfälle und Erdbeben können hingegen das Kräftegleichgewicht beeinträchtigen, indem sie Widerstandskräfte vorübergehend reduzieren oder Lasten temporär hinzufügen. Diese Arbeit untersucht die Verteilung und Orientierung von Hangrutschungen in Abhängigkeit von Auslösern (z.B. Niederschlag) auf verschiedenen Skalenebenen (6–4·10^5 km^2) und verknüpft die Bewegung des Niederschlagssystems mit der Hangrutschungsverteilung. Zudem werden lokale Auswirkungen von extremen Gewittern auf Hangrutschungen untersucht, sowie vorausgehende Stabilitätsbedingungen, die durch ein früheres Ereignis, beispielsweise ein Erdbeben, verändert werden können.

Extremer Niederschlag ist ein weithin bekannter Auslöser für Hangrutschungen. Obwohl mehrere Studien die Verteilung von Hangrutschungen mit der Niederschlagsintensität und -dauer verglichen haben, beachteten nur wenige Fallstudien das räumliche Bewegungsmuster des Niederschlags, i.e. den orographischen Effekt. Eine solche Quantifizierung könnte die Vorhersage von hangrutschungsgefährdete Regionen in Japan verbessern. Hierfür habe ich ein nicht-lineares Korrelationsmaß (event synchronization) auf regionale Sturmbahnen in Japan angewendet, um deren räumliche Verteilung durch satellitengestützen Regenschätzungen nachzuvollziehen. Die durchgeführten Untersuchungen zeigten, dass sich die Verteilung von Hangrutschungen nur unzureichend mit den Zugbahnen von Taifunen und Sturmtiefen erklären lässt. Die Stabilität von Hängen scheint mehr durch mittlere Jahresniederschlagsmengen beeinflusst zu werden.

Erzielte Ergebnisse zeigen, dass weitere Untersuchungen auf lokaler Ebene nötig sind, um die unmittelbare Auswirkungen von Extremniederschlägen auf Hangstabilität und -rutschungen besser zu verstehen. Im Mai 2016 kam es in Süddeutschland zu einem heftigen Gewitter, das Hochwasser und Hangrutschungen ausgelöst hat. Der höchste Schaden wurde in Braunsbach, dessen Zentrum sich am Zufluss des Orlacher Bachs befindet, gemeldet. Der Orlacher Bach ist ∼3 km lang und hat ein Einzugsgebiet von etwa 6 km^2. Ich habe dieses Einzugsgebiet im Juni 2016 besucht und 48 Hangrutschungen entlang des Baches kartiert. Ich vermutete, dass mehrere Hangrutschungen durch Sturzfluten ausgelöst wurden, welche die Hänge entlang des Orlacher Baches unterspülten. Ich stellte fest, dass morphometrische Merkmale wie die lokale Hangneigung und -krümmung eine wichtige Rolle bei der Hangrutschungsverteilung auf dieser Mikroskala spielen (<10 km^2). Darüber hinaus könnte die hohe Anzahl von Hangrutschungen am Orlacher Bach auch durch Karstverwitterung über längere Zeiträume verstärkt werden.

Zahlreiche in der Vergangenheit liegende Ereignisse können die Stabilität eines Hanges beeinflussen. Der Einfluss solcher Ereignisse ist nur sehr schwer unabhängig voneinander abschätzbar. Beispielseise könnte ein Erdbeben die Entwicklung einer Landschaft über Jahrzehnte hin beeinflussen. Hier erforsche ich die Folgen des Kumamoto-Erdbebens 2016 (M_W 7.1) das im Zentrum von Kyushu, Japan, ca. 1500 Hangrutschungen in einem Gebiet von ∼4000 km^2 ausgelöst hat. Die Topographie (Hangneigung und -krümmung) verstärkte schwächte seismische Wellen gleichermaßen ab, wodurch der Auslösemechanismus dieser Hangrutschungen (z.B. progressiv) gesteuert wird. Ich konnte belegen, dass die Topographie die Verteilung und die bevorzugte Ausrichtung der Hangrutsche nach dem Erdbeben nicht erklären kann; stattdessen waren die Hangrutschungen um den Nordosten des Bruchgebiets herum konzentriert und standen meist senkrecht zur Bruchfläche. Diese bevorzugte Lage der Erdrutsche wurde hauptsächlich durch den Richtwirkungseffekt des Blattverschiebung-Erdbebens dominiert. Bei diesem handelt es sich um die Ausbreitung der Wellenenergie entlang des Bruches in Bruchrichtung, während Amplitudenvariationen der seismischen Strahlung die bevorzugte Orientierung ändern. Ich vermute, dass die Richtwirkung des Erdbebens und die Asymmetrie der seismischen Strahlung die Hangneigung an diesen bevorzugten Stellen schädigten und die Anfälligkeit für Hangrutschungen erhöhten. Daher könnte ein zukünftiges schwaches Ereignis wie z.B. ein unbedeutender Niederschlag an diesen beschädigten Hängen weitere Hangrutschungen auslösen.

Acknowledgements

This doctoral research was performed between October 2015 and March 2019. The total research work was partially carried out at the Potsdam Institute for Climate Impact Research (PIK). The study was embedded in the Research Training Group "Natural Hazards and Risks in a Changing World" (NatRiskChange; GRK 2043/1) funded by the "Deutsche Forschungsgemeinschaft" (DFG).

I would like to express my sincere gratitudes to my supervisors Oliver Korup and Jürgen Kurths, for their insightful advices, teachings, and endless patience. I am deeply indebted to Norbert Marwan for his deliberate guidance in each single step throughout the project. I would like to thank also to Hitoshi Saito for introducing me the Japanese climate and geomorphology, besides providing immediate data solutions during all the study.

I am particularly grateful for the assistance given by Nishant Malik for broadening my perspective about complex networks. Advices given by Aljoscha Rheinwalt and Bedartha Goswami has been a great help improving the quality of my results. I would also like to thank Veronika Stolbova for introducing me the event synchronization.

I want to thank Takashi Oguchi and Yuichi S. Hayakawa for hosting me at the Center for Spatial Information Science at the University of Tokyo to perform part of this doctoral research. They lead me to discover the Aso Region in Kyushu (Japan) and generously shared their expertise about geomorphological processes active in the region. I sincerely acknowledge Yuki Matsushi for letting me present this study in Geohazards Research Division of the Disaster Prevention Research Institute (DPRI) at the Kyoto University, and providing constructive suggestions.

I would like to thank Axel Bronstert for encouraging me to take part in the Braunsbach Task Force, in other case the study of Braunsbach (chapter 3) would not happen. I am particularly grateful to all NatRiskChange primary investigators for critically reviewing and improving my results at the periodical retreats.

My special thanks to Sebastian von Specht for helping me to uncover the secrets of signal processing, and programming. Further thanks to Dadiyorto Wendi, Irene Crisologo and Georg Veh for helping in geostatistics and geospatial analysis. Thanks to Ankit Agarwal for fruitful discussions about complex networks and event synchronization. I am especially grateful to my colleagues Jonas Laudan, Amelia Stolle, Massimilano Pittore, and Erwin Rottler for reviewing the early versions of this dissertation. I am lucky to have colleagues as, Swenja Rosenwinkel, Tobias Sieg, Kristin Vogel and all the other NatRiskChange research training school members, who are always ready to help.

Most greatest thanks to my wife Vera, parents, and sister, who were always there to support, listen and motivate.

Contents

List of Figures

List of Abbreviations

a.s.l.	**a**bove **s**ea **l**evel
JAXA	**J**apan **A**erospace **E**xploration **A**gency
AMeDAS	**A**utomated **Me**teorological **D**ata **A**cquisition **S**ystem
BKG	**B**undesamt für **K**artographie und **G**eodäsie (Federal Agency for Cartography and Geodesy)
DEM	**D**igital **E**levation **M**odel
DSM	**D**igital **S**urface **M**odel
DTM	**D**igital **T**errain **M**odel
DWD	**D**eutsche **W**etter **D**ienst (German Weather Service)
ES	**E**vent **S**ynchronization
ETT	**E**ye of the **T**yphoon **T**rack
GSI	**G**eo**S**patial **I**nformation Authority of Japan
IPCC	**I**ntergovernmental **P**anel for **C**limate **C**hange
JAXA	**J**apan **A**erospace **E**xploration **A**gency
JMA	**J**apan **M**eteorological **A**gency
LGRB	**L**andesamt für **G**eologie, **R**ohstoffe und **B**ergbau (The State Office of Geology, Raw Materials and Mining)
MAF	**M**edian **A**mplification **F**actor
MAP	**M**ean **A**nnual **P**recipitation
MERRA	**M**odern **E**ra **R**etrospective-analysis for **R**esearch and **A**pplications
NCEP	**N**ational **C**enters for **E**nvironmental **P**rediction
NCAR	**N**ational **C**enter for **A**tmospheric **R**esearch
NDVI	**N**ormalized **D**ifference **V**egetation **I**ndex
NIED	**N**ational Research **I**nstitute for **E**arth Science and **D**isaster Prevention
NOAA	**N**ational **O**ceanic and **A**tmospheric **A**dministration
PGA	**P**eak-**G**round **A**cceleration
RDN	**R**ainy **D**ay **N**ormal
RMS	**R**oot-**M**ean **S**quare
RSMC	**R**egional **S**pecialized **M**eteorological **C**enter
SOF	**s**tyle **o**f **f**aulting
TOA	**T**op **O**f **A**tmosphere
TRMM	**T**ropical **R**ainfall **M**easuring **M**ission
TWI	**T**opographic **W**etness **I**ndex
UTC	**U**niversal **T**ime **C**oordinated

Dedicated to my daughter Helena

Chapter 1

INTRODUCTION

The surface of the Earth changes. Terrestrial processes as part of plate dynamics deform the Earth's crust (Molnar and Tapponnier, 1977); whereas weathering and erosion due atmospheric circulation (the movement of air and moisture above the Earth's surface) and hydrological cycle (the movement of water above and below the surface of the Earth) further shape the landscape (Fielding, 1996). For instance, rainfall can trigger shallow landslides and simultaneously lead to high waters in natural streams, and those high waters could transfer loose material, which is supplied by the landslides, to a new location, in case foots of the landslides and the high waters intersect. As seen in this example, landslides play an important role in the evolution of landscapes (Keefer, 2002), by providing fresh material to the natural drainage systems (Yanites et al., 2010). However sudden occurrence of landslides as well as landslide triggers, such as rainstorms and earthquakes could harm society, and be perceived as natural hazards. Understanding the interaction between those natural phenomena could improve our knowledge of earth surface dynamics, hence aid hazard susceptibility. In this thesis I approach this complex interaction of earth surface processes from the landslides perspective.

A landslide is a downslope mass movement of earth materials under the force of gravity (Varnes, 1978). Landslides can be classified both by material (e.g., debris, rock) and movement types (e.g., flow, slide) (Varnes, 1978; Cruden and Varnes, 1996), which involves pre-failure deformations, the process of failure itself, and any post-failure displacements (Skempton and Hutchinson, 1969); from which I only refer to the failure process in this study. The total landslide-affected area can be subdivided into zones of initiation, transportation, and deposition (Hungr, 2005; Meyer, 2014). For example, Hungr et al. (2014) describe the following scenario to explain a debris flow type landslide:

"A landslide may begin with slow pre-failure deformation and cracking of surficial soil on a steep hillside. Then a shallow sliding failure develops. The landslide mass accelerates, disintegrates, enlarges through entrainment and becomes a flow-like debris avalanche. The avalanche enters a drainage channel, entrains water and more saturated soil and turns into a surging flow of debris. On entering a deposition fan, the flow drops the coarsest fractions and continues as a sediment-laden flood."

Landslide movement is governed by controlling factors such as topography and lithology, and triggers such as strong, short-lived ground motion during earthquakes or intensive rainfall during storms. Slope inclination is the main topographic parameter determining slope stability through the gravitational force (Imaizumi et al., 2017), while curvature (i.e. profile and planform) expresses the local changes in slope (Dou et al., 2015; Ohlmacher, 2007). Lithology can also cause high susceptibility. For example, clay layers can behave like a fluid with enough water content that counteracts the gravitational pull on the clay particles (Holtz et al., 2011; Stark et al., 2017), while karst can form voids between rock layers and decrease slope stability by reducing the area of the potential failure surface (Martinotti et al., 2017). Besides these controls, there is also vegetation that can increase or decrease slope stability, for instance, roots may contribute to the apparent cohesion that stabilizes the soil (Schmidt et al., 2001; McGuire et al., 2016), besides anchoring surface materials (Pollen and Simon, 2005; Arnone et al., 2016). In contrast vegetation can enhance slope instability by increasing the surcharge load on the slopes or by transmitting wind shear forces to the soil (Greenwood et al., 2004).

Some landslides lifetime is rather long, they happen slowly (<m/yr) perhaps over decades or even longer (Longoni et al., 2014), whereas most destructive landslides are short lived, they occur within seconds due to a triggering event (Dang et al., 2016). Landslide triggers change the force balance of an unstable slope that might initiate or accelerate landslide movement. Increases in rainfall totals may reduce

slope stability by rising water tables (Longoni et al., 2014), thus potentially reducing shear strength, suction and cohesion, while increasing the soil weight (Tacher and Bonnard, 2007). Increases in rainfall intensity may result in higher erosion initiating new landslides by removing basal slope support (Gariano and Guzzetti, 2016). High rainfall totals can also reactivate deep-seated landslides (Gariano and Guzzetti, 2016), while high intensity rainfalls mainly trigger shallow failures (Turkington et al., 2016). For instance, Fukuoka Prefecture of Japan were hit by about 800 mm of rain in half a day in July, 2017, that triggered about 2,000 shallow landslides according to the Geospatial Information Authority of Japan (GSI); whereas prolonged and intense rains during Hurricane Mitch triggered more than 10,000 different sized landslides (Devoli et al., 2007). Figure 1.1 shows rainfall-triggered landslide events around the world since 2007 (Kirschbaum et al., 2010, 2015). Dynamic seismic loading is another common trigger of landslides. Slope failures develop under seismic loading while seismic acceleration adds to the gravitation acceleration exceeding the cohesive and frictional resistive forces (Newmark, 1965). For example, the 2002 Denali earthquake (M_W 7.9) triggered about 1,500 landslides (Gorum et al., 2014), whereas the 2008 Wenchuan earthquake (with the same M_W 7.9 nominally) triggered more than 60,000 landslides (Figure 1.2, Gorum et al., 2011).

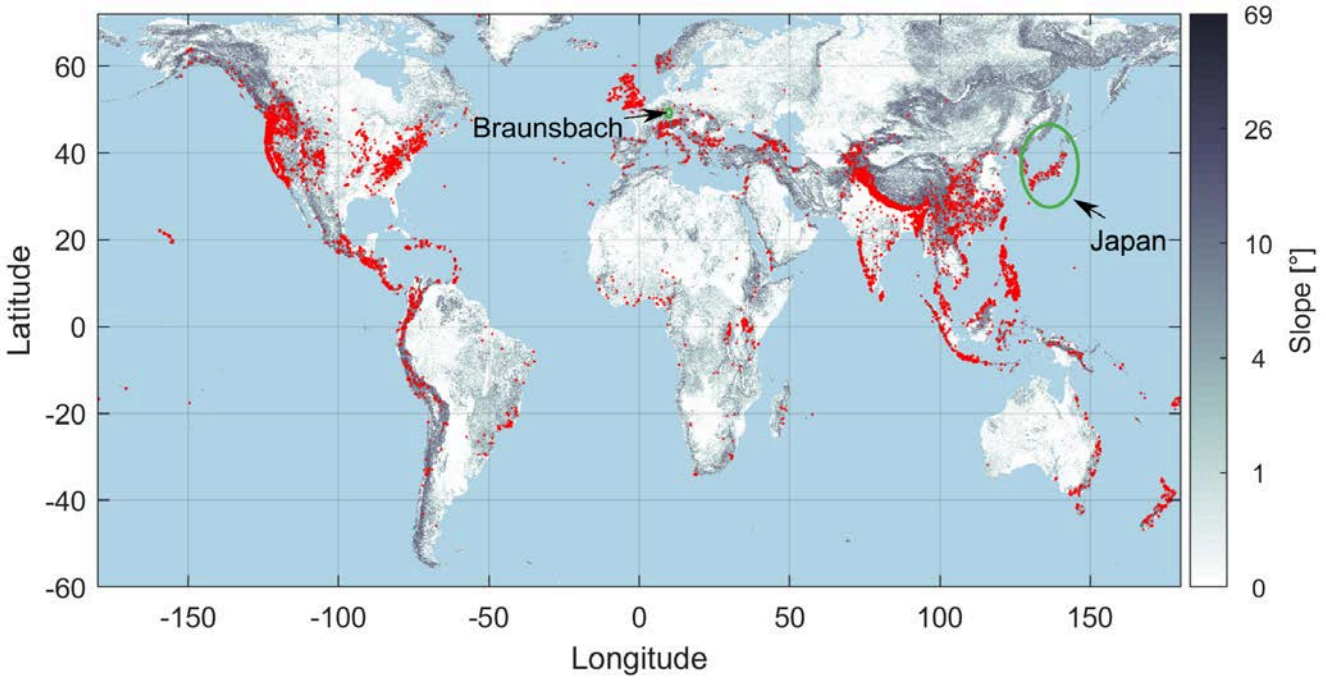

FIGURE 1.1: Global rainfall triggered landslide catalogue based on news reports, and scholarly articles in English since 2007 (Kirschbaum et al., 2010, 2015). Red dots show the location of landslides on the logarithmic scale slope map based on SRTM 30 digital elevation model by Hengl and Reuter (2010). Green circle show the location of the study sites (see section 1.3)

1.1 Motivation

Mountainous terrain is vulnerable to climate change, which boosts indirectly the landslide activity (Seneviratne et al., 2012) by decreasing the return periods of landslide triggering hydrological extremes, e.g., heavy precipitation (Gariano and Guzzetti, 2016); and by fostering permafrost degradation, glacial retreat (Knight and Harrison, 2009), and shorter snow cover duration (Beniston et al., 2003; Vanham et al., 2008). For instance, the 2003 heat wave in the European Alps (Keiler et al., 2010), which led to permafrost degradation that increased the rock-fall activity (Gruber, 2004; Fischer et al., 2006). The heat wave is also suspected to have advanced the expected failure time of the deep-seated slope instabilities, which may be delayed decades or centuries long (Gruber, 2004; Harris et al., 2009). In addition, Wang

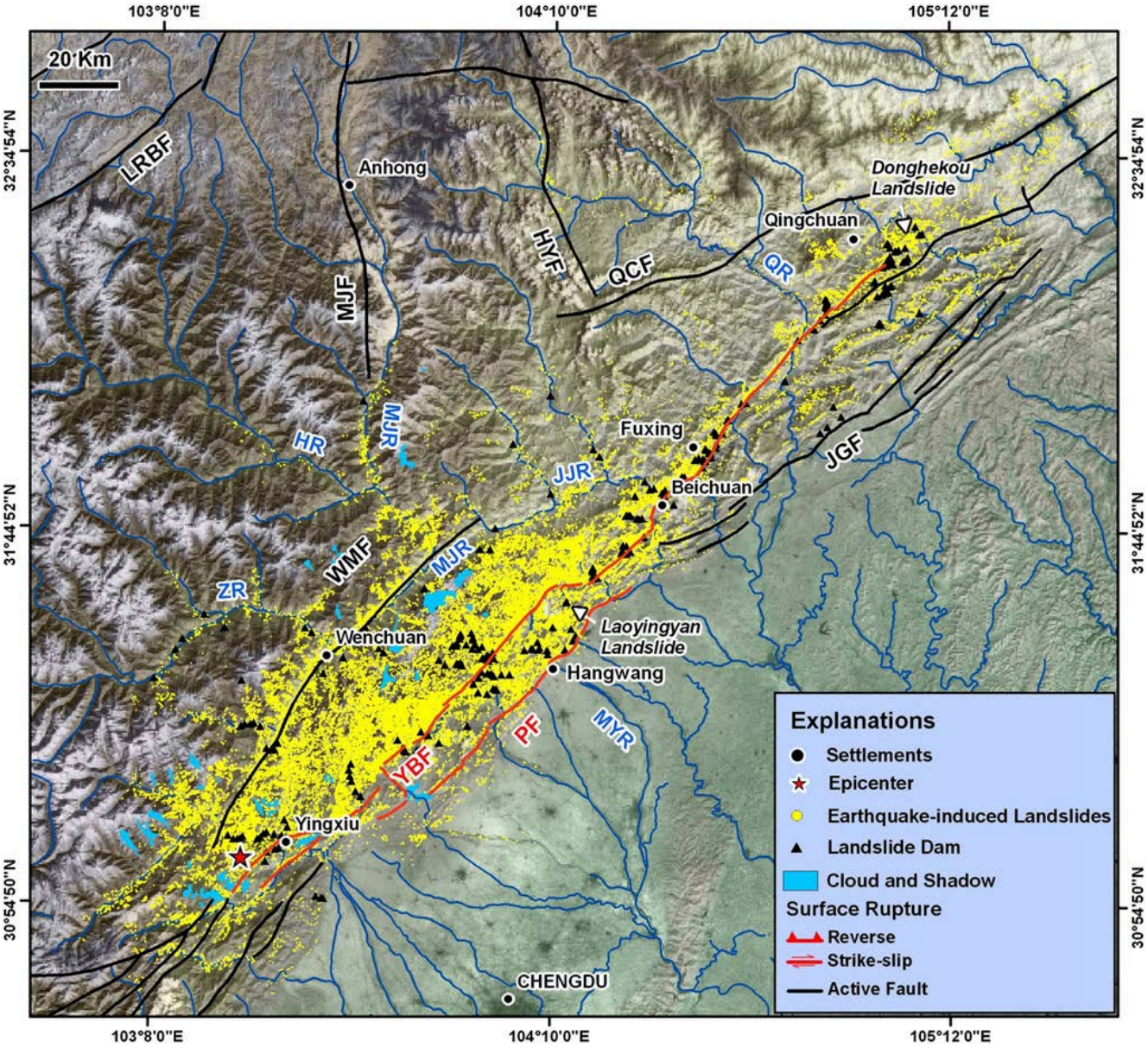

FIGURE 1.2: Landslides that were triggered by the Wenchuan Earthquake (M_W 7.9) together with the derived 257 landslides dam along the rivers by Gorum et al. (2011); MJR-Minjiang River, ZR-Zagunao River, HR-Heishuehe River, MYR-Mianyuan River, JJR-Jianjiang River, and QR-Qingzhu River. The faults in the region are WMF-Wenchuan–Maowen fault, YBF-Beichuan–Yingxiu fault, PF-Pengguan fault, JGF-Jiangyou–Guanxian fault, QCF-Qingchuan fault, HYF-Huya fault, MJF-Minjian fault.

and Towhata (2016) found out that the number of rainfall events in Japan with ≥100 (≥50) mm/hr intensity increased about 2.0 (1.3) times between 1976 and 2010, increasing the average landslide activity. Thus, it is essential to constrain better any relationship between extreme atmospheric events and landslide occurrence for providing temporal and spatial landslide predictions (van Westen et al., 2006).

An effective landslide risk assessment requires appropriate landslide maps depicting the associated susceptibility, hazard, and risk (Gaprindashvili and van Westen, 2016), in combination with the landslide inventories (e.g., Figure 1.1) that quantify the spatial distribution of landslides and help to calibrate those hazard and susceptibility maps (Galli et al., 2008; Iwahashi and Yamagishi, 2017). Landslide hazard refers to the probability of a landslide size (area or volume) to occur in a given location within a certain time interval (Crozier and Glade, 2012), whereas landslide susceptibility is the propensity of a region being exposed to a slope failure(Hervás and Bobrowsky, 2009). Susceptibility analysis should

ideally combine landslide controlling factors with landslide triggers to depict parts of the landscape that are especially prone to slope failure, assuming that past landslides identify those conditions likely leading to future ones (Nadim et al., 2006; Hong et al., 2007).

Landslide controlling factors are alone used to derive landslide susceptibility in some physical models. Accordingly over 1,200 such studies are listed in web of science database among the ∼2000 total publications, topic of which is landslide susceptibility (www.webofknowledge.com, accessed June 28, 2018). The controlling factors are primarily the topographic input data, such as local slope, aspect, and curvature; in addition to other factors, as nominal rock types of lithology, soil texture, frictional angle, water infiltration rate, and characteristics of vegetation such as the Normalized Difference Vegetation Index (NDVI) (Hong et al., 2007; Hong and Adler, 2008; Dou et al., 2015; Trigila et al., 2015). However, when these conditions are considered in global scale, the major mountain ranges (Pacific Rim, Rocky Mountains, Andes, and Alpine-Himalayan Arc) have a pronounced landslide susceptibility on a global scale (Figure 1.3), since the local slope in particular increases approaching those mountain ranges. The correlation (cross-correlation with zero-lag) is about 0.77 between slope by Hengl and Reuter (2010) and global landslide susceptibility map by Stanley and Kirschbaum (2017) in Figure 1.3.

There exists also statistical models to locate the landslide prone areas using solely the landslide triggering factors (Lee et al., 2018), assuming that the landslides are more dependent on landslide triggering factors such as rainfall, snowmelt and seismic activity than on differences in lithology or topography at the regional scale (Guzzetti et al., 2008; Lee et al., 2018). About 10% of all the landslide susceptibility related publications input primarily the rainfall or earthquake data in web of science (www.webofknowledge.com, accessed June 28, 2018). For example, rainfall intensity duration (ID) control for landslide triggering that is introduced by Caine (1980). Guzzetti et al. (2008) identified a globally applicable rainfall ID threshold above which landslides are triggered. Although an operational application of rainfall ID threshold is rather difficult on a global scale, because of validating the threshold and methodological incoherence in defining ID thresholds (Leonarduzzi et al., 2017), besides the inconsistency in landslide and rainfall data (Nikolopoulos et al., 2014; Iadanza et al., 2016); efforts on developing a global rainfall ID thresholds create a basis for effective local applications (e.g., Marra et al., 2016). Osanai et al. (2010) proposed a non-linear threshold for Japan that separates reported landslide occurrences and 'non-occurrences' for a given pair of rainfall ID conditions, and used this approach to estimate the landslide hazard for actual rainfall conditions in real time. Nevertheless, the accuracy of such models drops in smaller study areas, and the models require more information about controlling factors, such as lithology or local slope (e.g., Peruccacci et al., 2017; Jacobs et al., 2018). Landslide controlling factors are adopted in some few studies that consider controlling factors to improve the spatial accuracy of the rainfall ID thresholds (e.g., Pradhan et al., 2017).

Consequently landslide susceptibility studies should offer more mechanistic details on combined impacts of landslide controls and triggers, instead of analysing those impacts separately. Although there is no systematic standard for selecting landslide controlling factors in susceptibility studies (Ayalew et al., 2004), it is essential to combine those controls with landslide triggers, since selecting the right combination of these factors can increase the landslide prediction accuracy (Dou et al., 2015; Wilde et al., 2018). Considering all the issues above, I want to evaluate both landslide controlling and triggering factors in this study and explore their influence on landsliding from regional to local scales focusing mainly on heavy rainfall as landslide triggers. I will also investigate the earthquake induced landslides to understand potential long term influences of earthquakes on landsliding.

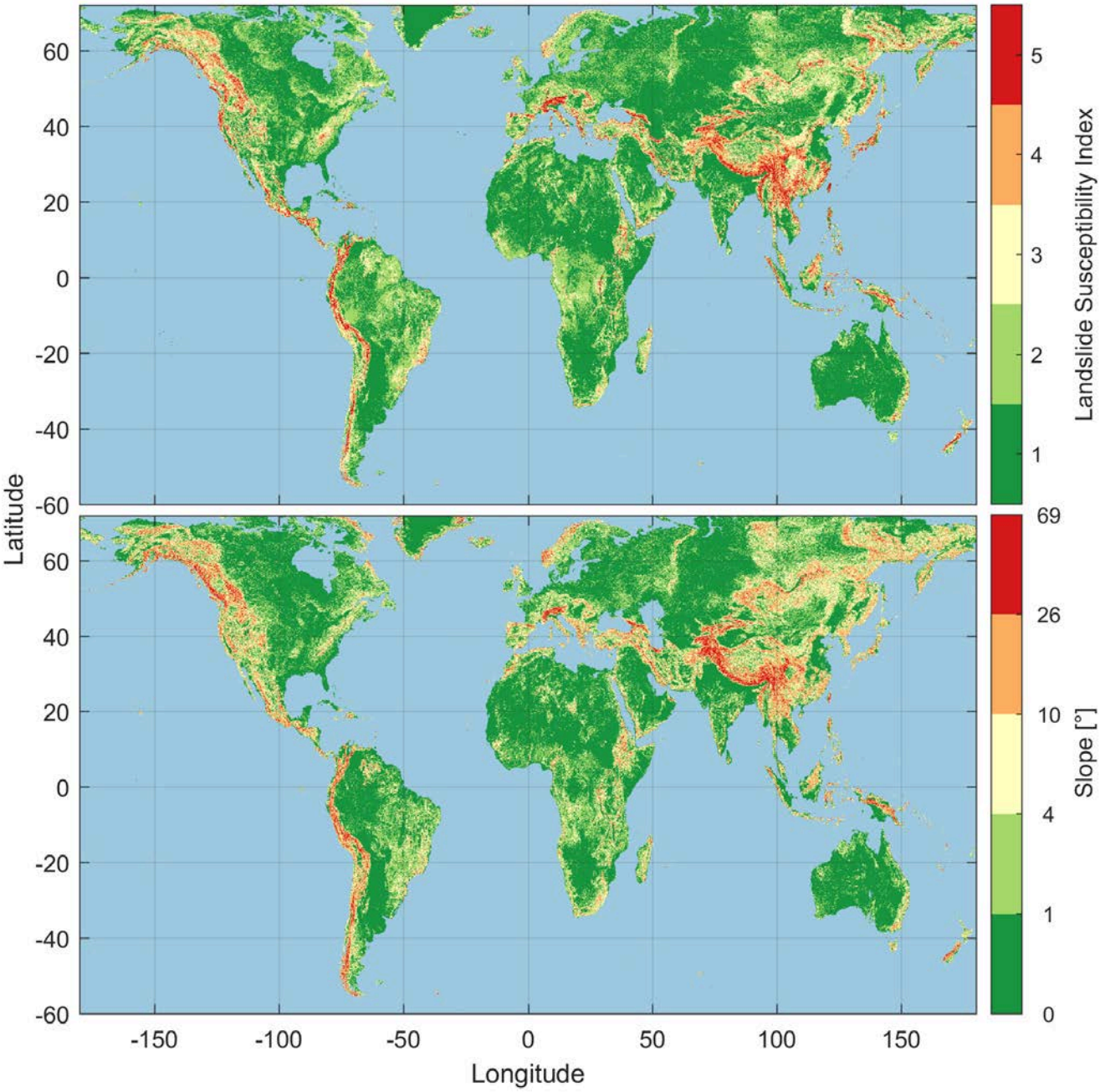

FIGURE 1.3: Global susceptibility map based on slope, distance to fault, road network, and forest loss by Stanley and Kirschbaum (2017); and logarithmic scale slope map based on SRTM 30 digital elevation model by Hengl and Reuter (2010).

1.2 Research Questions and Objectives

The distribution of landslides may mirror the distribution of rainfall, e.g., Harikumar (2016) claimed concordant landsliding and rainfall movement due to the orographic influences in their study site of southwestern India. In another example, Matsushi et al. (2014) argued that the spatial distribution of landslides were aligned with the rainfall anomaly (Figure 1.4) rather than the absolute rainfall amount (Figure 1.5) during the 2011 extreme rainfall event in Kii Mountains of Japan. They derive the rainfall anomaly, normalizing the total rainfall amount during the event by local maximum daily rainfall, which is the average of the 5 largest daily rainfalls in the last 30 years. In addition, Pike and Sobieszczyk (2008) showed that the rainfall on windward slopes is higher due to the constant wind direction during the rainstorm of January 3-5, 1982 increasing the number of debris-flows on those slopes in Oakland area of the United States. As seen in the above examples assessing variations in slope stability considering spatial rainfall patterns is mostly concentrated on a single rainstorm. There are a few studies that considered longterm (months to years) behaviour of the rainfall to assess landslide distribution: Minder et al. (2009) estimated variations in cohesion analytically based on a 7 year maximum 24 h average rainfall rate (4×4 km resolution) and found similar variations in landslide activity in the Olympic Mountains of the United States. Their study motivated e.g., Guimarães et al. (2017) to assess the landslide susceptibility in Southeastern Brazil, where orographic rainfall is a major influence on landslide initiation. Kumar et al. (2017) similarly discovered that the spatiotemporal distribution of rainfall triggered landslides coincide with the windward side of the Himalayan front (Figure 1.6). Both Guimarães et al. (2017) and Kumar et al. (2017) used consistent satellite rainfall estimates of the Tropical Rainfall Measuring Mission (TRMM, ∼25×25 km resolution) that operates since 1997. Examples above suggest that an objective and consistent quantification of the rain movement could add robust detail to studies of rainfall-triggered landslide susceptibility, though none has assessed this in country scale (e.g., Japan) and only a few adopted multi yearly rainfall data. This particular observation leads to my first research question:

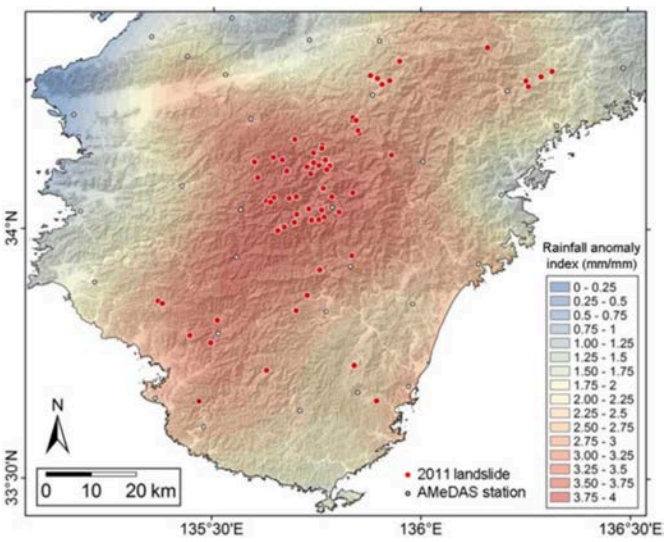

FIGURE 1.4: Landslide distribution at Kii Mountains of Japan by Matsushi et al. (2014). Rainfall anomaly is based on the radar-based cumulative rainfall from August 31 to September 5, and the local maxima that is derived by interpolating 30 years AMeDAS (Automated Meteorological Data Acquisition System) stations data.

Question RQ1: What (more) can we learn about regional-scale trajectories of extreme rainfall? Can this new knowledge aid landslide prediction eventually?

The main motivation behind the research question RQ1 is to understand spatial dynamics of the regional scale extreme rainfall and to link the extreme rainfall movement to landslide distribution, which can be addressed in a few steps. First, an "event" should be defined; there exist no conventional definition to determine a rainfall event from daily rainfall time series, each single quantity can be considered as an event (Stolbova et al., 2014; Malik et al., 2016), since the beginning and the end times of the rainfall are not provided. Several definitions concern "extreme rainfall", for example, IPCC (www.ipcc.ch, accessed April 12, 2018) defines "heavy or extreme rainfall" as a rare event within its statistical reference distribution in a certain spatial extent. The event is rare only when it occurs over a given threshold value above the right tail of the probability distribution (Fischer et al., 2017). This interpretation of extreme rainfall varies spatially by definition (Hamada et al., 2014); a few centimetres of rainfall can cover a large portion

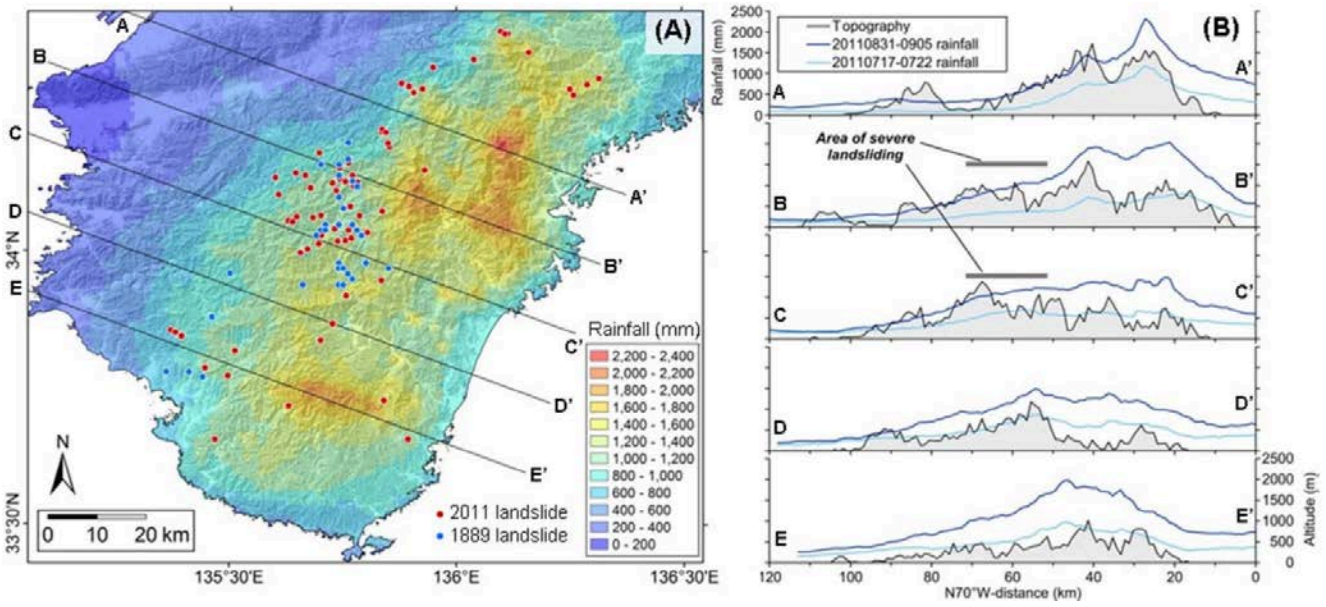

FIGURE 1.5: Landslide distribution at Kii Mountains, Japan by Matsushi et al. (2014). (A) Shaded area shows the radar-based cumulative rainfall distribution from August 31 to September 5, 2011. Red circles are the locations of deep-seated landslides triggered by the rainfall 2011 event, whereas blue circles indicate the historic landslides triggered by a similar rainfall event on 1889. (B) Location of landslides on the profiles of topography and rainfall, landslides are located out around the orographic rainfall center.

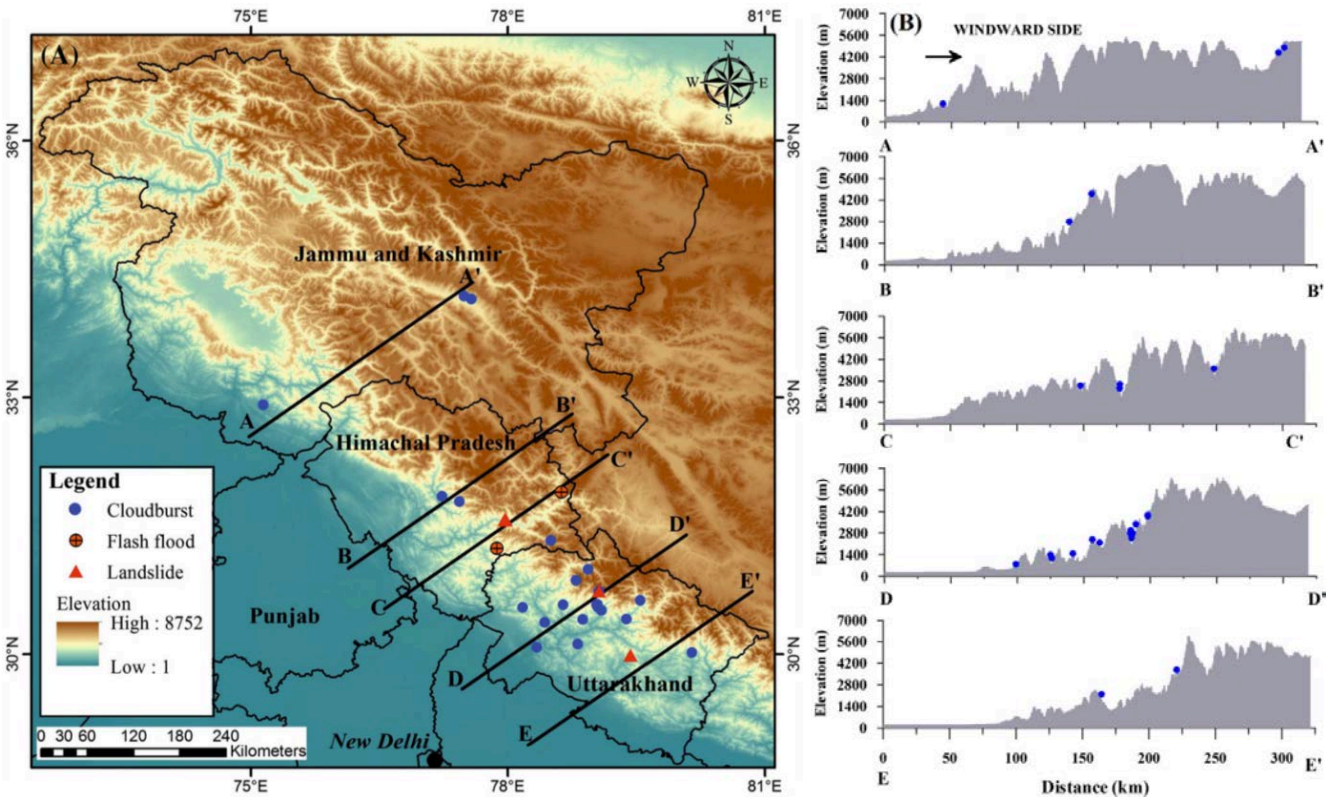

FIGURE 1.6: Extreme rainfall associated events in the Himalayan front by Kumar et al. (2017). Cloudbursts, flash floods, and landslides are given separately in (A), whereas they are shown all with blue circles in (B) along the profiles A–A' to E–E'.

of the annual rainfall in arid regions (Rasmussen and Houze, 2012; Youssef et al., 2016), whereas similar amounts could be ordinary in places such as Japan.

Then, I need to identify weather systems behind the rainfall extremes, such as orographic downpours linked to low-level jets (Monaghan et al., 2010; Sato, 2013), mesoscale convective systems (Houze, 2010; Prein et al., 2017), and tropical storms (Cheung et al., 2014; Zhang et al., 2018). In particular tropical storms are common triggers of landslides in Northwestern Pacific countries (Chang et al., 2014; Chung et al., 2017). For example, Typhoon Nabi triggered hundreds of landslides killing 27 people in Kyushu, Japan in 2005 (Taniguchi, 2008). Typhoon Talas similarly triggered more than 70 landslides in southern Japan causing some 50 casualties in 2011 (Chigira et al., 2013). Winds around the eye (center) of a tropical storm are the strongest in a cyclone system that boost evaporation of surface waters. Water vapour rises and rain bands form primarily around the eye ($\leq$100 km) and diverge outwards. Hence rainfall distribution during a tropical storm depends on the track of the storm, though rain clouds can form asymmetrically in longer distances (>100 km) from the eye. Frontal storms (e.g., monsoon driven Baiu Front) also trigger landslides such as those that were triggered by heavy rains in July 2012 (Duan et al., 2014) or in July 2003 (Sidle and Chigira, 2004) in Japan. I expect that the extreme rainfall trajectories of such dynamic weather systems show some correlation with the landslide distribution considering all the examples above. Though extreme rainfall triggering weather systems are impersistent throughout time, especially when long term behaviour (months to years) is studied, for example, July 2017 floods in Fukuoka prefecture of Japan were caused by frontal storms, while Typhoon Nanmodal was approaching to the same area, which was hit by another typhoon (named Noru) only a month after in August. Hence I need to study the spatiotemporal behaviour of those systems on such a study site that the seasonal patterns are distinct from each other.

Rainfall time series include also extremes that were triggered by convective systems (Houze et al., 2007). Those convections are mostly localized and spatially constraint (Malik et al., 2012), since they are linked to the heat driven vertical transfer of moisture. They might, nevertheless, bias a spatially dynamic model that investigates the rainfall movement. Hence, I need a method that could avoid such spatially static extremes. In this study, I adopted the method of complex networks, which simplifies assessing the complex real world phenomena by linking, e.g., remote rainfall systems that are not physically connected with a cloud system, but are linked to another atmospheric system, such as El Niño (Tsonis and Swanson, 2008; Yamasaki et al., 2008), or South Asian Monsoon (Malik et al., 2012), and thus happen simultaneously. Theoretically complex networks are defined as topological graphs that include nontrivial links (edges) between related objects (Newman, 2010), which are rainfall time series in this study. When those links are associated with a direction, the graph is called directed network, in which rainfall propagates from one cell to another. Over the years complex network tools are developed to reveal critical information in several fields, for instance to increase the efficiency of information transfer over internet by locating most used links, or to find the spread route of a disease through a community: during the 2014 Ebola outbreak 30% scheduled flights are canceled to/from the most exposed countries to mitigate the spread of the disease (Anderson, 2014). Although the use of network theory is fairly young in climate science (Tsonis et al., 2006), directed networks proved to be useful by, e.g., capturing lagged occurrence of extreme rainfalls at different locations in South America that can predict floods (Boers et al., 2014a).

A rainfall time series stands for a particular location (e.g. a cell in a grid domain), and correlation metrics are used to define links between individual rainfall time series (Tsonis and Roebber, 2004). I used the non-linear correlation metric of event synchronization (ES), which is suitable to assess rainfall time series, because they follow an heavy tailed distribution and include several recordings that are zero (no rain) (Malik et al., 2012; Stolbova et al., 2014). ES accounts for the delayed correlation between rainfall time series, since an event might move to a different cell in the grid, while continuing for several days (Rheinwalt et al., 2016; Agarwal et al., 2017). Hence ES allows setting directed networks, which can e.g. separate incoming and outgoing links. I used those directed links to estimate the general tendency of rainfall propagation within the grid.

The scales of these extreme rainfall triggering systems (e.g., tropical storms) are sometimes reaching

to 1000s of km expanding beyond land and cover also seas, it is therefore reasonable to study the spatial dynamics of rainfall, using e.g., coarse resolution (daily, ∼25×25 km) satellite rainfall estimates such as the one that is provided by TRMM. Nevertheless it is very unlikely that an entire country (e.g., Japan) is exposed to one single rainfall system simultaneously; even Super Typhoon Tip (known as Warling in the Philippines), the largest tropical cyclone ever recorded with a diameter of ∼2,220 km (Figure 1.7), made landfall only in southern Japan in 1979 (Dunnavan and Diercks, 1980). In contrast, the area of a rainstorm can easily exceed that of a catchment (Bronstert et al., 2018) requiring high resolution data (e.g., minutely radar data, ∼1×1 km). Controlling factors can greatly alter slope stability and landslide distribution under similar rainfall conditions within such small catchments, e.g., roads favouring infiltration rates (Lombardo et al., 2015), hydrological response of the landscape such as dynamics of the water content and pore water pressure of the soil (Bordoni et al., 2015). Hence regional scale susceptibility maps might be misleading when landslide susceptibility is assessed locally (van Westen, 2016). My second research question arises from this insight:

Question RQ2: What are the local impacts of extreme rainstorms on landslide triggering? Can we improve regional landslide susceptibility estimates including local effects, such as geology, topography, or other anthropogenic interventions?

The main motivation for this research question is to state the complexity of a local rainfall-induced landslide episode, through understanding the interaction between the landslide triggering and controlling factors in local scales. As discussed above properties of the rainstorm (i.e. intensity and duration) should be primarily explored to answer Research Question RQ2. The floods linked to the rainstorm could further enhance landsliding by undercutting river banks (Gupta and Sah, 2008). I will analyse those local influences retrospectively to study landslide distribution under extreme rainfall to demonstrate that the real trigger is really the rainstorm.

Landslides tend not to appear out of a sudden only because of a triggering event, such as rainfall, slope instabilities develop usually through weathering and erosion processes, for example when the lithology favours karstification. Each triggering event, such as rainfall or earthquakes, might increase the instability, eventually leading to the failure by the last trigger. In this regard the long-term legacy of earthquakes is rarely studied (Schwanghart et al., 2016), although they may continue shaping the landscape for centuries (Stolle et al., 2017). Earthquakes leave cracks on hillslopes besides triggered landslides; such disturbed hillslopes could further be reactivated by a future rainfall or earthquake (Parker et al., 2015), hence the landslide hazard persists (Tang et al., 2016). For instance, the post-earthquake sediment transport rate was higher than before the earthquake for about 6 years after the Chi-Chi earthquake (M_W 7.3) in 1999 (Hovius et al., 2011), and elevated sediment transport is predicted to last 20 years in the case of Wenchuan earthquake (M_W 7.9, 2008) (Huang and Fan, 2013). These increased rate of sediment transport is partly due to the dumped landslide deposits on the stream lines, but it might partly be fed by newly triggered landslides during post-earthquake triggers, such as new earthquakes or rainfall. In regard of all the above mentioned processes, damage accumulation on hillslopes can introduce biases when assessing landslide distribution due to a later trigger such as rainfall. As a result the last research question of this work is;

Question RQ3: How does precursory earthquake shaking change the stability conditions of a landscape and prepare it for rainfall-triggered landsliding?

Main goal of this research question is to explore whether long-term effects of earthquakes shaking can be quantified and influence future landsliding. I need to answer first what is the dominant or characteristic failure mechanism (i.e. progressive, retrospective) of landslides under seismic loading in order to determine the susceptible controlling parameters, which could eventually help understanding the landslide distribution after an earthquake. Many observations show that landslide area decreases with the distance from the ruptured fault line (Keefer, 2000), as well as with decreasing earthquake magnitude (Malamud et al., 2004). A universal approach, however, fails to represent the relationship between earthquake magnitude and landslide area (Tanyaş et al., 2017). The fault type and the slip rate

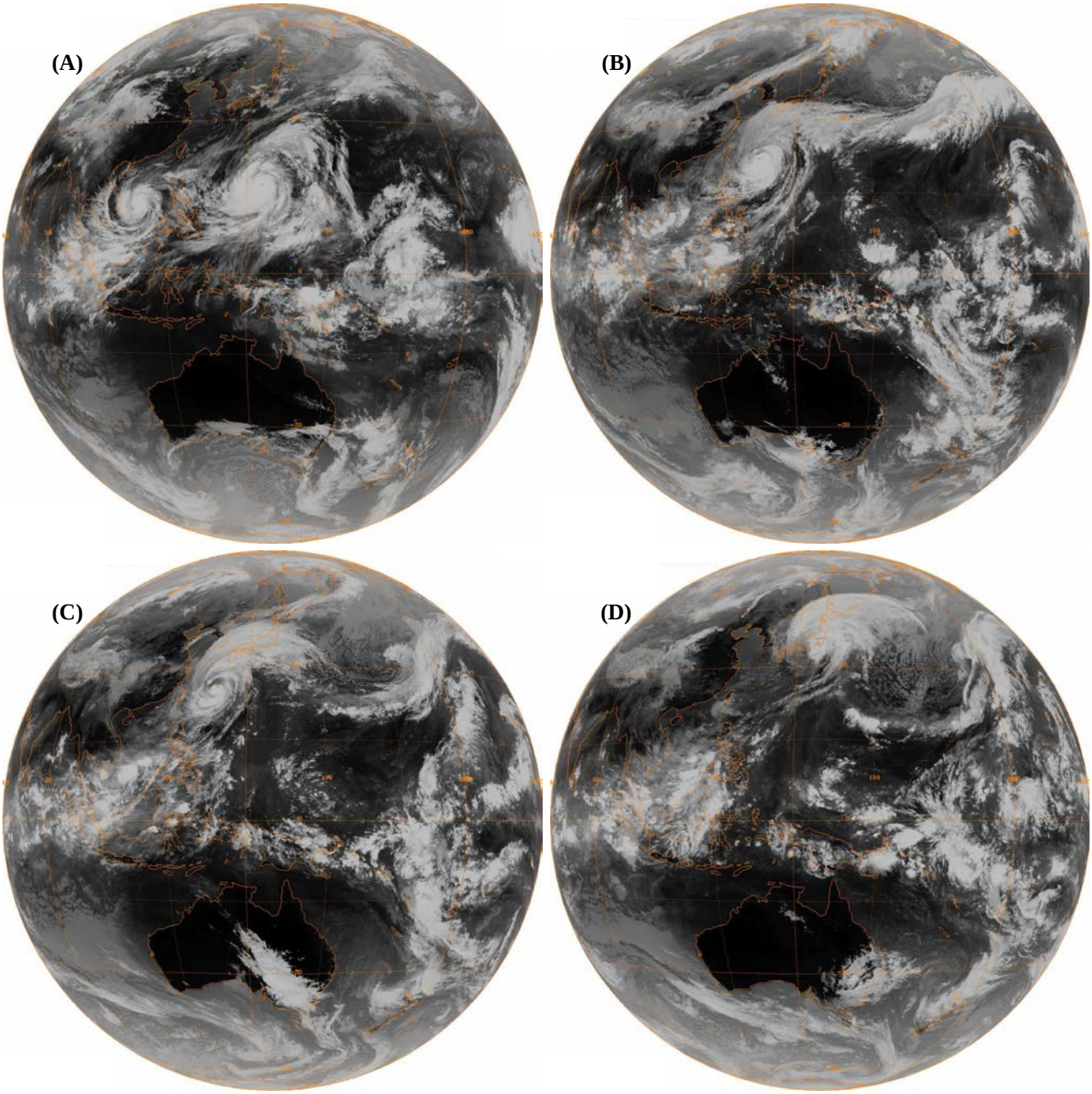

FIGURE 1.7: Global satellite (GMS-1 Satellite, http://www.ncdc.noaa.gov/gibbs/, accessed July 19, 2018) images of Typhoon Tip (1979) provided by National Oceanic and Atmospheric Administration (NOAA). (A) Typhoon Tip near its peak strength in the center, and Typhoon Sarah heading toward Vietnam, image at 3am on October 12, 1979. (B) Typhoon Tip approaching to Japan, image at 3pm on October 17, 1979. (C) Typhoon Tip was covering entire Japan expect Hokkaido, northernmost main island of Japan, image at 3pm on October 18, 1979. (D) Typhoon Tip was losing it is power in higher latitudes, image at 3pm on October 19, 1979.

of the earthquake could be crucial to study the spatial clustering of landslides (Huang and Fan, 2013), since Meunier et al. (2007) claim that local geological and geomorphological conditions to have little effect on earthquake-triggered landslide distributions. For example, landslides, which are triggered by the 2008 Wenchuan earthquake (M_W 7.9), are concentrated on the hanging wall of the fault rupture (Figure 1.8), and they align normal to the rupture, indicating the directivity effect of the seismic waves (Chigira et al., 2010). I want to further test these claims and explore the influence of landscape conditions after an earthquake.

All these research questions are derived based on the literature, and they aim to advance the understanding of interaction between landslide triggers and controls to better assess landslide susceptibility. The questions cover a broad area of research that is beyond the capacity of a thesis. Hence, I try to answer them at least partially in chapters 2 to 4, and discuss the remaining issues to the best of my knowledge in the Chapter 5.

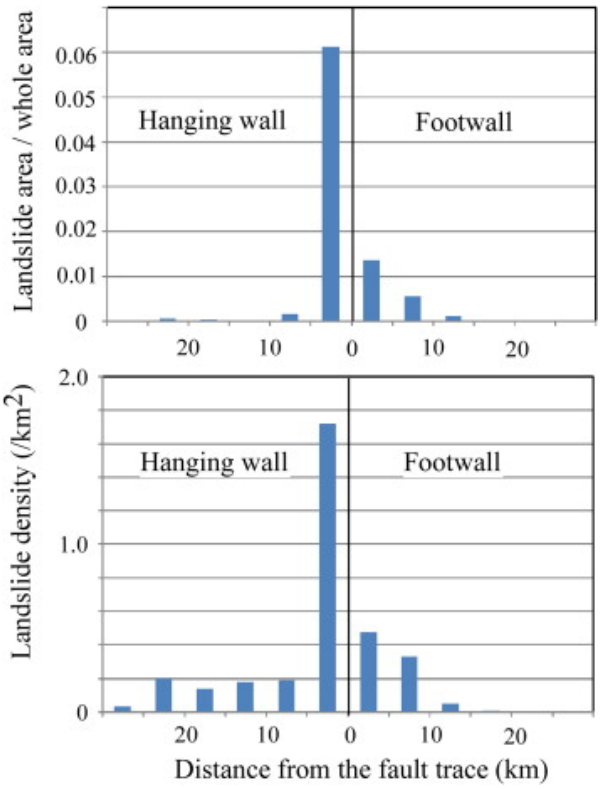

FIGURE 1.8: Landslide areas on the hanging- and foot-walls of the YBF-Beichuan–Yingxiu fault (Figure 1.2) after the Wenchuan Earthquake (M_W 7.9) by Chigira et al. (2010). Relatively fewer landslides occurred on the footwall. The ratio of landslide areas and the whole areas is shown above, whereas bottom plot shows only the landslide density.

1.3 Study Sites

About 2,500 non-seismic landslides killed nearly 32,000 people between 2004 and 2010, with the highest toll concentrating in South and Southeast Asia, mainly India, China, Japan, and the Philippines (Petley, 2012). The Japanese islands are among the regions with the highest landslide occurrence worldwide (Figure 1.3, Stanley and Kirschbaum, 2017). This motivated me to choose Japan as my first study region (Figure 1.1) in order to explore the influences of the triggering and controlling factors on rainfall-induced landslides. Japan has a long history of rainfall and/or earthquake induced landslides due to its topographic features, about 70% of the terrain is mountainous and rugged. The country is surrounded by the Pacific Ocean, Sea of Japan, and the East China Sea; hence it is frequently exposed to typhoons, extreme rainfall, and heavy snowfall. Annual rainfalls vary from 700 mm in North to up to 3000 mm in South, which are expected to increase in a warming climate with more extreme rainstorms (Manda et al., 2014), as projected by the Intergovernmental Panel on Climate Change, IPCC (Hartmann et al., 2013). IPCC expects landslide activity to increase in the future accordingly, raising the need for more landslide prediction campaigns and risk mitigation studies (Dou et al., 2014). Frontal and tropical storms-derived rains are the major contributors of extreme rainfall in Japan (Ohba et al., 2015), and they often trigger landslides (Yamao et al., 2016). The Baiu front dominates heavy rainfall events in the early summer months of June and July, and tropical storms are more effective then up to November providing excellent seasonal contrast to study the individual impacts of both separately. More details about the precipitation regime of Japan are provided in chapter 2. Japanese research institutes additionally offer extensive publicly available datasets that cover land use conditions and geology besides countrywide landslide databases that is necessary to fulfil the objectives of this study (i.e., RQ2 and RQ3).

In April 2016 Kumamoto (Japan) was struck by an earthquake (M_W 7.1) that caused heavy structural damage and about 1500 landslides, mostly debris flows. 10 (from a total of 50) casualties were associated directly to the landslides (Fukuoka et al., 2017). Nearly all the landslides are detached in tephra layers

of different age around the Aso Caldera. Cracks on these unstable slopes increased the susceptibility to further slope failures in the following months during the rainy season from May to November (Kiyota et al., 2017). Accordingly rainstorms followed the earthquake soon after (∼5 days) increasing the chance of further landsliding. Here I investigated the geomorphic legacy of this strong earthquake in preparing the landscape for further landsliding under future triggers (i.e. rainfall) at the regional scale. Such earthquakes might dominate the preferred aspect and spatial distribution of landslides in the Japanese archipelago.

My third study site is Braunsbach in the low-relief humid parts of southern Germany (Figure 1.1). Braunsbach is nearly free from seismic influences; only two events are recorded for 1976-2018 around ∼150 km azimuthal distance according to the global centroid moment tensor catalog (GCMT, Dziewonski et al., 1981; Ekström et al., 2012). Southern Germany receives relatively less annual rainfall (<∼1000 mm) (Bronstert et al., 2018), when compared to Japan (∼2000 mm). Nonetheless the area is prone to landslides and soil erosion, given the increased high-intensity and short-lasting heavy rainfalls (Mueller and Pfister, 2011). There happened a devastating flash flood with high number of landslides (∼40) along 1.5 km-long Orlacher Bach in May 29, 2016 as a result of heavy rainstorms. Braunsbach village, located on the fan of the Orlacher Bach, took heavy damage from this flash flood. This event captured our attention particularly due to the high debris concentration that destroyed parts of the village, in contrast to the surrounding areas within ∼100 km, where nearly equal or more rainfall totals were recorded with lower damage rates. Further details of the study site are presented in the chapter 3. I had the opportunity to conduct fieldwork in the Orlacher Bach valley within a group of fellow doctoral students and investigated the geomorphic changes along the stream about a month after the area was secured. This field campaign provided us a unique opportunity to investigate the interaction between an extreme rainfall and landslides at the scale of a small catchment.

1.4 Outline

The research questions (section 1.2) of this thesis requires combining analysis that are acquired in different scales (section 1.3, figure 1.9). Hence, chapter 2, 3, and 4 address the three research questions (i.e. RQ1, RQ2, and RQ3) in stand-alone scientific papers that were published work in peer-reviewed journals. Chapter 2 describes the methods I developed for tracking extreme rainfall, and was published in "Chaos: An Interdisciplinary Journal of Nonlinear Science" (AIP). Chapter 3 investigates the topographic and geological factors that are active during extreme rainfall that triggered landslides, and was published in "Science of the Total Environment" (Elsevier). Chapter 4 studies the earthquake directivity and topographic amplification effects on spatial landslide distribution, and was submitted to "Earth and Planetary Science Letters" (Elsevier), it is currently under review. I discuss the overall outcome of these studies in a broader framework focusing on the main research questions in Chapter 5, and end with some conclusions and outlook for future research in Chapter 6.

1.5 Contribution to Publications

The scientific papers that merge the core of the thesis is as follows:

Paper I

Ozturk U., Marwan N., Korup O., Saito H., Agarwal A., Grossman M. J., Zaiki M., and Kurths J.: Complex networks for tracking extreme rainfall during typhoons, Chaos: An Interdisciplinary Journal of Nonlinear Science, 28(7), 075301. doi: 10.1063/1.5004480, 2018.

I am the lead author of this manuscript, I performed the main study and wrote the manuscript. Norbert Marwan and Ankit Agarwal helped developing the method introduced in the manuscript. Hitoshi Saito, Michael J. Grossman and Masumi Zaiki contributed writing the introduction section and review the manuscript. Oliver Korup and Jürgen Kurths supervised the study, besides reviewing the manuscript.

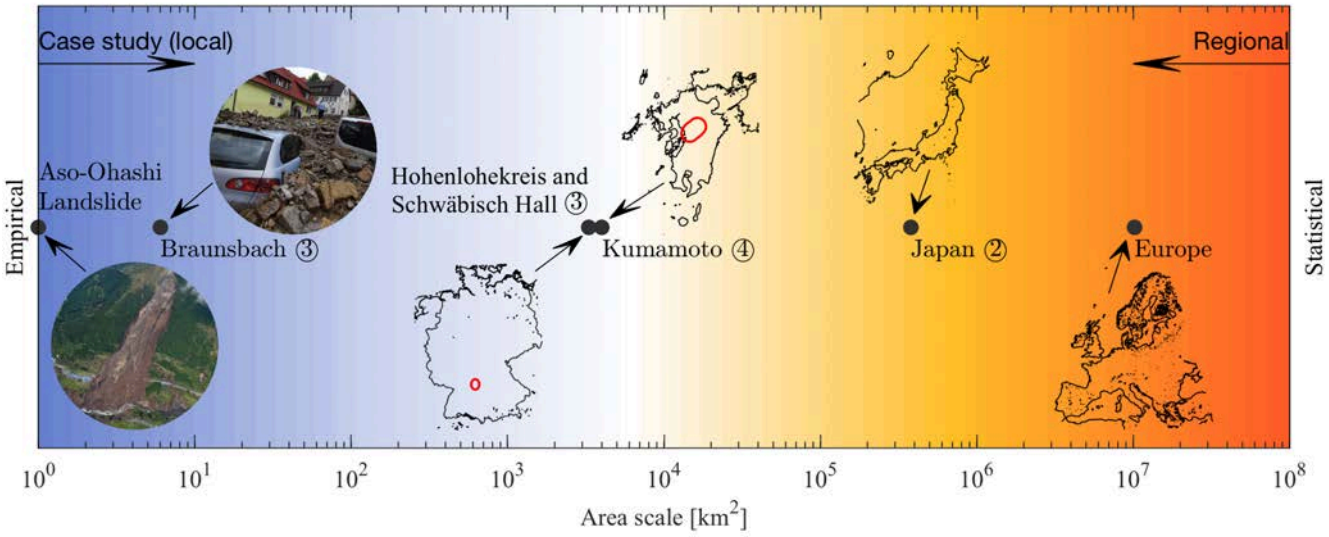

FIGURE 1.9: Structure of the thesis with regard to the study sites (section 1.3). Research question RQ1 is investigated in Japan applying statistical methods; whereas RQ2 is analysed in Braunsbach and the surrounding areas of Braunsbach, i.e. Hohenlohekreis and Schwäbisch Hall, combining empirical and statistical models; and RQ3 is assessed using statistical models in Kumamoto, Japan. The background color indicates the transition from empirical to statistical assessment models in relation to the area scale of the study sites as a visual aid. Chapters numbers are given after the respective study site. Aso-Ohashi landslide shows how small a huge landslide (∼0.16 km^2) is, when compared to the areas of regional landslide susceptibility models, such as the European Landslide Susceptibility Map, Elsus V1 (∼10^7 km^2, Günther et al., 2014b). The photo of the Aso-Ohashi landslide is taken from a Mainichi helicopter on April 22, 2016 (mainichi.jp, accessed on 31st August, 2018). The photo that shows the deposited material in Braunsbach (by Marijan Murat, Goetz, 2016).

Paper II

Ozturk U., Wendi D., Crisologo I., Riemer A., Agarwal A., Vogel K., López-Tarazón A. J., Korup O.: Rare flash floods and debris flows in southern Germany, Science of the Total Environment, doi: 10.1016/j.scitotenv.2018.01.172, 2018.

I am the lead author of this manuscript, I performed the main study and wrote the manuscript. Dadiyorto Wendi partly contributed performing the geostatistical analysis, whereas Irene Crisologo investigated the rainfall characteristics based on rainfall radar data. Adrian Riemer and Ankit Agarwal helped in the field work and writing the introduction and study site sections. Kristin Vogel, José Andrés López-Tarazón and Oliver Korup supervised the study and reviewed the manuscript.

Paper III

von Specht S., Ozturk U., Veh G., Cotton F., Korup O.: Landslides lean on long-period seismic directivity: analyzing the geomorphic response to the Kumamoto M_W7.1 earthquake, Solid Earth, doi: 10.5194/se-2018-101, 2019.

I am the second author of this manuscript, in which the lead author is Sebastian von Specht. He investigated the seismic data, whereas I performed the assessment about the topographic effects. The manuscript is written equally by both of us. Georg Veh contributed in visualization, and helped in improving the manuscript. Fabrice Cotton and Oliver Korup supervised the study and reviewed the manuscript.

Chapter 2

COMPLEX NETWORKS FOR TRACKING EXTREME RAINFALL DURING TYPHOONS

This chapter is published as:

Ozturk U., Marwan N., Korup O., Saito H., Agarwal A., Grossman M. J., Zaiki M., and Kurths J.: Complex networks for tracking extreme rainfall during typhoons, Chaos: An Interdisciplinary Journal of Nonlinear Science, 28(7), 075301. doi: 10.1063/1.5004480, 2018.

Abstract

Reconciling the paths of extreme rainfall with those of typhoons remains difficult despite advanced forecasting techniques. We use complex networks defined by a nonlinear synchronization measure termed event synchronization to track extreme rainfall over the Japanese islands. Directed networks objectively record patterns of heavy rain brought by frontal storms and typhoons but mask out contributions of local convective storms. We propose a radial rank method to show that paths of extreme rainfall in the typhoon season (August-November, ASON) follow the overall southwest-northeast motion of typhoons and mean rainfall gradient of Japan. The associated eye-of-the-typhoon tracks deviate notably and may thus distort estimates of heavy typhoon rainfall. We mainly found that the lower spread of rainfall tracks in ASON may enable better hindcasting than for westerly-fed frontal storms in June and July.

Plain language summary

Complex network is a special type of graph describing meaningful interactions of real life systems (e.g., social, biological); it is also a popular tool to investigate the spatiotemporal dynamics of climate systems, such as extreme precipitation. Tropical storms incur substantial losses each year, particularly in the western Pacific. Despite many advances in their monitoring and forecasting, the dynamics of extreme rainfall patterns remains partly unresolved. We use complex networks for investigating how extreme rainfall correlates in space and time during the passage of tropical storm over the Japanese archipelago. We found that the rainfall tracks consistently diverge from eye-of-the-typhoon tracks, while the mean difference in track azimuths decreases from frontal storm (June-July) to typhoon seasons (August-November). This outcome might increase the predictability of the extreme precipitation during the typhoon season.

2.1 Introduction

The Northwest Pacific has the world's highest frequency of tropical storms, and Japan is hit by an average of 26 tropical storms (defined as having sustained wind speeds >17 m/s, and referred to here as "typhoon") each year according to the Japan Meteorological Agency (JMA). Together with extra-tropical lows, the Baiu Front and local convection cells bring nearly 75% of Japan's total annual precipitation between April and October (Kanae et al., 2004; Saito et al., 2014). Yet typhoons and the Baiu Front are largely responsible for the highest rainfalls (Fukui, 1970). The Baiu Front brings early summer rainfall as part of the Asian monsoonal system (Krishnan and Sugi, 2001). The front extends from eastern China east-northeastward into the Pacific following the island arc of Japan and forms where warm maritime

tropical air mass intersects with cool polar maritime air (Matsumoto, 1989). Polar and subtropical jets push this moisture eastwards onto Japan from early June to late July (Sampe and Xie, 2010). This eastward moisture flow at around $35°N$ is unique in the northern hemisphere (Ninomiya, 1984). Except for Hokkaido, most of Japan experiences Baiu-derived heavy rainfall, which is most pronounced in Kyushu (Matsumoto, 1989), shown with the colors light green to red tones in Figure 2.1c. Typhoons also have links to the Asian monsoon and the Madden-Julian Oscillation (Nakazawa, 2006; Heistermann et al., 2013a) and bring heavy rainfall from August to November.

Recent studies suggest that typhoon tracks in the Northwest Pacific have shifted west towards South Korea since the 1950s with rising intensities (Webster, 2005; Kim et al., 2006). The number of typhoons that make landfall in Japan grows according to the scenarios of the Intergovernmental Panel for Climate Change, IPCC (Murakami et al., 2011; Manda et al., 2014). Hence, quantifying the tracks and intensities of extreme rainfall is essential for informing quantitative assessments of concomitant flood and landslide hazards. Previous work identified major eye-of-the-typhoon (center of the tropical storm) tracks (ETTs) over Japan (Grossman and Zaiki, 2009; Grossman et al., 2016) and interpreted their temporal trends as proxies for atmospheric warming (Knutson et al., 2010). Several approximately stationary long lasting downpour structures (rainbands) evolve around the eye-of-the-typhoon (Willoughby et al., 1984; Marchok, 2014). Rain structures around the eye wall up to 100 km are distributed nearly symmetrically (Li et al., 2015), and they behave asymmetrically in increasing distance from the eye (Hence and Houze, 2012; Yu et al., 2015). The ETTs deviate from those of extreme rainfall and a proposed "docked inner rain shield" mainly within $150 - 250$ km northeast to southeast of the eye, and a rarer "outer rain shield" up to 500 km northwest to southwest of the eye (Shimazu, 1998). Yet this phenomenon awaits further systematic documentation and tracking.

To approach this problem of objectively capturing rainfall trajectories (information transfer) alongside the ETTs, we use complex networks, an approach that has recently emerged for analysing geoscientific data (Phillips et al., 2015), particularly in climate science (Steinhaeuser and Tsonis, 2014; Marwan and Kurths, 2015), hydrology (Sivakumar and Woldemeskel, 2014; Halverson and Fleming, 2015; Jha et al., 2015; Agarwal et al., 2017), seismology (Abe and Suzuki, 2007), and geomorphology (Heckmann et al., 2015). Such networks capture the dynamics (information flow) of vertical wind field interactions (Donges et al., 2011), decadal climate variability (Tsonis and Swanson, 2012), or extreme floods (Boers et al., 2014a).

Our aim is to use complex networks to objectively and consistently track extreme rainfall caused by tropical and frontal storms over Japan (causal links), and to check for systematic offsets from EETs. The underlying idea is to determine the correlation between rainfall time series at gridded geographic locations. Two locations are linked if their correlation coefficient exceeds a defined threshold (Tsonis and Roebber, 2004). Network analysis focuses mostly on the existence of such edges instead of the details of their interaction, though edges can be weighted by their correlation strength (Onnela et al., 2003, 2004). All edges form an adjacency matrix to encode a complex network (Tsonis et al., 2006). Cumulative rainfall data are mostly heavy tailed (Papalexiou et al., 2013), calling for non-linear functions to capture correlations between event series (Donner and Barbosa, 2008; Donges et al., 2009). Event synchronization (ES) is an intermediate non-linear tool to detect delayed correlation between spatially separated event series (Quiroga et al., 2002). Complex networks based on ES express the correlation between extreme rainfall events such as those during the South Asian (Malik et al., 2012) or South American (Boers et al., 2014a,b) monsoons and yield good agreement with modeled wind directions from National Centers for Environmental Prediction (NCEP) and National Center for Atmospheric Research (NCAR) or Modern Era Retrospective-analysis for Research and Applications (MERRA) reanalysis data.

2.2 Data

We analysed satellite-derived daily (1998-2015) rainfall estimates from the Tropical Rainfall Measuring Mission (TRMM 3B42V7) at 0.25° spatial resolution (Bolvin and Huffman, 2015). We split the data into

those linked to the Baiu frontal storm season from June 1 to July 31 (JJ, Figure 2.1a, c) and those linked to the typhoon season from August 1 to November 30 (ASON, Figure 2.1b, d) (Matsumoto, 1989), defining rainfalls above the $95th$ percentile as extreme (Im et al., 2015; Castellano and DeGaetano, 2016). The Regional Specialized Meteorological Center (RSMC) in Tokyo and the Japanese Meteorological Agency (JMA) provide ETT data (1998-2015), including storm names, dates, and geographic positions of the eye at 6-hourly intervals for sustained wind speeds >17 m/s (Figure 2.2).

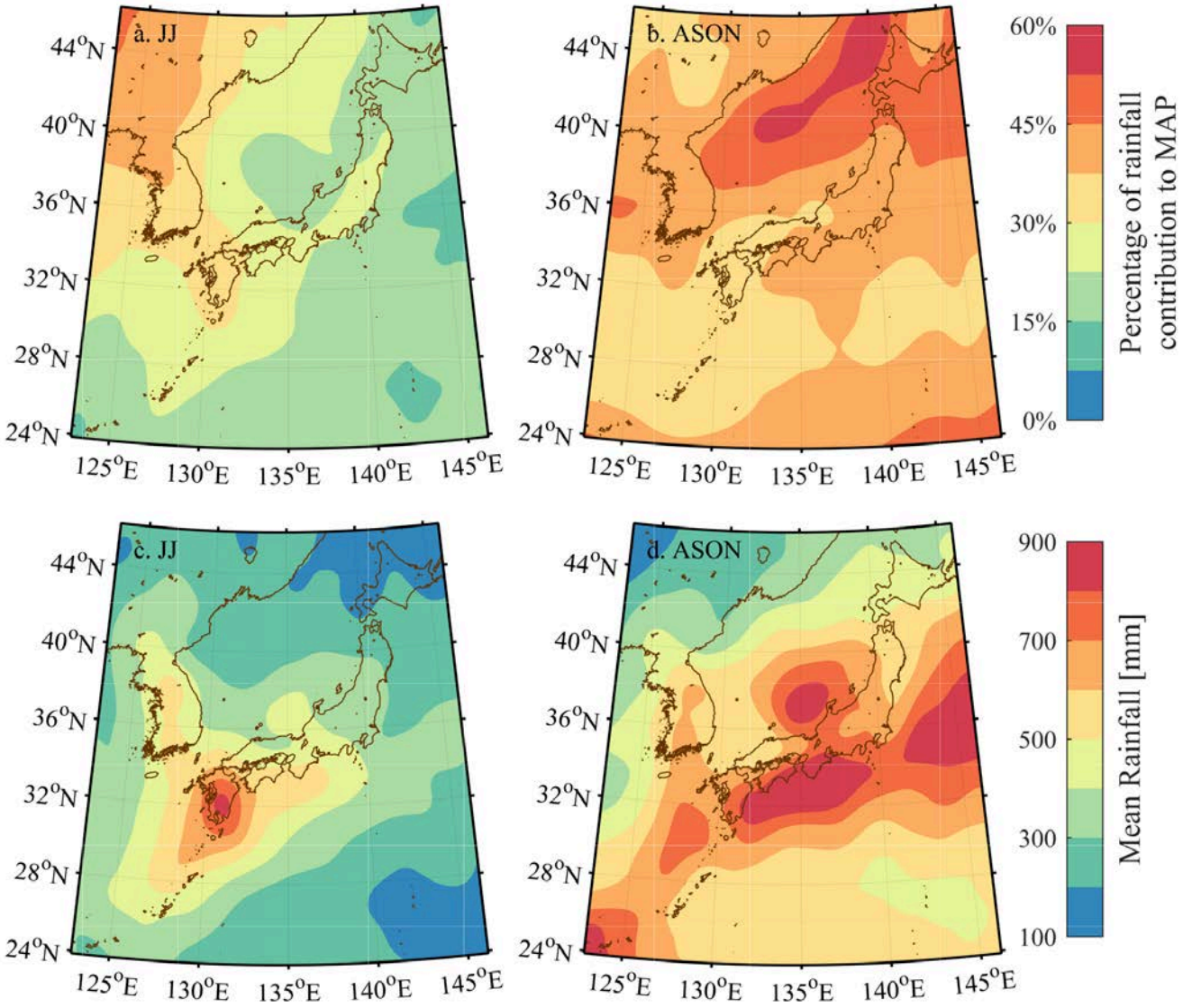

FIGURE 2.1: Rainfall distribution in the study area based on the TRMM data. a. and b. Ratio of rainfall during JJ and ASON and mean annual rainfall (MAP, 1998-2015). c. and d. Mean annual rainfall in JJ and ASON.

2.3 Methods

Event synchronization (ES) and the radial ranks R^r_{ij} are used together to estimate the information flow on a network in order to track the extreme rainfall. ES is characterized by a time-delay parameter q_{ij} and a strength parameter Q_{ij} (Section 2.3.1). We used q_{ij} to build directed networks A^q_{ij}, in which the edges also define directions (Section 2.3.2). Then we identified sources and sinks of extreme rainfall with a centrality measure termed network divergence Δk_i, which is the difference between the number

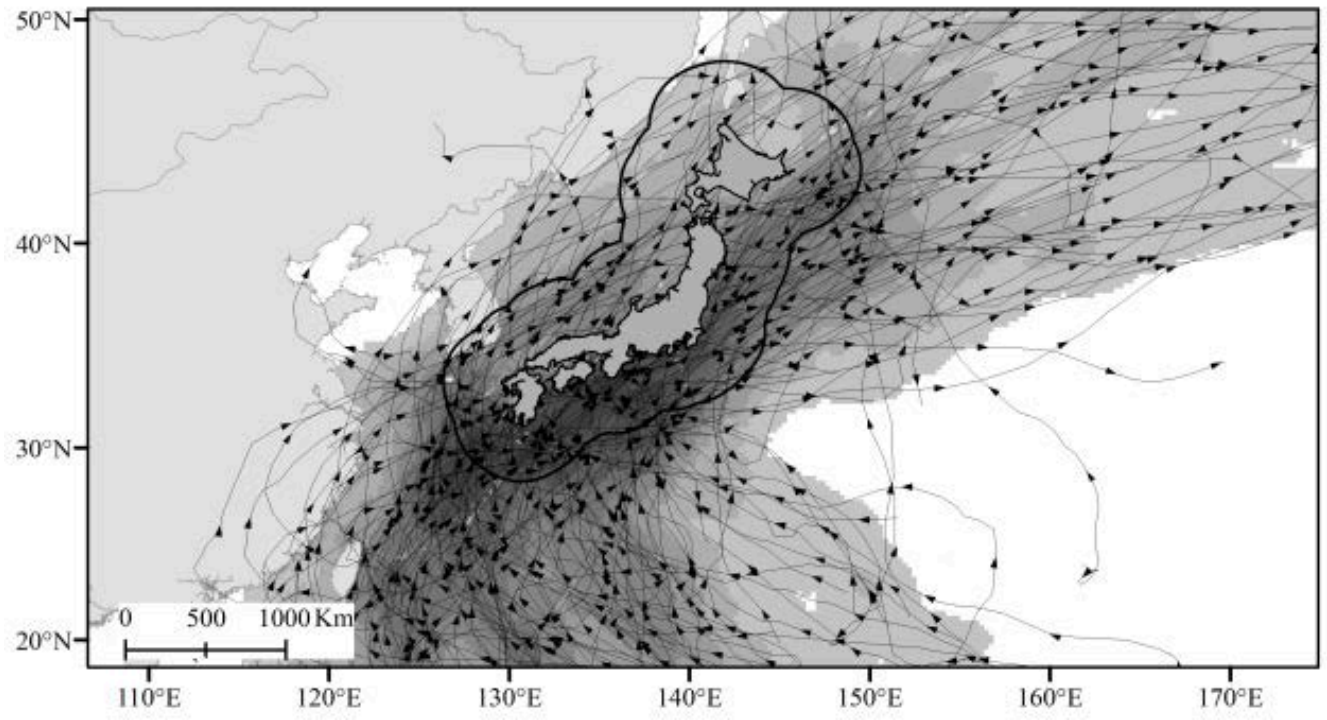

FIGURE 2.2: Tracks of tropical storms that came within 300 km of the four main islands of Japan between 1998 and 2015. Darker shades indicate higher density of tracks.

of incoming and outgoing edges that a node has (Section 2.3.3). In theory, low and high values of Δk_i locate the sources and sinks of rainfall, respectively. Finally, we coupled Q_{ij} with the radial ranks R^r_{ij} to estimate the trajectories of the network flux (Section 2.3.4).

2.3.1 Event synchronization

In event synchronization of TRMM data, each spatial rainfall grid cell represents a network node. Event synchronization determines the correlation between extreme rainfall events at two grid cells i and j, as well as the time delay between them. For example, an extreme event l occurring at grid point i at time t^i_l is considered synchronized with another event m occurring at grid cell j at time t^j_m, within interval T^{ij}_{lm}. This time interval T^{ij}_{lm} is based on the shortest interval between two successive extreme events $l \pm 1$ and $m \pm 1$ in each time series (Stolbova et al., 2014):

$$T^{ij}_{lm} = \frac{\min\{t^i_{l+1} - t^i_l, t^i_l - t^i_{l-1}, t^j_{m+1} - t^j_m, t^j_m - t^j_{m-1}\}}{2} \tag{2.1}$$

Thus, T^{ij}_{lm} indicates the potential for linked events in the two time series, as it depends on the frequency of extreme events. Each paired link is weighted with a coefficient J_{ij} reflecting whether an event occurred first at location i ($J_{ij} = 1$) or j ($J_{ji} = 0$); if they occur simultaneously at both locations, $J_{ij} = J_{ji} = 0.5$. Each event is counted once through this weighting. We measure synchronization by counting the number of synchronized events in both time series $c(i|j)$ and $c(j|i)$ (Malik et al., 2010; Stolbova et al., 2014), which are the weighted count of the events in i and j, respectively,

$$c(i|j) = \sum_{l=1}^{s_i} \sum_{m=1}^{s_j} J_{ij} \tag{2.2}$$

where s_i and s_j are the total numbers of extreme events; $c(i|j)$ and $c(j|i)$ define a strength parameter Q_{ij} between two grid cells (Stolbova et al., 2014),

$$Q_{ij} = \frac{c(i|j) + c(j|i)}{\sqrt{(s_i - 2) \cdot (s_j - 2)}} \tag{2.3}$$

and the delay parameter (or direction) q_{ij},

$$q_{ij} = \frac{c(i|j) - c(j|i)}{\sqrt{(s_i - 2) \cdot (s_j - 2)}} \tag{2.4}$$

The strength of the event synchronization is normalized to $0 \leq Q_{ij} \leq 1$, whereas for the delay parameter $-1 \leq q_{ij} \leq 1$. For example, $q_{ij} = 1$ means that an extreme event at location i was always followed by an extreme event at grid cell j, whereas $q_{ij} = -1$ expresses this relationship in the opposite direction; q_{ij} infers the migration of extreme precipitation in the sense of directed propagation in networks.

2.3.2 Undirected and directed adjacency matrices

Strength parameter Q_{ij} expresses a correlation between two grid points. We set an arbitrary chosen threshold θ_{ij}^{Q} to determine the highest synchronization between two grid cells. We chose this threshold such that only 5% of the strongest correlations build the network following the examples of Malik et al. (2010) and Stolbova et al. (2014). From this network we derive an adjacency matrix,

$$A_{ij}^{Q} = \begin{cases} 1 \leftarrow Q_{ij} \geq \theta_{ij}^{Q} \\ 0 \leftarrow else \end{cases} \tag{2.5}$$

where $A_{ij}^{Q} = 1$ denotes a link (edge) between i and j, and $A_{ij}^{Q} = 0$ denotes no link. This adjacency matrix is symmetric and has zeros along its diagonal. The edges have no ranks. We also calculate a non symmetrical directed adjacency matrix A_{ij}^{q} to encode the movement direction of extreme rainfall from the asymmetrical q_{ij} matrix. We select the threshold θ_{ij}^{q} in the same way as we did for the threshold for the strength parameter θ_{ij}^{Q}. However, in this case the notation of A_{ij}^{q} is different, because $-1 \leq qij \leq 1$.

$$A_{ij}^{q} = \begin{cases} \left.\begin{array}{l} 1 \leftarrow q_{ij} \geq \theta_{ij}^{q} \\ 0 \leftarrow q_{ij} < \theta_{ij}^{q} \end{array}\right\} 0 \leq q_{ij} \leq 1 \\ \left.\begin{array}{l} 0 \leftarrow q_{ij} > -\theta_{ij}^{q} \\ 1 \leftarrow q_{ij} \leq -\theta_{ij}^{q} \end{array}\right\} -1 \leq q_{ij} < 0 \\ 0 \leftarrow else \end{cases} \tag{2.6}$$

2.3.3 Network flux of the directed network

In a directed network, all the edges have a direction into (k^{in}) or out (k^{out}) from a node. The asymmetry of A_{ij}^{q} allows us to compute the network divergence (Malik et al., 2012; Boers et al., 2014a).

$$\Delta k_i = k_i^{in} - k_i^{out} \tag{2.7}$$

The network divergence is a centrality measure describing the difference of in-degree (the number of incoming edges of a node) and out-degree centrality (the number of outgoing edges of a node). Centrality measures are biased by spatial embedding due to distance-based costs of the edges, e.g., border cut edges that in reality exist with the outside of the study site. Centrality measures are thus distorted, unless the entire globe (without study site borders) is considered with equidistant grid; thus, we need to correct for boundary effects, e.g., using surrogate ensembles (Heitzig et al., 2012). We approximated the edge-length distribution in our network A_{ij}^{q} using azimuthal distances (as integer) between nodes. We calculated the

probability of an edge for each approximated distance in our network. We then generated 1000 spatially embedded random networks based on this distribution and computed the network divergence for each to estimate boundary effects (Rheinwalt et al., 2012) and used these to normalize the boundary effects.

2.3.4 Radial ranks

The R^r_{ij} metric is inspired by the fast marching method (Sethian, 1996) and finds the most plausible flux direction in the spatially embedded correlation matrix of Q_{ij}. The fast marching method systematically computes the propagation times of waves from a source node in a grid (Sethian and Popovici, 1999). It is originated from the Dijkstra's algorithm (Dijkstra, 1959). Dijkstra's algorithm computes the shortest path on a network, in which each path is assigned a cost to travel. It selects a starting node (i) with "0" travel cost and checks the cost of travelling to the neighbouring nodes (j), eventually shifting the selected node (i) to the lowest cost distant neighbour ($j_{cheapest}$). The process is repeated iteratively until the final destination is reached. It is inconvenient when a continuous meshed domain is considered, since it follows a stair step pattern throughout the representative nodes of the meshed domain. The fast marching method instead runs by setting the investigation area to an arbitrary zone around the center. Retaining the Dijkstra's principle of a single-pass allowance, the fast marching method approximates the gradient between nodes, which makes it more suitable for meshed grids. Then, the selected zone of interest propagates in the marching direction stepwise with the propagation time following the cheapest path (Sethian and Popovici, 1999). The method to determine the directions of propagation is repeated iteratively from a center point in all directions until the end point(s) is(are) reached.

We are inspired by this algorithm to determine the cost of travel in all possible directions for all the nodes in their neighbourhoods. When the information flow is slow, the adaptive time interval T^{ij}_{lm} [Equation 2.1] between the two events will increase, decreasing the strength parameter Q_{ij}. High Q_{ij} means that the information transfer between the nodes is rather fast. Thus, Q_{ij} is inversely linked to the distant costs in the Dijkstra's example. A node has several potential directions, along which synchronization is high. The radial rank method approximates the gradient between an arbitrary number of nodes z^{inv}_i around the source node. We determined the cost of travel in 1°-steps of azimuthal direction for different search radii. Summing Q_{ij} radially along vectors within z^{inv}_i (in our case seven grid cells), we calculated R^r_{ij} for the azimuthal directions (Figure 2.3).We used the intersection of the vector with a given grid cell as a weight w^{inv}_{ij} for R^r_{ij}:

$$R^r_{ij}(\varphi) = \sum_{1}^{z^{inv}_i} Q_{i'j'} \cdot w^{inv}_{i'j'} \rightarrow (i'j') = f(i, j, \varphi, z^{inv}_i) \tag{2.8}$$

We choose the vector with the maximum rank φ^{max}_i as the representative direction for the grid cell in question (Figure 2.3):

$$\varphi^{max}_i = \underset{\varphi}{\operatorname{argmax}}[R^r_{ij}(\varphi)] \tag{2.9}$$

The network flux reveals details of Δk_i, whereas φ^{max}_i shows the paths of extreme rainfall, thus reflecting directions of synoptic weather patterns.

2.4 Results

In this section, we present how network measures together with our proposed radial rank metric can show extreme precipitation flux over the Japanese archipelago, and then we will discuss these results in the following discussion section.

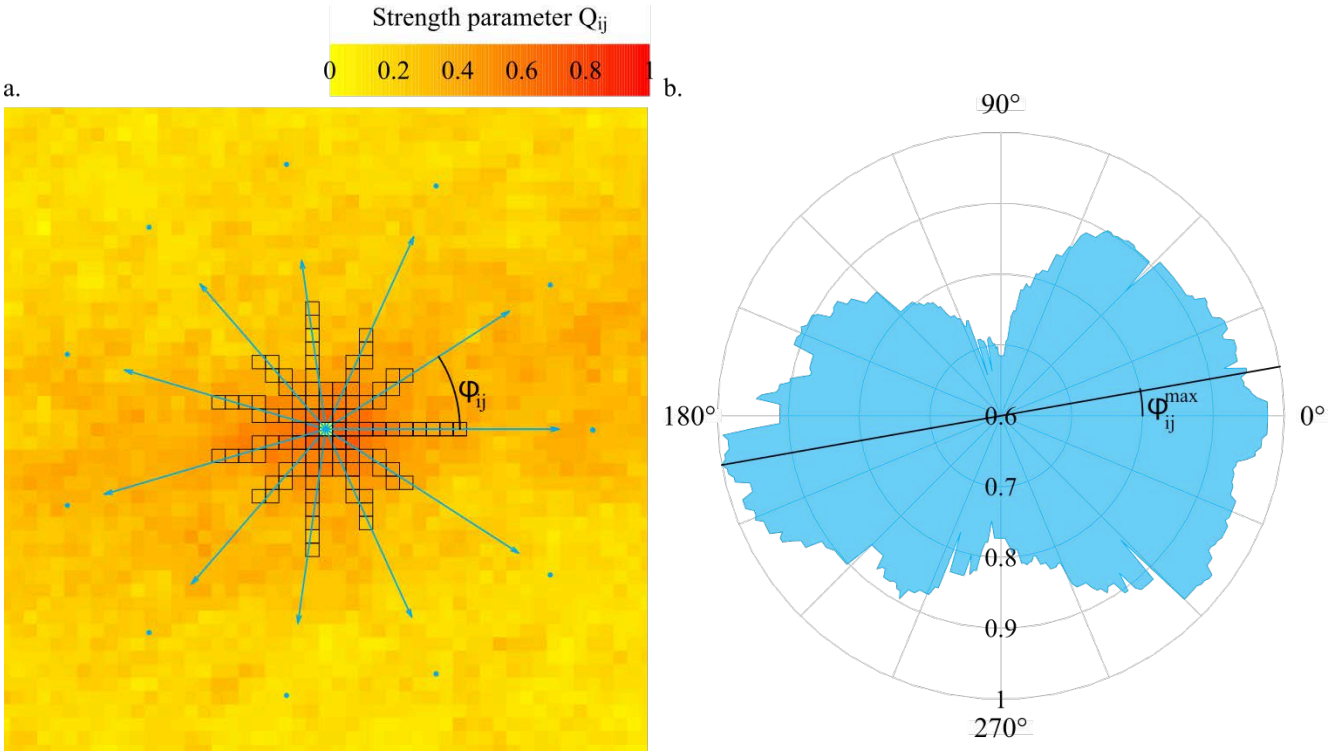

FIGURE 2.3: a. Sample view of an extreme rainfall grid with 11 sample vectors (we computed 360 vectors in total at 1°-intervals). The lengths of the vectors are scaled to strength parameters Q_{ij} of the first ten grid cells that the vector intersects with ($z_i^{inv} = 10$). Each grid cell has a weight w_{ij}^{inv} in this scaling, based on the intersection of the vector with that grid cell. b. 2π domain of the radial ranks R_{ij}^r. Black line is the maximum ranked vector φ_i^{max} , which is either 11° or 191° in this example.

2.4.1 Network divergence

We find that network divergence Δk_i has a northwest trend in JJ and ASON, clearly spatially separating sources and sinks of extreme rainfall in the nearly two decades that we analysed (Figure 2.4a, b). The dominant motion of extreme rainfall is from southwest to northeast, roughly along the axis of the island arc and the overall gradient in mean annual rainfall. Along the source-sink transition (the dark blue line) the noise is somewhat higher in JJ than in ASON, with a distinct shift of the sink towards Kyushu (Figure 2.4a, b). In ASON, the sources are pushed further to the northwest compared to conditions in JJ (Figure 2.4c). The sinks over southern Honshu and Kyushu vanish during ASON, while the source-sink transition rotates slightly clockwise centred roughly about the Japanese Alps.

2.4.2 Radial ranks

Typhoons can travel 400 to 500 km within a day. Hence, we examined R_{ij}^r over larger distances to account for effects of individual storms, guided by the size of Typhoon "Tip", which was some 2000 km in diameter and the largest recorded (Dunnavan and Diercks, 1980). By default R_{ij}^r linearises the trajectories of rainfall extremes over longer distances but remains noisy for shorter distances ($z_i^{inv} < 6$). Selecting a search radius $z_i^{inv} > 15$, however, fully masks the meandering movement of extremes. The angular deviation of φ_i^{max} is up to 45° (Figure 2.4e, f). Beyond a distance of about seven grid cells, φ_i^{max} converges to an azimuth within a range of 2°. We note that all angles refer to two possible directions (e.g., $3\pi/4 = -\pi/4$), since the angle is computed in $[-\pi/2, \pi/2]$.

We find that in the Sea of Japan and far eastern Asia, the general northeast flux is suppressed during JJ (Figure 2.4c). Directions vary between −15° and 30° but remain between 15° and 30° in the East China Sea and north of the Philippine Sea. This easterly influence decays over longer distances ($z_i^{inv} > 6$).

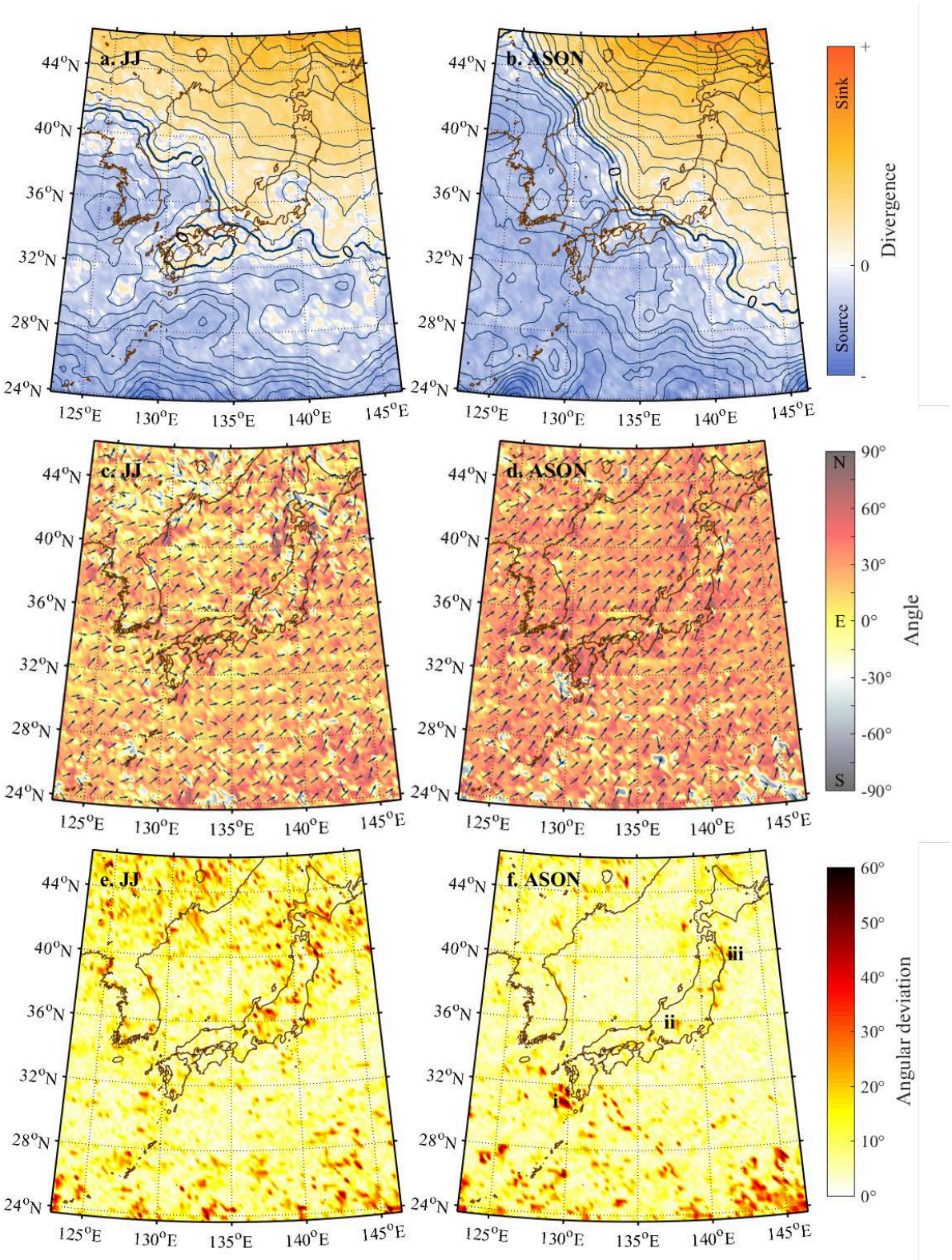

FIGURE 2.4: [a. and b.] Network divergence Δk_i in a. JJ and b. ASON, defined as the difference of incoming and outgoing links at each grid cell. Positive (negative) values are sinks (sources) in the directed network. Contours are irregularly spaced for visual aid. [c. and d.] Maximum radial ranks φ_i^{max} based on seven grid cells ($z_i^{inv} = 7$) for c. JJ and d. ASON. Tones of orange are φ_i^{max} directions from southwest to northeast (or opposite); tones of gray are φ_i^{max} directions from southeast to northwest (or opposite). [e. and f.] Angular deviation of φ_i^{max} for step-wise extension of radial ranks from 7 ($z_i^{inv} = 7$) to 15 grid cells ($z_i^{inv} = 15$) (nine angles for each grid cell); σ_c is the circular standard deviation of all directions for e. JJ and f. ASON. Divergent zones with high angular deviation are marked as "i", "ii", and "iii".

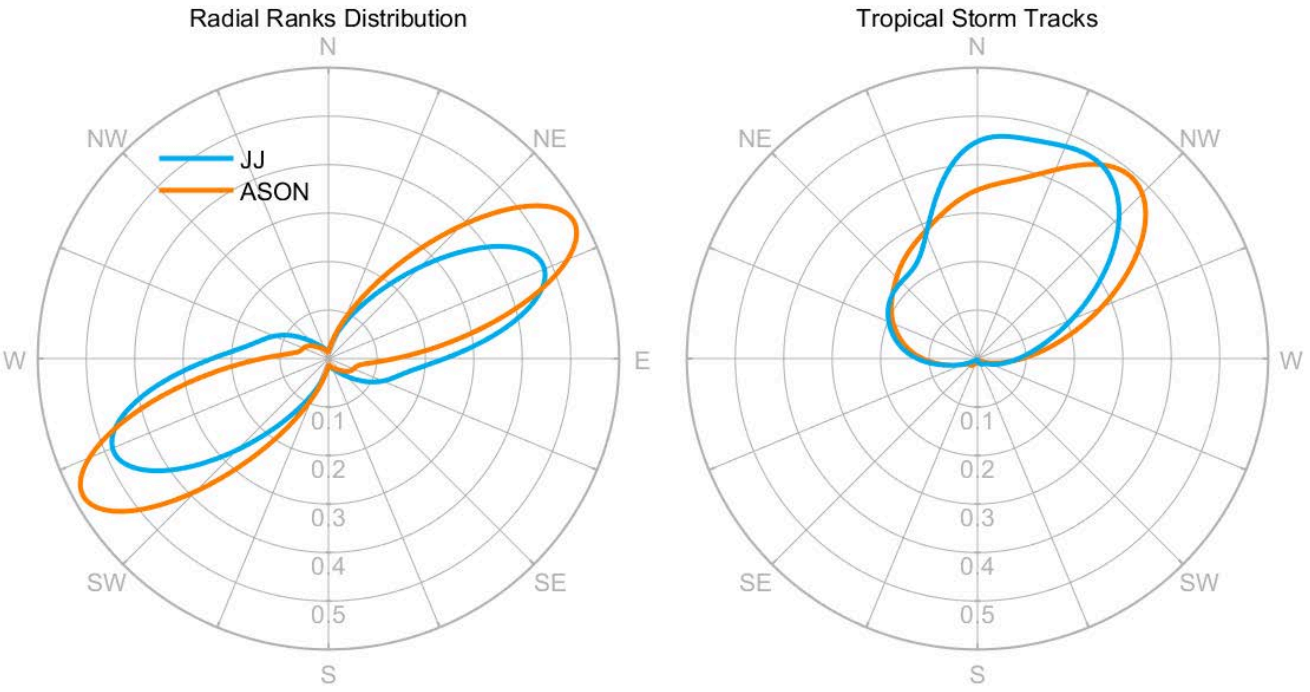

FIGURE 2.5: Azimuthal directions of maximum radial ranks φ_i^{max} of extreme rainfall (left) compared to those of eye-of-the-typhoon tracks (ETTs, right). Probability density functions are estimated from kernel densities.

The extreme rainfall tracks tend to follow the coastline of Honshu during both periods. In JJ, deviations increase over the Asian mainland and the Japan Sea. High deviations also occur near the $25°N$ parallel in JJ. In ASON, these tracks are oriented $30° \pm 10°$ and less spread out than in JJ (Figure 2.4d). Local deviations from this field are north of the Philippine Sea, around southwest of Kyushu (Figure 2.4f, i), over the Japanese Alps (Figure 2.4f, ii), and at about 40°N 143°E (Figure 2.4f, iii).

2.5 Discussion

Typhoons mainly originate in the central western Pacific and move first towards the Philippines or Taiwan before veering north to Japan, and travelling to the east once more in mature stages. Most typhoons traverse Japan from southwest to northeast (Grossman et al., 2015), influencing how extreme rainfall propagates, particularly during ASON (Figure 2.5b). Ninomiya (1984) and Sampe and Xie (2010) argued that early summer (JJ) extreme rainfall is mainly derived from east-northeast moisture transport during the Baiu Front.

The influence of the ETT is apparent in the high local deviations (Figure 2.4f, i and iii), where ETTs form two groups within ±1.5° of azimuthal direction ($n > 50$). About a third of all the ETTs move northwest (southeast in Figure 2.4d; circular mean $\mu_{c1} = -47° \pm 30°$, the error margin is the circular standard deviation), while the others move northeast ($\mu_{c2} = 56° \pm 21°$) around southwest of Kyushu (Figure 2.4f, i). Although nearly all the ETTs point to the northeast in Figure 2.4f, iii, they form two equally probable clusters ($\mu_{c1} = 73° \pm 11°$ and $\mu_{c2} = 31° \pm 10°$). The spread is higher between 24° and $30°N$ in both periods and reflects at least two distinct groups of ETT [$\mu_{c1} = -39° \pm 32°$, $\mu_{c2} = 54° \pm 27°$; Figure 2.4e, f, although ETTs tend to converge north of $>30°N$. The high angular deviation over the Japanese Alps (Figure 2.4f, ii) might reflect orographic effects on rainfall (Malik et al., 2010).

Underlying factors that generate rainfall within a typhoon vary, due to cyclonic wind speed, vertical wind shear, and land–sea contrast (surface friction, moisture supply). These factors are closely linked to

the angular deviation of maximum radial ranks φ_i^{max}. When there is a large-scale vertical wind shear (e.g., in mid-latitudes, westerlies), a convection maximum is expected on the right hand side of the shear vector (Corbosiero and Molinari, 2002; Li et al., 2015), while a decrease in the velocity might enhance the rainfall intensity (Revadekar et al., 2016). In the western North Pacific, most intense rains were observed on the right side of the eye due to the frictional convergence at the coastal terrains; wind retardation on the onshore side (creating surface convergence) and wind acceleration (creating surface divergence) on the offshore side (Gao et al., 2009).

Westerly frontal storms influence the maximum radial ranks φ_i^{max} during JJ, despite some five typhoons per year on average that add to the variability of φ_i^{max} (Figure 2.4c). This variability is higher on the Sea of Japan, where we expect high σ_c given the influence of westerly frontal storms. Values of φ_i^{max} tend to reflect the coastline configuration of the Japanese islands (Figure 2.4c, d). However, ETTs influence the propagation of rainfall extremes as far as northern Honshu and seem to push rainfall extremes further east. This influence increases for higher search radii z_i^{inv} [Figure 2.4f, iii).

Overall, our method objectively highlights an angular deviation of $\sim 10^\circ$ of radial-rank-derived extreme rainfall tracks from ETT (Figure 2.5, ASON), supporting Shimazu's (1998) notion of a northeast to southeast deviation of the inner rain shield. Similarly, Houze (2010) noted that the most of the inner rain shields of Hurricanes "Katrina" and "Rita" were also located around east of the eye (Hence and Houze, 2008). Clearly, the extreme rainfall does not systematically follow the ETT (Figure 2.5, ASON) but occurs mainly east-northeast of the eye. In JJ, however, the rainfall extremes are more widely spread, possibly compromising their automatic tracking during that season.

The source-sink relation also reveals a moisture source in the northern Philippine Sea (Figure 2.4a, b) in both periods (ASON, JJ), which we interpret as linked to the Asian monsoon. Frontal rainfalls instead come from the East China Sea, though ETTs follow a similar direction. In ASON, this source area extends northeast (Figure 2.4b), possibly showing a more poleward monsoonal influence (Krishnan and Sugi, 2001). Northern Japan receives more than half of its rain during ASON (Figure 2.1b), which explains the strong sink in (Figure 2.4b). Although this rainfall contribution in the high latitudes is mostly delivered by recurving typhoons over the western North Pacific, the influence of the westerlies on higher latitudes may further generate heavy rainfall while the typhoons lose energy. The sharper transition between the source and sink in ASON (as opposed to JJ) may reflect the role of typhoons over the study area, since the flux is based on a single moisture body. Smaller frontal storms, in contrast, would produce more scatter in the data as in JJ (Figure 2.4c); these storms can form rapidly depending on the presence of moisture linked to, for example, jet streams (Kurita et al., 2016) or atmospheric modes (Sato and Takahashi, 2003). In turn, adjacency matrix A_{ij}^q may contain edges regardless of moisture transfer along them.

Kyushu receives the heaviest rains during JJ (Figure 2.1c), which explains the local sink zone in Figure 2.4a. Sinks around Kyushu in JJ change into sources in the transition to ASON (Figure 2.4b), partly showing the northward shift of the Baiu front (Sato and Takahashi, 2003). This is related to the shifting of the subtropical jet in late July (Ueda et al., 1995), and to increasingly active typhoons that push the sink zones northeast compared to the pattern in JJ. Although the influence of typhoons is apparent in Δk_i (Figure 2.4a), future work needs to map the effects of individual ETT on extreme rainfall tracks. Nonetheless, we find that directed networks objectively identify regional patterns of extreme rainfall in frontal storms and typhoons and allow masking out contributions of local convective storms that hardly change their position.

2.6 Conclusions

We used complex networks to track extreme rainfall propagation over Japan and its surrounding seas. Directed networks reveal regional sources and sinks of extreme weather patterns. Moreover, we introduced radial ranks R_{ij}^r to extend this approach, and to determine the details of the direction of rainfall extremes linked to typhoons (Figure 2.4d). R_{ij}^r is easy to set up and can mimic the network flux on large spatial

scales. It requires prior knowledge about the dominant atmospheric patterns to confidently select the final direction of the flux. Derived rainfall tracks mimic the dominant southwest-northeast trend of typhoons and also Japan's mean rainfall gradient in ASON. This pattern is noisier when the more westerly frontal storms are active in JJ. Our network analysis captured an angular deviation of rainfall tracks from ETT (Figure 2.5), supporting the observations of Shimazu (1998). Consequently, the lower spread of maximum radial ranks φ_i^{max} may aid tracking extreme rainfall during the typhoon season.

Acknowledgements

We thank Irene Crisologo, Aljoscha Rheinwalt, and Bedartha Goswami for helping with some of the computations. Our research is funded by the Deutsche Forschungsgemeinschaft (DFG) within the Research Training Group "Natural Hazards and Risks in a ChangingWorld (NatRiskChange)" (DFG GRK 2043/1) at the University of Potsdam.

Chapter 3

RARE FLASH FLOODS AND DEBRIS FLOWS IN SOUTHERN GERMANY

This chapter is published as:

Ozturk U., Wendi D., Crisologo I., Riemer A., Agarwal A., Vogel K., López-Tarazón A. J., Korup O.: Rare flash floods and debris flows in southern Germany, Science of the Total Environment, doi: 10.1016/j.scitotenv.2018.01.172, 2018.

Abstract

Flash floods and debris flows are iconic hazards in mountainous regions with steep relief, high rainfall intensities, rapid snowmelt events, and abundant sediments. The cuesta landscapes of southern Germany hardly come to mind when dealing with such hazards. A series of heavy rainstorms dumping up to 140 mm in 2 h caused destructive flash floods and debris flows in May 2016. The most severe damage occurred in the Braunsbach municipality, which was partly buried by $42,000$ m^3 of boulders, gravel, mud, and anthropogenic debris from the small catchment of Orlacher Bach ($\sim$6 km^2). We analysed this event by combining rainfall patterns, geological conditions, and geomorphic impacts to estimate an average sediment yield of $14,000$ t/km^2 that mostly ($\sim$95%) came from some 50 riparian landslides and channel-bed incision of $\sim$2 m. This specific sediment yield ranks among the top 20% globally, while the intensity-duration curve of the rainstorm is similarly in the upper percentile range of storms that had triggered landslides. Compared to similar-sized catchments in the greater region hit by the rainstorms, we find that the Orlacher Bach is above the $95th$ percentile in terms of steepness, storm-rainfall intensity, and topographic curvatures. The flash flood transported a sediment volume equal to as much as $20-40$% of the Pleistocene sediment volume stored in the Orlacher Bach fan, and may have had several predecessors in the Holocene. River control structures from 1903 and records of a debris flow in the 1920s in a nearby catchment indicate that the local inhabitants may have been aware of the debris-flow hazards earlier.

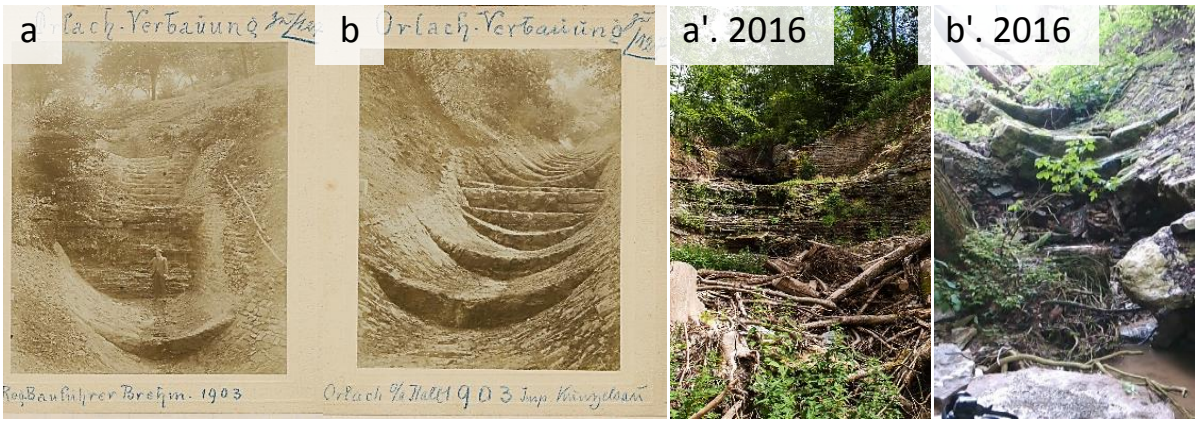

FIGURE 3.1: Historical (a and b, 1903) and after flood (c, d, 2016) state of the Orlacher Bach.

Such recurring and destructive events elude flood-hazard appraisals in humid landscapes of gentle relief, and broaden mechanistic views of how landslides and debris flows contribute to shaping small and deeply cut tributaries in the southern Germany cuesta landscape.

3.1 Introduction

Flash floods involve rapidly rising river-water levels, mostly after heavy and intense rainfall (Rozalis et al., 2010; Roux et al., 2011). Flash floods can be destructive in steep mountain streams and semiarid climates (Longoni et al., 2016a; Radice et al., 2016), where infiltration capacity is low because of crusted soils, sparse vegetation, and sealed surfaces (Sedlar, 2016). Fast moving overland flows and runoff concentrations exert high shear stresses on soil surfaces and in channels, allowing for little warning time (Bronstert et al., 2017b). Research on flash floods was rare until the 1990s before automatic monitoring tools, such as remote data transmission networks, cost-efficient distributed sensor networks, or rainfall radar equipment became routinely available, eventually affording more systematic insights (Creutin and Borga, 2003; Creutin et al., 2009; Berne and Krajewski, 2013; Ficchì et al., 2016; Longoni et al., 2016b). Detailed monitoring campaigns now elucidate the coupling of hydrological and geomorphic processes during flash floods (Archer et al., 2007; Gorczyca et al., 2014), for example landslides that transform into debris flows (Borga et al., 2014). Still, many flash floods remain unreported, particularly in humid areas with moderate relief where they are hardly studied or even documented (Bradford et al., 2012; Morss et al., 2016).

We study the geomorphic legacy of flash floods triggered by convective rainstorms in the moderate-relief cuesta landscape of southwestern Germany in late May 2016. The rainfall in the study area around the municipality of Braunsbach (∼2500 inhabitants) began on 29 May at around 4 pm (UTC). By 5 pm intensive rainfall poured down over the area, remaining high for some 70min, triggering a flash flood and debris flow that damaged >75 households in town (Laudan et al., 2017). Braunsbach and nearby small villages suffered losses of €104 million as a result (Landkreis Schwäbisch Hall, 2016). The rainfall topped the average monthly totals of May and June of nearby stations in just 4 h. Both the 24-hour and 7-day storm rainfall totals exceeded the 200-year return period (Piper et al., 2016), whereas Bronstert et al. (2018) estimated the 4-hour rainfall total to be a 1000-year event, producing a peak discharge of 125 ± 50 m^3/s in Braunsbach. We offer a first appraisal of the magnitude and frequency of the associated geomorphic impacts, and address the following research questions:

- What can we learn from the 2016 event in terms of flash-flood and debris-flow hazards in the greater region?
- What is the geomorphic relevance of flash floods and debris flow in steep tributaries of the cuesta landscape in southern Germany?
- How severe is the 2016 event compared with global data on landslide occurrence and catchment sediment yields?

We focus on the geomorphic impacts of the flash flood and debris flow that hit Braunsbach. Our main objectives are (i) to estimate the amount of sediment eroded and moved during the event and to identify the sources of sediment and modes of its delivery; (ii) to test whether various hydro-meteorological, topographic, geological, and geomorphic catchment characteristics were unique for the Orlacher Bach or whether neighbouring catchments in the region were similarly susceptible; and (iii) to place the geomorphic relevance of this event into a global context.

3.2 Study Site

The municipality of Braunsbach is located in Baden-Württemberg, Germany (Figure 3.2a). The town is situated in the Kocher River valley that cuts through the Hohenloher, Haller, and Kocher-Jagst plateaus

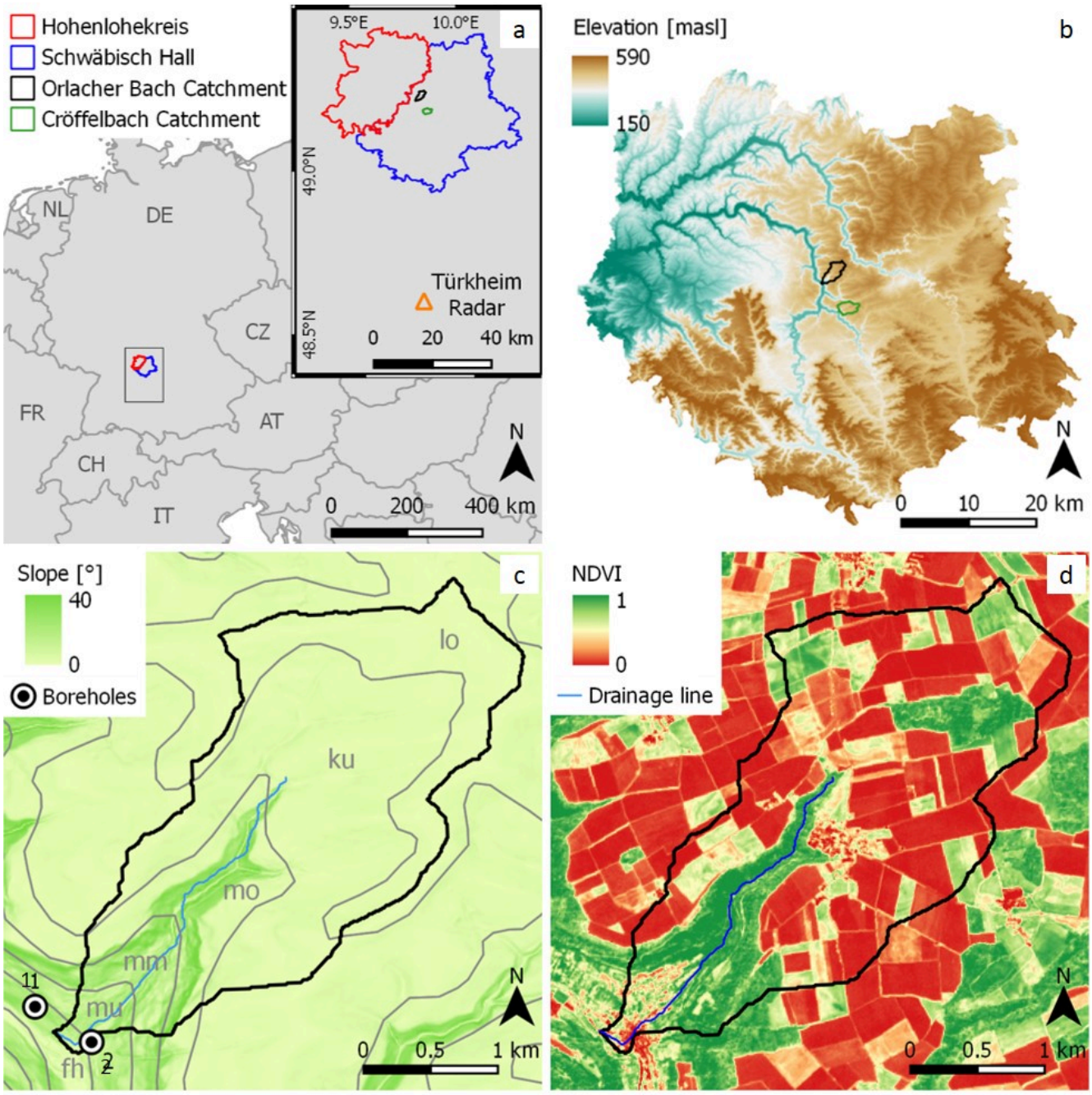

FIGURE 3.2: a. Study area of Braunsbach and the Orlacher Bach catchment, Baden-Württemberg, Germany; b. elevation profile of the study area (black polygon is Orlacher Bach catchment, green polygon is Cröffelbach catchment). c. Geology and slope with locations of boreholes, geological formations; fh = flood sediments, los =Loess, ku = Lower Keuper, mm = Middle Muschelkalk, mo=Upper Muschelkalk, mu=Lower Muschelkalk, d. Normalized Difference Vegetation Index (NDVI): high values indicate densely forested areas, whereas low values indicate scarce or no vegetation (in Orlacher Bach catchment, this is mainly agricultural land).

made up mostly by Triassic limestones. Small and steep, gully-like tributaries (locally called "Klingen") of the Kocher River emphasize the dissected nature of this cuesta landscape. The historic center of Braunsbach is built on a tributary-mouth fan formed by the Orlacher Bach that drains a catchment of ~6 km^2. The stream has a pronounced, and mostly dry, head cut at ~440 m above sea level (a.s.l.) and meets the Kocher after descending ~180 m over 3.1 km of horizontal distance. The plateaus in the headwaters of the upper catchment are mostly sustaining agricultural fields, whereas dense forest flanks

much of the channel and steep side slopes of the Orlacher Bach (Figure 3.2d).

The formation of the modern landscape around Braunsbach began in Cretaceous times, when southwest Germany experienced crustal uplift, followed by the formation of the Upper Rhine Graben in the Upper Eocene (Rotstein and Schaming, 2011). The resulting southeast tilt and dissection of the South German Basin pronounced the differences in mechanical rock resistance to erosion, and formed a cuesta landscape between 150 m and 580 m a.s.l. (Figure 3.2b), exposing in distinct morphological steps successively older rock formations towards the shoulders of the Upper Rhine Graben. Braunsbach and the upper Orlacher Bach catchment are cut in Middle Triassic limestones known as Muschelkalk, which is rich in karst landforms such as dolines, caves, and springs. Water infiltration into the fissured limestones may have promoted the growth of the short and steep V-shaped Klingen of the Orlacher valley (Hagdorn and Simon, 1985). A simplified geological profile of the catchment from top to bottom goes from Lower Upper-Triassic (Lower Keuper) in the plateau headwaters to Lower Middle-Triassic (Lower Muschelkalk) rocks at the fan head (Figure 3.2c). The region has a subhumid climate with a mean annual temperature of 9.5 °C varying between 0 °C (January) and 18 °C (July). The mean annual precipitation (MAP) is ∼650 mm; June is the wettest month (80 mm) with 15 rainy days, while March is the driest (40 mm) according to the nearest weather station at Kirchberg/Jagst–Herboldshausen (Agarwal et al., 2016).

3.3 Methods and Data

3.3.1 Rainfall

We used weather radar estimates of rainfall to complement the spatially limited data of rain gauges (Borga et al., 2007). We analysed the 5-minute DX product of the Türkheim radar (48.58 °N, 9.78 °E) 68 km south of Braunsbach provided by the German Weather Service (DWD) for the interval from 27 to 30 May 2016 (Figure 3.2a). The DX product consists of raw polar reflectivity data with a 1° beam width, and we used the open-source library wradlib to process the radar data (Heistermann et al., 2013b). We cross checked our estimates with hourly data from the DWD rain gauges (Kirchberg/Jagst–Herboldshausen; 49.18 °N, 9.98 °E; Kupferzell-Rechbach; 49.24 °N, 9.68 °E; Vellberg-Kleinaltdorf; 49.12 °N, 9.89 °E; Ingelfingen-Stachenhausen; 49.33 °N, 9.70 °E). Attenuation effects in the raw radar data returned some rainfall estimates below those recorded by the rain gauges (Bronstert et al., 2018). Thus, we corrected the radar data using the modified Kraemer approach (Jacobi and Heistermann, 2016), and then derived the rainfall amounts from the corrected reflectivity using the standard Marshall-Palmer $Z - R$ relation ($Z = 200R^{1.6}$), where Z is the radar reflectivity in dBZ and R is the rainfall amount in mm/h. The rainfall estimates from the radar were summed up for 48 h prior to the event (midnight to midnight of 27 to 29 May 2016) to determine the antecedent rainfall. We also summed up the radar estimates of the storm event (1 pm to 1 pm, 29 to 30 May, 2016) to estimate cumulative rainfall in the catchment right before the flash flood hit Braunsbach.We also calculated the maximum hourly rainfall intensity in each catchment for comparison.

We then computed from the 5-minute radar rainfall estimates the rainfall intensity and cumulated totals for different moving time intervals ranging from 5 min to 24 h. We also calculated a rainfall intensity-duration (ID) curve normalized by the MAP and rainy-day-normal (RDN), a ratio of the mean yearly precipitation by a mean number of rainy days (Wilson and Jayko, 1997). ID curves offer a simple means to document rainfall characteristics thought to be responsible for triggering erosive processes such as landslides (Caine, 1980; Aleotti, 2004; Godt et al., 2006; Saito et al., 2010). At Braunsbach, such landslides could have contributed to the high sediment yields documented on several amateur videos capturing the flash flood. MAP is computed based on monthly rainfall data since 1936 and RDN based on daily data since 1982 from the DWD rain gauge station closest to the Orlacher Bach catchment (Kirchberg/Jagst–Herboldshausen) with a threshold of 1 mm to distinguish rainy from non-rainy days.

3.3.2 Catchment characteristics

To compare the setting at Braunsbach with the greater region, we focused on the districts of Hohenlohekreis and Schwäbisch Hall. We classified this area into 850 hydrological catchments (e.g., Figure 3.3a) using ArcHydro tools (Djokic et al., 2011) to obtain a hydrological drainage network (Li, 2014) with a minimum supporting catchment area of 3 km^2, which is in the order of magnitude of the Orlacher Bach catchment area ($\sim$6 km^2) (Figure 3.2b).We computed the local slope angle as the maximum rate of elevation drop in a 30×30 m cell neighbourhood for both individual catchments and a buffer of 50 m fringing the channel (riparian zone) based on a 10 m resolution digital terrain model (DTM, courtesy of the Federal Agency for Cartography and Geodesy of Germany BKG). We approximated the local polynomial curvatures to characterize areas of convergent flow of water-sediment (plan curvature) and flow velocities (profile curvature) (Zevenbergen and Thorne, 1987). We also computed the Normalized Difference Vegetation Index (NDVI) to capture the greenness of vegetation (USGS, 2015), using the near infrared (band 8) and red bands (band 4) of the Sentinel-2a level 1C top-of-atmosphere reflectance (TOA) imagery. We employed TOA imagery from 26 August 2015 to capture cloud-free conditions in the catchment before the flood event. NDVI values range from -1 to $+1$ at 10 m resolution, and values of <0.1 characterize bare ground or rock; agricultural lands have values of 0.2 to 0.5, and dense forest has values of about 0.6 (USGS, 2015).

3.3.3 Erosion and sedimentation

We made detailed field observations (22 June 2016) and measurements with a TruPulse 360R® laser rangefinder to estimate the total material eroded from the Orlacher Bach catchment during the rainstorm. The measurements covered the geometry of numerous landslide scars along the channel, including the height and width of the crown above the channel bed, the width of the toes, the lengths from the measurement position, and the position in the catchment. We computed the minimum volume of each landslide considering pyramid shapes that we triangulated. A standard deviation (σ_{1D}) of $\sim$12% can be derived under the assumption of a normal distributed measurement error, comparing two independent height measures for the crown of each landslide (Vogel et al., 2017). This error leads to a standard deviation (σ_{3D}) of $\sim$36% in the estimated volume for a single landslide. The standard deviation (σ_s) is much smaller for the estimate of the total mobilized volume, which corresponds to the sum of all measured landslides. According to the law of large numbers σ_s ($\sigma_s = \frac{\sigma_{3D}}{\sqrt{n}}$) would converge to $\sim$5%, if all landslides were of equal size, since errors balance each other out. Yet, the landslides differ in size increasing the actual σ_s ($>$5%), so that a more accurate error assessment is beyond the scope of this reconnaissance.

3.4 Results

3.4.1 Rainfall

The radar data reveal that $3-4$ mm of rain fell in the 48 h prior to the flash flood in the Orlacher Bach catchment (Figure 3.3a). The rainfall intensity peaked at $\sim$100 mm/h between 5 pm and 6 pm (Figure 3.3b, e), amounting to a total of $\sim$140 mm within 24 h (Figure 3.3c); catchments northwest of Orlacher Bach received even higher rainfall totals. The 126 mm of rain that fell in Orlacher Bach catchment between 4 pm and 6 pm on 29 May 2016 came from a small convective cell (Figure 3.3d). Both radar and rain gauges (Figure 3.3e) are $10-20$ km apart and captured the high variability of rainfall around the catchment. The rainfall in the Orlacher Bach catchment was more intense compared to the surrounding areas. Although the radar estimates differ from the rain gauge measurements by -22% to 12%, interpolated rain-gauge data underestimate the rainfall amounts derived from the small thunderstorm cell over the catchment.

We compared the corresponding rainfall ID curve in the Orlacher Bach catchment with worldwide data for landslide occurrence compiled by Guzzetti et al. (2008) (Figure 3.4). The Braunsbach event falls

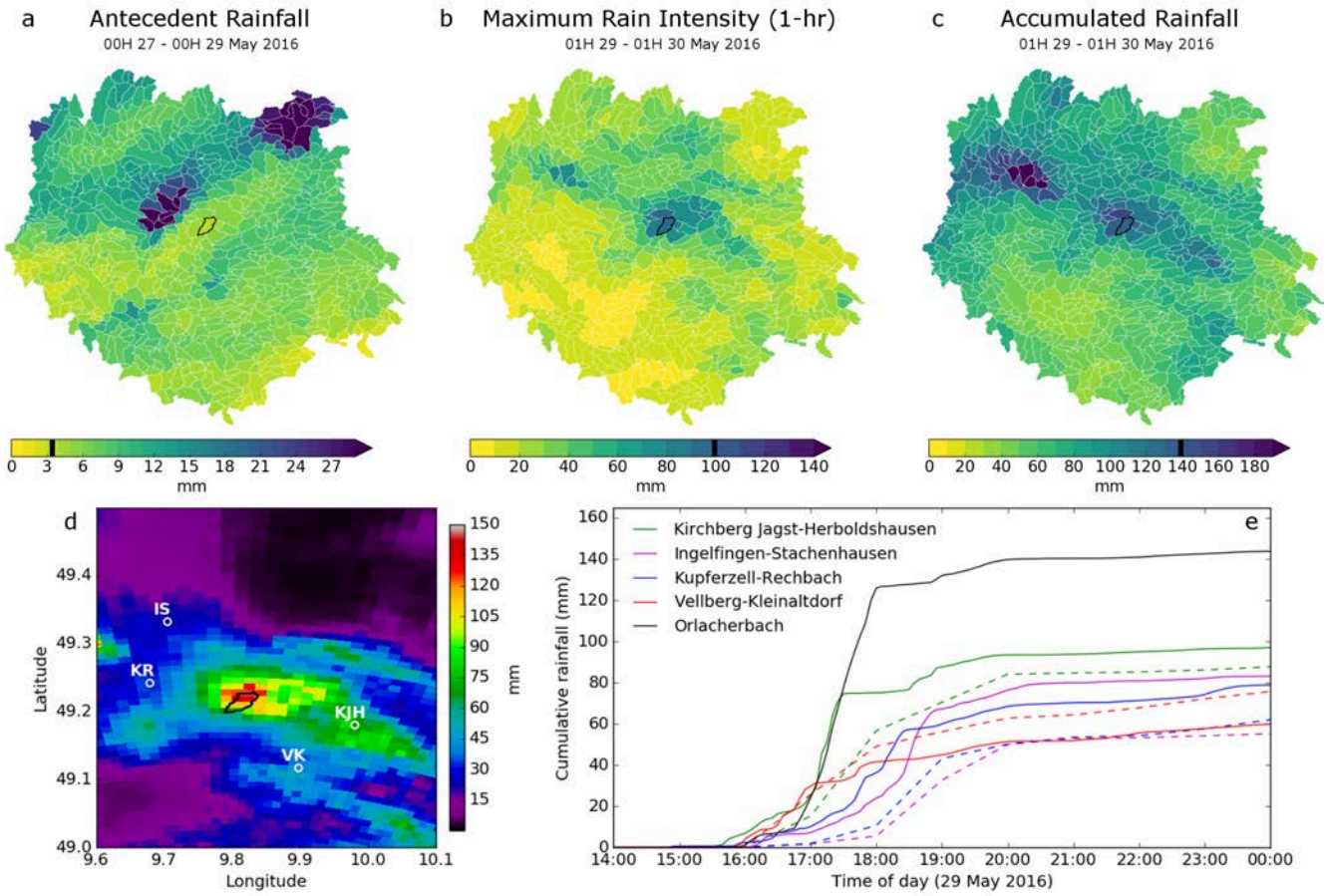

FIGURE 3.3: Estimated rainfall totals from radar measurements. Orlacher Bach catchment is the black polygon on the map and the black line on the colour bars: a. 48-hour rainfall totals prior to the event (0 am 27.05.2016 – 0 am 29.05.2016); b. maximum hourly rainfall intensity in 24 h (1 am 29.05.2016 – 1 am 30.05.2016); c. total accumulated rainfall for the entire event (1 am 29.05.2016 – 1 am 30.05.2016). d. Radar estimate accumulation from 4 pm – 6 pm on 29 May 2016. KJH stands for Kirchberg/Jagst–Herboldshausen (49.18 °N, 9.98 °E), KR for Kupferzell-Rechbach (49.24 °N, 9.68 °E), VK for Vellberg-Kleinaltdorf (49.12 °N, 9.89 °E), IS for Ingelfingen-Stachenhausen (49.33 °N, 9.70 °E). e. Rain gauge measurements (dashed lines) and corresponding radar measurements (solid lines); black line shows radar estimates for the Orlacher Bach catchment.

below the 80th percentile of global data after 4 h of duration (Figure 3.4a–b). If normalized by RDN or MAP, the curve falls below the 80th percentile after three to 4 h of duration (Figure 3.4c–d, e–f). For landslide-triggering rainstorms lasting <2 h, the ID curve for Braunsbach is well above the 80th percentile of worldwide data. The Braunsbach event also remains close to the 80th percentile even if considering 4-hour intervals. The intensity of precipitation decreases quickly for longer durations, nevertheless the ID curve remains above the global median.

3.4.2 Catchment characteristics

We compared the characteristics of the Orlacher Bach catchment with those of 850 similar-sized catchments in the region, focusing on slope, curvature, and NDVI (Figure 3.5). The slopes and curvatures of Orlacher Bach catchment hardly stand out unless the riparian buffer zone is considered separately. The Orlacher Bach buffer zone ranks 16th, 21st, and 25th (>95th percentiles overall) in terms of slope, planform and profile curvatures, respectively, and the NDVI is below the 35th rank. The Orlacher Bach catchment has a distinct knick line separating the plateaus that sustain agricultural fields from the steep (>30°) and forested valley slopes (Figure 3.2d, c). This contrast largely reflects different rock hardness

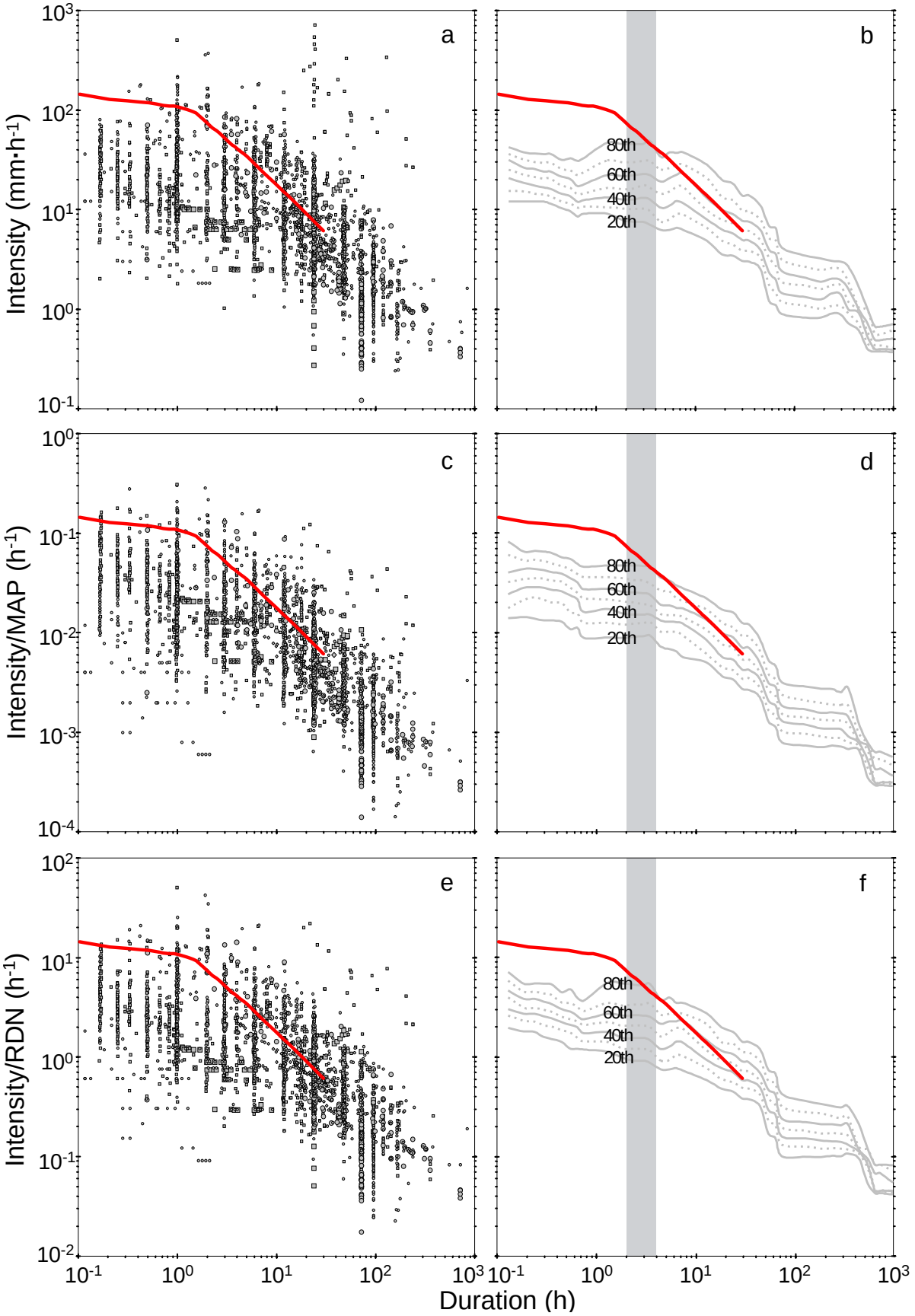

FIGURE 3.4: Global intensity-duration (ID) data of rainstorms that triggered mostly shallow landslides and debris flows and the ID curve of Braunsbach (red line). Squares are debris flows, circles are shallow landslides, and large symbols are landslide episodes. Grey rectangle emphasizes 2− to 4 − hour intervals, ∼95% rain fell within 4 h. a. Raw data; b. percentiles of raw data; c. normalized by mean annual precipitation (MAP); d. percentiles of the MAP normalized data; e. normalized by rainy day normal (RDN); f. percentiles of the RDN normalized data (Modified from Guzzetti et al. (2008)).

and weathering resistance. Clay dominated Lower Keuper rocks form milder slopes, whereas limestone dominated Upper Muschelkalk rocks form steeper slopes (Figure 3.2c) (Hagdorn and Simon, 1985; Prinz and Strauss, 2011). Accordingly slope is more distinctive when Lower Keuper, Middle Muschelkalk (refer to Figures 3.6a, and 3.5) and Upper Muschelkalk (refer to 3.6a, and 3.5) zones are considered in the riparian buffer zone. The NDVI is between the $50th$ and $75th$ percentiles, as the Orlacher Bach catchment is covered by dense vegetation in the riparian zone (Figure 3.2d).

3.4.3 Erosion and sedimentation

Numerous amateur videos recorded a rapid, turbulent, and sediment-laden flow that traversed the inner town of Braunsbach, impacting buildings, widening drainage channels, and dislodging trees, boulders, and cars. The exceptional rainfall also triggered several erosion processes in the channel upstream, for which no video coverage is available. We divided the Orlacher Bach into different sections (Figure 3.7): valley section 1 covers the main creek, valley section 2 covers the Kräuchelbach (a tributary of the Orlacher Bach), and valley section 3 is the upstream part west of Kräuchelbach. We identified and mapped 48 small- to medium sized (∼10 to ∼1350 m^3) shallow landslides, mostly earth and debris slides and falls; 42 along the Orlacher Bach, and six along the Kräuchelbach (valley section 2; Figure 3.7).

The landslide material contains loose soil, plant remnants and tree trunks, but also gravel and boulders. We estimated the minimal landslide volume at 6400 m^3 with a standard deviation of $5-36\%$ due to measurement errors assuming straight scarps. The pavement of the Orlacher Street (∼500 m long) was also completely stripped (Figure 3.7), involving an estimated 1050 ± 150 m^3 of asphalt, considering that a village road in Germany has 35 ± 5 cm depth and is 6 m wide. The anthropogenic material volume would increase by another 1000 ± 250 m^3, if including the property damage along the Orlacher Street based on the categories by Laudan et al. (2017). They reported that four houses were damaged in category D5 (very heavy structural damage), and we assumed that two were entirely removed; another four houses were damaged in category D4 (heavy structural damage), having lost parts of their outer walls. In the catchment, dozens of trees were felled or had their barks stripped; at one location we found a pebble wedged into a debarked tree trunk some 2 m above the channel floor.

Channel-bed incision and bank erosion provided most of the sediment for the flash flood and

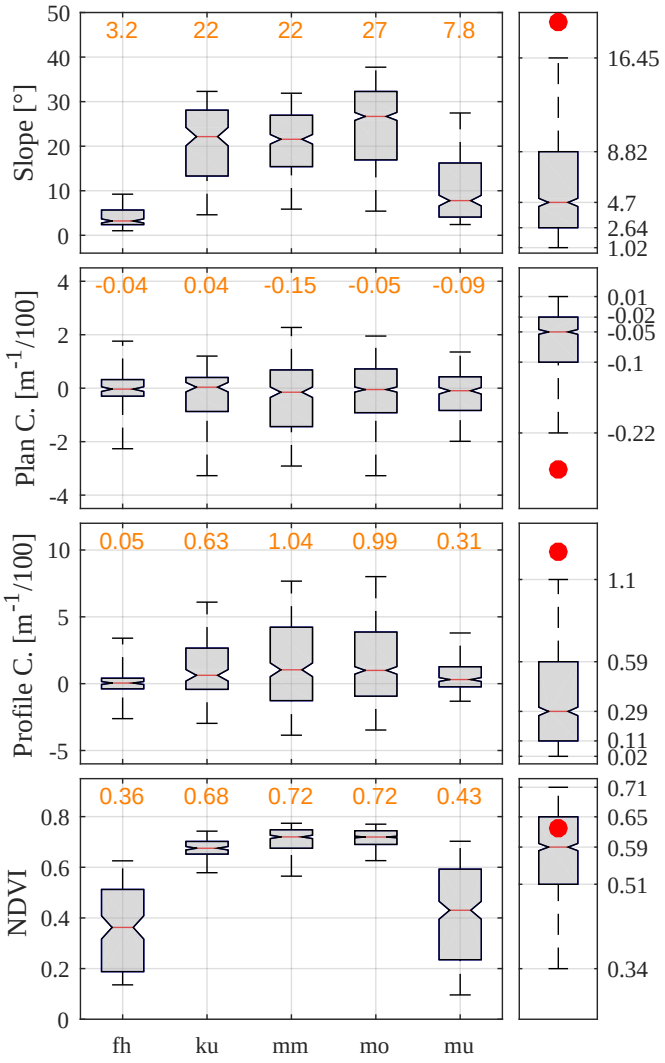

FIGURE 3.5: Boxplots show percentiles ($5th$, $25th$, $50th$, $75th$, and $95th$) of selected catchment characteristics of Orlacher Bach in its riparian buffer stratified by geological formation; fh=flood sediments, ku=Lower Keuper, mm=Middle Muschelkalk, mo=Upper Muschelkalk, mu=Lower Muschelkalk. Orange text shows medians ($50th$ percentile). Right panels are the average catchment characteristics of the Orlacher Bach in the riparian buffer (red dots) compared to those of 850 similar-sized catchments in the region. The y-axes of the right panels show the $1st$ and the $99th$ percentiles.

FIGURE 3.6: Erosion in the Orlacher Bach (as of 23 June 2016). a. View of landslide number 9 (Figure 3.7) taken from the main body of landslide number 8. b. Intact flow-control structure,which was installed in the early 20*th* century. c. Right bank along valley section 1, downcutting is >2 m down to bedrock. Incised former fill is poorly sorted, cobbly, and angular. d. Left bank along valley section 1, downcutting is 0.5 to 1.5 m. e. Left bank along valley section 3, downcutting is ∼1.5 m. Flow-control structure is entirely removed. f. Tree trunks on the Orlacher Street (photo by Kai Pfaffenbach; Sim, 2016). g. Bedrock (Upper Muschelkalk) outcrop in valley section 3.

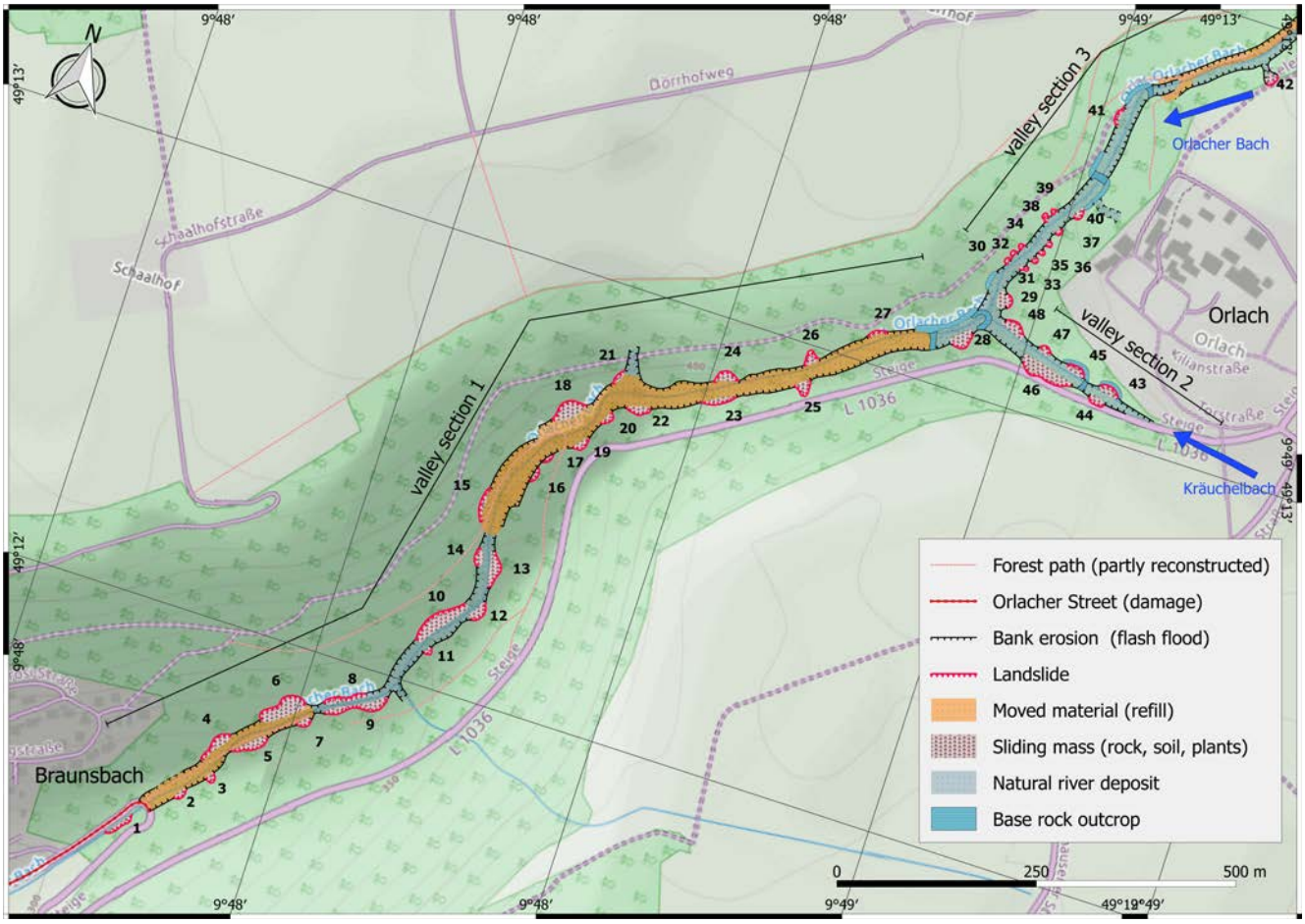

FIGURE 3.7: Geomorphic map of landslides (numbers along the Orlacher Bach and the Kräuchelbach) (modified from Agarwal et al., 2016). Moved material refers to sediments that were artificially refilled after the 2016 flash flood and debris flow.

debris flow. We found that the valley fill was incised by >2 m locally (Figure 3.6c, d, e), exposing the Muschelkalk bedrock upstream of valley section 1 and along the entire valley section 3 (Figures 3.6g, 3.7), and creating fresh terrace treads. Several channel pavements that had been installed in 1903 were entirely removed (Figure 3.6b, e), and erosion scars also dot the Kräuchelbach (Figure 3.7). Natural constrictions (e.g., landslide 8 and 9, Figure 3.7) of the channel favoured small and short-lived landslide dams along valley section 1 (Figure 3.6a). The total volume of coarse fluvial sediment that repair works removed from Braunsbach village was $\sim 42,000$ m^3 (Leonhard Weiss GmbH & Co. KG, pers. comm., 2016). We estimated the contribution of channel-bed incision and bank erosion at $\sim 33,550$ m^3 by subtracting the estimated landslide volume and anthropogenic material (pavement and houses) from the total of $42,000$ m^3.

Erosion of agricultural soils on the plateau may have further contributed sediment (Figure 3.8b). Assuming an average soil erosion of $2-3$ mm over a plateau area of ~ 5 km^2 would amount to a total of $10,000-15,000$ m^3 (Bronstert et al., 2017a). We ignored this volume since most of it would have been flushed through the village as suspended sediment load in highly turbulent runoff (López-Tarazón et al., 2012; Vogel et al., 2017). We did not distinguish between organic and non-organic material, as both were well mixed on the floodplain, and also excluded large woody debris such as tree trunks from our estimates (Figre 3.6f).

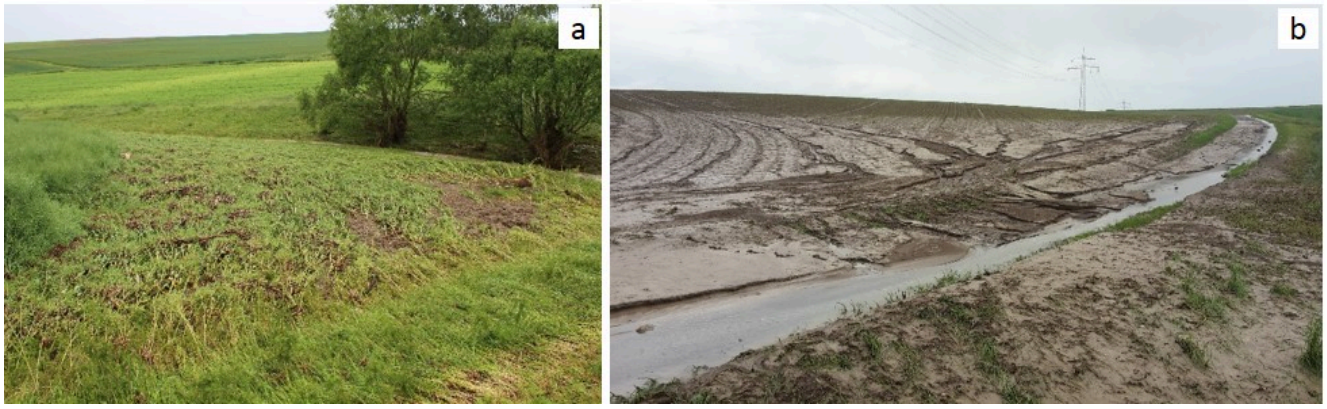

FIGURE 3.8: Local soil erosion on the plateaus above Orlacher Bach (Source: Lisei Köhn, 03.06.2016). a. Slight plant disturbance with negligible erosion. b. Barren field with concentrated rill erosion; which was the only location with noticeable soil erosion in the entire catchment.

3.5 Discussion

Our fieldwork shows that channel erosion and riparian landslides contributed much of the material transported during the flash flood and debris flow in Orlacher Bach. Some 78% of the entire landslide volume involved Upper Muschelkalk rocks, which are fractured and thus prone to rapid water infiltration, high groundwater flow rates, and chemical weathering. Local tracer measurements show that groundwater can percolate at rates of up to 350 m/h (Hagdorn and Simon, 1985). Karst may also gradually promote slope instabilities by widening rock joints and fractures, and reducing the strength of the rock mass (Figure 3.9; Frank Harsch, pers. comm., 2016; Simon, 1980). The clay horizon in the Upper Muschelkalk (close to the Lower Keuper boundary) is also a focal plane for chemical dissolution (Simon, 1980), where mixed corrosion takes place when ground- and infiltration water meet with different carbonic acid concentrations (Figure 3.10). This model highlights long-term losses in rock-mass strength, but cannot explain the mechanisms of sudden failure. Also, most of the shallow landslides that we surveyed involved soil and debris; only in the headwaters did we map small rock topples and rotational rockslides undermining the plateau rims. Some small landslides happed due to the disturbance at toes by the momentum of the flash flood.

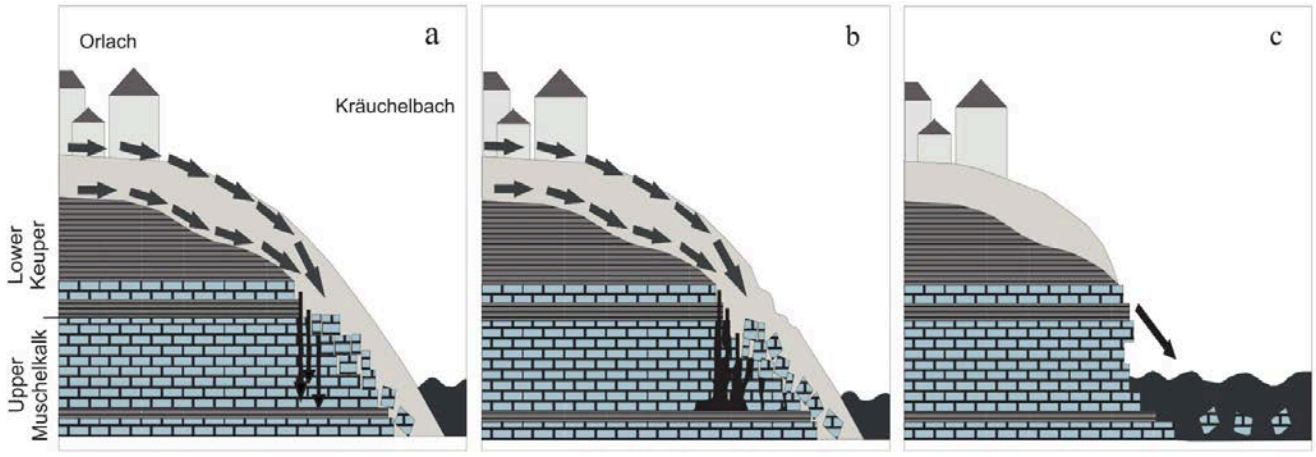

FIGURE 3.9: a. Chemical weathering at the contact between Lower Keuper and Upper Muschelkalk through mixed corrosion (Simon, 1980), which happens when underground water and infiltration water from the surface meet at the clay horizon within the Upper Muschelkalk (close to the Lower Keuper boundary) with different carbonic acid concentrations. b. Initial disintegration of the rock mass via large cavities and fractures. c. Slope failure (rockfall) and landslide during a flood (after Hagdorn and Simon, 1985).

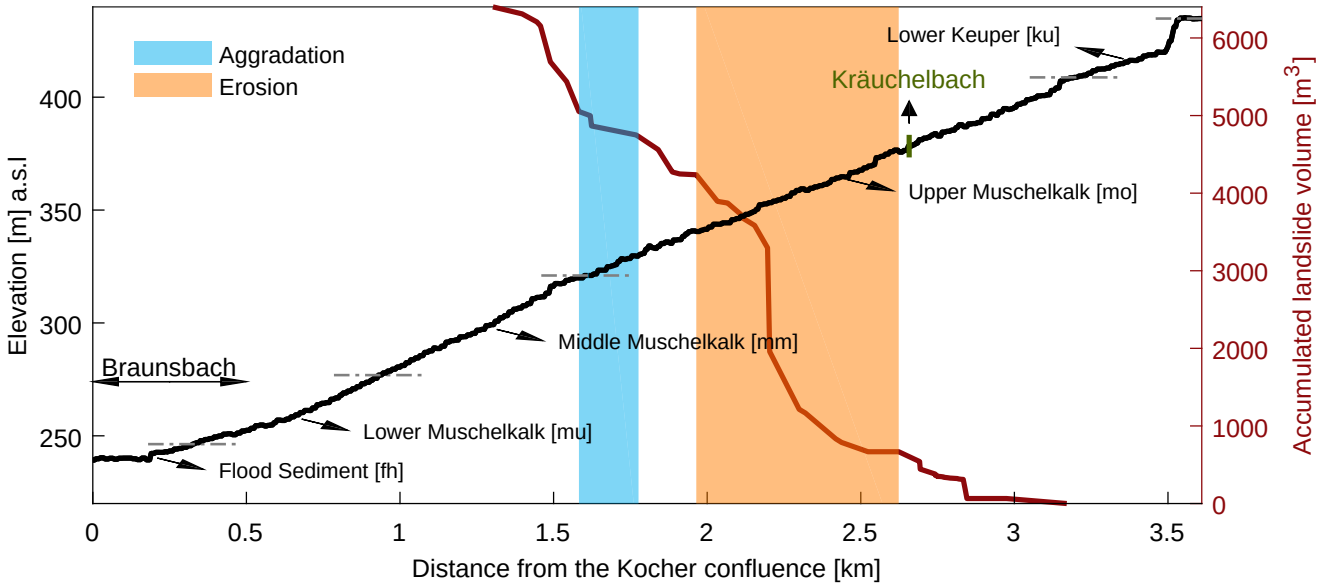

FIGURE 3.10: Longitudinal profile (black line), and estimated cumulative landslide volume (brown line) of the Orlacher Bach. Shaded areas delimit reaches of net aggradation (blue) and erosion (orange). Note the rectilinear profile coincident with outcrops of Upper Muschelkalk rocks.

Several landslides had occurred opposite of each other (Figure 3.7), constricting the channel and possibly forming small, short-lived dams (Figures 3.6a, 3.10). These dams were most likely overtopped when peak flow arrived, hence suddenly releasing temporarily ponded water, trees, and sediment downstream. The peak discharge would have increased abruptly after such small outbursts. The flow also stripped several types of river-control structures, which had been in place for about a century, hinting at the rarity of such highly erosive flows (Figure 3.6e).

The 2016 Braunsbach rainstorm was exceptional not only for southern Germany, but also globally, if comparing from its rainfall ID curve with those obtained for other landslide-triggering storms. Less than a fifth of all those events required higher rainfall intensities and durations to trigger landslides. This observation is consistent with the rarity of documented flash floods, debris flows, and rainfall-triggered landslides, and the apparent geomorphic quiescence in this part of southern Germany. However, we recall that different measurement methods make rainfall characteristics difficult to compare, so that we estimated the rainfall ID curve instead of point data to allow an objective comparison, as rainfall ID sampling requires the exact timing of landslides (Guzzetti et al., 2008). It is likely that several of the mapped landslides happened when rainfall was most intensive (between 5 pm and 6 pm). This hypothesis is supported by the observed high amount of debris that reached the town during between 5 and 8 pm (Bronstert et al., 2017a). Fresh scarps (Figure 3.6a) are strong evidence of landslide activity upstream during the event, or at least before we conducted our fieldwork. The low antecedent rainfall indicates that soils were unsaturated, so that the rainstorm and the flash flood remain as plausible landslide triggers. Several shallow landslides occurred up to two days after the flash flood; some are still episodically occurring one year after the event, judging from freshly fallen trees with undisturbed foliage spanning the channel of the Orlacher Bach. Still, our calculations indicate that in-channel sediment were the main sources of the debris carried by the flow, which scoured the channel to bedrock in many places.

Compared to global sediment yield data, the 2016 Braunsbach event also seems to take a prominent place among the more severe records. The total mass of eroded sediment (river bank erosion and bed incision) of about $\sim 33,550$ m^3 (or $\sim 40,000$ m^3 if including the landslide volume) is equivalent to some $62,000 - 90,000$ t ($73,000$ to $107,000$ t), assuming a bedrock density of $1.8 - 2.6$ t/m^3 based on the deposits and ignoring any sediment lost to the Kocher. This leads to a specific load of at least $10,000$ to $15,000$ t/km^2 (or $12,000$ to $18,000$ t/km^2 if including the landslides). Simplistically assuming that the sediment transported during the Braunsbach event is the bulk of material flux during the whole year (thus

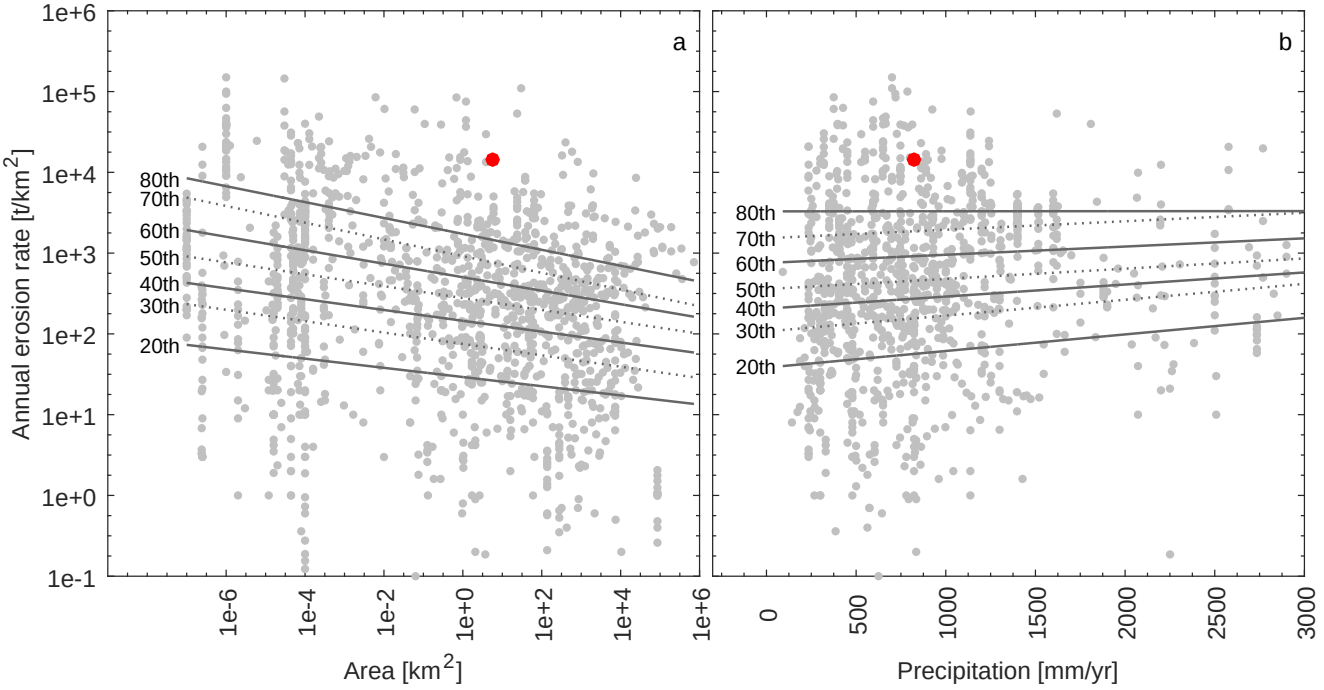

FIGURE 3.11: a. Sediment yields versus catchment area for >4000 catchments worldwide. b. Same data compared to mean annual precipitation (MAP) (data from García-Ruiz et al., 2015). Red circle is Orlacher Bach; the lines (solid, dashed) are linear quantile regression models.

neglecting any other sediment transport), the Braunsbach event is above the $80th$ percentile of >4000 reported annual catchment sediment yields worldwide reported from differing climates, lithologies, and catchment shapes (Figure 3.11; García-Ruiz et al., 2015). The yield from the humid, low-relief, and densely forested Orlacher Bach catchment compares to annual sediment yields reported from semiarid Mediterranean catchments with highly erodible rocks, badlands, or dramatic land-use changes (López-Tarazón et al., 2009; Brosinsky et al., 2014; Francke et al., 2014; Estrany et al., 2016).

How does this geologically instantaneous and short-term sediment yield relate to the longer-term evolution of the Orlacher Bach? Stratigraphic profiles from two shallow boreholes (Figure 3.2c) provided by the LGRB (Landesamt für Geologie, Rohstoffe und Bergbau, Baden-Württemberg), allow a crude estimate of the fan deposits at the mouth of the catchment. Borehole-1 is 12 m deep and drilled through 9.3 m of Pleistocene floodplain deposits of the Kocher on top of claystone-dominated bedrock of the uppermost Buntsandstein locally known as "Röt-Ton" (Figure 3.12; Strasser, 2009). Borehole-2 is 13m deep on the Holocene alluvial fan of the Orlacher Bach (LGRB, 2012). In the uppermost part the core shows a prominent, $4{-}m$ thick layer of poorly rounded limestone gravel. More rounded sandy to gravelly material likely represents floodplain deposits of the Kocher River below the alluvial fan of the Orlacher Bach. This stratigraphy indicates that debris flows may have had occurred previously in the Orlacher Bach, accumulating at least 4 m of sediment in the Holocene (Figures 3.12 and 3.13). First-order estimates from the digital elevation data and other unpublished borehole data indicate that the coarse and dominantly angular fan sediments have a total volume of roughly $100,000 - 200,000$ m^3. Hence, the estimated net deposition of the 2016 flash flood and debris flow on the fan is equivalent to $20 - 40\%$ of the total fan volume, indicating the possibility that the fan was formed by few catastrophic events as opposed to long-term gradual low-energy deposition.

More evidence of recurring flash floods and debris flow comes from a report 5 km upstream along the Kocher River. There, large amounts of debris destroyed houses and buried streets in Cröffelbach (Figure 3.13c, d, Brigitte Blum-Karsch, pers. comm., 2016) in 1927, comparable to the 2016 event in Braunsbach (Figure 3.13a, b). The bank of the Orlacher Bach was reinforced around the late 1920s, but eroded to large extent during the recent flash flood.

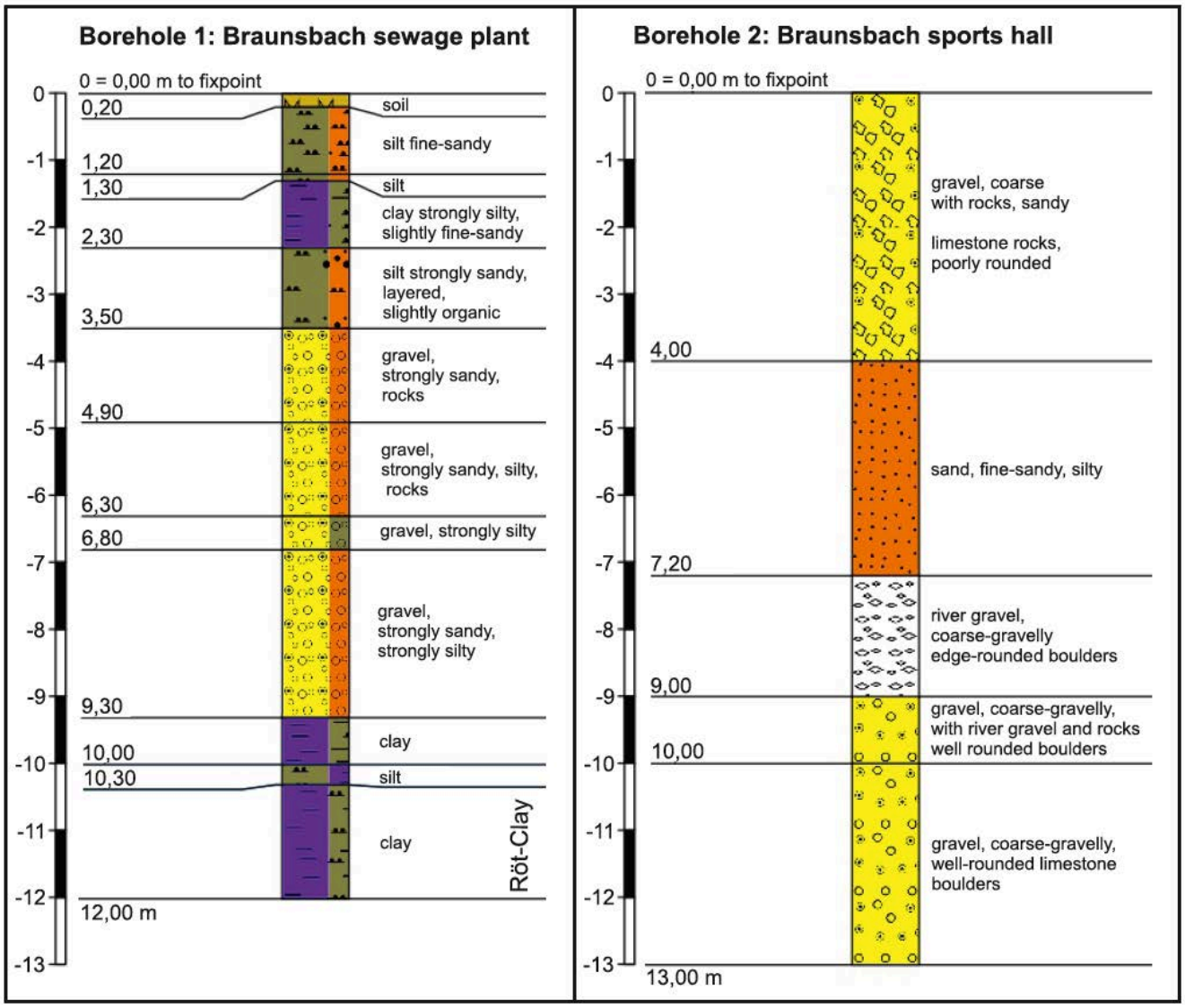

FIGURE 3.12: Stratigraphic logs of the 2 shallow boreholes in the Braunsbach. Borehole 1 is located in the Kocher flood plain, and the borehole 2 is in the Braunsbach city center, close to the city hall (Figure 3.2c). The figure was provided by the LGRB (Landesamt für Geologie, Rohstoffe und Bergbau, Baden-Württemberg).

3.6 Conclusions

Extreme precipitation in combination with rapid runoff, channel incision, and unstable slopes along the Orlacher Bach, promoted the 2016 flash flood and debris flow at Braunsbach. This event is noteworthy in several ways:

- The measured heavy and intensive precipitation has a return period of 200 to 1000 years;
- The amount of total coarse fluvial sediment ($\sim 40,000$ m^3) delivered to the village of Braunsbach as a metric of specific sediment load is among the highest annual catchment yields documented in the world, although sourced from a humid temperate area of moderate relief. We estimated that 80% of the material came from river-bed incision and bank erosion, 15% from landslides, and 5% from anthropogenic origin;
- The rainfall intensity-duration curve is among the highest globally recorded thresholds for landslide triggering intensities (Figure 3.4). Much of the rainfall generating the landslides happened only

FIGURE 3.13: Debris deposits and damaged households following the Braunsbach flash flood of 29 May 2016 (source: Ana Lucía Vela, 01.06.2016) and historic photos from nearby Cröffelbach (∼5 km upstream of Braunsbach, Figure 3.2b), which was hit by a flash flood on 12 June 1927 (Source: Brigitte Blum-Karsch). a. View towards upstream on Orlacher Street in Braunsbach. b. View towards downstream on Orlacher Street in Braunsbach. c. Damaged household in Cröffelbach. d. Buried street in Cröffelbach.

within less than 2 h prior, with intensities of up to 100 mm/h in the Orlacher Bach catchment and a total of 140 mm within 4 h. Although the 24-h rainfall accumulation was not the highest in the Hohenlohekreis and Schwäbisch Hall, the Orlacher Bach catchment had the highest rainfall intensities;

- The geomorphology of the Orlacher Bach catchment, i.e. slope, planform and profile curvatures ($>95th$ percentile) (Figure 3.5) and its geology (Figure 3.2c) favoured high erosion rates. Compared with 850 similarly sized catchments in the region only five other catchments share characteristics similar to those of the Orlacher Bach. All are sparsely populated and media focused on the flood-waters at Braunsbach, where the losses were high. Nevertheless, damage also occurred in these catchments in small villages downstream of Gerabronn, and elsewhere in the region (Gerabronn, 2016).

Even though the event related precipitation intensities have high return periods, evidence of similar

past events remains in the sedimentary record. Considering the karstic structures and material characteristics in the study area as well as the global ID data for landslide triggering rainstorms, it is likely that also less intense precipitation may cause landslides and massive debris flows that pose a hazard especially to settlements on small fans downstream of these steep, gully-like catchments. Clearly, there is a need to study rare geomorphic events in such a sub-humid landscape of gentle relief approaching a more systematic insight.

Acknowledgements

We acknowledge the fieldwork conducted by Irene Hahn and Ana Lucía Vela. We appreciate the suggestions made by Darwin Fox that improved the quality of this study. We also acknowledge the Secretariat for Universities and Research of the Department of the Economy and Knowledge of the Autonomous Government of Catalonia for supporting the Consolidated Research Group 2014 SGR 645 (RIUS- Fluvial Dynamics Research Group). We thank the Federal Agency for Cartography and Geodesy in Germany (BKG) for provision of the digital terrain model of Germany and to the German Weather Service (DWD) for the weather radar data. During the elaboration of the manuscript José Andrés López-Tarazón was in receipt first of a Marie Curie Intra-European Fellowship (Project 'Floodhazards', PIEF-GA-2013-622468, Seventh EU Framework Programme) and then of a Vicenç Mut postdoctoral fellowship (CAIB PD/038/2016). This research was carried out within the Research Training Group "Natural Hazards and Risks in a Changing World" (NatRiskChange; GRK 2043/1) funded by the "Deutsche Forschungsgemeinschaft" (DFG). We thank two anonymous referees for their comments on an earlier version of this study.

Chapter 4

EFFECTS OF FINITE SOURCE RUPTURE ON LANDSLIDE TRIGGERING: THE 2016 M_W 7.1 KUMAMOTO EARTHQUAKE

This chapter is published as::

von Specht S., Ozturk U., Veh G., Cotton F., Korup O.: Effects of finite source rupture on landslide triggering: The 2016 M_W 7.1 Kumamoto earthquake, Solid Earth, doi: 10.5194/se-2018-101, 2019.

Abstract

The propagation of a seismic rupture on a fault introduces spatial variations in the seismic wave field surrounding the fault. This directivity effect results in larger shaking amplitudes in the rupture propagation direction. Its seismic radiation pattern also causes amplitude variations between the strike-normal and strike-parallel components of horizontal ground motion. We investigated the landslide response to these effects during the 2016 Kumamoto earthquake (M_W 7.1) in central Kyushu (Japan). Although the distribution of some 1,500 earthquake-triggered landslides as a function of rupture distance is consistent with the observed Arias intensity, the landslides are more concentrated to the northeast of the southwest–northeast striking rupture. We examined several landslide susceptibility factors: hillslope inclination, the median amplification factor (MAF) of ground shaking, lithology, land cover, and topographic wetness. None of these factors can sufficiently explain the landslide distribution or orientation (aspect), although the landslide head scarps coincide with elevated hillslope inclination and MAF. We propose a new physics-based ground-motion model (GMM) that accounts for the seismic rupture effects, and we demonstrate that the low-frequency seismic radiation pattern consistent with the overall landslide distribution. Its spatial pattern is influenced by the rupture directivity effect, whereas landslide aspect is influenced by amplitude variations between the fault-normal and fault-parallel motion at frequencies <2 Hz. This azimuth dependence implies that comparable landslide concentrations can occur at different distances from the rupture. This quantitative link between the prevalent landslide aspect and the low-frequency seismic radiation pattern can improve coseismic landslide hazard assessment.

4.1 Introduction

Landslides are one of the most obvious and hazardous consequences of earthquakes. Acceleration of seismic waves alters the force balance in hillslopes and temporarily exceeds shear strength (Newmark, 1965; Dang et al., 2016). Greatly increased landslide rates have been reported on hillslopes close to earthquake rupture, mostly tied to ground acceleration (Gorum et al., 2011) and lithology (Chigira and Yagi, 2006). Substantial geomorphological and seismological data sets are required to assess the response of landslides to ground motion, and a growing number of studies have shed light on the underlying links (e.g. Lee, 2013; Allstadt et al., 2018; Fan et al., 2018; Roback et al., 2018). Several seismic measures, such as vertical and horizontal peak ground acceleration (PGA; Miles and Keefer, 2009), root-mean-square (RMS) acceleration, or Arias intensity (I_A) (Arias, 1970; Keefer, 1984; Harp and Wilson, 1995; Jibson

et al., 2000; Jibson, 2007; Torgoev and Havenith, 2016), seismic source-moment release, hypocentral depth, and rupture extent and propagation (Newmark, 1965), correlate with landslide density (Meunier et al., 2007).

Landslides concentrate in the area of strongest ground acceleration (Meunier et al., 2007), whereas total landslide area decreases from the earthquake rupture with the attenuation of peak ground acceleration (Dadson et al., 2004; Taylor et al., 1986). This general pattern is modified by morphometrics (e.g. local hillslope inclination and curvature) and geological parameters (e.g. lithology, geological structure, land cover) (Gorum et al., 2011; Havenith et al., 2015) that influence landslide susceptibility (Pawluszek and Borkowski, 2017)on top of seismic amplification (Maufroy et al., 2015). For instance, Tang et al. (2018) found that lithology, PGA, and distance from the rupture plane are important in assessing the distribution of landslides triggered by the 2008 Wenchuan earthquake (M_W 7.9). Fan et al. (2018) found that hillslope aspect and slope were important determinants of the landslide distribution resulting from the 2017 Jiuzhaigou earthquake (M_W 6.5).

On April 16, 2016 at 16:25 (UTC) central Kyushu was hit by a M_W 7.1 earthquake (Figure 4.1). The left-lateral dip-slip event ruptured along the Futagawa and Hinagu faults, striking NW-SE, with a hypocentral depth of 11 km (e.g. Kubo et al., 2016). The rupture propagated northeastward and stopped at Mt. Aso. Fault source inversion studies show a northeast propagation of the rupture originating under Kumamoto City with highest slip near the surface at the western rim of the Aso caldera (e.g. Kubo et al., 2016; Asano and Iwata, 2016; Moore et al., 2017; Uchide et al., 2016; Yagi et al., 2016; Yoshida et al., 2017). The earthquake triggered approximately $1,500$ landslides (National Research Institute for Earth Science and Disaster Prevention, 2016) that concentrated mainly inside the caldera and the flanks of Mt. Aso on the Pleistocene and Holocene lava flow deposits (Paudel et al., 2008; Sidle and Chigira, 2004), although most of the terrain near the earthquake rupture is rugged (Figure 4.1). Thus, we hypothesize that rupture directivity causes an asymmetric distribution of landslides around the rupture plane, because of more severe ground motion along the propagating rupture (Somerville et al., 1997). Similarly asymmetric landslide distributions attributed to rupture directivity were reported for the 2002 Denali earthquake (M_W 7.9; Frankel, 2004; Gorum et al., 2014), and the 2015 Gorkha earthquake (M_W 7.8; Roback et al., 2018). In the case of the 1999 Chi-Chi earthquake, Lee (2013) speculated that the prevalent landslide aspects were correlated to the fault movement direction (Ji et al., 2003; Meunier et al., 2008). These observations indicate that the rupture process introduces variations on the incoming energy on hillslopes.

Here we link those dominant near-surface seismic characteristics relevant to the pattern and orientation of coseismic landslides. We investigate the geological conditions (lithology, aspect, hillslope inclination, topographic amplification and soil wetness) in central Kyushu as well as seismic waveform records from 240 seismic stations within 150 km of the rupture (Figure 4.1). The two most prominent seismic effects—well founded in seismological theory (e.g. Aki and Richards, 2002) and documented in empirical relationships (e.g. Somerville et al., 1997)—are the rupture directivity and amplitude variations in fault-normal and fault-parallel motion. We examine whether the geomorphic characteristics around the Aso caldera made this area more susceptible to landslides than the surrounding topography near the earthquake rupture or instead rupture effects control the asymmetric distribution of the landslides. We introduce a ground-motion metric related to azimuth-dependent seismic energy (i.e. related to seismic velocity) because these effects attenuate with increasing frequency and are less captured by acceleration-based metrics. From this we propose a new ground-motion model that is consistent with the observed coseismic landslide pattern.

4.2 Data

We combine data sets on the response of landslides to the earthquake, including topography, land cover, geology, seismic waveforms, velocity structure, near-surface characteristics, and landslide location and planform (Figure 4.2).

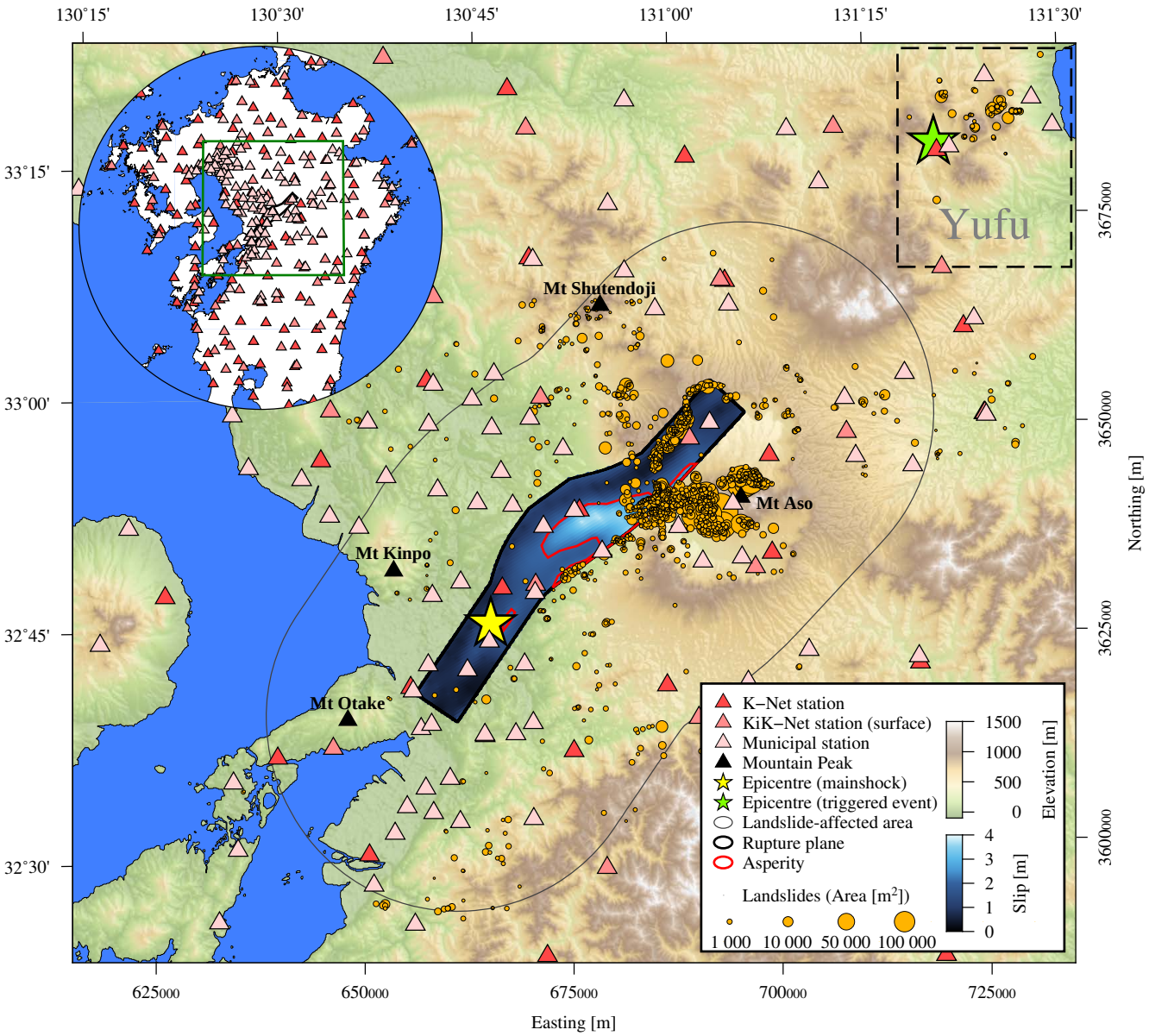

FIGURE 4.1: The area of Kyushu affected by coseismic landslides triggered by the 2016 M_W 7.1 Kumamoto earthquake. The colored patch is the slip distribution of the rupture model of Kubo et al. (2016), and the dashed box encompasses landslides related to the triggered event in Yufu (epicenter location after Uchide et al. (2016)). The inset map shows the station network within 150 km of the rupture.

4.2.1 Topographic data

Most topographic data used in this study are provided by the Japan Aerospace Exploration Agency (JAXA) and its Advanced Land Observing Satellite (ALOS) project with a horizontal resolution of 1" (∼30 m). This digital surface model (DSM) forms the basis for computing aspect, hillslope inclination (Figure 4.2a), the median amplification factor (MAF; Maufroy et al., 2015) (Figure 4.2b), and the topographic wetness index (Böhner and Selige, 2006) (Figure 4.2c). The ALOS project also provides data on land cover including anthropogenic influence (sealing and agriculture) and vegetation (Figure 4.2g), while data on major geological units are from the Seamless Digital Geological Map of Japan (scale of 1:200000) by the Geological Survey of Japan (Figure 4.2d).

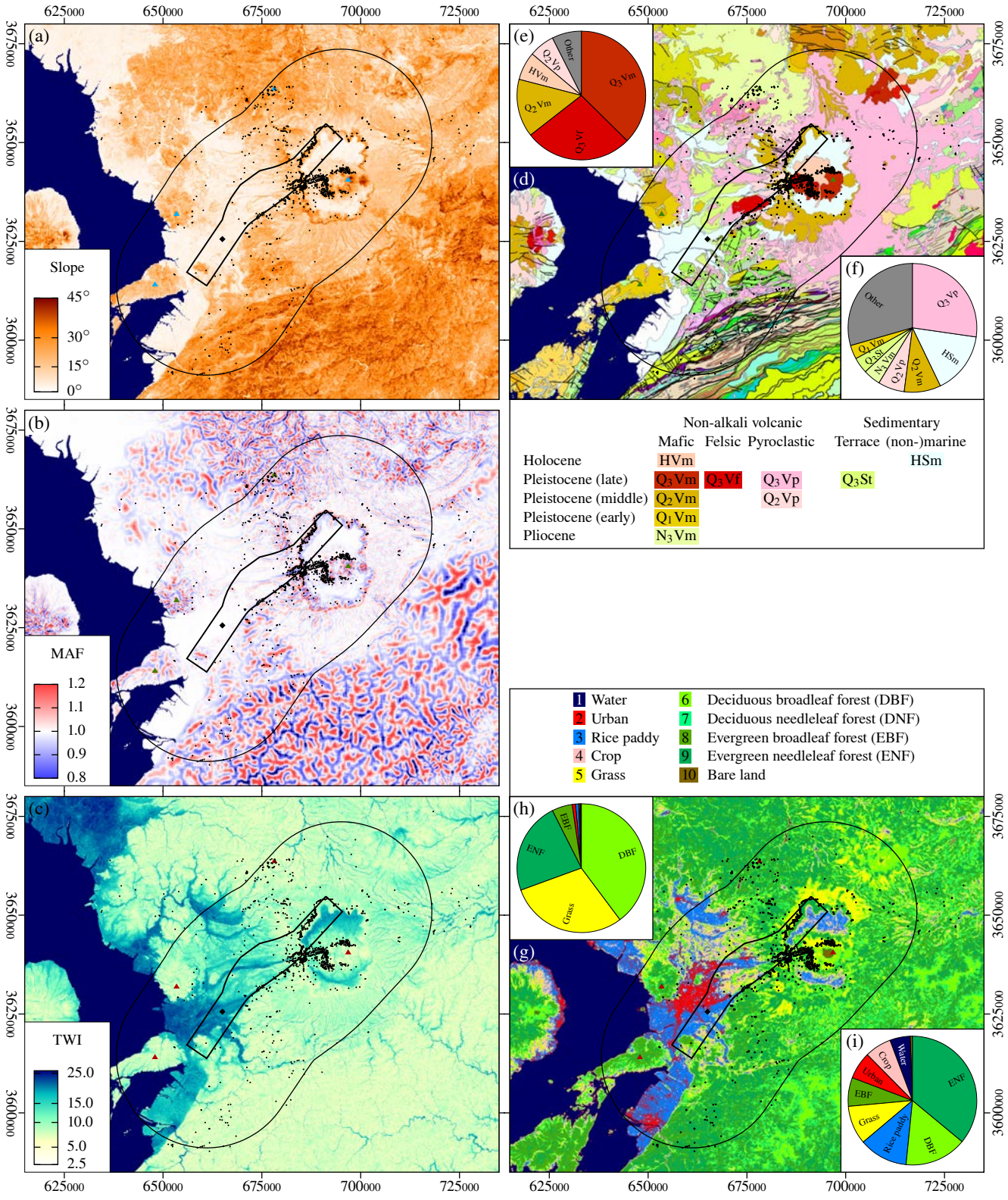

FIGURE 4.2: Topographic and geological features of central Kyushu with landslides (black dots), landslide-affected area (outer black line), rupture area (inner black line), hypocenter (black diamond), and mountain peaks from Fig 1 (triangles). a) Hillslope inclination. b) Median amplification factor (MAF). c) Topographic wetness index (TWI). d) Geology of central Kyushu. The most common geological units of the landslides are shown in e). For the landslide-affected area the dominant geological units are in f). g) Land cover. Land cover in the landslide areas is shown in h) and is shown for the entire landslide-affected area in i).

4.2.2 Topographic amplification of ground motion

Topographic features, such as mountains and valleys, can amplify or attenuate seismic waves (Massa et al., 2014; Maufroy et al., 2012, 2015). The largest ground-motion variations occur on hillslopes and summits, whereas variations are intermediate on narrow ridges, and low on valley floors. Maufroy et al. (2015) introduced proxies for these topographic site effects, of which we use the median amplification factor (MAF), based on the topographic curvature, and the S-wave velocity v_S traveling at frequency f:

$$MAF(f) = 8 \cdot 10^{-4} \frac{v_S}{f} C_S \left(\frac{v_S}{2f} \right) + 1 \tag{4.1}$$

where $C_S \left(\frac{v_S}{2f} \right)$ is the topographic curvature convolved with a normalized smoothing kernel based on two 2D boxcar functions as a function of v_S and f.

The curvature is estimated from the DSM (Zevenbergen and Thorne, 1987; Maufroy et al., 2015), and the seismic velocity v_S is the average S-wave velocity of the uppermost 500 m from the model by Koketsu et al. (2012).

Another site effect that influences landslide potential is the local soil or groundwater content, which can be modeled for uniform conditions to the first order using the topographic wetness index (TWI) of Böhner and Selige (2006):

$$TWI = \log \frac{A_c}{\tan \beta}, \tag{4.2}$$

where A_c is the upslope catchment area and β is the hillslope inclination derived from the DSM with filled sinks (Planchon and Darboux, 2001).

4.2.3 Ground-motion data

Ground-motion data are from the Kik-Net and K-Net of the National Research Institute for Earth Science and Disaster Prevention (NIED) of Japan. NIED operates both borehole and surface stations for Kik-Net, and we use the latter only. The Japan Meteorological Agency (JMA) also released seismic data from the municipal seismic network for the largest earthquakes of the Kumamoto sequence. In total, data from 240 stations in Kyushu are available with complete azimuthal coverage within 150 km of the earthquake rupture (Figure 4.1).

The analysis of seismic waveforms is based on accelerometric data only. Both the NIED and JMA data are unprocessed, and we follow the strong motion processing guidelines of Boore and Bommer (2005). We use both acceleration and velocity in further processing and integrate the accelerograms to obtain velocity records. We correct the data with the automated baseline correction routine by Wang et al. (2011). The JMA accelerometric data further require a piecewise baseline correction prior to the displacement baseline correction due to abrupt (possibly instrument-related) jumps (Boore and Bommer, 2005; Yamada et al., 2007). We use the automated correction for baseline jumps by (von Specht, 2018 [in. prep.]).

An earthquake was triggered ∼80 km to the northeast in Yufu 32 s after the Kumamoto earthquake (Figure 4.1; Uchide et al., 2016). Due to the close succession of the two events, waveforms of the triggered event interfere with the coda of the Kumamoto earthquake. We taper the data to reduce signal contributions by the triggered event. The taper position is based on theoretical travel time differences between the P wave ($v_P = 5700\,\mathrm{m/s}$) arrival of the Kumamoto earthquake and the S wave arrival ($v_S = 3300\,\mathrm{m/s}$) of the triggered event. The respective travel paths to the stations are measured from the hypocenters. Since fewer instruments are located to the northeast and the triggered event close to the sea, less than 10% of the data are strongly contaminated by the triggered event.

NIED hosts the rupture-plane model of Kubo et al. (2016), which describes the slip history on a curved rupture plane (based on the surface traces of the Futagawa and Hinagu faults) with a total length of 53.5 km and 24 km width (Figure 4.1). We use the extent and shape of the rupture plane to estimate the landslide-affected area and to define the rupture plane distance r_{rup}, the shortest distance from the

rupture-plane. We follow the approach of Somerville et al. (1999) to identify the asperity from the rupture-plane model, which is the area with more than 1.5 times the average slip.

The underground structure in terms of seismic velocities (v_P, v_S) and density (ρ; Koketsu et al., 2012) is available for 23 layers down to the mantle in ∼0.1 degree resolution covering all of Japan; we only consider the layers of the upper 0.5 km to compute a velocity average for the MAF.

NIED provides data for the subsurface shear wave velocities (v_{S30}) as well as site amplification factors S_{amp}. Contrary to v_S from Koketsu et al. (2012), v_{S30} is derived for the upper 30 m only and is more suitable for energy estimates, which require velocities at the surface (recording station). The site amplification factor S_{amp} describes how much seismic waves are amplified by, independent of their frequency.

4.2.4 Landslide data

Detailed landslide data are provided by NIED as polygons (Figure 4.1), mapped from aerial imagery with sub-meter resolution at different times after the Kumamoto earthquake. The first data set contains landslides that were identified between April 16 and 20, though the area close to the summit of Mt. Aso was not covered. A second data set was collected on April 29, 2016 and covers those parts of Mt. Aso that remained unmapped. However, the second data set may contain rainfall-induced landslides, since the rainy season in Kyushu starts in May (Matsumoto, 1989), and there was rainfall after the Kumamoto earthquake and landslides triggered by volcanic activity. We selectively combine the two data sets for this study, using only those landslides from the second database, which are also partly present in the first data set. We exclude any rainfall triggered landslides with this approach, though possibly omitting seismically induced landslides exclusive to the second database. However, the area in question is comparatively small to the full extent of the study area, and the missing landslides are minor in terms of their area.

Several landslides cluster ∼80 km to the northeast of the mainshock in the municipalities Yufu and Beppu (Figure 4.1), which were hit by a triggered earthquake (Uchide et al., 2016). We believe that the distant northeastern landslides were induced by this triggered event. This also explains the considerable gap in landslides (∼50 km) between Yufu and Aso (Figure 4.1) in otherwise steep topography. Hence we exclude the landslides from Yufu and Beppu (<10% of all landslides, <3% of the total landslide area) from our database.

Apart from the special release of landslide data for the 2016 Kumamoto earthquake, NIED hosts a landslide database for all Japan (National Research Institute for Earth Science and Disaster Prevention, 2014). This database covers unspecified landslides of any origin. We extract a subset from this landslide database to compare it with the landslides triggered by the Kumamoto earthquake. Contrary to the special Kumamoto release, only the landslide deposits are given as polygons, whereas the scarps are mapped as lines. We manually define polygons representing the total landslide area bound by the scarp line and covering the deposit area to make both data sets comparable and because the landslide source area is generally not identical to the deposit area.

4.3 Total area affected by landsliding

We define the landslide-affected area, in which coseismic landsliding occurred, as the area spanned by the rupture-plane distance covering 97.5% of the total landslide area (Harp and Wilson, 1995; Marc et al., 2017). Thus the total landslide-affected area is 3968.6 km^2 and is within 22.9 km distance from the rupture plane.

An M_W 7.1 event with a fault length of 53.5 km and an asperity length of 12.78 km (3 km) results in a landslide-affected area of 3914 km^2 (4406 km^2) using parameters proposed by Marc et al. (2016). We derived the event depth of 11.1 km as the moment weighted average of the rupture model of Kubo et al. (2016). Both estimates are consistent with our area estimate. Marc et al. (2016) introduced a topographic constant, A_{topo}, relating the total landslide area to the area that excludes basins and inundated areas. We estimate A_{topo} from the ALOS land cover that 97% of all landslides occurred in

areas without anthropogenic influence, i.e. land with urban and agricultural use, and water bodies. We exclude water bodies, urban areas—predominantly the metropolitan area of Kumamoto City, and rice paddies from the topographic analysis, obtaining an affected area of 3037 km^2, i.e. $A_{topo} = 0.68$.

4.4 Total landslide area

Total landslide area is linked to several earthquake parameters, mostly magnitude and hypocenter or average rupture-plane depth (Keefer, 1984; Marc et al., 2017). We adopted the relation by Marc et al. (2017) to check for completeness of the total landslide area of 6.38 km^2. The actual landslide failure plane is likely smaller, as the NIED data set provides the combined area of depletion and accumulation. The modal hillslope inclination is estimated at 15°. Instead of the earthquake magnitude scaling relation (Leonard, 2010) used by (Marc et al., 2017), we use the rupture extent reported by Kubo et al. (2016). The area model requires the average length of the seismic asperities, which Marc et al. (2017) globally assumed to be 3 km. However, Somerville et al. (1999) derived a relationship of asperity sizes based on the seismic moment that results in an average asperity length of 12.78 km for the 2016 Kumamoto earthquake. This length is consistent with the asperity sizes found by Yoshida et al. (2017) for their finite rupture model. The estimated landslide area with an asperity length of 3 km results in a predicted total landslide area of 12.90 km^2, while with the magnitude scaled asperity size of Somerville et al. (1999), the landslide area is 3.03 km^2. The landslide area estimates with constant asperity length and moment-dependent asperity length differ by a factor of 2 and 0.5 from the NIED data set, respectively.

Landslide concentration is defined as landslide area per area at a given distance band (Meunier et al., 2007). For the seismic processing, we consider the rupture-plane distance r_{rup} based on the rupture model instead of the hypocentral distance (Meunier et al., 2007) or the Joyner–Boore distance (Harp and Wilson, 1995).

4.5 Ground motion and seismically induced landsliding

4.5.1 Coseismic landslide displacement

The sliding-block model of Newmark (1965) is widely used to estimate coseismic hillslope performance (e.g. Kramer, 1996; Jibson, 1993, 2007). The model estimates the permanent displacement on a hillslope affected by ground motion. Newmark (1965) established a relation for hillslope displacement in terms of the maximum velocity at the hillslope for a single rectangular pulse, v_{max} [m/s]

$$d_s = \frac{v_{max}^2}{2}\left(\frac{1}{Aa_y} - \frac{1}{A}\right) \tag{4.3}$$

where A is the magnitude of the acceleration pulse and a_y [m/s^2] is the yield acceleration, which is the minimum pseudostatic acceleration required to produce instability. For downslope motion along a sliding plane, a_y is related to the angle of internal friction, ϕ_f, and the hillslope inclination, δ, by

$$a_y = g\left(\frac{\tan\phi}{\tan\delta}\right)\sin\delta = g(\overline{FS} - 1)\sin\delta \tag{4.4}$$

with the average factor of safety $\overline{FS}$. Chen et al. (2017) characterized unstable hillslopes—related to both rainfall and earthquakes—by a safety factor of $FS < 1.5$.

An upper bound for the displacement, d_s, is based on two ground-motion parameters (Newmark, 1965; Kramer, 1996):

$$d_{max} = \frac{PGA}{a_y}\frac{PGV^2}{a_y}, \tag{4.5}$$

where PGA [m/s^2] and PGV [m/s] are the peak ground acceleration and velocity, respectively. Thus, the coseismic hillslope performance can be characterized by velocity and acceleration. In the following sections, we derive a ground-motion model based on the acceleration-related Arias intensity and the velocity-related radiated seismic energy.

4.5.2 Ground-motion metrics

Though PGA is the most widely used ground-motion metric in geotechnical engineering, the Arias intensity I_A (Arias, 1970) is widely used to characterize strong ground motion for landslides.

$$I_A = \frac{\pi}{2g} \int_{T_1}^{T_2} a(t)^2 dt, \tag{4.6}$$

where $g = 9.80665\,\mathrm{m/s^2}$ is standard gravity and T_1 and T_2 are the times where strong ground motion starts and cedes (the acceleration $a(t)$ is given in units of m/s^2 and the Arias intensity has units of m/s). The Arias intensity captures both the duration and amplitude of strong motion. Empirical relationships between I_A and d_s in terms of earthquake magnitude and epicenter distance have been developed (e.g. Jibson, 1993; Bray and Travasarou, 2007; Jibson, 2007).

Since PGA and I_A are related to each other (e.g. Romeo, 2000) and the hillslope displacement depends on both velocity and acceleration (Eq. 4.3, 4.5), it is reasonable to characterize velocity similarly to Arias intensity. The velocity counterpart to I_A is $IV2$, the integrated squared velocity (Kanamori et al., 1993; Festa et al., 2008):

$$IV2 = \int_{T_1}^{T_2} v(t)^2 dt \tag{4.7}$$

The squared velocity is also used in radiated seismic energy estimates. The quantity j_E is the radiated energy flux of an earthquake and estimated by (Choy and Cormier, 1986; Kanamori et al., 1993; Newman and Okal, 1998)

$$j_E = \frac{\rho c}{S_{amp}^2} e^{-k r_{rup}} IV2 \tag{4.8}$$

where ρ and c are the density and seismic wave velocity at the recording site and S_{amp} is the site specific amplification factor. The distance from the rupture is given by r_{rup} and k is a term for along-path attenuation (Anderson and Richards, 1975), and effects of transmission and reflection (Kanamori et al., 1993). The attenuation constant k is also influenced by anisotropy and structure heterogeneity (Campillo and Plantet, 1991; Bora et al., 2015). The full definition of the energy flux includes two terms for compressional waves ($c = v_P$) and shear waves ($c = v_S$), respectively. The radiated energy of an earthquake, E_S, results from the integral over the wavefront surface

$$E_S = \iint j_E dA, \tag{4.9}$$

where A is the area of the surface through which the wave passes at the recording station and represents the geometrical spreading.

The radiated seismic energy E_S describes the energy leaving the rupture area and is related to the seismic moment (Hanks and Kanamori, 1979):

$$E_S = \frac{\Delta\sigma}{2\mu} M_0, \tag{4.10}$$

where $\Delta\sigma$ is the stress drop and μ the shear modulus, and M_0 the seismic moment. We make use of this relation when considering the magnitude-related term in the ground-motion model. Since most seismic energy is released as shear waves, we apply the shear wave velocity at the recording site (v_S) to the

entire waveform, i.e. we assume that all waves arrive with velocity v_S at a site. This assumption has the advantage that it does not require a separation of the record into P- and S-waveforms, simplifying the computation. In appendix 4.10 we show from a theoretical perspective that using a uniform v_S has only a small impact on the overall energy estimate. The site-specific correction term for the energy estimate $\hat{E}$ based on Eq. (4.8) and (4.9) becomes

$$\hat{E} = \frac{\hat{A}\rho v_S}{S_{amp}^2} e^{-kr_{rup}} IV2 \tag{4.11}$$

While E_S is the radiated seismic energy at the source, $\hat{E}$ is estimated from the velocity records at a station and only approximates E_S. Therefore, $\hat{E}$ may differ from the true and unknown radiated energy E_S (Kanamori et al., 1993). Several assumptions characterize $\hat{E}$:

- All energy is radiated as S-waves in an isotropic, homogeneous medium
- Geometrical spreading is corrected for an isotropic, homogeneous medium
- Since $IV2$ (Eq. 4.7) depends on the radiation pattern, $\hat{E}$ depends on the azimuth
- Attenuation is homogeneous
- Surface waves are not considered
- Site amplification is frequency-independent

Below, we investigate the azimuthal variation in the energy estimates to characterize the radiation pattern.

The estimated wavefront area $\hat{A}$ is related to the rupture extent and r_{rup}, and $\hat{A}$ corresponds to a simplified version of the wavefront area approximation by Schnabel and Bolton Seed (1973) and Shojataheri and Anderson (1988):

$$\hat{A} = 2WL + \pi r_{rup}(L + 2W) + 2\pi r_{rup}^2 \tag{4.12}$$

The extent of the rupture is assumed to be rectangular with length L and width W. Eq. 4.12 describes a cuboid with rounded corners and with only half of its surface considered, because no energy flux is assumed to be transmitted aboveground.

While the geometrical spreading correction is expressed analytically as the wavefront area $\hat{A}$, we estimate the attenuation parameter k. Attenuation changes with distance, as a power law at short distances (< 150 km) (Anderson and Richards, 1975) and longer distances are not considered. An empirical attenuation relationship is

$$\ln Y = C + kr_{rup}, \tag{4.13}$$

where Y is

$$Y = \frac{\hat{A}\rho v_S}{S_{amp}^2} \int_{T_1}^{T_2} IV2, \tag{4.14}$$

i.e. the logarithm of the energy estimate without the attenuation term $e^{-kr_{rup}}$ from Eq. 4.11. The dummy variable C is only used for estimating k and not in the final correction for attenuation. A distance-independent form of the Arias intensity, i.e. corrected for geometrical spreading and attenuation, is defined by

$$I_{A,A} = \frac{\hat{A}}{S_{amp}^2} e^{-kr_{rup}} I_A, \tag{4.15}$$

where k is determined by Eq. 4.13 and setting $Y = I_A\hat{A}$. The corrected Arias intensity $I_{A,A}$ is the acceleration-based counterpart to $\hat{E}$.

Low-frequency effects, like directivity, are better captured with a velocity-based metric (e.g. azimuth-dependent energy estimate) than an acceleration-based metric (Arias intensity) alone.

In terms of the Fourier transform, the sensitivity of acceleration at higher frequencies becomes apparent, as the Fourier transform of the time derivative of any function is

$$\mathcal{F}(\dot{f}(t)) = i\omega\mathcal{F}(f(t)) \tag{4.16}$$

and thus scales with frequency in the spectrum. The frequency sensitivity of $IV2$ and I_A is related to the squared spectrum given the metrics. For example, in Figure 4.3 we show the different spectral sensitivities of $IV2$ and I_A for a theoretical seismic source spectrum (Brune, 1970). $IV2$, and thus $\hat{E}$, has a higher sensitivity to lower frequencies than I_A. The low-frequency part of the spectrum can be accounted for by considering $IV2$ in a ground-motion model.

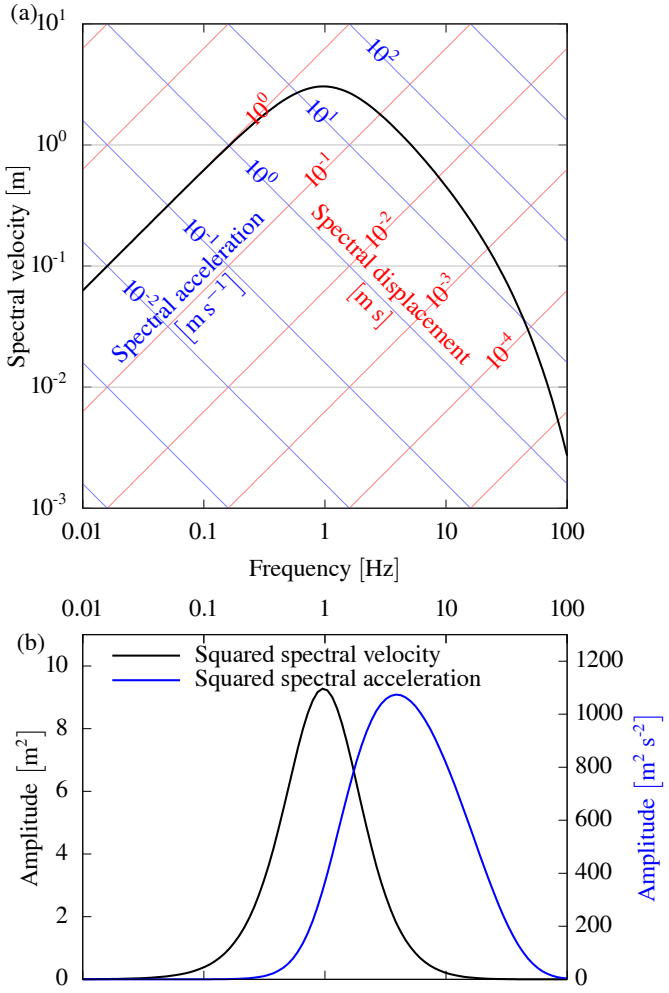

FIGURE 4.3: The spectrum can be read as displacement (red), velocity (black), and acceleration (blue). b) The squared Brune spectrum corresponds to the frequency sensitivity of velocity-based $IV2$ (blue) and the acceleration-based I_A (black).

4.5.3 Landslide-related ground-motion models

The basic form of landslide-related ground-motion models for Arias intensity is based on earthquake magnitude M and distance from the earthquake rupture r (e.g. Harp and Wilson, 1995).

$$\ln I_A = p_1 + p_2 M + p_3 \ln r \tag{4.17}$$

This form is widely used (Keefer, 1984; Harp and Wilson, 1995). In engineering seismology, ground-motion models usually have an additional distance term for anelastic attenuation:

$$\ln I_A = c_1 + c_2 M + c_3 r + (c_4 + c_5 M) \ln r \tag{4.18}$$

This is a modified version of the model template by Kramer (1996). While Eq. 4.17 and Eq. 4.18 share some parameters (p_1, c_1 and p_2, c_2), the geometric spreading term includes not only distance dependence (p_3, c_4) but also has a magnitude-dependent component (c_5). In addition, anelastic attenuation is included as well (related to c_3) in Eq. 4.18. The template of Kramer (1996) relates to the majority of ground-motion prediction equations (GMPEs) in engineering seismology. Models of this kind address strong motion in the context of landsliding (Travasarou et al., 2003; Bray and Rodriguez-Marek, 2004). The incorporation of anelastic attenuation is less common in landsliding GMMs and not mentioned in these studies but is included in more recent studies (Meunier et al., 2007, 2013; Yuan et al., 2013).

We exchange the magnitude term from Eq. 4.18 with a site-dependent energy term, assuming that landsliding is more related to the energy of incoming seismic waves than to the moment at the source. We replace moment magnitude by the logarithm of energy (Eq. 4.11), since energy is proportional to the

seismic moment M_0 (Eq. 4.9). Based on the site-dependent energy estimate $\hat{E}$, we propose the model

$$\ln I_A = c_1 + c_2 \ln \hat{E} + c_3 r + (c_4 + c_5 \ln \hat{E}) \ln r \tag{4.19}$$

The five coefficients are inferred by non-linear least squares (e.g. Tarantola, 2005). We use the rupture-plane distance (r_{rup}), i.e. the shortest distance between a site and the rupture plane.

4.5.4 Rupture directivity model

In the NGA-west2 guidelines (Spudich et al., 2013), the directivity effect is modeled by isochrone theory (Bernard and Madariaga, 1984; Spudich and Chiou, 2008) or the azimuth between epicenter and site (Somerville et al., 1997). We use the latter approach and model directivity for estimated energy and corrected Arias intensity in a simplified way:

$$\ln \hat{E}_\theta = \ln \hat{E}_0 + a_E \cos(\theta - \theta_E) \tag{4.20}$$

$$\ln I_{A,A,\theta} = \ln I_{A,A,0} + a_I \cos(\theta - \theta_I) \tag{4.21}$$

where $\hat{E}_0$ and $I_{A,A,0}$ are the offset (average), a_E and a_I the amplitude of variation with azimuth and θ_E and θ_E are the azimuths of the maximum. The definition of θ is similar to that of Somerville et al. (1997) for the angle measured between the epicenter and the recording site with the difference of being measured clockwise from the north. The azimuths of the maximum, θ_E and θ_I, are free parameters because (1) the rupture is assumed to have occurred on two faults and has thus variable strike and (2) the event is not pure strike-slip and has a normal faulting component. We therefore do not expect a match between the rupture strike and θ_E and θ_I. The geometrical spreading is already incorporated in the energy estimate as a distance term (Somerville et al., 1997; Spudich et al., 2013).

4.5.5 Model for fault-normal-to-fault-parallel ratio

The ratio of the response spectra of the horizontal sensor components is a function of oscillatory frequency f_{osc}.

The north and east components (E, N) of the sensor are rotated to be fault-normal (FN) and fault-parallel (FP).

$$FN = E \cos\phi - N \sin\phi \tag{4.22}$$

$$FP = E \sin\phi + N \cos\phi \tag{4.23}$$

$$FN/FP = \frac{SA_{FN}(f_{osc})}{SA_{FP}(f_{osc})} \tag{4.24}$$

The response spectra are calculated from accelerograms after Weber (2002) with a damping of $\zeta = 0.05$.

The amplitudes of waves parallel to rupture propagation differ from waves normal to propagation on top of the directivity effect. This variation depends on the azimuth and is larger only at high periods. The fault-normal response amplitude is larger than the fault-parallel response if directed parallel or antiparallel to the rupture. We model the ratio similar to Somerville et al. (1997):

$$\ln FN/FP = (b_1 + b_2 f_{osc}^{b_3} \cos(2(\theta - \theta_R)) H(b_1 + b_2 f_{osc}^{b_3}) \tag{4.25}$$

where parameters b_i describe the relationship of the oscillatory frequency to the ratio, θ is the azimuth (Eq. 4.20), and θ_R is the azimuth of the maximal ratio. The ratio azimuth is as subject to assumptions like its counterpart θ_E. The Heaviside function $H(\cdot)$ avoids negative values in the model, which would be equivalent to an undesired phase shift in the cosine term.

We introduced a functional form for oscillatory frequency dependence with four parameters in Eq. 4.25. We did not introduce a distance term and apply the model only to data with $r_{rup} \leq 50$ km.

4.6 Results

4.6.1 Topographic analysis

Landslides occurred mostly in tephra layers (Figure 4.2a,b) covered by forests (Figure 4.2d,e) and predominantly along the NE rupture segment. Nearly all landslides concentrated on hillslopes with a steepness between 15° and 45° and an MAF ∼1 (Figure 4.4a,c). Hillslope inclination and the MAF were higher towards the landslide crown (Figure 4.4b,d), indicating a landslide failure process starting from the crown and according to simulations by Dang et al. (2016). The TWI is linked to land cover and is highest in areas with rice paddies (Figure 4.2i). Terrain with landslides has uniformly low TWI, thus we cannot evaluate the hydrological impact on the earthquake-related landslides (e.g. Tang et al., 2018).

Most landslides originated at locations with amplified ground accelerations and steep hillslopes and ran out on flatter areas with less amplified ground accelerations. Landslides—interpreted as shear failure—start as mode II (in-plane shear) failure at the scarp and mode III (anti-plane shear) failure at the flanks (McClung, 1981; Fleming and Johnson, 1989; Martel, 2004). At later stages of the landslide rupture, mode I (widening) failure can also occur in the process (Martel, 2004). Simulations of elliptic landslides by Martel (2004) show that either the most compressive or the most tensile stresses are parallel to the major axis of the landslide, coinciding with the average landslide aspect. Yamada et al. (2013) and

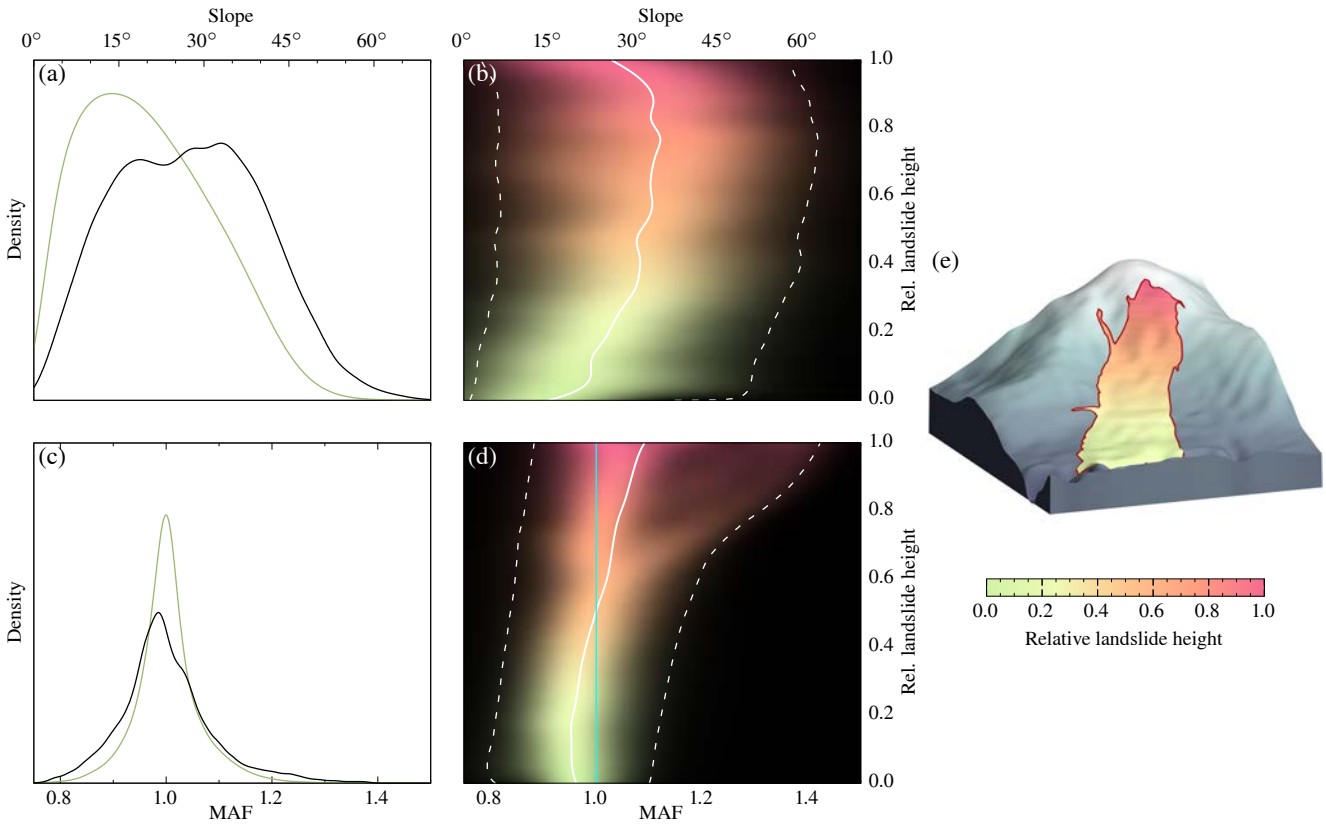

FIGURE 4.4: Distribution of hillslope inclination and MAF. The left column shows a) hillslope inclinations and c) MAF within the landslide-affected area (green) and within the landslide areas (black). The right column presents b) hillslope inclinations and d) MAF in different segments of the landslide areas which is expressed as relative height. Segments towards to the toe (relative height 0.0–0.5) are in green, and segments towards the crown are in red (relative height 0.5–1). The solid line is the mean, and the dashed lines enclose the 95% uncertainty range. The concept of relative height is illustrated for the Aso Ohashi landslide in e). MAF$<$ 1 indicates attenuation and MAF$>$ 1 amplification of seismic waves due to topography. The cyan line in d) highlights MAF = 1, i.e. no amplification or attenuation.

Yamada et al. (2018) show for several Japanese landslides that peak forces were aligned parallel to the long side of the landslides; Allstadt (2013) shows from waveform inversion for the Mt. Meager landslide that force and acceleration were parallel to the long side of the landslide source area.

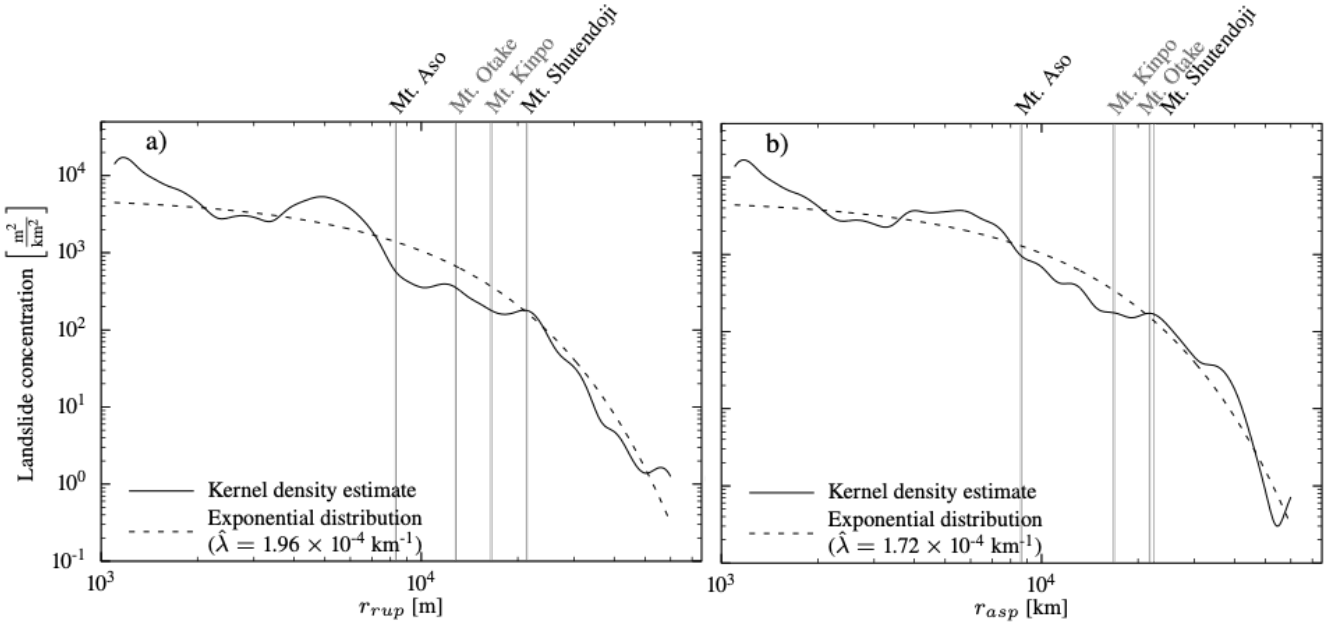

FIGURE 4.5: a) Landslide concentration with a) rupture distance r_{rup} and b) asperity distance $r_{asp}$of the Kumamoto earthquake landslides. The rate parameter of the exponentially decaying landslide concentration is estimated by maximum likelihood. The distances to the four peaks shown in Figure 4.1 are given. Densities change little with distance metric, as highlighted by the similar kernel density estimates and the near-identical rate parameter estimates $\hat{\lambda}$. The landslide concentration for Mt. Aso depends more on the distance metric than for the other three locations. The more distant mountains have very similar concentrations despite differences in distances (in particular Mt. Otake). However, when compared to Figure 4.6, Mt. Shutendoji has a higher landslide concentration than Mt. Kinpo and Mt. Otake, despite being the farthest away.

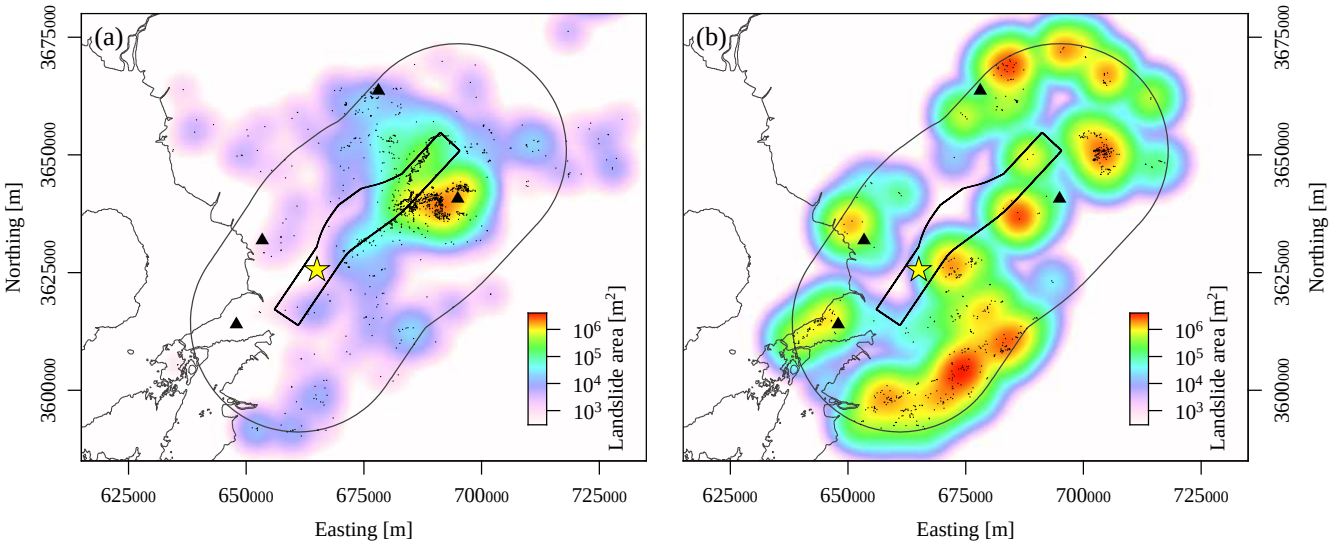

FIGURE 4.6: Spatial distribution of landslides. a) Coseismic landslides. The total landslide area at a location is shown as a color-coded smooth function in the background; b) same as in (a) but for unspecified landslides within the landslide-affected area of the Kumamoto earthquake.

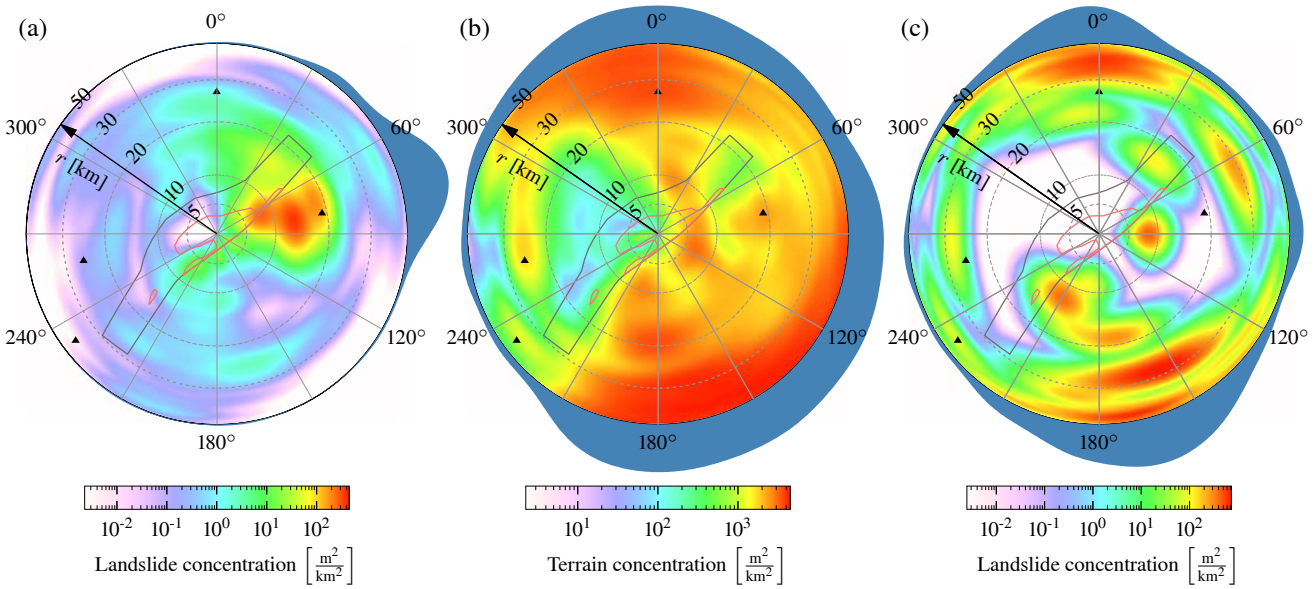

FIGURE 4.7: Kernel density estimates of azimuth and distance of a) landslide concentration of the coseismic landslides, b) concentration of landslide-affected terrain with hillslope inclinations >19°, and landslide concentration of unspecified landslides. Azimuth and distance are with respect to the asperity centroid. The marginal densities with respect to azimuth are shown in blue as outer ring. The densities are normalized to their maxima.

Mt. Aso and its caldera and Mt. Shutendoji had a high density of landslides (Figure 4.5), whereas Mt. Kinpo and Mt. Otake lack landslides, despite being closer to the epicenter and being comparably close to the rupture (Figure 4.5). All these locations have the same rock type and land cover, hillslope inclination and MAFs. Hence, lithology, land cover, and topographic characteristics are insufficient in explaining the landslide distribution and concentration with respect to the hypocenter or the asperity.

The azimuthal density—with respect to the asperity centroid—of the unspecified landslides follows to some extent the distribution of hillslope inclinations $\geq 19°$ in the landslide-affected area (Figure 4.7). This similarity shows that the abundance of unspecified landslides mimics the steepness of topography in the region. Densities are higher towards Mt. Kinpo (NW), Mt. Otake (WSW), Mt. Shutendoji (N), Mt. Aso (NE), and the Kyushu Mountains (SE). The coseismic landslide distribution differs completely from the distributions of unspecified landslides and their surrounding topography (Figure 4.7), respectively, as nearly all landslides happened to the northeast of the epicenter close to the rupture plane (Figure 4.6). Chen et al. (2017) identified only 29 landslide reactivations during the Kumamoto earthquake. The contrast between the distributions of unspecified landslides

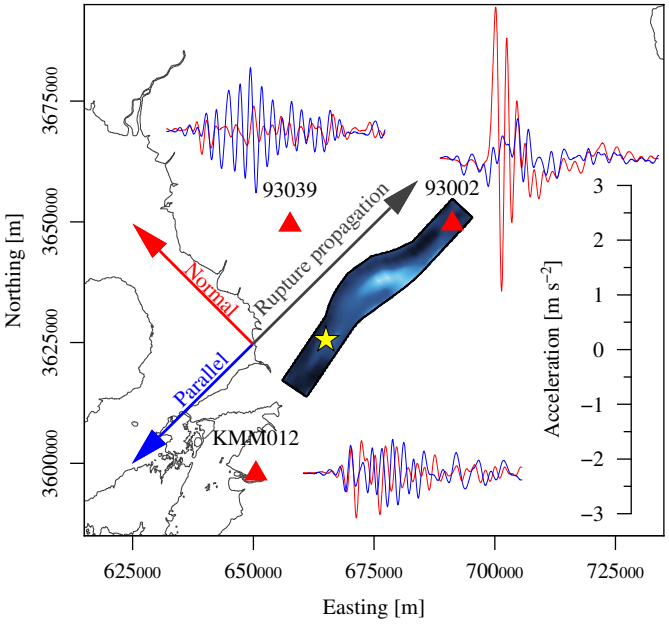

FIGURE 4.8: Characteristic waveforms observed in the vicinity of the rupture exhibiting rupture directivity effects. Station 93002 is in the forward-directivity region with a large amplitude pulse on the fault-normal component. Station 93039 is also in the forward-directivity region but with an offset to the rupture. In this region the fault-parallel component has higher amplitudes. The station KMM012 is in the backward-directivity region, and waveforms have longer duration without large amplitudes. The waveforms are in low-passed filter at 1.2 Hz.

and earthquake-related landslides indicates a contribution by the rupture process.

4.6.2 Impact of finite source on ground motion and landslides

The results of the seismic analysis are given for waveforms, the basis for $\hat{E}$ and I_A, and response spectra, used for FN/FP. To the northeast, signals with forward directivity are shorter in duration, with one or a few strong pulses (Figure 4.8, top right). Waveforms with backward directivity to the southwest of the rupture are longer, with no dominant pulse (Figure 4.8, bottom left). Waveforms parallel to the rupture have an intermediate duration. Waveforms in either a forward or backward direction have stronger amplitudes in the fault-normal direction, whereas waveforms outside the directivity-affected regions have stronger amplitudes in the fault-parallel direction (Figure 4.8, top left).

We estimated energies $\hat{E}$ from the three-component waveforms. For the Arias intensity, both horizontal components are used. The geometrical spreading A is calculated according to Eq. (4.12), with a rupture length of L =53.5 km and width of W =24.0 km. Any remaining distance dependence has been corrected for by estimating and applying the attenuation parameter k (Eq. (4.13))

After the determination of k, $\hat{E}$ and $I_{A,A}$ are considered distance-independent and can be investigated for azimuthal variations. With a reference point for the azimuth at the epicenter, $\hat{E}$ shows oscillating variations in amplitude with azimuth (Figure 4.9a), while $I_{A,A}$ exhibits a similar amplitude variations over the entire azimuthal range (Figure4.9b). The running average based on a von Mises kernel ($\kappa_{vM} = 50$) of $\hat{E}$ and $I_{A,A}$ shows increased $\hat{E}$ between 45° and 135°, i.e. approximately parallel to the strike. Minimal values of $\hat{E}$ occur in the opposite direction (200° - 300°). The running average of $I_{A,A}$ shows several fluctuations, but not as wide and large as those of $\hat{E}$. The azimuthal variation in $\hat{E}$ indicates the rupture directivity and the absence of large variations in $I_{A,A}$ indicates that the directivity effect is only evident at lower frequencies (compare with Figure 4.3).

The azimuthal variation in $\hat{E}$ and $I_{A,A}$ is modelled according to Eq. 4.20. We estimate parameters for two scenarios:

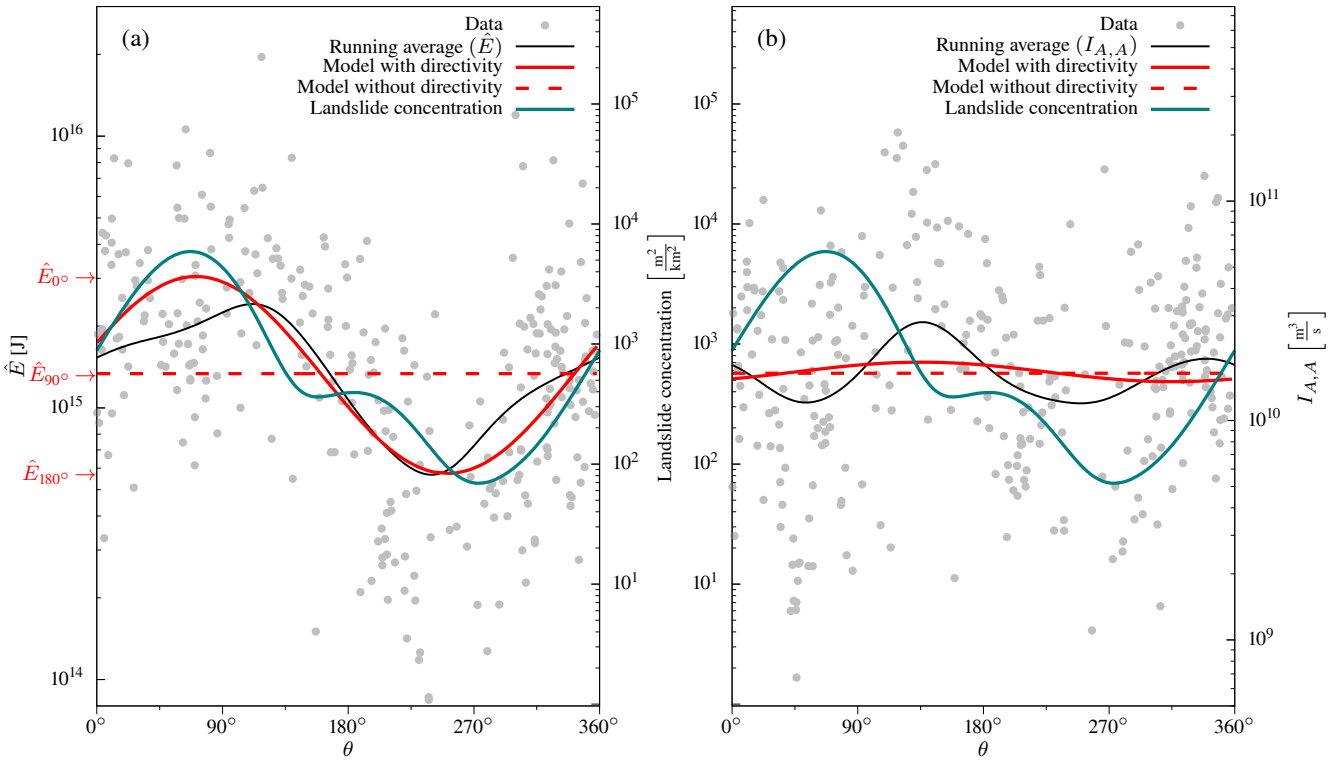

FIGURE 4.9: a) Energy estimates ($\hat{E}$) over azimuth; b) same as in a) but for Arias intensity with correction for geometrical spreading ($I_{A,A}$).

- directivity is assumed, resulting in azimuthal variations where a_E and a_I are free parameters,
- directivity is not assumed, resulting in no azimuthal variations with $a_E = a_I = 0$.

The two models are compared with the Bayesian information criterion (BIC; Schwarz, 1978) for a least squares fit:

$$BIC = n \ln N + N \ln \hat{\sigma}^2, \tag{4.26}$$

where n is the number of estimated parameters ($n = 4$ for the first case and $n = 2$ for second case), N is the number of data, and $\hat{\sigma}^2$ is the variance of the model residuals. The model with the smaller BIC is preferred. The starting values of the parameters are the mean of $\hat{E}$ and $I_{A,A}$, no azimuthal variation ($a_d = 0$), and the azimuths of the maximum of $\hat{E}_\theta$ and $I_{A,A,\theta}$ are set to the strike of the fault ($\theta_E = \theta_I = 225°$).

The directivity model for $\hat{E}$ follows the trend of the data and the running average closer than the model without directivity (Figure 4.9a). According to BIC, the model with directivity is preferable ($BIC_{directivity} = -110$, $BIC_{nodirectivity} = -11$). In the case of the Arias intensity, the difference in BIC between the two models is less compared to the azimuth-dependent energy (Figure 4.9b). Here, the model without directivity is the preferred one ($BIC_{directivity} = 30$, $BIC_{nodirectivity} = 22$). In consequence, azimuthal variations in wave amplitudes and energy related to the directivity effect occur at lower frequencies.

The forward-directivity waves contain a very strong low-frequency pulse (Figure 4.8). The pulse amplitude depends on the ratio of rupture and shear wave velocity and the length of the rupture (Spudich and Chiou, 2008). The forward-directivity pulse is superimposed by high-frequency signals in acceleration traces but becomes more prominent in velocity traces (Baker, 2007) due to its low-frequency nature, i.e. below 1.6 Hz (Somerville et al., 1997).

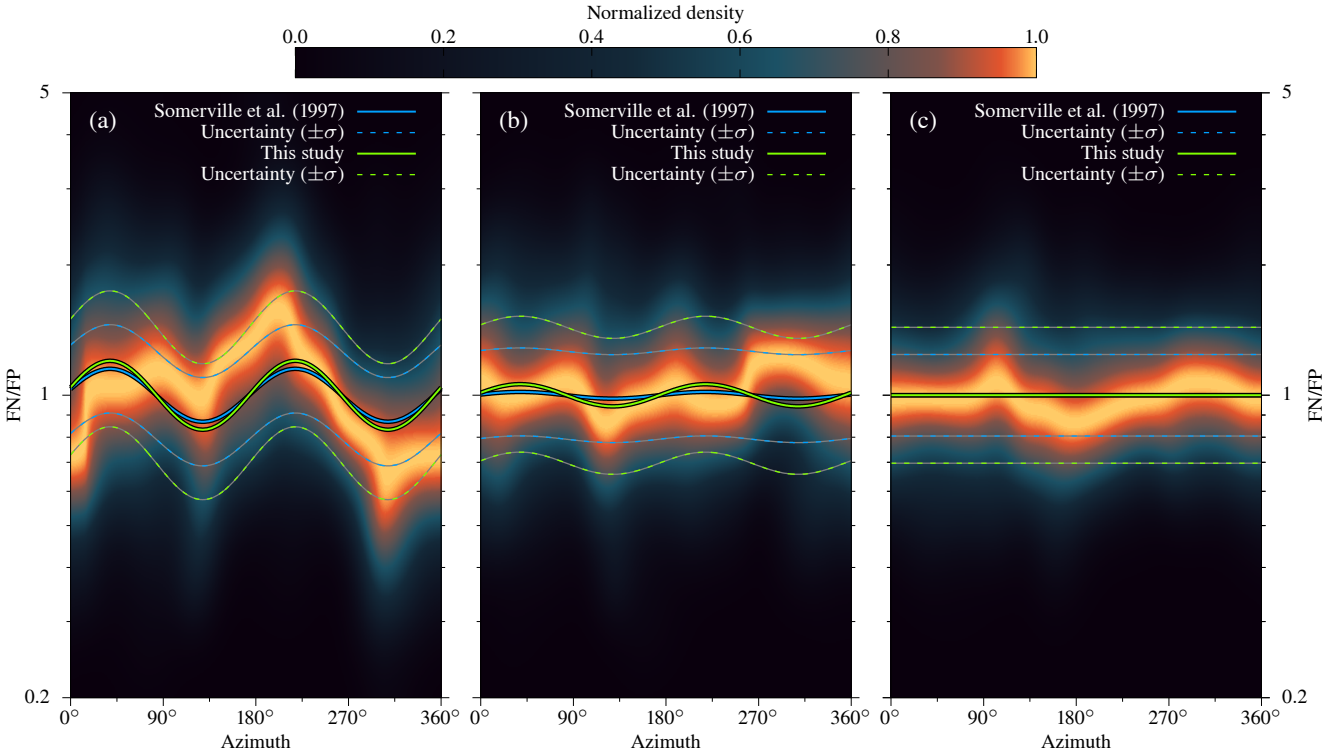

FIGURE 4.10: Kernel density estimate of FN/FP with azimuth obtained from response spectra for three different oscillatory frequency ranges: a) 0.1 – 1 Hz, b) 1.0 – 2.5 Hz, and c) >2.5 Hz. For each plot, our FN/FP model and the model of Somerville et al. (1997) are shown for a) 0.55 Hz, b) 1.75 Hz, and c) 4 Hz. As in Figure 4.11, amplitudes decrease with increasing oscillatory frequency.

The low-frequency azimuthal variations are also reflected in the spectral response of the waveforms. Spectral accelerations of stations with $r_{rup} \leq 50$ km were computed from 0.1 Hz to 5 Hz at intervals of 0.01 Hz for the fault-normal and fault-parallel component. The distribution of FN/FP shows decreasing azimuthal variability with increasing oscillatory frequency (Figure 4.10). FN/FP is most variable with azimuth at low oscillatory frequencies (0.1 – 1 Hz; Figure 4.10a); variations are much smaller between 1 and 2.5 Hz (Figure 4.10b) and nearly absent above 2.5 Hz (Figure 4.10c). This decrease with frequency is captured by the FN/FP model (Eq. 4.25; Figure 4.11). Since our model is an average over the covered distance, with an average rupture distance of 25.06 km, we compare it to the FN/FP model of Somerville et al. (1997) at 25 km (Figures 4.11, 4.10). Both models show a similar decay with frequency, with our model predicting a slightly higher FN/FP. Therefore, the wave polarity ratio related to rupture directivity is pronounced at lower frequencies and dissipates with increasing frequency, similar to the azimuthal variations observable in energy estimates (lower frequencies) but not in Arias intensity (higher frequencies).

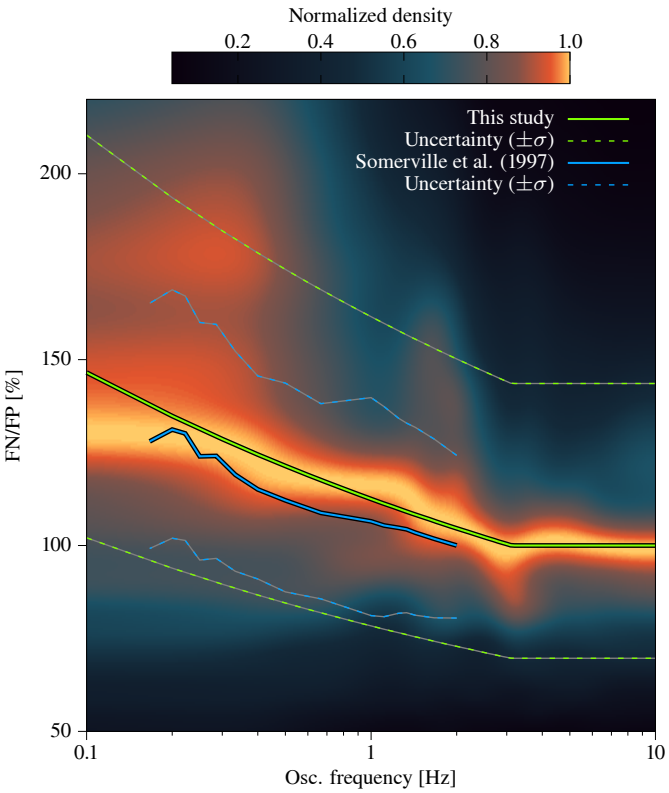

FIGURE 4.11: Kernel density estimate of the amplitude ratio from response spectra of fault-normal and fault-parallel components (FN/FP) respective to oscillatory frequency. Beyond 2–3 Hz FN/FP variations cease, as highlighted in our model and the model by Somerville et al. (1997).

The pattern of low-frequency ground motion is well reflected in that of landslides. The azimuthal variation in $\hat{E}$ coincides with that of landslide concentration (Figure 4.9). Both azimuth-dependent energy and landslide concentration have a similar trend, with the maximum being parallel to rupture direction and the minimum strike being antiparallel. The orientation of maximum FN/FP is also reflected in the landslide aspect. The northwest and east directions show higher landslide density (Figure 4.12a). The highest density of landslides has a northwestern aspect in agreement with maximum FN/FP, both perpendicular to the strike. The eastward increased density is mostly due to landslides very close to the rupture. A look at different distances reveals that the increased density of landslides facing east by southeast is at very short distances ($r_{rup} \leq 2.5$ km; Figure 4.14), while the northwest-facing landslides are further away (2.5 km $< r_{rup} \leq 6$ km). Only minor landslides are farther away, with no specific pattern.

The distribution of aspect and hillslope inclination in the landslide-affected area varies little with aspect (Figure 4.12b). The distinct northwest and east orientation of landslides is not an artifact of the orientation of the topography in the landslide-affected area (Figure 4.12a,b). The unspecified landslides in the affected area have a near-northward aspect and deviate by ∼30° from the earthquake-triggered landslides (Figure 4.12c). This highlights that the earthquake affects landslide locations (Figure 4.7 and will force failure on specific slopes facing in the direction of ground motion (Figures 4.12,4.6).

4.6.3 Ground motion model

We derived two ground-motion models for Arias intensity from data with $r_{rup} \leq 150$ km (Table 4.1; Figure 4.15). One model incorporates the azimuth-dependent seismic energy (Eq. 4.19). The other is a conventional isotropic moment-magnitude dependent model (Eq. 4.18). The decay of Arias intensity

	Model using $\hat{E}$	Model using M_W
c_1	4.083	5.879
c_2	$1.162 \cdot 10^{-1}$	$-3.201 \cdot 10^{-2}$
c_3	$-3.052 \cdot 10^{-5}$	$-3.172 \cdot 10^{-5}$
c_4	$-4.343 \cdot 10^{-1}$	$-2.349 \cdot 10^{0}$
c_5		$5.565 \cdot 10^{-2}$

TABLE 4.1: Parameters for ground-motion models

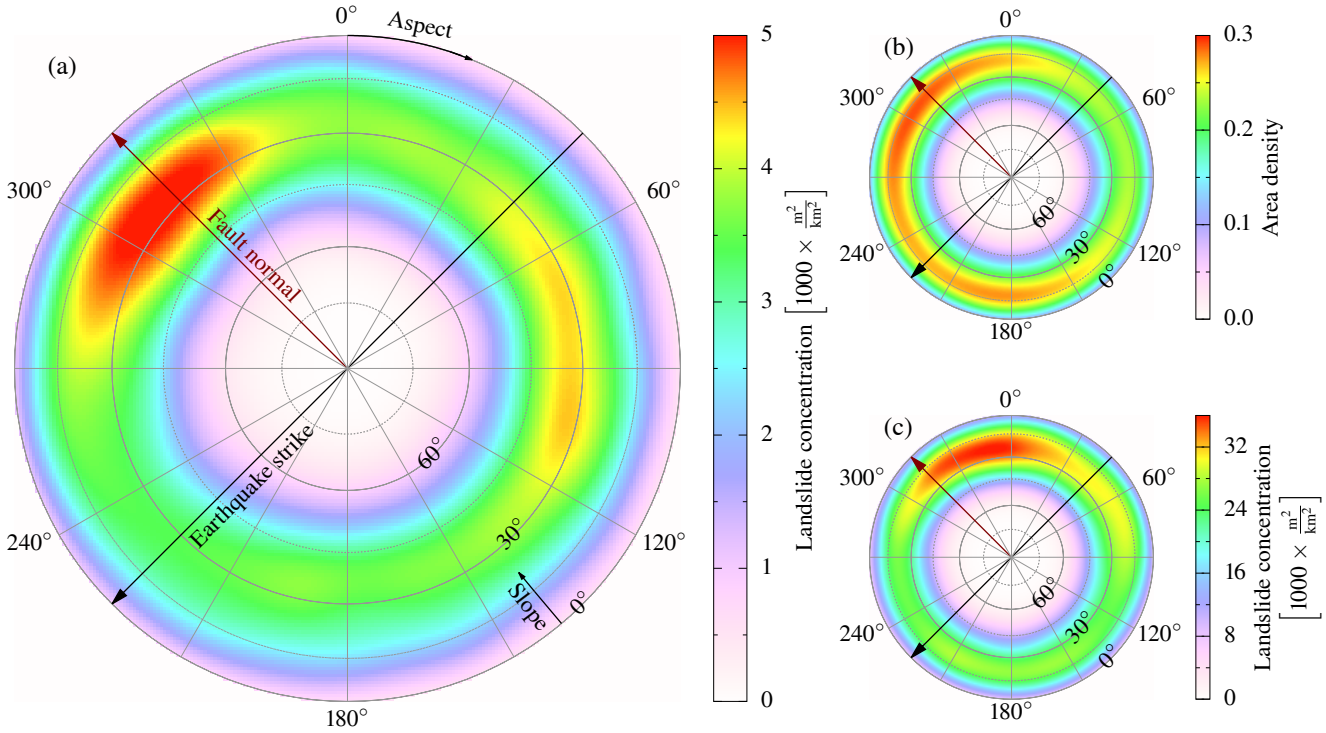

FIGURE 4.12: a) Aspect and hillslope inclination distribution within areas of the earthquake-triggered landslides. This distribution is normalized by the distribution of the aspect of all hillslopes in the landslide-affected area. The black line denotes the strike of the Kumamoto earthquake (225°). b) Distribution of aspect and hillslope inclination in the landslide-affected area; c) same as in a) but for unspecified landslides.

with distance for both models fits the running average well and is proportional to the decrease in landslide density with distance. Variation in estimated energy is well covered by the model and spans more 2 two orders of magnitude, resulting in variation in Arias intensity of nearly 1 order of magnitude.

The magnitude-based model is nearly equivalent to the energy-based model with $\hat{E} = 1.2 \cdot 10^{15}$ J. This value is close to the average energy estimate found from energy estimates of the directivity model from Eq. 4.20 ($\hat{E} = 1.3 \cdot 10^{15}$ J). The closeness of the two values implies that the magnitude-based model can be seen as an average over the azimuth of the energy-based model.

4.7 Discussion

We provide a framework for characterizing coseismic landslides with an integrated approach of geomorphology and seismology, emphasizing here the role of low-frequency seismic directivity and a finite source. Given the observations of ground motion of the Kumamoto earthquake, two questions arise: (1) How specific is the observed ground motion, i.e. is the Kumamoto rupture particularly distinct? (2) As a rupture very close to the surface, how much does seismic near-field motion contribute? The second question arises

because many landslides occurred very close to the rupture plane. However, it is not possible to separate the observed waveforms into near-, intermediate-, and far-field terms. To investigate both questions, we computed theoretical waveforms after Haskell (1964); Savage (1966); Aki and Richards (2002) from a circular rupture on an elliptic finite source with constant rupture velocity in a homogeneous, isotropic, and unbound medium (see Appendix).

Despite the simplified assumptions behind this waveform model, low-frequency ground motion captures the most prominent features of the observed waveforms. Simulated waveforms close to the rupture plane change in polarity orientation towards east–west, while the strong fault-normal polarity appears at larger distances. A decomposition into a near-field term and combined intermediate- and far-field term reveals that the former highly contributes to the ground motion at short distances. The impact of the near-field term may explain the dominance of east-facing landslides close to the rupture (Figure 4.14).

The simulations also demonstrate the effect of directivity on estimates of radiated energy and Arias intensity. The azimuthal variations in simulated $\hat{E}$ are similar to the observed variations. The Arias intensity of the simulations also displays azimuthal variations with same characteristics as the energy estimate. These variations in Arias intensity are absent in the observed data, indicating that Arias intensity is more influenced by local heterogeneities and scattering than the energy estimates, as these are ignored in the simulations.

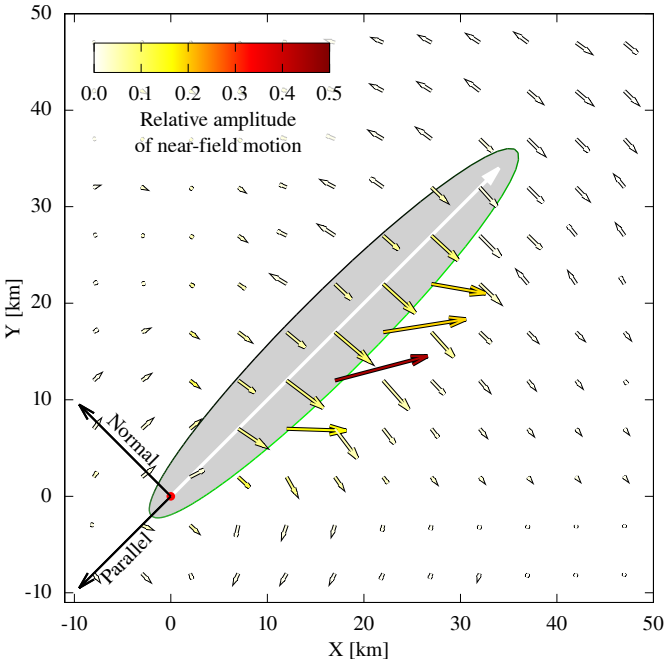

FIGURE 4.13: Orientation of horizontal peak ground acceleration for the simulated waveforms. The arrow length scales with magnitude of acceleration. The simulated rupture plane is oriented as the rupture plane of the Kumamoto earthquake (strike: 225°, dip: 70°) and of elliptic shape (gray). The upper side is denoted by the green line, and the lower half is denoted by black. The rupture process originated at the hypocenter (red dot) with circular propagation outwards (white arrow).

The results show that the Arias intensity is not as susceptible to the directivity effect and variations in fault-normal to fault-parallel amplitudes as the radiated energy; Because of its higher sensitivity towards higher frequencies, these effects are masked by high-frequency effects, e.g. wave scattering and a heterogeneous medium. We found that the radiation pattern related to the directivity effect is recoverable from energy estimates but not from Arias intensity. This low-frequency dependence is also seen in the response spectra ratios for FN/FP where directivity-related amplitude variations with azimuth have been identified only for frequencies <2 Hz, in agreement with previous work (Spudich et al., 2004; Somerville et al., 1997). We introduced a modified model for Arias intensity using site-dependent seismic energy estimates instead of the source-dependent seismic magnitude to better capture the effects of low-frequency ground motion.

The conventional magnitude-based isotropic model and the azimuth-dependent seismic energy model correlate with the landslide concentration over distance (Figure 4.15). As in Meunier et al. (2007) it is therefore feasible to use the ground-motion model to model the landslide concentration, $P_{ls}(I_A)$, by a linear relationship:

$$\ln P_{ls}(I_A) = a_I + b_I \ln I_A \tag{4.27}$$

Azimuthal variations in landslide density correspond to azimuthal variations in seismic energy and can be described by a similar relationship

$$\ln P_{ls}(E) = a_E + b_E \cos(\theta - \theta_E) \tag{4.28}$$

For the Kumamoto earthquake data, we estimate $a_I = 2.1$, $b_I = 2.6$, and $a_E = -31.5$, $b_E = 2.3$. The azimuth-dependent landslide concentration implies similar landslide concentrations at different distances from the rupture, thus partly explaining some of the deviation in Figure 4.5 and Figure 4.15.

Compared to the model of Harp and Wilson (1995) (Figure 4.15) our model uses rupture-plane distance, as opposed to the Joyner–Boore distance (r_{JB}). When using the hypocentral depth as pseudo-depth, the model of Harp and Wilson (1995) overpredicts I_A both at shorter and longer distances—irrespective of the pseudo-depth at larger distances. This misestimate is most likely due to the lack of an additional distant-dependent attenuation term in their model (Eq. 4.17).

The use of the MAF instead of curvature alone provides a proxy by how much a seismic wave is amplified (or attenuated) for a given wavelength and location. We showed that both hillslope inclination and the MAF tend to be lower towards the landslide toe (Figure 4.4). This effect is linked to the convention that landslide polygons cover both the zone of depletion and accumulation. (Sato et al., 2017) consider the tephra layers rich in halloysite to be the main sliding surfaces indicating shallow landslides (Song et al., 2017). When relating coseismic landsliding to the seismic rupture, only the failure plane of the landslide matters because this is the hillslope portion that failed under seismic acceleration. Chen et al. (2017) noted, for example, that landslide susceptibility and safety factor calculation depend on whether the entire landslide or only parts—scarp area or area of dislocated mass—are considered. The reconstruction of the landslide failure planes is limited to statistical assessments of landslide inventories (DOMEJ et al., 2017; Marc et al., 2019). However, failure may have likely originated close to the crown and then progressively propagated downward the hillslope, because MAF > 1 indicates an amplification of ground motion towards the crown of the landslides.

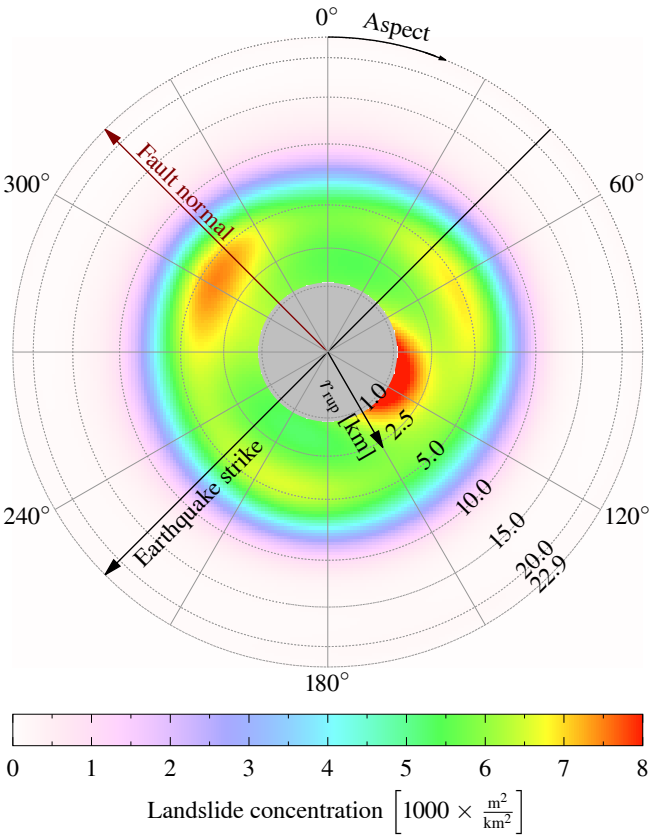

FIGURE 4.14: Distribution of landslides with aspect and rupture distance. The rupture distance is measured from the model of Kubo et al. (2016). This model does not completely reach the surface, truncating distances below 1 km. The distribution has been normalized by the distribution of aspect of the affected area.

Coseismic landslide locations have a uniformly low topographic wetness index, indicating that hydrology may have added little variability to the pattern of the earthquake-triggered landslides; at least we could not trace any clear impact of soil moisture on the coseismic landslide pattern (Tang et al., 2018).

4.8 Conclusions

We investigated seismic waveforms and resulting landslide distribution of the 2016 Kumamoto earthquake, Japan. We demonstrate that ground motion at higher frequencies controls the isotropic (azimuth-independent) distance dependence of Arias intensity with landslide concentration. In addition, ground motion at lower frequencies influences landslide location and hillslope failure orientation, due to directivity and increased amplitudes normal to the fault, respectively. Topographic controls (hillslope inclination and the MAF) are limited predictors of coseismic landslide occurrence because areas with similar topographic and geological properties at similar distances from the rupture showed widely differing landslide

activity (Havenith et al., 2016; Massey et al., 2018). Nonetheless landslides concentrated only to the northeast of the earthquake rupture, while unspecified landslides have been identified throughout the affected region.

We introduced a modified model for Arias intensity using site-dependent radiated seismic energy estimates instead of the source-dependent seismic magnitude to better model low-frequency ground motion in addition to the ground motion at higher frequencies covered by the Arias intensity.

Compared to previous models widely used in landslide-related ground-motion characterization our model is based on state of the art ground-motion models used in engineering seismology, which have two different distance terms, one for geometrical spreading and one for along-path attenuation. The latter is rare in landslide studies (e.g. Meunier et al., 2007; Massey et al., 2018). Our results emphasize that the attenuation term should be considered in ground-motion models, as the landslide concentration with distance mirrors such ground-motion models.

The effect of the earthquake rupture on the rupture process of the landslides results in landslide movements parallel to the strongest ground motion. Due to the surface proximity of the earthquake rupture plane, near-field ground motion influences the aspect of close landslides to be east–southeast. The intermediate- and far-field motion of the earthquake promoted more landslides on northwestern exposed hillslopes, an effect that overrides those of steepness and orientation of hillslopes in the region.

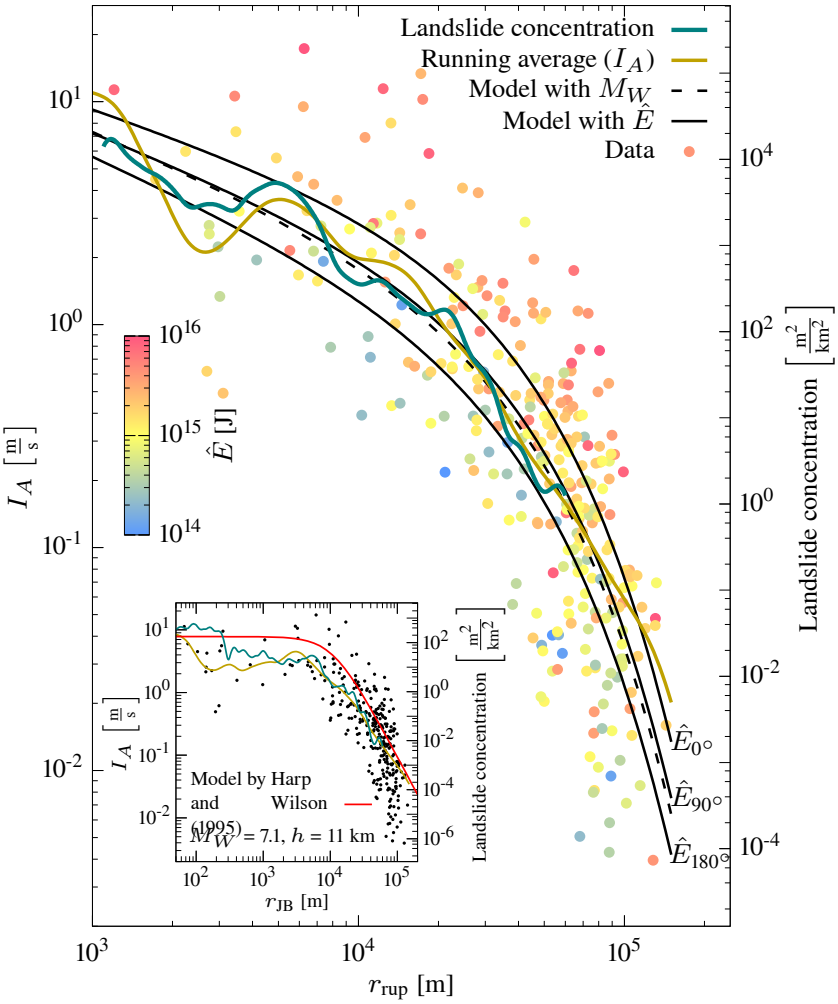

FIGURE 4.15: Ground motion model for I_A. The solid lines are the model with energy estimates for three different energy levels as in Figure 4.9a. The inset figure shows for comparison the ground motion model of Harp and Wilson (1995) (green), landslide concentration density (red).

We highlight that coseismic landslide hazard estimation requires an integrated approach of both detailed ground-motion and topographic characterization. While the latter is well established for landslide hazard, ground-motion characterization has been only incorporated by simple means, i.e. without any azimuth-dependent finite rupture effects. Our results for the Kumamoto earthquake demonstrate that seismic waveforms can be reproduced by established methods from seismology. We suggest that these methods can improve landslide hazard assessment by including models for finite rupture effects.

Acknowledgements

We highly appreciate the help of Tomotaka Iwata and Kimiyuki Asano for providing links to additional seismic data from the municipal and NIED networks and for several helpful discussions on the specifics of the data. We are sincerely grateful to Takashi Oguchi, Yuichi Hayakawa, Hitoshi Saito, and Yasutaka

Haneda for the field trip to the Aso region and fruitful discussions. We also thank Hendy Setiawan, Tao Wang, and Qiang Xu for reviewing and helping to improve the paper. Thanks to Arno Zang, John Anderson and Odin Marc for various discussions and comments. Sebastian von Specht, Ugur Ozturk, and Georg Veh acknowledge support from the DFG research training group "Natural Hazards and Risks in a Changing World" (grant no. GRK 2043/1).

4.9 Appendix

Synthetic waveforms from displacement of a finite rupture

We illustrate the generation of ground displacement as a discontinuity across a rupture fault (e.g. Haskell, 1964, 1969; Anderson and Richards, 1975; Aki and Richards, 2002). The displacement for any point x at time t is given by

$$u_i(\mathbf{x},t) = \iint_{\Sigma} c_{jkpq} \frac{\partial G_{ip}(D_j(\boldsymbol{\xi},t))}{\partial x_q} n_k d\Sigma \quad (4.29)$$

where c is the fourth-order elasticity tensor from Hooke's law, G is the Green's function describing the response of the medium, $\mathbf{D}(\boldsymbol{\xi},t)$ is the displacement on the fault with area Σ and coordinates $\boldsymbol{\xi}$, and $\mathbf{n}$ is the fault-normal vector. Summation over i,j,p, and q is implied.

While the surface integral is carried out numerically, the derivatives of Green's function for an isotropic, homogeneous, and unbound medium can be solved analytically:

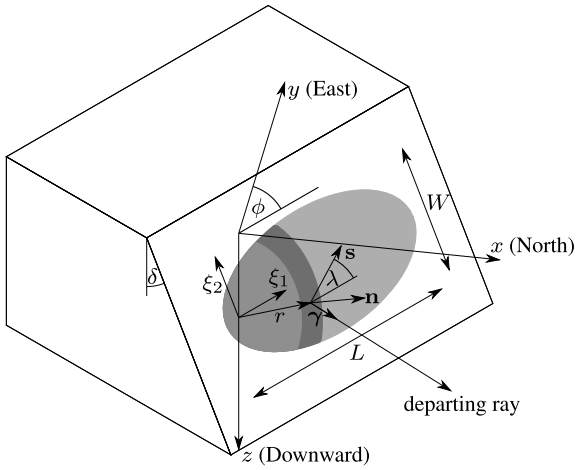

FIGURE 4.16: Set-up of the rupture model. Gray ellipse represents the rupture: light gray area is unruptured, medium gray area is slipping, and the dark gray area is after slip arrest.

$$\frac{\partial}{\partial x_q} G_{ip}(D_j(\boldsymbol{\xi},t)) = \quad (4.30a)$$

$$\frac{15\gamma_i\gamma_p\gamma_q - 3(\delta_{ip}\gamma_q + \delta_{iq}\gamma_p + \delta_{pq}\gamma_i)}{4\pi\rho r^4} \int_{\frac{r}{\alpha}}^{\frac{r}{\beta}} D_j(\boldsymbol{\xi}, t-\tau)\tau d\tau \quad (4.30b)$$

$$+\frac{6\gamma_i\gamma_p\gamma_q - (\delta_{ip}\gamma_q + \delta_{iq}\gamma_p + \delta_{pq}\gamma_i)}{4\pi\rho\alpha^2 r^2} D_j\left(\boldsymbol{\xi}, t-\frac{r}{\alpha}\right) \quad (4.30c)$$

$$-\frac{6\gamma_i\gamma_p\gamma_q - (2\delta_{ip}\gamma_q + \delta_{iq}\gamma_p + \delta_{pq}\gamma_i)}{4\pi\rho\beta^2 r^2} D_j\left(\boldsymbol{\xi}, t-\frac{r}{\beta}\right) \quad (4.30d)$$

$$+\frac{\gamma_i\gamma_p\gamma_q}{4\pi\rho\alpha^3 r} \dot{D}_j\left(\boldsymbol{\xi}, t-\frac{r}{\alpha}\right) \quad (4.30e)$$

$$-\frac{\gamma_i\gamma_p\gamma_q - \delta_{ip}\gamma_q}{4\pi\rho\beta^3 r} \dot{D}_j\left(\boldsymbol{\xi}, t-\frac{r}{\beta}\right) \quad (4.30f)$$

where,

$$r = |\mathbf{x}-\boldsymbol{\xi}| \text{ and } \gamma_i = \frac{x_i - \xi_i}{r} \quad (4.31)$$

and δ_{ij} is Kronecker's delta. The terms into Eq. 4.30 are commonly separated in groups with respect to their distance r. In Eq. 4.30a is the near-field (NF) term; as its amplitude decays with r^{-4}, it affects the immediate vicinity of a rupture only. Terms with a distance attenuation proportional to r^{-2} are called intermediate-field (IF) terms for P-waves (Eq. 4.30c) and S-waves (Eq. 4.30d). The remaining two terms

are the far-field (FF) terms for P-waves (Eq. 4.30e) and S-waves (Eq. 4.30f) with a decay proportional to r^{-1}. A major difference between the NF and IF terms, and the FF terms is that the former depend on the slip on the rupture and they are the cause for static and dynamic displacement; whereas the latter are functions of the time derivative of slip and result in dynamic displacement only.

The slip function in time is related to the Yoffe function of Yoffe (1951) and Tinti et al. (2005), with rise time T. We use the slip distribution of Savage (1966) to describe the amplitude distribution of the slip on the rupture as well as the elliptical fault shape and rupture propagation from Savage (1966). The slip amplitude is given by

$$D(\boldsymbol{\xi}) = D_0 \sqrt{1 - \left(\frac{\xi_1 - p\epsilon\frac{L}{2}}{\frac{L}{2}} \right)^2 - \left(\frac{\xi_2}{\frac{W}{2}} \right)^2} \tag{4.32}$$

where D_0 is the maximum displacement at the center of the fault, L and W are the length and width of the fault with eccentricity $\epsilon = \sqrt{1 - (\frac{W}{L})^2}$, and p determines whether the rupture starts at the focus at the front of the rupture plane (strike-parallel, $p = 1$) or at the focus at the end (strike-antiparallel, $p = -1$). The rupture originates in one of the two foci and propagates radially away from the source with constant velocity ζ and terminates when it reaches the rupture boundary. The slip vector $\hat{\mathbf{s}}$ describes the orientation of the displacement $D(\boldsymbol{\xi})$ on the fault plane. We follow the definition of $\hat{\mathbf{n}}$ and $\hat{\mathbf{s}}$ in terms of fault strike ϕ_s, dip δ, and rake λ from Aki and Richards (2002):

$$\hat{\mathbf{n}} = \begin{pmatrix} -\sin\delta\sin\phi_s \\ \sin\delta\cos\phi_s \\ -\cos\delta \end{pmatrix} \tag{4.33}$$

$$\hat{\mathbf{s}} = \begin{pmatrix} \cos\lambda\cos\phi_s + \cos\delta\sin\lambda\sin\phi_s \\ \cos\lambda\sin\phi_s - \cos\delta\sin\lambda\cos\phi_s \\ -\sin\lambda\sin\delta \end{pmatrix} \tag{4.34}$$

The displacement vector $\mathbf{D}$ in Eq. 4.30 is given by

$$\mathbf{D} = D(\boldsymbol{\xi})\hat{\mathbf{s}} \tag{4.35}$$

We consider that an isotropic medium and the elasticity tensor c from Eq. (4.29) is

$$c_{jkpq} = \delta_{jk}\delta_{pq}\lambda_M + (\delta_{jp}\delta_{kq} + \delta_{jq}\delta_{kp})\mu_M \tag{4.36}$$

where λ_M and μ_M are the Lamé constants of the isotropic medium:

$$\lambda_M = \rho(v_P^2 + 2\mu_M), \qquad \mu_M = \rho v_S^2 \tag{4.37}$$

We set $\lambda_M = \mu_M$, resulting in the widely observed relation $v_P = v_S\sqrt{3}$.

With the assumptions outlined above it is possible to calculate the displacement of an earthquake at location x with 12 parameters (Figure 4.16):

- fault size and orientation, including length L, width W, strike ϕ, and dip δ;
- material, including first and second Lamé constants λ and μ and density ρ (alternatively: compressional and shear wave velocities v_P and v_S and density ρ)
- rupture and slip, including rupture velocity ζ, slip D_0, rise time T, rake λ and rupture orientation with respect to strike p.

The fault size and displacement of earthquakes are correlated with each other and are scaled to the magnitude. The number of parameters reduces to 10 (9 if the Lamé constants are equal) when scaling relations (e.g. Leonard, 2010; Strasser et al., 2010) are used in combination with the seismic moment M_0.

The moment can be decomposed in

$$M_0 = \mu A \bar{D} \tag{4.38}$$

with shear modulus (second Lamé constant) μ, the rupture area—here an ellipse—$A = \frac{\pi}{4}LW$, and average displacement $\bar{D}$, which follows from Eq. 4.32 as $\bar{D} = \frac{2}{3}D_0$.

The results are not strictly comparable to observed data due to the model simplicity. The computed amplitudes will be smaller than observed values because no free surface is assumed. Assuming a free surface would nearly double the amplitudes from wave reflection as well as the amplifications from wave transmissions (from high- to low-velocity zones). Only direct waves are computed, and effects of reflections of different layers are not covered due to the isotropy and homogeneity. Corresponding waveforms—in particular surface waves—are not exhibited. However, the purpose of this model is to show (1) the general behavior of waveforms in the vicinity of a rupture, which is dominated by direct waves, and (2) how amplitudes distribute relatively in space.

4.10 Radiated seismic energy estimation

The exact calculation of radiated seismic energy is challenging. One simplifying assumption is that all waves arrive at the site with shear wave speed, which is a very good approximation for the far-field term. The reasoning can be justified from a theoretical perspective: for most earth media the ratio between the P-wave velocity α and S-wave velocity β is

$$\frac{\alpha}{\beta} = \sqrt{3} \tag{4.39}$$

From this and Eq. 4.30e and 4.30f, it follows that the amplitude of compressional waves is $\approx \frac{1}{\sqrt{3^3}}$ of the shear wave amplitude. If we say that the P-wave train has a similar duration as the S-wave train, then the energy contribution of the P-waves with respect to the S-waves becomes $(\frac{1}{\sqrt{3^3}})^2 = \frac{1}{27}$. The total energy of a signal is (Rudnicki and Freund, 1981)

$$E_{total} = E_P + E_S \tag{4.40}$$

and can be estimated by

$$\hat{E}_{total} = \alpha_S aIV2_\alpha + \beta_S aIV2_\beta, \tag{4.41}$$

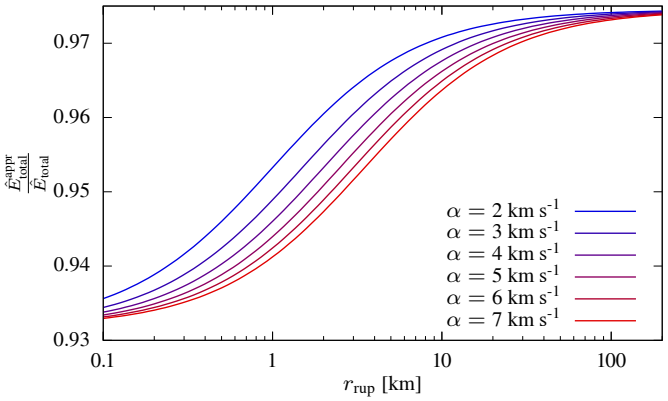

FIGURE 4.17: Ratio between the approximate and exact energy estimates for different P-wave velocities in the medium. The exact estimate assumes that P- and S-waves arrive at different velocities at the recording site, while the approximate estimate assumes that all waves arrive with shear wave velocity at the site. This approximation introduces only a minor underestimation, since most radiated energy is released as S-waves. The distance variation arises from the different distance and velocity dependencies of the intermediate-field terms and the far-field terms.

with the integrated squared velocity ($IV2$) for P- and S-waves from Eq. 4.7, the P- and S- wave velocities α_P and α_S at the recording site, and a constant a covering the remaining factors which are identical for both terms (compare with Eq. 4.8). If we express the energy contribution of P-waves in terms of S-waves, we can summarize the above relation to

$$\hat{E}_{total} = aIV2_\beta \left(\frac{\alpha_P}{27} + \beta_S \right) \tag{4.42}$$

$$= aIV2_\beta \left(\frac{\beta_S \sqrt{3}}{27} + \beta_S \right) \tag{4.43}$$

$$\approx aIV2_\beta \left(\frac{\beta_S}{27} + \beta_S \right). \tag{4.44}$$

The last expression is differs only by 2.6% from the exact term. While slightly underestimating the energy, this approximate definition of using α_S instead of β_S does not require the identification of P- and S- waves. This is useful, since at short distances the S-wave train is usually inseparable from the P-wave train.

At shorter distances, the intermediate-field term needs also to be taken into consideration. The amplitude of the intermediate term decays with r^2 (Eq. 4.30c, 4.30d), while the far-field amplitude decays with r (Eq. 4.30e, 4.30f). That is, the amplitude scales by distance and velocities and thus the $IV2$ are

$$IV2_\alpha = \alpha^{-4} r^{-2} (r^{-1} + \alpha^{-1})^2, \tag{4.45}$$
$$IV2_\beta = \beta^{-4} r^{-2} (r^{-1} + \beta^{-1})^2. \tag{4.46}$$

Again by replacing all P-wave terms by S-wave terms, the total energy becomes

$$\hat{E}_{total} = \alpha_S a IV2_\alpha + \beta_S a IV2_\beta \tag{4.47}$$
$$= a r^{-2} \left(\alpha_S \alpha^{-4} (r^{-1} + \alpha^{-1})^2 + \beta_S \beta^{-4} (r^{-1} + \beta^{-1})^2 \right) \tag{4.48}$$
$$= a r^{-2} \left(\sqrt{3}^{-3} \beta_S \beta^{-4} (r^{-1} + \sqrt{3}^{-1} \beta^{-1})^2 + \beta_S \beta^{-4} (r^{-1} + \beta^{-1})^2 \right) \tag{4.49}$$
$$\tag{4.50}$$

With the assumption that $\alpha_S = \beta_S$, Eq. 4.48 becomes

$$\hat{E}^{appr}_{total} \approx a r^{-2} \left(\beta_S \alpha^{-4} (r^{-1} + \alpha^{-1})^2 + \beta_S \beta^{-4} (r^{-1} + \beta^{-1})^2 \right) \tag{4.51}$$
$$= a r^{-2} \left(\sqrt{3}^{-4} \beta_S \beta^{-4} (r^{-1} + \sqrt{3}^{-1} \beta^{-1})^2 + \beta_S \beta^{-4} (r^{-1} + \beta^{-1})^2 \right) \tag{4.52}$$

The ratio between the approximation and the exact solution is

$$\frac{\hat{E}^{appr}_{total}}{\hat{E}_{total}} = \frac{\sqrt{3}^{-4} (r^{-1} + \sqrt{3}^{-1} \beta^{-1})^2 + (r^{-1} + \beta^{-1})^2}{\sqrt{3}^{-3} (r^{-1} + \sqrt{3}^{-1} \beta^{-1})^2 + (r^{-1} + \beta^{-1})^2} \tag{4.53}$$

The two limits with respect to distance are

$$\lim_{r \to 0} \frac{\hat{E}^{appr}_{total}}{\hat{E}_{total}} = \frac{\sqrt{3}^{-4} + 1}{\sqrt{3}^{-3} + 1} \tag{4.54}$$
$$\approx 0.932 \tag{4.55}$$
$$\lim_{r \to \infty} \frac{\hat{E}^{appr}_{total}}{\hat{E}_{total}} = \frac{\sqrt{3}^{-5} + 1}{\sqrt{3}^{-6} + 1} \tag{4.56}$$
$$\approx 0.974 \tag{4.57}$$

The second limit is identical to the far-field case derived above. The two limits show that even in the range of the intermediate-field term, the energy estimate deviates little when assuming that all waves arrive with β_S at the recording site. A comparison of the approximate energy estimate and the exact estimate as a function of distance and velocity is shown in Figure 4.17.

Chapter 5

DISCUSSION

The research questions of this thesis deal with the interaction between landslide triggers and controls at different scales in a broad scope. First the regional trajectories of the extreme rainfall are analysed in Japan as explained in chapter 2. In this chapter I elaborate rainfall triggered landslides in Japan focusing on extreme rainfall, mean annual rainfall, and snowmelt. Landslides seem not to follow regional trajectories of the extreme rainfall, but rather the rainfall totals. The local effects of the extreme rainfall are investigated in Braunsbach Germany, in chapter 3, where the interaction between extreme rainfall and landsliding is investigated focusing mainly on topographic and geological landslide controls in this chapter. At last the failure mechanism and distribution of landslides under seismic loading are explored in Kumamoto, southern Japan in chapter 4. Here I provide additional insights on its legacy on landscape for potential future landsliding. I also give information about the limitations of my results and what could be the potential reasons for those limitations.

RQ1: What (more) can we learn about regional-scale trajectories of extreme rainfall? Can this new knowledge aid landslide prediction eventually?

Landslide triggers (e.g., rainfall, snowmelt) are widely used in landslide susceptibility studies, where slope is the most influential attribute, whereas factors such as lithology are considered to have meager influence in some studies (e.g., Guzzetti et al., 2008; Lee et al., 2018), which might be true for regional study sites, e.g., continental or global scales. Accordingly, my first objective was to investigate the properties of the extreme rainfall; how to identify extreme rainfall, and what is its origin and spatial dynamics at the regional scale, to find out whether there is a spatial correlation with the landslide distribution, which is derived from an inventory of 4744 events between 2001 and 2011 by Saito et al. (2014).

I used event synchronization based complex networks in the analyses in chapter 2, and excluded convective cell-derived extreme rainfall automatically by using directed network measures, e.g., divergence. The extreme rainfall events were selected via the peaks-over-threshold method in the event synchronization algorithm, considering all events as extremes above the $95th$ percentile (e.g., Feldmann et al., 2013; Lind et al., 2016). The approach picks all observations above this threshold, selecting a larger number of extreme events compared to the commonly used block maxima method (Bezak et al., 2014), a model for the probability distribution of maxima from blocks of a certain time interval, e.g., monthly or annual (Fischer et al., 2018). The main advantage of the block maxima method is its ability to ensure independence between successive rainfall events (Rutkowska et al., 2017); while it might miss some of the high observations in case two or more events fall into the same block.

A tropical storm can bring several days of extreme rainfall. Hence I choose to apply the peaks-over-threshold method to include all these extremes in the analyses, and minimize the biases that could develop from block size (Thiombiano et al., 2017). A shortcoming of the peaks-over-threshold method is that some extremes can continue a couple of days, sometimes several days (in daily resolution data), which are considered as independent in our study. This particular shortcoming remains even if I would consider different time resolutions (e.g., half daily), since the principal assumption behind the peaks-over-threshold method rests on time series that capture extreme events in a representative manner. I selected the 95% threshold to ensure independence between thus selected events (Rutkowska et al., 2017). Another short coming of the peaks-over-threshold method is that it disregarded events with low-intensity and long-duration, although these might also trigger landslides due on rainfall accumulations (Nikolopoulos et al.,

2017; Palladino et al., 2018). This particular issue would nonetheless remain also if using the block maxima method. There is no method to re-organize daily rainfall time series into independent rainfall event series to our knowledge. Future work should address this gap of converting daily or hourly rainfall time series to consistent rainfall event series.

Our network model detected the extreme rainfall tracks using the radial ranks approach in a gridded domain (see chapter 2). I interpolated these vectors to stream lines over the entire Japan using the Matlab streamline tool. Those stream lines represent the most common trajectories of extreme precipitation in the study period, which should agree with the landslide-dense regions, since the likelihood of landslide occurrence increases with higher rainfall intensity and duration (Oguchi, 1996; Finlay et al., 1997; Guzzetti et al., 2008; Li et al., 2011); e.g., Typhoon Talas (Yamada et al., 2012), or 2011 extreme rainfall events in Kii Mountains of Japan (Matsushi et al., 2014). Hence I extracted the streamlines over the four main islands of Japan to derive a track-density map based on the daily Tropical Rainfall Measuring Mission (TRMM) rainfall estimates from 1998 to 2015 (Figure 5.1), and to test whether it correlates with the landslide dense regions. I summed the track densities for both the study periods (i.e. JJ and ASON) and correlate them with the normalized rainfall-triggered landslide density over Japan based on 4744 events between 2001 and 2011 by Saito et al. (2014)(Figure 5.1c). I would expect to see more rainfall-induced landslides along the regions with higher track density, but there was no correlation between the two. Although there seem to be a slight agreement around Kyushu, Shikoku and Hokkaido; it is inconsistent throughout Honshu when I focus on smaller regions (prefecture scale). High values on the Niigata, Fukui, and Nagano prefectures in central Honshu, indicates high landslide activity despite low track density of extreme rainfall. For example, a frontal storm triggered hundreds of landslides in Niigata prefecture in July 2004 (Yamagishi and Iwahashi, 2007), and had similar impacts on the Fukui prefecture (Mizuhashi et al., 2006). Another Baiu-related long-duration/low-intensity rainfall in July 2006 induced several landslides in Nagano prefecture (Okada et al., 2007). In contrary along (i) the northern coasts of western Honshu, (ii) the coastline from Kii Peninsula to the Izu and Bōsō Peninsulas in Honshu; and (iii) Oshima Peninsula in Hokkaido; and (iv) Central Kyushu the density of extreme rainfall trajectories seems to show similar patterns with the landslide density. However the trajectories alone are insufficient to explain the landslide distribution in Japan, due to, e.g., data resolution and completeness, other potential triggers like snowmelt, or non-linear interaction of rainfall with landslides, which are all discussed in paragraphs below respectively. The model accuracy could be better assessed by including only the landslides that are directly linked to extreme rainfall, however the occurrence times of the landslides are mostly unknown in data bases.

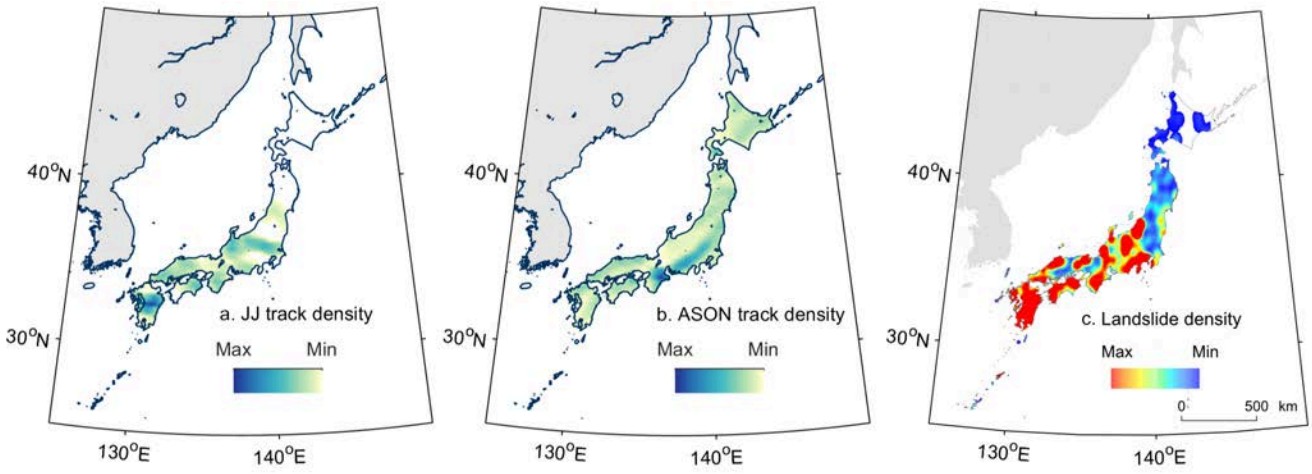

FIGURE 5.1: Interpolated extreme precipitation streamline density for the study period JJ (a) and ASON (b), normalized by cumulative above 95*th* percentile extreme rainfall for the same period between 1998 and 2015. c. Normalized rainfall-triggered spatial landslide density weighted by log-transformed landslide volumes calculated from an inventory of 4744 events, and smoothed by kernel density estimation onto 5×5 km grid by Saito et al. (2014); white areas have no data.

Meaningful spatial correlation between landslides and the rainfall trajectories are hard to find also due to the resolution differences in databases or the incomplete landslide inventories. The available spatial rainfall data resolutions were 0.25° (TRMM), 0.1° (GPM) or 0.05° (AphroJP). Minimum grid size is about $\sim 25^2$ km^2 for TRMM data, while most landslides are smaller than $\sim$0.01 km^2. I have not used the AphroJP, because it lacks data on the seas surrounding Japan, while GPM (2014-present) provided only $\sim$2 year of data during the analysis. A gridded rainfall data of $\sim$0.01 km^2 could improve our results; however it is currently not available. In contrary data with higher resolution than $\sim$0.01 km^2 would substantially increase the computation times and storage space. Contemporary efforts on rainfall radar technology could be remedy in this matter (e.g., Crisologo et al., 2018), referring to the analysis in chapter 3, it would be impossible to recognize the real intensity of rainfall over Braunsbach catchment (6 km^2) without the radar data.

Incomplete landslide inventories bias the predictive capacity of models (Günther et al., 2014a), and hinder an objective assessment of the directivity of landslides and extreme precipitation. Unless a landslide in populated areas is mapped within short time, the dense vegetation might quickly mask its recognition in Japan. Hence the databases might include more deep-seated landslide (linked mainly to rainfall totals) than debris flows (triggered mostly by intense rainfalls). Another potential issue is the occurrence times of the landslides that are mostly missing in data bases. Although I could argue for a link between landslides and an extreme rainfall at the local scale, e.g., Braunsbach was above the $80th$ percentile when ID curve is compared with other rainfall triggered landslides globally (Figure 3.4); it gets harder when the scale grows to regional, e.g., entire Japan. In the case of Braunsbach, I had the chance to walk along the valley only a month after the heavy rainfall event in 2016. Hence some of the landslides might have occurred later, and are linked to other processes, such as another rainfall, or anthropogenic vibrations due to construction works. Additionally, our inventory covers only Braunsbach in the districts of Hohenlohekreis and Schwäbisch Hall. There was more damage and debris flow reports along the sparsely populated small villages downstream Gerabronn Catchment associated with the Braunsbach rainfalls. However, no research group invested time on mapping those landslides due to their substantially smaller damage, less than 1% of the damage in Braunsbach (Gerabronn, 2016).

Another important influence on landslide triggering is snowmelt, especially along the western coasts of central Honshu Kawagoe et al. (2009). Snow cover also modulates landslide activity by increasing snow load which contributes to displacement on active landslides (Matsuura et al., 2017). The high landslide activity on the Japan Sea coasts of Honshu might be related to such snowmelt effects (Figure 5.2).

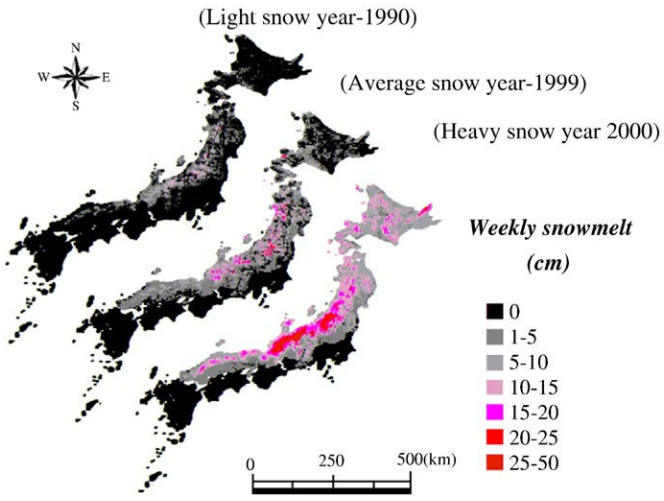

FIGURE 5.2: Example distributions of snowmelt in three different levels (light, average, and heavy years) by Kawagoe et al. (2009).

The non-linear relationship between rainfall characteristics (i.e. intensity and duration) and the landslides could also bias the correlation of extreme rainfall trajectories with landslide distribution (Dai and Lee, 2001; Saito et al., 2014). Rainfall intensity-duration (ID) thresholds vary between regions (Baum and Godt, 2010; Osanai et al., 2010), indicating other major parameters such as soil moisture (Crozier, 1999; Ponziani et al., 2012; Lin et al., 2016) or antecedent rainfall (Rahardjo et al., 2001; Bogaard and Greco, 2018) that may contribute to landsliding, as the driving mechanisms of landslides may act very slowly (months to decades) (Hungr et al., 2014). For example, one year after the Braunsbach event there were still fresh landslides (see Chapter 3). Another example would be the landslides in Nicaragua that were associated with Hurricane Mitch (October 1998) even after five years (accounting also the rains afterwards) (Devoli et al., 2007). Though the antecedent soil moisture

is rarely included in regional landslide susceptibility models because data on infiltration capacity and other parameters are sparsely available at this scale (Eichenberger et al., 2013), unlike widely available rainfall estimates or measurements. Consequently, the extreme rainfall may not be as important in terms of landslide triggering; rainfall totals might be a better predictor of landslides mobilized during typhoons and frontal storms (Saito et al., 2014; Scheevel et al., 2017).

Saito et al. (2014) compared rainfall duration, intensity (maximum and minimum) and totals to the accumulated landslide volume in Japan (Figure 5.3). They found out that the high accumulation rainfall coincide with higher landslide volumes, while the rainfall intensity or duration are insufficient to explain the associated distribution of landslide volume. Most rainfall contributes to the surface flow assuming that rainfall intensity exceeds the infiltration rate, when the downpours occur with high intensity and low duration (Horton, 1933). For example, the cumulative rainfall is equally high with lower intensity rates during JJ (frontal storm season). Thus, the infiltrated rainfall might be higher, increasing the saturation rates during JJ. It rains on average for 18 days around Kyushu during June, compared to 11 days during May, July and August (Figure 5.4).

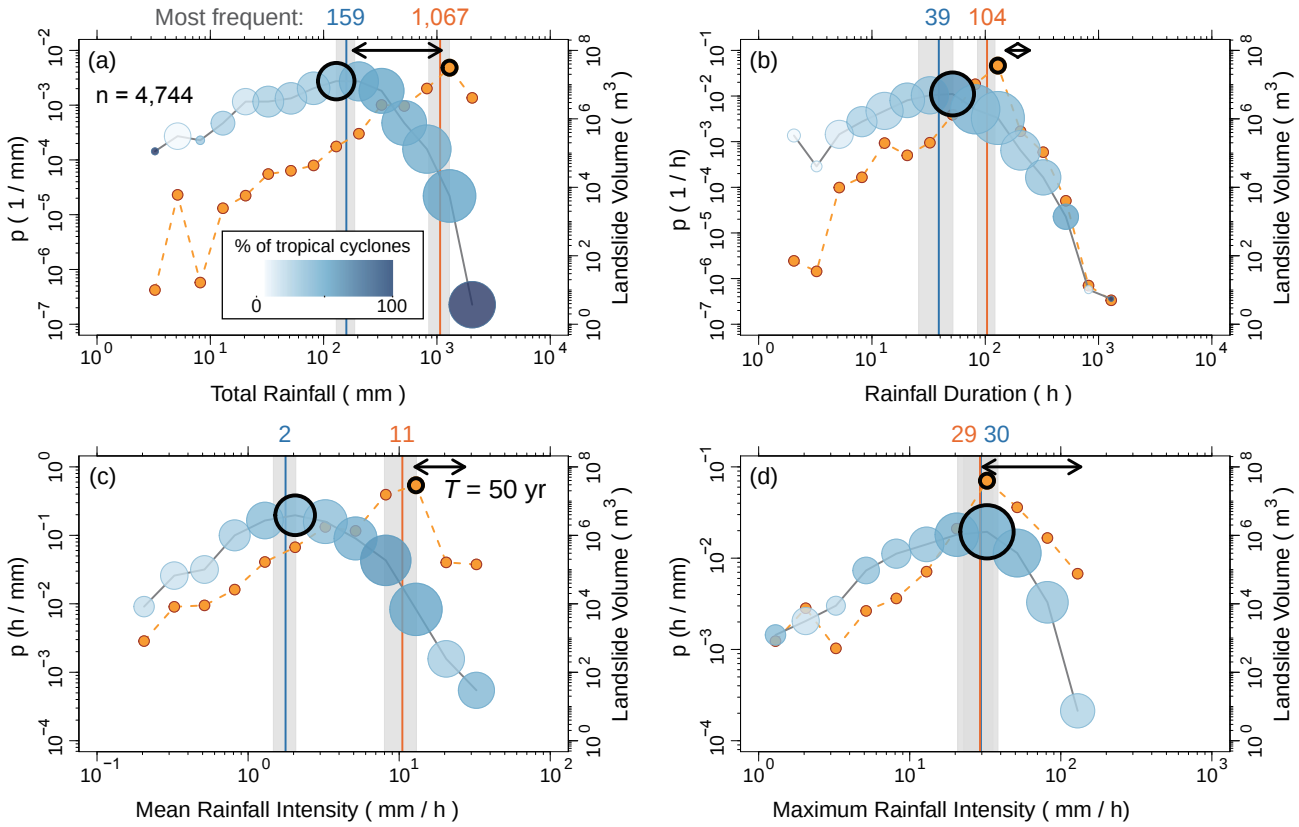

FIGURE 5.3: Log-binned probability density estimates of total landslide volume (orange dashed curves) and rainfall parameters (blue solid curves); for (a) Rainfall totals, (b) Rainfall duration, (c) Mean rainfall intensity, and (d) Maximum intensity by Saito et al. (2014). Vertical lines are means and gray shades around are error bars of $\pm 2\sigma$ (based on multiple bin widths), σ stands for standard deviation, of rainfall parameters that were most frequent (blue), and associated with the highest total landslide volumes in the study period (orange). Black circles outline rainfall parameter values most frequently associated with landslide reports. Bubble size is scaled to total landslide volume per bin; bubble brightness represents percentage of tropical cyclones out of total number of landslide-rainfall events; darker tones indicate higher fractions. Black arrows span range of 1-in-50-yr rainfall events computed for Abashiri (Northern Hokkaido) and Owase (Kii Peninsula, Honshu), and represent regions of the lowest and highest heavy rainfall frequencies in Japan.

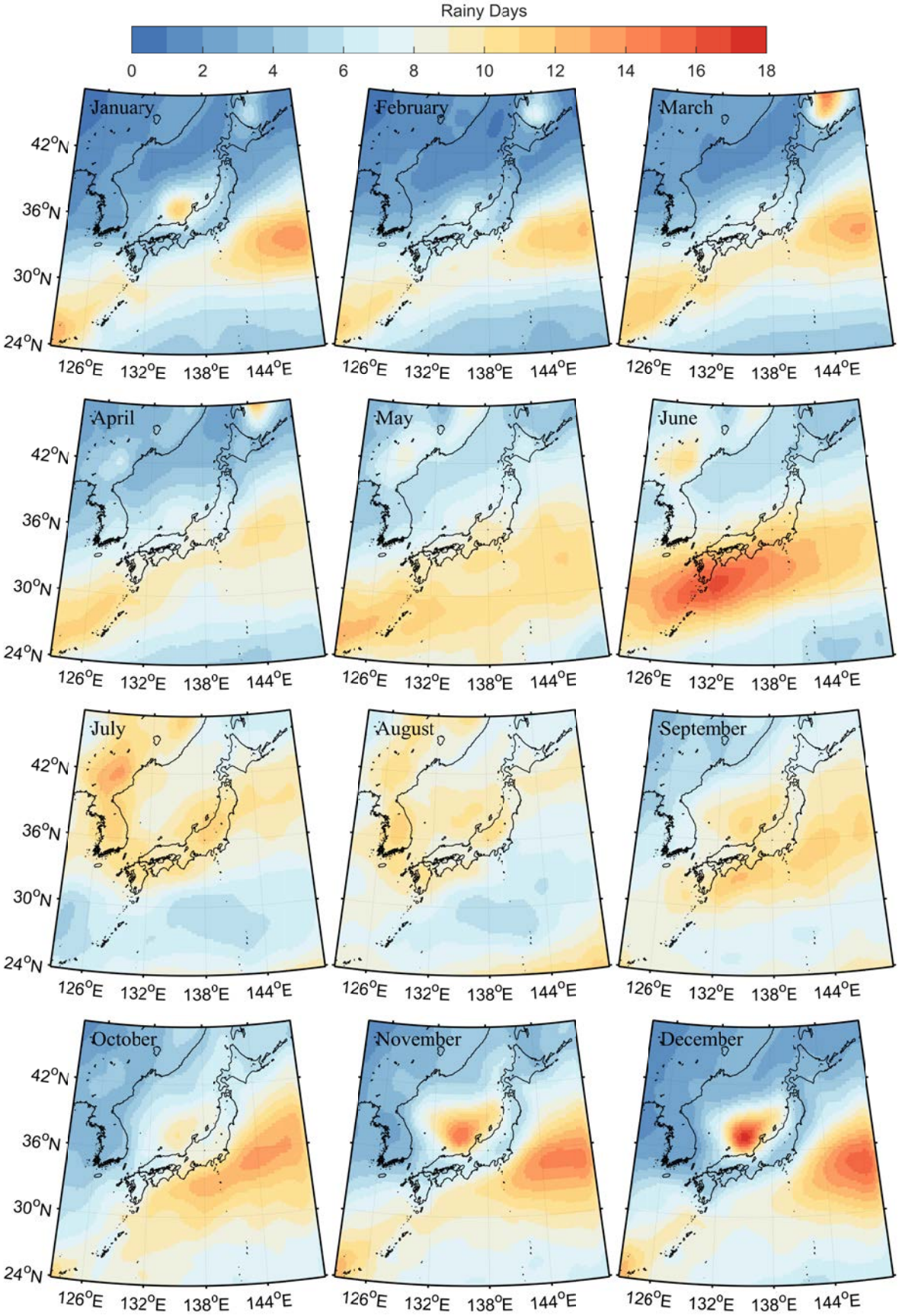

FIGURE 5.4: Average rainy days (more than 2 mm rain a day) in each month from 1998 to 2015 based on TRMM rainfall estimates. Rainy days get higher on land from May on until September covering the Baiu and tropical storm seasons.

RQ2: What are the local impacts of extreme rainstorms on landslide triggering? Can we improve regional landslide susceptibility estimates including local effects, such as geology, topography, or other anthropogenic interventions?

The second aim was to study the local effects of extreme rainstorms as landslide triggering factor in relation to topographic (i.e. slope, planform and profile curvatures) and geological (i.e. lithology) factors to suggest improvements for regional landslide susceptibility maps.

Local high-intensity rainfalls lead to surface runoff, which can initiate flash floods (Belachsen et al., 2017; Destro et al., 2018). The bank erosion process is considered to be the primary trigger of the landslides along catchment drainage lines in some of the state of the art literature (Borga et al., 2014; Gupta et al., 2016), where flood waters erode the banks of the river channel removing the lateral support of the unstable slopes (Dai et al., 2005; Gupta and Sah, 2008); besides the secondary effects of porewater pressure, suction, and seepage (Sidle et al., 2011; Bogaard and Greco, 2016; Chitu et al., 2017). For example, porewater pressure reduces the effective stress in shear surfaces, thus accelerating (e.g., from rates of mm/yr to cm/yr) the movement of landslides (Preisig et al., 2016). The increase of the slow movement process can reduce expected failure time of a landslide from years to months, even to days (Longoni et al., 2014). Accordingly, the fresh scarps along the Orlacher Bach, about one year after the 2016 Braunsbach event, indicate that some slopes still continue deforming, which might be related to the above mentioned secondary effects. Higher slope increases the flow velocity, which determines the solid transport capacity of the flood waters, and hence increase the erosive power of the flood waters along the river channel (Radice et al., 2006). Landslide abundance positively correlates with the steepness of river gradient (Rickenmann et al., 2016), which is observed along Orlacher Bach when the Orlacher Bach catchment is compared with the other neighbouring catchments (Figure 3.5), though I did not encounter preferred locations of landslides along the Orlacher Bach catchment (Figure 3.7).

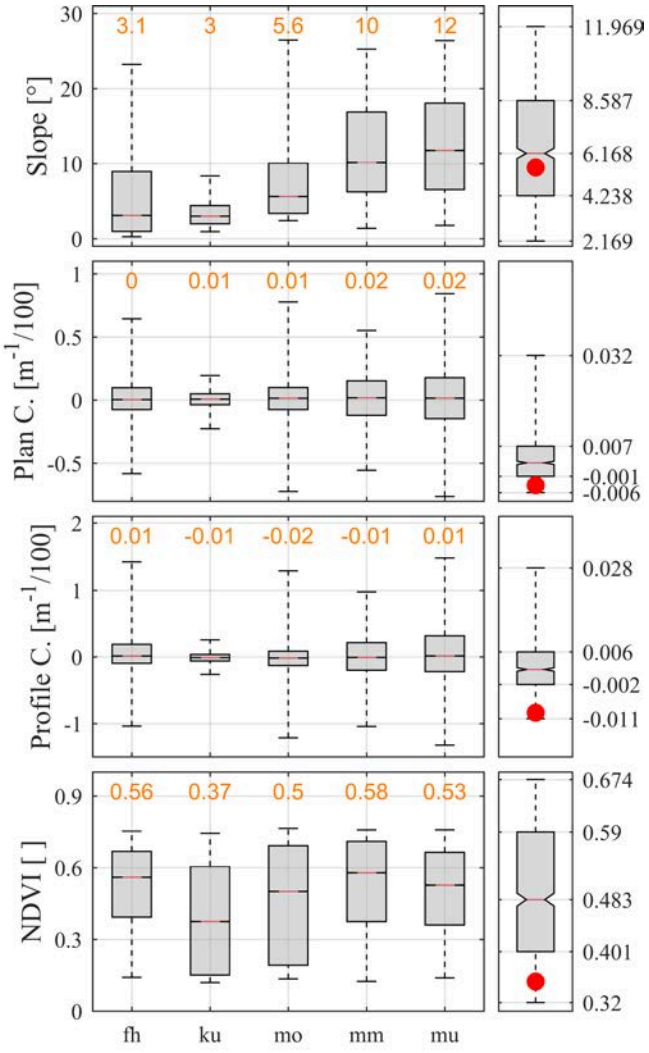

FIGURE 5.5: Boxplots show percentiles ($5th$, $25th$, $50th$, $75th$, and $95th$) of selected catchment characteristics of Orlacher Bach stratified by geological formation; fh=flood sediments, ku=Lower Keuper, mm=Middle Muschelkalk, mo=Upper Muschelkalk, mu=Lower Muschelkalk. Orange text shows medians ($50th$ percentile). Right panels are the average catchment characteristics of the Orlacher Bach (red dots) compared to those of 850 similar-sized catchments in the region. The y-axes of the right panels show the $1st$ and the $99th$ percentiles.

The topographic factors (i.e. slope, profile curvature and planform curvature) of the Orlacher Bach drainage line are always in the extreme ranges (>95%) in Braunsbach catchment along the riparian buffer zone (Figure 3.5), when compared with the other 850 catchments in the wider study area of Hohenlohekreis and Schwäbisch Hall, which is about 3300 km^2. I also observed that analysing the topography (e.g., slope and curvatures) of the entire catchment is misleading that dissembles the extremeness of topography along the Orlacher Bach catchment. Orlacher Bach catchment has a slope

near the median of the region, and below the $95th$ percentile in case of the NDVI, and planform and profile curvatures (Figure 5.5). Although the findings above suggest that the morphometric features of catchments are helpful for assessing debris-flow impacts (Stolle et al., 2015), those topographic factors are more important to assess around the drainage line rather than in the entire catchment.

Costanzo et al. (2012) tried to rank several landslide controlling factors (e.g., slope, lithology, and land use) for analysing landslide susceptibility and found that the geological factors (e.g., lithology) are unnecessary in modelling shallow landslides (e.g., earth and debris flows), but are moderately important for medium-size landslides (e.g., translational slides) in Rio Beiro basin ($\sim$10 km^2) Spain. The landslides seem to be randomly distributed along the channel of Orlacher Bach (Figure 3.7). The channel mainly cuts through the lithological units of Middle and Upper Muschelkalk, while Lower Keuper outcrops higher up and Lower Muschelkalk outcrops close to Braunsbach. The longitudinal profile shows that the landslide volume increases along the Upper Muschelkalk (Figure 3.10), although the topography (i.e. slope, profile and planform curvatures) is nearly homogeneous along Lower Keuper, Middle, Upper and Lower Muschelkalk (Figure 3.5). Other catchments also have Upper Muschelkalk bedrock, where debris flows were reported within Hohenlohekreis and Schwäbisch Hall; while there are catchments without any report of debris flows or landslide occurrence around Braunsbach despite intense rainfall.

Simon (1980) discovered that the Upper Muschelkalk is susceptible to hydro-chemical processes (chemical dissolution, karstification) along the intersection zone with the Lower Keuper. Karst features sinkholes that decrease the contact of the landslide with the shear surfaces (Parise et al., 2015), increasing the slope instability (Martinotti et al., 2017). Accordingly, horizontal Upper Muschelkalk layers were outcropped along the river banks and boulders of about 0.1 m^3 were deposited along the Orlacher Bach and in the Braunsbach village, carried by the flood waters, which could be supporting evidence of Karst-driven rockslides along the Upper Muschelkalk. Although I have not encountered any rockslide deposition along the Orlacher Bach, which are presumably either not occurred or carried by the flood waters; I suspected that the landslide concentration in the lithological unit Upper Muschelkalk could be explained by those long active hydro-chemical processes that could weaken the slopes along the Upper Muschelkalk decades long. In contrary such sinkholes might additionally store water decreasing the volume of flood wave, while increasing the hydrostatic force on the unstable slopes that could enhance slope failures during the Braunsbach rainstorm.

The chemical dissolution process depends primarily on the existence of the material prone to chemical dissolution, like Upper Muschelkalk. However, Braunsbach case is an example that the landslide controlling factors (e.g., lithology) could be activated by several local features in such a local scale, while topographic factors are constantly present. Thus the latter seem to have a stronger contribution to landslide distribution at the regional scale as it was shown in figure 3.5 (Roering et al., 2005).

Another important influence of flood-induced landslides is that they affect not only their close surroundings, but they also travel downstream along channels as debris flows (Hobley et al., 2012; Borga et al., 2014), thus enhancing the physical impact of floods (Salvati et al., 2010). For example, flood impact was magnified due to debris content during the 2017 Fukuoka floods (Figure 5.6, Hiroshi Fukuoka, pers. comm., 2018). Landslides contributed to about 15% of the accumulated material that is deposited in the Braunsbach village, which enhanced the total damage in the village (Laudan et al., 2017).

Many susceptibility maps are produced in grids such as the European Landslide Susceptibility Map (ELSUS 1000 v1 and v2), which depicts landslide susceptibility at $1-km$ resolution (Günther et al., 2014b). The Elsus-V1 model reflects the slope gradient extensively; the correlation (cross-correlation with zero-lag) between Elsus-V1 and slope gradient is about 0.82 in Germany (Figure 5.7), though slope certainly has a paramount influence on landslide susceptibility (Costanzo et al., 2012). In case of Southern Germany's cuesta landscape 90% of the area is relatively flat except for the channel network (Figure 3.2). An alternative approach would be focusing on these channels alone in landslide susceptibility studies to catch the flood triggered landslides instead of producing gridded maps. This approach in turn would miss out landslides detaching from upper hillslopes without any undercutting trigger. Lithology is another important control for landslide susceptibility, for instance, Wilde et al. (2018) improved the predictive capacity of the Elsus-V1 model by 10% with expanding the landslide inventory and increasing

FIGURE 5.6: A landslide in Oita Prefecture, Japan at 11:33 on July 7, 2017, foot of which reached to the stream network during the 2017 Fukuoka floods (mainichi.jp, accessed August 6, 2018). It is likely that part of the slumped material is carried further downstream by the high waters.

the quality of the lithology data. Including further topographic features (planform and profile curvatures) could additionally enhance the accuracy of such models.

RQ3: How does precursory earthquake shakings change the boundary conditions of a landscape and prepare for rainfall-triggered landsliding?

Finally I explore the rainfall triggered landslides that occurred up to about 1.5 month after the 2016 Kumamoto Earthquake (M_W 7.1) which changed the boundary conditions as a precursory earthquake shaking. I did so by investigating the failure mechanism of landslides under earthquake forcing, and the influence of the earthquake directivity effect on spatial landslide distribution.

Modelling slope performance under seismic loading is essential to estimating landslide susceptibility (Jibson, 2011). The dynamics of the earthquake rupture process are rather complex in terms of geometry of the seismic slip and rupture propagation (Dor et al., 2006; Fukuyama, 2009). Several studies investigated the relationship of seismic signals, e.g., magnitude, peak-ground acceleration (PGA), depth, and earthquake-triggered landslides, some also include topographic landslide control factors (Chigira and Yagi, 2006; Gorum et al., 2011). For example, PGA is the most common property to explain landslide distribution (Meunier et al., 2007; Shinoda and Miyata, 2017). Ghosh and Carranza (2010) suggested that the distance to the rupture is more deterministic in triggering landslides than the topographic factors (i.e. slope and aspect). Gorum and Carranza (2015) further found that the distance of the landslides from the ruptured fault is influenced also by the style of the faulting (i.e. thrust-slip, oblique-slips, and strike-slip), while Chigira et al. (2010) argued that the landslides concentration was higher on the hanging wall in the case of the Wenchuan earthquake (M_W 7.9, Figure 1.8). Accordingly, I found that most

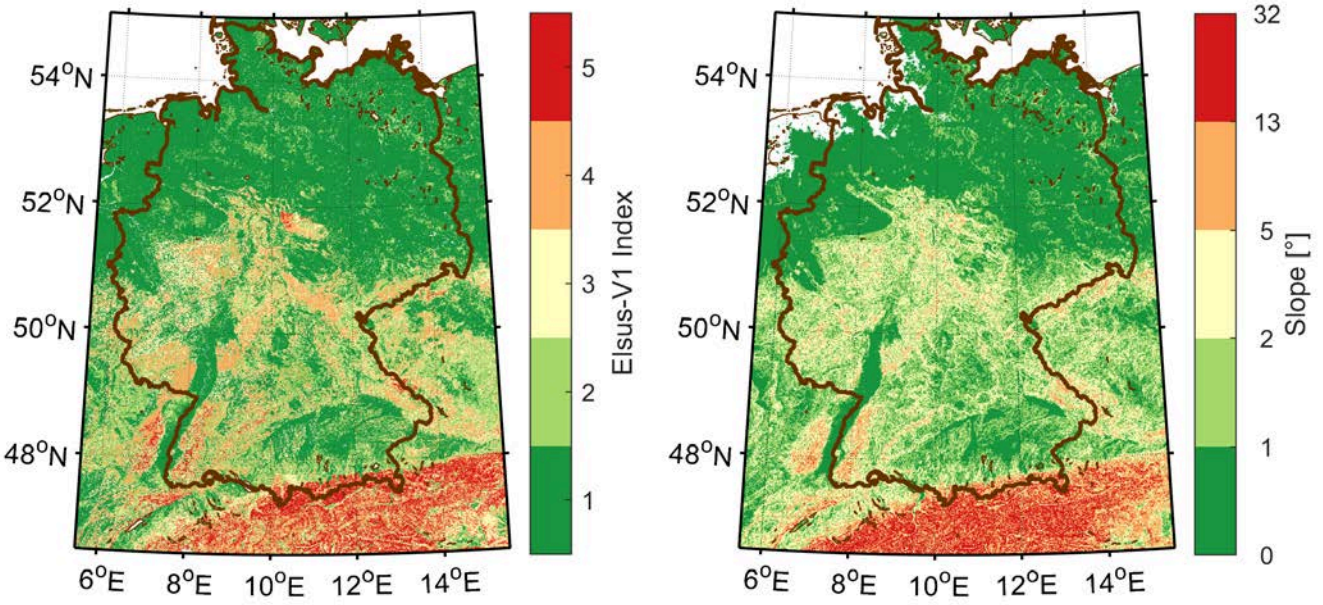

FIGURE 5.7: Elsus-V1 landslide susceptibility compared to logarithmic scale slope gradient in Germany (modified from Günther et al. (2014a). Slope is computed from ETOPO1 1 arc-minute global DEM by Amante (2009).

landslides followed the earthquake-normal direction in the strike-slip earthquake of Kumamoto (Figure 4.12), besides the high landslide concentration south of the rupture. Thus, inclusion of local site effects, the variation of fault-normal to fault parallel ratio (FN/FP) of the seismic signal, and rupture directivity are essential for comprehensive landslide susceptibility analysis (Meunier et al., 2013; Tanyaş et al., 2017).

The spatial extent of the landslides is limited up to 50 km from the rupture in case of the 2016 Kumamoto Earthquake (M_W 7.1) (Figure 4.5), while seismic signals attenuate due to damping of the geological units with distance from the source (Semblat et al., 2005). Meza-Fajardo et al. (2016) argued that the geometry of the topography also influenced the site amplification besides lithology. I estimate median amplification factor (MAF) following the method by Maufroy et al. (2015) based on the topographic curvature. A higher MAF and slope coincides with the crown area of the landslides in the Kumamoto (Figure 4.4). Thus I suspect that the movement of earthquake-triggered landslides starts from the crown area unlike rainfall- or flood- triggered landslides. This feature of a progressive failure is also observed by Dang et al. (2016), where they modelled the failure of the Takanodai and Aso-ohashi landslides after the 2016 Kumamoto earthquake (M_W 7.1), both of which started failing from the crown. Chen et al. (2017) accordingly developed a model to estimate landslide susceptibility before the 2016 Kumamoto earthquake (M_W 7.1) based on the geomorphological conditions and compared these results with the situation after the earthquake. Their model underestimated landslide susceptibility when the morphometric conditions of the moving masses were considered; the model captured all the landslides only when the morphometric of the scarps was used. They further claimed that the latter model led to ∼55% overestimation of landslide susceptibility; however I suspected that this overestimated locations might be biased by the directivity effect of the earthquake: They might have accurately captured landslides at one side of the rupture area, whereas the model assumed similar activity on the other side of the rupture area as well, since the topography is similar (Figure 4.4). The results could be improved considering the directivity effect.

Landslide response under earthquake loading is often instantaneous or mostly directly after the earthquake. Large earthquakes additionally change the boundary conditions of the terrain by e.g., introducing lateral tension cracks around the crown that may fail in the months or years following the transient impact of the earthquake (Saba et al., 2010). The displacement around the crown could further accumulate with subsequent events, such as new earthquakes (Gischig et al., 2016). Those weakened slopes could influence

the behaviour of the landscape decades long (Parker et al., 2015), both by increasing the debris flows and the occurance of shallow landslides. Landslides that lay on hillslopes damaged by past earthquakes could also be activated by rainfalls (Hovius et al., 2011). For instance, Tang et al. (2011) reported a 30% increase on the total landslide area by post-earthquake rainfall within four months after the Wenchuan earthquake (M_W 7.9). Considering all above findings, I suspect that the locations with higher MAF to accommodate damage on the slopes nearby, which could be reactivated or fail via another trigger. Thus the spatial distribution of the rainfall-induced landslides after the Kumamoto earthquake (M_W 7.1) may partly inherit the spatial patterns of the earthquake-induced landslides.

The number of landslides dropped down from about 1500 within a week to about 60 within six weeks in the case of Kumamoto. These 60 landslides were either triggered by aftershocks or heavy rains (most likely Baiu-derived) that began about ten days after the earthquake and dominated the weather for several weeks (Figure 5.8). This first group of 60 landslides face towards the earthquake normal direction, but the aspect of the second group was facing southwards. Aftershock-triggered landslides are poorly explored, since it is hard to distinguish the triggering mechanism: thus the aspect of the first group could be due to the main shock as well as to the subsequent rainfalls. The aspect of the second group faced slightly towards the extreme rainfall directions, which arrives from south-southwest (Figure 2.5). Hence the question arises, can the FN/FP ratio of earthquake signal be used to distinguish earthquake- from rainfall-triggered landslides?

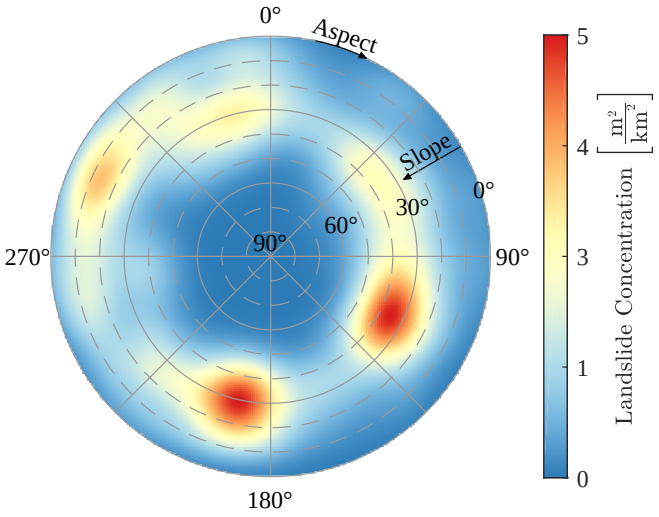

FIGURE 5.8: Aspect and slope distribution of the DEM grids that are within landslide polygons based on the observation of 1.5 half months after the 2016 Kumamoto Earthquake (M_W 7.1) on 30 May, 2016. The distribution is normalized by the topography (Figure 4.12).

Chapter 6

SYNTHESIS AND PERSPECTIVES

The damage due to natural hazards has been increasing, since the human settlements keep expanding. Thus it is fundamental to study the interaction of human environment with the natural hazards to mitigate the monetary losses and preserve human health. The recognition of the hazard is the primary key to an effective risk mitigation. Then we can spend efforts to locate the potentially exposed regions to the natural hazards. Accordingly in this section I synthesis my results and suggest ways to improve the predictive capacities of landslide susceptibility and hazard studies. First I summarize the directivity effect of earthquakes as part of the earthquakes interaction with the landscape. Then I explain about the rainfall triggered landslides and their spatial behaviour under rainfall loading.

Earthquakes occur along faults due to sudden stress release resulting in dynamic and static displacements along the faults. The direction of displacement determines the style of faulting (SOF) and is approximately oriented in the direction of the maximum resolved shear stress (Wallace, 1951; Bott, 1959). The three end members of faulting according to Anderson (1905, 1951) are normal, reverse and strike-slip. Combinations of the three end members are possible, as can be exemplified by the 2016 Kumamoto earthquake (M_W 7.1), which is a right-lateral strike-slip event with a slight normal component. The earthquake happened along the Futagawa–Hinagu right-lateral strike-slip fault system which itself is located in the extensional stress regime of central Kyushu. Topographic amplification MAF of the earthquake shaking increases within the landslide polygons towards the crown, so as the slope, indicating that the landslide movement might have started form the crown. Variation of MAF and slope do not follow any spatial pattern in the study site; high slopes and MAF are homogenously distributed around the rupture. Those topographic parameters (i.e. slope and curvature) help explaining the failure mechanism of individual landslides that occurred during the 2016 Kumamoto Earthquake (M_W 7.1). Although lithology is not homogeneous, the lithological formations are not diverse within the vicinity of the 2016 Kumamoto Earthquake (M_W 7.1) rupture, mostly tephra layers of different age. We conclude that the seismic loading (i.e. energy, directivity) is the primary factor determining the spatial landslide distribution in case of the 2016 Kumamoto Earthquake (M_W 7.1). Hence earthquake triggered landslide susceptibility maps could be improved by including the earthquake directivity in similar strike-slip faults.

Seismic loading changes the force balance of the slopes instantly, while the rainfall loading is through the secondary causes i.e. flood waters, surface flow, changes in the perched water level. The main influence of the rainstorms on landsliding seem to be through the concomitant floods by eroding the banks of the river channel removing the lateral support of the unstable slopes (toes of the landslides) in case of the Braunsbach. Hence the landslide controlling factors (i.e. lithology, slope, curvature) gain importance in explaining the spatial landslide distribution. Accordingly topographic controlling factors (i.e. slope, curvature) were in the extreme ranges in Braunsbach along the natural drainage line, where the landslides were mainly observed in the study area of Hohenlohekreis and Schwäbisch Hall. However physical landslide susceptibility methods assess the susceptibility in gridded domains mostly due to the underlying data that is provided in gridded domain, such as digital elevation models. The catchment wise susceptibility is then derived as the average of these grids. This assumption might bias the final estimation especially in cuesta like landscapes, where only about 10% of the area is dominated by high slope gradients. Accordingly Braunsbach ranks only above average within the 850 catchments in the study area, when the topographic controls are averaged in catchments, which are more extreme along the drainage line. Thus, investigating the landslide controlling factors along the catchment drainage line could increase the predictive capacity of the rainfall triggered landslide susceptibility and hazard studies.

Another feature of those rainfall triggered landslides is their elongated accumulation zone, which sometimes includes also a zone of transportation, in case the accumulation zone is fully separated from the detachment zone. Margins of this transportation zone could extent along drainage lines due to the velocity of the flood waters. The fresh landslide material is likely deposited on flood plains, where the flow velocity drops, such as Braunsbach. Hence a low landslide risk zone might be exposed to landslide related damage when lying along a drainage line. Not only landslide susceptibility studies but also flood damage studies should consider the potential accumulation zone, since debris content could multiply the monetary flood damage.

I also investigated the regional extreme rainfall trajectories along Japan. I showed that the extreme rainfall trajectories align roughly with the Japanese island arc. I was expecting to observe meaningful spatial patterns that connect extreme rainfall trajectories to past observed landslides. In contrast the spatial landslide distribution seems to be mainly connected to the mean annual rainfall rates in Japan as Saito et al. (2014) claims. Future work should focus rather on a single storm that has a directional behaviour in order to try deriving correlation of landsliding and extreme precipitation trajectories.

Another important point to study is the influence of the recent past landslide triggering incidents that they might have prepared the landscape for future landsliding by changing the boundary conditions. 2016 Kumamoto earthquake (M_W 7.1) left a clear footprint on the topography by inducing landslides that are oriented towards the earthquake normal direction. We suspect the slopes, which are aligned towards earthquake normal direction, to suffer from damages, which can increase landslide susceptibility due to other triggers (e.g. rainfall, earthquake) in the coming years.

Landslides are essential on evolving landscapes as discussed all along this thesis. They are additionally responsible for thousands of casualties worldwide every year according to USGS (www.usgs.gov, accessed July 26 2018). This number might be underestimated, when catastrophic single events are considered. For example debris flows in Peru in 1962 killed $2,000 - 4,000$ in a single swift (news.bbc.co.uk, accessed July 26 2018). Hence the annual global death toll is very high, considering the exponentially increasing scientific efforts that is invested on landslide research (Figure 6.1). As demonstrated in this thesis, researchers as myself should focus more on learning from past disasters that could contribute to the existent knowledge about the interaction of landslides with the other earth surface processes. Such efforts eventually help improving predictive landslide models and help decreasing the high number of lost lives.

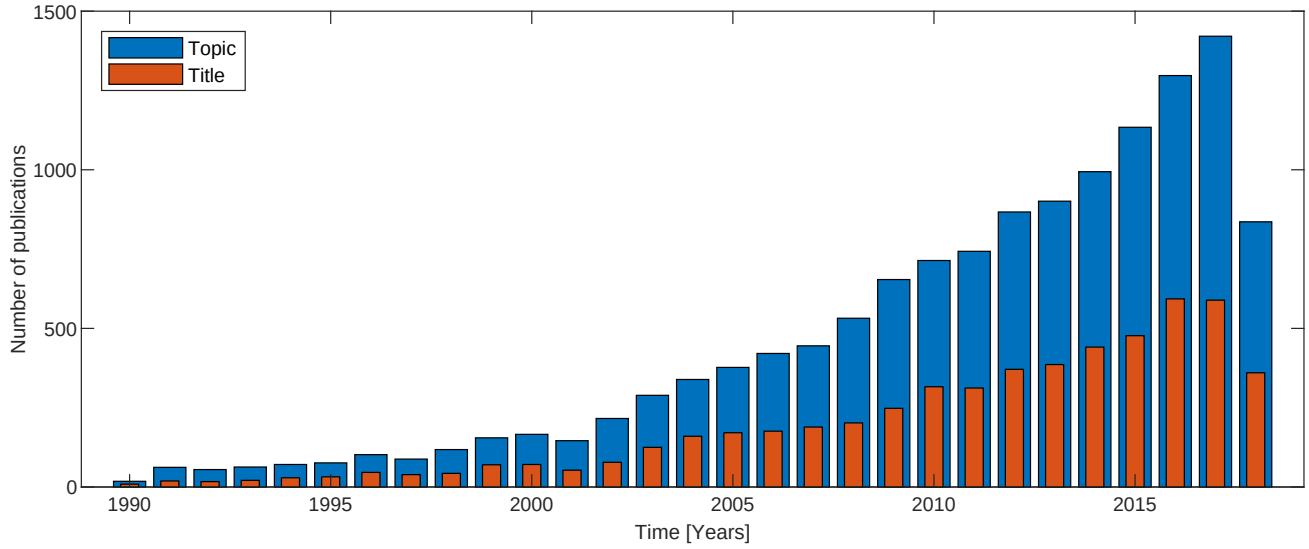

FIGURE 6.1: Number of published articles topic/title of which include the keyword "landslide" in blue/orange (www.webofknowledge.com, accessed June 28, 2018).

"*Japan issues weather warnings early, but its dense population means that almost every bit of usable land, including some flood plains, is built on in the mostly mountainous country, leaving it prone to disasters.*"

Takashi Tsuchida

Chapter 7

ADDITIONAL PUBLICATIONS

I also contributed to the following publications during the course of the doctoral research, besides the manuscripts that are listed in section 1.5,

as first author:

Ozturk U., Marwan N., Specht S., Korup O., Jensen J.: Contemporary centennial sea-level record at Antalya (eastern Mediterranean), Journal of Geophysical Research-Oceans, doi: 10.1029/2018JC013906, 2018.

Ozturk U., Malik N., Cheung K., Marwan N., Kurths J.: A network-based comparative study of extreme tropical and frontal storm rainfall over Japan, Climate Dynamics, doi: 10.1007/s00382-018-4597-1, 2019.

as co-author:

Agarwal A., Marwan N., Rathinasamy M., Ozturk U., Merz B., Kurths J.: Optimal Design of Hydrometric Station Networks Based on Complex Network Analysis, HESSD, doi: 10.5194/hess-2018-113, 2018.

Bronstert A., Agarwal, A., Boessenkool B., Crisologo I., Fischer M., Heistermann M., Köhn-Reich L., Moran T., Ozturk U., Reinhardt-Imjela C., Wendi D.: Forensic hydro-meteorological analysis of an extreme flash flood: The 29/05/2016 event in Braunsbach, SW Germany, Science of the Total Environment, doi: 10.1016/j.scitotenv.2018.02.241, 2018.

Vogel K., Ozturk U., Riemer A., Laudan J., Sieg T., Wendi D., Agarwal A., Rözer V., Korup O., Thieken A. H.: Die Sturzflut von Braunsbach am 29. Mai 2016 - Entstehung, Ablauf und Schäden eines „Jahrhundertereignisses“. Teil 2: Geomorphologische Prozesse und Schadensanalyse, HyWa, doi:10.5675/HyWa_2017,3_2, 2017.

Agarwal, A., Boessenkool, B., Fischer, M., Hahn, I., Köhn, L., Laudan, J., Moran, T., Öztürk, U., Riemer, A., Rözer, V., Sieg, T., Vogel, K., Wendi, D., Bronstert, A., Thieken, A.H.: Die Sturz ut in Braunsbach, Mai 2016 Eine Bestandsaufnahme und Ereignisbeschreibung (No. urn:nbn:de:kobv:517 -opus4 -394881). University of Potsdam, Potsdam, Germany, 2016.

Bibliography

Abe, S. and Suzuki, N. (2007). Dynamical evolution of clustering in complex network of earthquakes. *The European Physical Journal B*, 59(1):93–97.

Agarwal, A., Boessenkool, B., Fischer, M., Hahn, I., Köhn, L., Laudan, J., Moran, T., Öztürk, U., Riemer, A., Rözer, V., Sieg, T., Vogel, K., Wendi, D., Bronstert, A., and Thieken, A. H. (2016). Die Sturz ut in Braunsbach, Mai 2016 Eine Bestandsaufnahme und Ereignisbeschreibung. Technical Report urn:nbn:de:kobv:517 -opus4 -394881, University of Potsdam, Potsdam, Germany.

Agarwal, A., Marwan, N., Rathinasamy, M., Merz, B., and Kurths, J. (2017). Multi-scale event synchronization analysis for unravelling climate processes: a wavelet-based approach. *Nonlinear Processes in Geophysics*, 24(4):599–611.

Aki, K. and Richards, P. G. (2002). *Quantitative seismology*. University Science Books.

Aleotti, P. (2004). A warning system for rainfall-induced shallow failures. *Engineering Geology*, 73(3-4):247–265.

Allstadt, K. (2013). Extracting source characteristics and dynamics of the August 2010 Mount Meager landslide from broadband seismograms. *Journal of Geophysical Research: Earth Surface*, 118(3):1472–1490.

Allstadt, K. E., Jibson, R. W., Thompson, E. M., Massey, C. I., Wald, D. J., Godt, J. W., and Rengers, F. K. (2018). Improving Near-Real-Time Coseismic Landslide Models: Lessons Learned from the 2016 Kaikoura, New Zealand, Earthquake. *Bulletin of the Seismological Society of America*, 108(3B):1649–1664.

Amante, C. (2009). ETOPO1 1 Arc-Minute Global Relief Model: Procedures, Data Sources and Analysis.

Anderson, E. M. (1905). The dynamics of faulting. *Transactions of the Edinburgh Geological Society*, 8(3):387–402.

Anderson, E. M. (1951). *The dynamics of faulting and dyke formation with applications to Britain*. Hafner Pub. Co.

Anderson, J. G. and Richards, P. G. (1975). Comparison of Strong Ground Motion from Several Dislocation Models*. *Geophysical Journal of the Royal Astronomical Society*, 42(2):347–373.

Anderson, M. (2014). Ebola: airlines cancel more flights to affected countries. *The Guardian*, 22.

Archer, D. R., Leesch, F., and Harwood, K. (2007). Learning from the extreme River Tyne flood in January 2005. *Water and Environment Journal*, 21(2):133–141.

Arias, A. (1970). Measure of earthquake intensity. Technical report, Massachusetts Inst. of Tech., Cambridge. Univ. of Chile, Santiago de Chile.

Arnone, E., Caracciolo, D., Noto, L. V., Preti, F., and Bras, R. L. (2016). Modeling the hydrological and mechanical effect of roots on shallow landslides. *Water Resources Research*, 52(11):8590–8612.

Asano, K. and Iwata, T. (2016). Source rupture processes of the foreshock and mainshock in the 2016 Kumamoto earthquake sequence estimated from the kinematic waveform inversion of strong motion data. *Earth, Planets and Space*, 68(1):147.

Ayalew, L., Yamagishi, H., and Ugawa, N. (2004). Landslide susceptibility mapping using GIS-based weighted linear combination, the case in Tsugawa area of Agano River, Niigata Prefecture, Japan. *Landslides*, 1(1):73–81.

Baker, J. W. (2007). Quantitative Classification of Near-Fault Ground Motions Using Wavelet Analysis. *Bulletin of the Seismological Society of America*, 97(5):1486–1501.

Baum, R. L. and Godt, J. W. (2010). Early warning of rainfall-induced shallow landslides and debris flows in the USA. *Landslides*, 7(3):259–272.

Belachsen, I., Marra, F., Peleg, N., and Morin, E. (2017). Convective rainfall in a dry climate: relations with synoptic systems and flash-flood generation in the Dead Sea region. *Hydrology and Earth System Sciences*, 21(10):5165–5180.

Beniston, M., Keller, F., and Goyette, S. (2003). Snow pack in the Swiss Alps under changing climatic conditions: an empirical approach for climate impacts studies. *Theoretical and Applied Climatology*, 74(1-2):19–31.

Bernard, P. and Madariaga, R. (1984). a New Asymptotic Method for the Modeling of Near-Field Accelerograms. *Bulletin of the Seismological Society of America*, 74(2):539–557.

Berne, A. and Krajewski, W. (2013). Radar for hydrology: Unfulfilled promise or unrecognized potential? *Advances in Water Resources*, 51:357–366.

Bezak, N., Brilly, M., and Šraj, M. (2014). Comparison between the peaks-over-threshold method and the annual maximum method for flood frequency analysis. *Hydrological Sciences Journal*, 59(5):959–977.

Boers, N., Bookhagen, B., Barbosa, H. M. J., Marwan, N., Kurths, J., and Marengo, J. A. (2014a). Prediction of extreme floods in the eastern Central Andes based on a complex networks approach. *Nature Communications*, 5:5199.

Boers, N., Rheinwalt, A., Bookhagen, B., Barbosa, H. M. J., Marwan, N., Marengo, J., and Kurths, J. (2014b). The South American rainfall dipole: A complex network analysis of extreme events. *Geophysical Research Letters*, 41(20):7397–7405.

Bogaard, T. and Greco, R. (2018). Invited perspectives: Hydrological perspectives on precipitation intensity-duration thresholds for landslide initiation: proposing hydro-meteorological thresholds. *Natural Hazards and Earth System Sciences*, 18(1):31–39.

Bogaard, T. A. and Greco, R. (2016). Landslide hydrology: from hydrology to pore pressure: Landslide hydrology. *Wiley Interdisciplinary Reviews: Water*, 3(3):439–459.

Böhner, J. and Selige, T. (2006). Spatial prediction of soil attributes using terrain analysis and climate regionalisation. *SAGA - Analysis and Modelling Applications*, 115:13–27.

Bolvin, D. T. and Huffman, G. J. (2015). Transition of 3b42/3b43 Research Product from Monthly to Climatological Calibration/Adjustment. Technical report, NASA, USA.

Boore, D. M. and Bommer, J. J. (2005). Processing of strong-motion accelerograms: Needs, options and consequences. *Soil Dynamics and Earthquake Engineering*, 25(2):93–115.

Bora, S. S., Scherbaum, F., Kuehn, N., Stafford, P., and Edwards, B. (2015). Development of a Response Spectral Ground-Motion Prediction Equation (GMPE) for Seismic-Hazard Analysis from Empirical Fourier Spectral and Duration Models. *Bulletin of the Seismological Society of America*, 105(4):2192–2218.

Bordoni, M., Meisina, C., Valentino, R., Bittelli, M., and Chersich, S. (2015). Site-specific to local-scale shallow landslides triggering zones assessment using TRIGRS. *Natural Hazards and Earth System Science*, 15(5):1025–1050.

Borga, M., Boscolo, P., Zanon, F., and Sangati, M. (2007). Hydrometeorological Analysis of the 29 August 2003 Flash Flood in the Eastern Italian Alps. *Journal of Hydrometeorology*, 8(5):1049–1067.

Borga, M., Stoffel, M., Marchi, L., Marra, F., and Jakob, M. (2014). Hydrogeomorphic response to extreme rainfall in headwater systems: Flash floods and debris flows. *Journal of Hydrology*, 518:194–205.

Bott, M. H. P. (1959). The mechanics of oblique slip faulting. *Geological Magazine*, 96(2):109–117.

Bradford, R. A., O'Sullivan, J. J., van der Craats, I. M., Krywkow, J., Rotko, P., Aaltonen, J., Bonaiuto, M., De Dominicis, S., Waylen, K., and Schelfaut, K. (2012). Risk perception – issues for flood management in Europe. *Natural Hazards and Earth System Science*, 12(7):2299–2309.

Bray, J. D. and Rodriguez-Marek, A. (2004). Characterization of forward-directivity ground motions in the near-fault region. *Soil Dynamics and Earthquake Engineering*, 24(11):815–828.

Bray, J. D. and Travasarou, T. (2007). Simplified Procedure for Estimating Earthquake-Induced Deviatoric Slope Displacements. *Journal of Geotechnical and Geoenvironmental Engineering*, 133(4):381–392.

Bronstert, A., Agarwal, A., Boessenkool, B., Crisologo, I., Fischer, M., Heistermann, M., Köhn-Reich, L., López-Tarazón, J. A., Moran, T., Ozturk, U., Reinhardt-Imjela, C., and Wendi, D. (2018). Forensic

hydro-meteorological analysis of an extreme flash flood: The 2016-05-29 event in Braunsbach, SW Germany. *Science of The Total Environment*, 630:977–991.

Bronstert, A., Agarwal, A., Boessenkool, B., Fischer, M., Heistermann, M., Köhn-Recih, L., Moran, T., and Wendi, D. (2017a). Die Sturzflut von Braunsbach am 29. Mai 2016 - Entstehung, Ablauf und Schäden eines „Jahrhundertereignisses". Teil 1: Meteorologische und hydrologische Analyse. *HyWa*, 61(3):150–162.

Bronstert, A., Bormann, H., Bürger, G., Haberlandt, U., Hattermann, F., Heistermann, M., Huang, S., Kolokotronis, V., Kundzewicz, Z. W., Menzel, L., Meon, G., Merz, B., Meuser, A., Paton, E. N., and Petrow, T. (2017b). *Hochwasser und Sturzfluten an Fluessen in Deutschland*, pages 87–101. Springer Berlin Heidelberg, Berlin, Heidelberg.

Brosinsky, A., Foerster, S., Segl, K., López-Tarazón, J. A., Piqué, G., and Bronstert, A. (2014). Spectral fingerprinting: characterizing suspended sediment sources by the use of vnir-swir spectral information. *Journal of Soils and Sediments*, 14(12):1965–1981.

Brune, J. N. (1970). Tectonic stress and the spectra of seismic shear waves from earthquakes. *Journal of Geophysical Research*, 75(26):4997–5009.

Caine, N. (1980). The Rainfall Intensity: Duration Control of Shallow Landslides and Debris Flows. *Geografiska Annaler. Series A, Physical Geography*, 62(1/2):23.

Campillo, M. and Plantet, J. (1991). Frequency dependence and spatial distribution of seismic attenuation in France: experimental results and possible interpretations. *Physics of the Earth and Planetary Interiors*, 67(1-2):48–64.

Castellano, C. M. and DeGaetano, A. T. (2016). A multi-step approach for downscaling daily precipitation extremes from historical analogues: downscaling precipitation extremes from historical analogues. *International Journal of Climatology*, 36(4):1797–1807.

Chang, K.-T., Chiang, S.-H., Chen, Y.-C., and Mondini, A. C. (2014). Modeling the spatial occurrence of shallow landslides triggered by typhoons. *Geomorphology*, 208:137–148.

Chen, C.-W., Chen, H., Wei, L.-W., Lin, G.-W., Iida, T., and Yamada, R. (2017). Evaluating the susceptibility of landslide landforms in Japan using slope stability analysis: a case study of the 2016 Kumamoto earthquake. *Landslides*, 14(5):1793–1801.

Cheung, K. K. W., Chang, L. T.-C., and Li, Y. (2014). Rainfall Prediction for Landfalling Tropical Cyclones: Perspectives of Mitigation. In Tang, D. L. and Sui, G., editors, *Typhoon Impact and Crisis Management*, volume 40, pages 175–201. Springer Berlin Heidelberg, Berlin, Heidelberg.

Chigira, M., Tsou, C.-Y., Matsushi, Y., Hiraishi, N., and Matsuzawa, M. (2013). Topographic precursors and geological structures of deep-seated catastrophic landslides caused by Typhoon Talas. *Geomorphology*, 201:479–493.

Chigira, M., Wu, X., Inokuchi, T., and Wang, G. (2010). Landslides induced by the 2008 Wenchuan earthquake, Sichuan, China. *Geomorphology*, 118(3-4):225–238.

Chigira, M. and Yagi, H. (2006). Geological and geomorphological characteristics of landslides triggered by the 2004 Mid Niigta prefecture earthquake in Japan. *Engineering Geology*, 82(4):202–221.

Chitu, Z., Bogaard, T., Busuioc, A., Burcea, S., Sandric, I., and Adler, M.-J. (2017). Identifying hydrological pre-conditions and rainfall triggers of slope failures at catchment scale for 2014 storm events in the Ialomita Subcarpathians, Romania. *Landslides*, 14(1):419–434.

Choy, G. L. and Cormier, V. F. (1986). Direct measurement of the mantle attenuation operator from broadband P and S Waveforms. *Journal of Geophysical Research: Solid Earth*, 91(B7):7326–7342.

Chung, M.-C., Tan, C.-H., and Chen, C.-H. (2017). Local rainfall thresholds for forecasting landslide occurrence: Taipingshan landslide triggered by Typhoon Saola. *Landslides*, 14(1):19–33.

Corbosiero, K. L. and Molinari, J. (2002). The Effects of Vertical Wind Shear on the Distribution of Convection in Tropical Cyclones. *Monthly Weather Review*, 130(8):2110–2123.

Costanzo, D., Rotigliano, E., Irigaray, C., Jiménez-Perálvarez, J. D., and Chacón, J. (2012). Factors selection in landslide susceptibility modelling on large scale following the gis matrix method: application to the river Beiro basin (Spain). *Natural Hazards and Earth System Science*, 12(2):327–340.

Creutin, J.-D. and Borga, M. (2003). Radar hydrology modifies the monitoring of flash-flood hazard. *Hydrological Processes*, 17(7):1453–1456.

Creutin, J. D., Borga, M., Lutoff, C., Scolobig, A., Ruin, I., and Créton-Cazanave, L. (2009). Catchment dynamics and social response during flash floods: the potential of radar rainfall monitoring for warning procedures. *Meteorological Applications*, 16(1):115–125.

Crisologo, I., Warren, R., Mühlbauer, K., and Heistermann, M. (2018). Enhancing the consistency of spaceborne and ground-based radar comparisons by using quality filters. *Atmospheric Measurement Techniques Discussions*, 2018:1–20.

Crozier, M. J. (1999). Prediction of rainfall-triggered landslides: a test of the Antecedent Water Status Model. *Earth Surface Processes and Landforms*, 24(9):825–833.

Crozier, M. J. and Glade, T. (2012). Landslide Hazard and Risk: Issues, Concepts and Approach. In Glade, T., Anderson, M., and Crozier, M. J., editors, *Landslide Hazard and Risk*, pages 1–40. John Wiley & Sons, Ltd, Chichester, West Sussex, England.

Cruden, M. D. and Varnes, J. D. (1996). Landslide Types and Processes. In *Landslides: Investigation and Mitigation*, number 247 in Special Report(National Research Council (U.S.) Transportation Research Board), pages 36–75. National Academy Press, Washington, D.C.

Dadson, S. J., Hovius, N., Chen, H., Dade, W. B., Lin, J.-C., Hsu, M.-L., Lin, C.-W., Horng, M.-J., Chen, T.-C., Milliman, J., and Stark, C. P. (2004). Earthquake-triggered increase in sediment delivery from an active mountain belt. *Geology*, 32(8):733.

Dai, F. and Lee, C. (2001). Frequency–volume relation and prediction of rainfall-induced landslides. *Engineering Geology*, 59(3-4):253–266.

Dai, F., Lee, C., Deng, J., and Tham, L. (2005). The 1786 earthquake-triggered landslide dam and subsequent dam-break flood on the Dadu River, southwestern China. *Geomorphology*, 65(3-4):205–221.

Dang, K., Sassa, K., Fukuoka, H., Sakai, N., Sato, Y., Takara, K., Quang, L. H., Loi, D. H., Van Tien, P., and Ha, N. D. (2016). Mechanism of two rapid and long-runout landslides in the 16 april 2016 kumamoto earthquake using a ring-shear apparatus and computer simulation (ls-rapid). *Landslides*, 13(6):1525–1534.

Destro, E., Amponsah, W., Nikolopoulos, E. I., Marchi, L., Marra, F., Zoccatelli, D., and Borga, M. (2018). Coupled prediction of flash flood response and debris flow occurrence: Application on an alpine extreme flood event. *Journal of Hydrology*, 558:225–237.

Devoli, G., Strauch, W., Chávez, G., and Høeg, K. (2007). A landslide database for Nicaragua: a tool for landslide-hazard management. *Landslides*, 4(2):163–176.

Dijkstra, E. W. (1959). A note on two problems in connexion with graphs. *Numerische Mathematik*, 1(1):269–271.

Djokic, D., Ye, Z., and Dartiguenave, C. (2011). Arc hydro tools overview. *Redland, Canada, ESRI*, pages 1–189.

DOMEJ, G., BOURDEAU LOMBARDI, C., Lenti, L., MARTINO, S., and Pluta, K. (2017). Mean Landslide geometries inferred from a global database of earthquake - and non earthquake - triggered landslides. *Italian Journal of Engineering Geology and Environment*, 2(17):pp. 87–107.

Donges, J. F., Schultz, H. C. H., Marwan, N., Zou, Y., and Kurths, J. (2011). Investigating the topology of interacting networks: Theory and application to coupled climate subnetworks. *The European Physical Journal B*, 84(4):635–651.

Donges, J. F., Zou, Y., Marwan, N., and Kurths, J. (2009). The backbone of the climate network. *EPL (Europhysics Letters)*, 87(4):48007.

Donner, R. V. and Barbosa, S. M., editors (2008). *Nonlinear time series analysis in the geosciences: applications in climatology, geodynamics and solar-terrestrial physics*. Number 112 in Lecture notes in earth sciences. Springer, Berlin.

Dor, O., Ben-Zion, Y., Rockwell, T. K., and Brune, J. (2006). Pulverized rocks in the Mojave section of the San Andreas Fault Zone. *Earth and Planetary Science Letters*, 245(3-4):642–654.

Dou, J., Oguchi, T., S. Hayakawa, Y., Uchiyama, S., Saito, H., and Paudel, U. (2014). GIS-Based Landslide Susceptibility Mapping Using a Certainty Factor Model and Its Validation in the Chuetsu Area, Central Japan. In Sassa, K., Canuti, P., and Yin, Y., editors, *Landslide Science for a Safer Geoenvironment*, pages 419–424. Springer International Publishing, Cham.

Dou, J., Yamagishi, H., Pourghasemi, H. R., Yunus, A. P., Song, X., Xu, Y., and Zhu, Z. (2015). An integrated artificial neural network model for the landslide susceptibility assessment of Osado Island, Japan. *Natural Hazards*, 78(3):1749–1776.

Duan, W., He, B., Takara, K., Luo, P., Nover, D., Yamashiki, Y., and Huang, W. (2014). Anomalous atmospheric events leading to Kyushu's flash floods, July 11–14, 2012. *Natural Hazards*, 73(3):1255–1267.

Dunnavan, G. M. and Diercks, J. W. (1980). An Analysis of Super Typhoon Tip (October 1979). *Monthly Weather Review*, 108(11):1915–1923.

Dziewonski, A. M., Chou, T.-A., and Woodhouse, J. H. (1981). Determination of earthquake source parameters from waveform data for studies of global and regional seismicity. *Journal of Geophysical Research: Solid Earth*, 86(B4):2825–2852.

Eichenberger, J., Ferrari, A., and Laloui, L. (2013). Early warning thresholds for partially saturated slopes in volcanic ashes. *Computers and Geotechnics*, 49:79–89.

Ekström, G., Nettles, M., and Dziewoński, A. (2012). The global CMT project 2004–2010: Centroid-moment tensors for 13,017 earthquakes. *Physics of the Earth and Planetary Interiors*, 200-201:1–9.

Estrany, J., López-Tarazón, J. A., and Smith, H. G. (2016). Wildfire effects on suspended sediment delivery quantified using fallout radionuclide tracers in a mediterranean catchment. *Land Degradation & Development*, 27(5):1501–1512.

Fan, X., Scaringi, G., Xu, Q., Zhan, W., Dai, L., Li, Y., Pei, X., Yang, Q., and Huang, R. (2018). Coseismic landslides triggered by the 8th August 2017 Ms 7.0 Jiuzhaigou earthquake (Sichuan, China): factors controlling their spatial distribution and implications for the seismogenic blind fault identification. *Landslides*.

Feldmann, H., Schädler, G., Panitz, H.-J., and Kottmeier, C. (2013). Near future changes of extreme precipitation over complex terrain in Central Europe derived from high resolution RCM ensemble simulations: near future changes of heavy Precipitation. *International Journal of Climatology*, 33(8):1964–1977.

Festa, G., Zollo, A., and Lancieri, M. (2008). Earthquake magnitude estimation from early radiated energy. *Geophysical Research Letters*, 35(22):L22307.

Ficchì, A., Perrin, C., and Andréassian, V. (2016). Impact of temporal resolution of inputs on hydrological model performance: An analysis based on 2400 flood events. *Journal of Hydrology*, 538:454–470.

Fielding, E. J. (1996). Tibet uplift and erosion. *Tectonophysics*, 260(1-3):55–84.

Finlay, P. J., Fell, R., and Maguire, P. K. (1997). The relationship between the probability of landslide occurrence and rainfall. *Canadian Geotechnical Journal*, 34(6):811–824.

Fischer, L., Kääb, A., Huggel, C., and Noetzli, J. (2006). Geology, glacier retreat and permafrost degradation as controlling factors of slope instabilities in a high-mountain rock wall: the Monte Rosa east face. *Natural Hazards and Earth System Science*, 6(5):761–772.

Fischer, M., Rust, H., and Ulbrich, U. (2017). A spatial and seasonal climatology of extreme precipitation return-levels: A case study. *Spatial Statistics*.

Fischer, M., Rust, H. W., and Ulbrich, U. (2018). Seasonal Cycle in German Daily Precipitation Extremes. *Meteorologische Zeitschrift*, 27(1):3–13.

Fleming, R. W. and Johnson, A. M. (1989). Structures associated with strike-slip faults that bound landslide elements. *Engineering Geology*, 27(1-4):39–114.

Francke, T., Werb, S., Sommerer, E., and López-Tarazón, J. A. (2014). Analysis of runoff, sediment dynamics and sediment yield of subcatchments in the highly erodible Isábena catchment, Central Pyrenees. *Journal of Soils and Sediments*, 14(12):1909–1920.

Frankel, A. (2004). Rupture Process of the M 7.9 Denali Fault, Alaska, Earthquake: Subevents, Directivity, and Scaling of High-Frequency Ground Motions. *Bulletin of the Seismological Society of America*, 94(6B):S234–S255.

Fukui, E. (1970). Distribution of Extraordinarily Heavy Rainfalls in Japan. *Geographical Review of Japan*, 43(10):581–593.

Fukuoka, H., Bhoopendra, D., Sakai, N., Sassa, K., and Dang, K. (2017). Landslides triggered by April 2016 Kumamoto Earthquake, Japan. In *Geophysical Research Abstracts*, Vienna, Austria. EGU.

Fukuyama, E. (2009). Chapter 1 Introduction. In *International Geophysics*, volume 94, pages 1–13. Elsevier.

Galli, M., Ardizzone, F., Cardinali, M., Guzzetti, F., and Reichenbach, P. (2008). Comparing landslide inventory maps. *Geomorphology*, 94(3-4):268–289.

Gao, S., Meng, Z., Zhang, F., and Bosart, L. F. (2009). Observational Analysis of Heavy Rainfall Mechanisms Associated with Severe Tropical Storm Bilis (2006) after Its Landfall. *Monthly Weather Review*, 137(6):1881–1897.

Gaprindashvili, G. and van Westen, C. J. (2016). Generation of a national landslide hazard and risk map for the country of Georgia. *Natural Hazards*, 80(1):69–101.

García-Ruiz, J. M., Beguería, S., Nadal-Romero, E., González-Hidalgo, J. C., Lana-Renault, N., and Sanjuán, Y. (2015). A meta-analysis of soil erosion rates across the world. *Geomorphology*, 239:160–173.

Gariano, S. L. and Guzzetti, F. (2016). Landslides in a changing climate. *Earth-Science Reviews*, 162:227–252.

Gerabronn, G. (2016). Bericht aus der Gemeinderatssitzung vom 14. Juni 2016. Technical Report 15, Stadt Gerabronn, Gemeinderat.

Ghosh, S. and Carranza, E. J. M. (2010). Spatial analysis of mutual fault/fracture and slope controls on rocksliding in Darjeeling Himalaya, India. *Geomorphology*, 122(1-2):1–24.

Gischig, V., Preisig, G., and Eberhardt, E. (2016). Numerical Investigation of Seismically Induced Rock Mass Fatigue as a Mechanism Contributing to the Progressive Failure of Deep-Seated Landslides. *Rock Mechanics and Rock Engineering*, 49(6):2457–2478.

Godt, J. W., Baum, R. L., and Chleborad, A. F. (2006). Rainfall characteristics for shallow landsliding in Seattle, Washington, USA. *Earth Surface Processes and Landforms*, 31(1):97–110.

Goetz, U. (2016). Die uhr ist stehen geblieben. *Länderreport*.

Gorczyca, E., Krzemień, K., Wrońska-Wałach, D., and Boniecki, M. (2014). Significance of extreme hydro-geomorphological events in the transformation of mountain valleys (Northern Slopes of the Western Tatra Range, Carpathian Mountains, Poland). *CATENA*, 121:127–141.

Gorum, T. and Carranza, E. J. M. (2015). Control of style-of-faulting on spatial pattern of earthquake-triggered landslides. *International Journal of Environmental Science and Technology*, 12(10):3189–3212.

Gorum, T., Fan, X., van Westen, C. J., Huang, R. Q., Xu, Q., Tang, C., and Wang, G. (2011). Distribution pattern of earthquake-induced landslides triggered by the 12 May 2008 Wenchuan earthquake. *Geomorphology*, 133(3-4):152–167.

Gorum, T., Korup, O., van Westen, C. J., van der Meijde, M., Xu, C., and van der Meer, F. D. (2014). Why so few? Landslides triggered by the 2002 Denali earthquake, Alaska. *Quaternary Science Reviews*, 95:80–94.

Greenwood, J. R., Norris, J. E., and Wint, J. (2004). Assessing the contribution of vegetation to slope stability. *Geotechnical Engineering*, 157(4):199–207.

Grossman, M. and Zaiki, M. (2009). Reconstructing typhoons in Japan in the 1880s from documentary records. *Weather*, 64(12):315–322.

Grossman, M. J., Zaiki, M., and Nagata, R. (2015). Interannual and interdecadal variations in typhoon tracks around Japan: interannual and interdecadal variations in typhoon tracks around Japan. *International Journal of Climatology*, 35(9):2514–2527.

Grossman, M. J., Zaiki, M., and Oettle, S. (2016). An Analysis of Typhoon Tracks Around Japan Using ArcGIS. *Papers in Applied Geography*, 2(3):352–363.

Gruber, S. (2004). Permafrost thaw and destabilization of Alpine rock walls in the hot summer of 2003. *Geophysical Research Letters*, 31(13).

Guimarães, R. F., Machado, W. P., de Carvalho, O. A., Montgomery, D. R., Gomes, R. A. T., Greenberg, H. M., Cataldi, M., and Mendonça, P. C. (2017). Determination of areas susceptible to landsliding using spatial patterns of rainfall from tropical rainfall measuring mission data, rio de janeiro, brazil. *ISPRS International Journal of Geo-Information*, 6(10):289.

Gupta, V., Nautiyal, H., Kumar, V., Jamir, I., and Tandon, R. S. (2016). Landslide hazards around Uttarkashi township, Garhwal Himalaya, after the tragic flash flood in June 2013. *Natural Hazards*, 80(3):1689–1707.

Gupta, V. and Sah, M. P. (2008). Impact of the Trans-Himalayan Landslide Lake Outburst Flood (LLOF) in the Satluj catchment, Himachal Pradesh, India. *Natural Hazards*, 45(3):379–390.

Guzzetti, F., Peruccacci, S., Rossi, M., and Stark, C. P. (2008). The rainfall intensity–duration control of shallow landslides and debris flows: an update. *Landslides*, 5(1):3–17.

Günther, A., Hervás, J., van den Eeckhaut, M., Malet, J.-P., and Reichenbach, P. (2014a). Synoptic Pan-European Landslide Susceptibility Assessment: The ELSUS 1000 v1 Map. In Sassa, K., Canuti, P., and Yin, Y., editors, *Landslide Science for a Safer Geoenvironment*, pages 117–122. Springer International Publishing, Cham.

Günther, A., van den Eeckhaut, M., Malet, J.-P., Reichenbach, P., and Hervás, J. (2014b). Climate-physiographically differentiated Pan-European landslide susceptibility assessment using spatial multi-criteria evaluation and transnational landslide information. *Geomorphology*, 224:69–85.

Hagdorn, H. and Simon, T. (1985). *Geologie und Landschaft des Hohenloher Landes*, volume 28. Jan Thorbecke Verlag Sigmaringen.

Halverson, M. J. and Fleming, S. W. (2015). Complex network theory, streamflow, and hydrometric monitoring system design. *Hydrology and Earth System Sciences*, 19(7):3301–3318.

Hamada, A., Murayama, Y., and Takayabu, Y. N. (2014). Regional Characteristics of Extreme Rainfall Extracted from TRMM PR Measurements. *Journal of Climate*, 27(21):8151–8169.

Hanks, T. C. and Kanamori, H. (1979). A moment magnitude scale. *Journal of Geophysical Research*, 84(B5):2348.

Harikumar, R. (2016). Orographic effect on tropical rain physics in the Asian monsoon region: Orographic effect on tropical rain physics. *Atmospheric Science Letters*, 17(10):556–563.

Harp, E. L. and Wilson, R. C. (1995). Shaking Intensity Thresholds for Rock Falls and Slides : Evidence from 1987 Whittier Narrows and Superstition Hills Earthquake Strong-Motion Records. *Bulletin of the Seismological Society of America*, 85(6):1739–1757.

Harris, C., Arenson, L. U., Christiansen, H. H., Etzelmüller, B., Frauenfelder, R., Gruber, S., Haeberli, W., Hauck, C., Hölzle, M., Humlum, O., Isaksen, K., Kääb, A., Kern-Lütschg, M. A., Lehning, M., Matsuoka, N., Murton, J. B., Nötzli, J., Phillips, M., Ross, N., Seppälä, M., Springman, S. M., and Vonder Mühll, D. (2009). Permafrost and climate in Europe: Monitoring and modelling thermal, geomorphological and geotechnical responses. *Earth-Science Reviews*, 92(3-4):117–171.

Hartmann, D., Klein Tank, A., Rusicucci, M., Alexander, L., Broenniman, B., Charabi, Y., Dentener, F., Dlugokencky, E., Easterling, D., and Kaplan, A. (2013). Observations: Atmosphere and Surface. In *Climate Change 2013: The Physical Science Basis*, Contribution of Working Group I to the Fifth Assessment Report of the Intergovernmental Panel on Climate Change, pages 159–254. Cambridge University Press, Cambridge, United Kingdom.

Haskell, N. (1969). Determination of earthquake energy release and ML using TERRAscope. *Bulletin of the Seismological Society of America*, 59(2):865–908.

Haskell, N. A. (1964). Total energy and energy spectral density of elastic wave radiation from propagating faults. *Bulletin of the Seismological Society of America*, 54(6):1811–1841.

Havenith, H.-B., Torgoev, A., Braun, A., Schlögel, R., and Micu, M. (2016). A new classification of earthquake-induced landslide event sizes based on seismotectonic, topographic, climatic and geologic factors. *Geoenvironmental Disasters*, 3(1):6.

Havenith, H. B., Torgoev, A., Schlögel, R., Braun, A., Torgoev, I., and Ischuk, A. (2015). Tien Shan Geohazards Database: Landslide susceptibility analysis. *Geomorphology*, 249:32–43.

Heckmann, T., Schwanghart, W., and Phillips, J. D. (2015). Graph theory—Recent developments of its application in geomorphology. *Geomorphology*, 243:130–146.

Heistermann, M., Crisologo, I., Abon, C. C., Racoma, B. A., Jacobi, S., Servando, N. T., David, C. P. C., and Bronstert, A. (2013a). Brief communication "Using the new Philippine radar network to reconstruct the *Habagat of August 2012* monsoon event around Metropolitan Manila". *Natural Hazards and Earth System Science*, 13(3):653–657.

Heistermann, M., Jacobi, S., and Pfaff, T. (2013b). Technical Note: An open source library for processing weather radar data (wradlib). *Hydrology and Earth System Sciences*, 17(2):863–871.

Heitzig, J., Donges, J. F., Zou, Y., Marwan, N., and Kurths, J. (2012). Node-weighted measures for complex networks with spatially embedded, sampled, or differently sized nodes. *The European Physical Journal B*, 85(1).

Hence, D. A. and Houze, R. A. (2008). Kinematic structure of convective-scale elements in the rainbands of Hurricanes Katrina and Rita (2005). *Journal of Geophysical Research*, 113(D15).

Hence, D. A. and Houze, R. A. (2012). Vertical Structure of Tropical Cyclone Rainbands as Seen by the TRMM Precipitation Radar. *Journal of the Atmospheric Sciences*, 69(9):2644–2661.

Hengl, T. and Reuter, H. (2010). Slope map in percent derived using the GDAL utilities and based on the DEMSRE3a.

Hervás, J. and Bobrowsky, P. (2009). Mapping: Inventories, Susceptibility, Hazard and Risk. In Sassa, K. and Canuti, P., editors, *Landslides – Disaster Risk Reduction*, pages 321–349. Springer Berlin Heidelberg, Berlin, Heidelberg.

Hobley, D. E., Sinclair, H. D., and Mudd, S. M. (2012). Reconstruction of a major storm event from its geomorphic signature: The Ladakh floods, 6 August 2010. *Geology*, 40(6):483–486.

Holtz, R. D., Kovacs, W. D., and Sheahan, T. C. (2011). *An introduction to geotechnical engineering*. Pearson, Upper Saddle River, NJ, 2nd ed edition. OCLC: ocn651011935.

Hong, Y., Adler, R., and Huffman, G. (2007). Use of satellite remote sensing data in the mapping of global landslide susceptibility. *Natural Hazards*, 43(2):245–256.

Hong, Y. and Adler, R. F. (2008). Predicting global landslide spatiotemporal distribution: Integrating landslide susceptibility zoning techniques and real-time satellite rainfall estimates. *International Journal of Sediment Research*, 23(3):249–257.

Horton, R. E. (1933). The Rôle of infiltration in the hydrologic cycle. *Transactions, American Geophysical Union*, 14(1):446.

Houze, R. A. (2010). Clouds in Tropical Cyclones. *Monthly Weather Review*, 138(2):293–344.

Houze, R. A., Wilton, D. C., and Smull, B. F. (2007). Monsoon convection in the himalayan region as seen by the trmm precipitation radar. *Quarterly Journal of the Royal Meteorological Society*, 133(627):1389–1411.

Hovius, N., Meunier, P., Lin, C.-W., Chen, H., Chen, Y.-G., Dadson, S., Horng, M.-J., and Lines, M. (2011). Prolonged seismically induced erosion and the mass balance of a large earthquake. *Earth and Planetary Science Letters*, 304(3-4):347–355.

Huang, R. and Fan, X. (2013). The landslide story. *Nature Geoscience*, 6(5):325–326.

Hungr, O. (2005). Classification and terminology. In *Jakob M., and Hungr O., Debris-flow Hazards and Related Phenomena*, pages 9–23. Springer.

Hungr, O., Leroueil, S., and Picarelli, L. (2014). The Varnes classification of landslide types, an update. *Landslides*, 11(2):167–194.

Iadanza, C., Trigila, A., and Napolitano, F. (2016). Identification and characterization of rainfall events responsible for triggering of debris flows and shallow landslides. *Journal of Hydrology*, 541:230–245.

Im, E., Ahn, J., and Jo, S. (2015). Regional climate projection over South Korea simulated by the HadGEM2-AO and WRF model chain under RCP emission scenarios. *Climate Research*, 63(3):249–266.

Imaizumi, F., Hayakawa, Y. S., Hotta, N., Tsunetaka, H., Ohsaka, O., and Tsuchiya, S. (2017). Relationship between the accumulation of sediment storage and debris-flow characteristics in a debris-flow initiation zone, Ohya landslide body, Japan. *Natural Hazards and Earth System Sciences*, 17(11):1923–1938.

Iwahashi, J. and Yamagishi, H. (2017). Spatial Comparison of Two High-resolution Landslide Inventory Maps Using GIS—A Case Study of the August 1961 and July 2004 Landslides Caused by Heavy Rainfalls in the Izumozaki Area, Niigata Prefecture, Japan. In Yamagishi, H. and Bhandary, N. P., editors, *GIS Landslide*, pages 13–29. Springer Japan, Tokyo.

Jacobi, S. and Heistermann, M. (2016). Benchmarking attenuation correction procedures for six years of single-polarized C-band weather radar observations in South-West Germany. *Geomatics, Natural Hazards and Risk*, 7(6):1785–1799.

Jacobs, L., Dewitte, O., Poesen, J., Sekajugo, J., Nobile, A., Rossi, M., Thiery, W., and Kervyn, M. (2018). Field-based landslide susceptibility assessment in a data-scarce environment: the populated areas of the Rwenzori Mountains. *Natural Hazards and Earth System Sciences*, 18(1):105–124.

Jha, S. K., Zhao, H., Woldemeskel, F. M., and Sivakumar, B. (2015). Network theory and spatial rainfall connections: An interpretation. *Journal of Hydrology*, 527:13–19.

Ji, C., Helmberger, D. V., Wald, D. J., and Ma, K.-F. (2003). Slip history and dynamic implications of the 1999 Chi-Chi, Taiwan, earthquake. *Journal of Geophysical Research: Solid Earth*, 108(B9).

Jibson, R. W. (1993). Predicting Earthquake-Induced Landslide Displacements Using Newmark's Sliding Block Analysis. *Transportation Research Record*, 1411(8):9–17.

Jibson, R. W. (2007). Regression models for estimating coseismic landslide displacement. *Engineering Geology*, 91(2-4):209–218.

Jibson, R. W. (2011). Methods for assessing the stability of slopes during earthquakes–A retrospective. *Engineering Geology*, 122(1-2):43–50.

Jibson, R. W., Harp, E. L., and Michael, J. A. (2000). A method for producing digital probabilistic seismic landslide hazard maps. *Engineering Geology*, 58:271–289.

Kanae, S., Oki, T., and Kashida, A. (2004). Changes in Hourly Heavy Precipitation at Tokyo from 1890 to 1999. *Journal of the Meteorological Society of Japan*, 82(1):241–247.

Kanamori, H., Mori, J. I. M., Hauksson, E., Heaton, T. H., Hutton, K., and Jones, L. M. (1993). Determination of Earthquake Energy Release and. *Bulletin of the Seismological Society of America*, 83(2):330–346.

Kawagoe, S., Kazama, S., and Ranjan Sarukkalige, P. (2009). Assessment of snowmelt triggered landslide hazard and risk in Japan. *Cold Regions Science and Technology*, 58(3):120–129.

Keefer, D. K. (1984). Landslides caused by earthquakes. *Geological Society of America Bulletin*, 95(4):406–421.

Keefer, D. K. (2000). Statistical analysis of an earthquake-induced landslide distribution — the 1989 Loma Prieta, California event. *Engineering Geology*, 58(3-4):231–249.

Keefer, D. K. (2002). Investigating Landslides Caused by Earthquakes – A Historical Review. *Surveys in Geophysics*, 23(6):473–510.

Keiler, M., Knight, J., and Harrison, S. (2010). Climate change and geomorphological hazards in the eastern European Alps. *Philosophical Transactions of the Royal Society A: Mathematical, Physical and Engineering Sciences*, 368(1919):2461–2479.

Kim, J.-H., Ho, C.-H., Lee, M.-H., Jeong, J.-H., and Chen, D. (2006). Large increase in heavy rainfall associated with tropical cyclone landfalls in Korea after the late 1970s: heavy rainfall and tropical cyclones in korea. *Geophysical Research Letters*, 33(18).

Kirschbaum, D., Stanley, T., and Zhou, Y. (2015). Spatial and temporal analysis of a global landslide catalog. *Geomorphology*, 249:4–15.

Kirschbaum, D. B., Adler, R., Hong, Y., Hill, S., and Lerner-Lam, A. (2010). A global landslide catalog for hazard applications: method, results, and limitations. *Natural Hazards*, 52(3):561–575.

Kiyota, T., Ikeda, T., Konagai, K., and Shiga, M. (2017). Geotechnical Damage Caused by the 2016 Kumamoto Earthquake, Japan. *Geotechnical Damage Caused by the 2016 Kumamoto Earthquake, Japan*, 4(2):78–95.

Knight, J. and Harrison, S. (2009). Sediments and future climate. *Nature Geoscience*, 2(4):230–230.

Knutson, T. R., McBride, J. L., Chan, J., Emanuel, K., Holland, G., Landsea, C., Held, I., Kossin, J. P., Srivastava, A. K., and Sugi, M. (2010). Tropical cyclones and climate change. *Nature Geoscience*, 3(3):157–163.

Koketsu, K., Miyake, H., and Suzuki, H. (2012). Japan Integrated Velocity Structure Model Version 1. *Proceedings of the 15th World Conference on Earthquake Engineering*, pages 1–4.

Kramer, S. L. (1996). Geotechnical earthquake engineering. In prentice–Hall international series in civil engineering and engineering mechanics. *Prentice-Hall, New Jersey*.

Krishnan, R. and Sugi, M. (2001). Baiu Rainfall Variability and Associated Monsoon Teleconnections. *Journal of the Meteorological Society of Japan*, 79(3):851–860.

Kubo, H., Suzuki, W., Aoi, S., and Sekiguchi, H. (2016). Source rupture processes of the 2016 Kumamoto, Japan, earthquakes estimated from strong-motion waveforms. *Earth, Planets and Space*, 2016:1–13.

Kumar, A., Asthana, A., Priyanka, R. S., Jayangondaperumal, R., Gupta, A. K., and Bhakuni, S. (2017). Assessment of landslide hazards induced by extreme rainfall event in jammu and kashmir himalaya, northwest india. *Geomorphology*, 284:72–87.

Kurita, N., Nakatsuka, T., Ohnishi, K., Mitsutani, T., and Kumagai, T. (2016). Analysis of the interdecadal variability of summer precipitation in central Japan using a reconstructed 106 year long oxygen isotope record from tree ring cellulose: Interdecadal modulation of Baiu rainfall. *Journal of Geophysical Research: Atmospheres*, 121(20):12,089–12,107.

Landkreis Schwäbisch Hall (2016). Unwetter-Schadensliste Landkreis Schwäbisch Hall.

Laudan, J., Rözer, V., Sieg, T., Vogel, K., and Thieken, A. H. (2017). Damage assessment in Braunsbach 2016: data collection and analysis for an improved understanding of damaging processes during flash floods. *Natural Hazards and Earth System Sciences*, 17(12):2163–2179.

Lee, C.-F., Huang, W.-K., Chang, Y.-L., Chi, S.-Y., and Liao, W.-C. (2018). Regional landslide susceptibility assessment using multi-stage remote sensing data along the coastal range highway in northeastern Taiwan. *Geomorphology*, 300:113–127.

Lee, C.-T. (2013). Re-Evaluation of Factors Controlling Landslides Triggered by the 1999 Chi–Chi Earthquake. In *Earthquake-Induced Landslides*, number June in Springer Natural Hazards, pages 213–224. Springer Berlin Heidelberg, Berlin, Heidelberg.

Leonard, M. (2010). Earthquake Fault Scaling: Self-Consistent Relating of Rupture Length, Width, Average Displacement, and Moment Release. *Bulletin of the Seismological Society of America*, 100(5A):1971–1988.

Leonarduzzi, E., Molnar, P., and McArdell, B. W. (2017). Predictive performance of rainfall thresholds for shallow landslides in Switzerland from gridded daily data: Rainfall thresholds for landslides in Switzerland. *Water Resources Research*, 53(8):6612–6625.

LGRB (2012). GK50: Geologische Einheiten (Flächen).

Li, C., Ma, T., Zhu, X., and Li, W. (2011). The power–law relationship between landslide occurrence and rainfall level. *Geomorphology*, 130(3-4):221–229.

Li, Y., Cheung, K. K. W., and Chan, J. C. L. (2015). Modelling the effects of land-sea contrast on tropical cyclone precipitation under environmental vertical wind shear. *Quarterly Journal of the Royal Meteorological Society*, 141(687):396–412.

Li, Z. (2014). Watershed modeling using arc hydro based on DEMs: a case study in Jackpine watershed. *Environmental Systems Research*, 3(1):11.

Lin, L., Lin, Q., and Wang, Y. (2016). Landslide susceptibility mapping on global scale using method of logistic regression. *Natural Hazards and Earth System Sciences Discussions*, pages 1–20.

Lind, P., Lindstedt, D., Kjellström, E., and Jones, C. (2016). Spatial and Temporal Characteristics of Summer Precipitation over Central Europe in a Suite of High-Resolution Climate Models. *Journal of Climate*, 29(10):3501–3518.

Lombardo, L., Cama, M., Conoscenti, C., Märker, M., and Rotigliano, E. (2015). Binary logistic regression versus stochastic gradient boosted decision trees in assessing landslide susceptibility for multiple-occurring landslide events: application to the 2009 storm event in Messina (Sicily, southern Italy). *Natural Hazards*, 79(3):1621–1648.

Longoni, L., Ivanov, V. I., and Brambilla, D. (2016a). Analysis of the Temporal and Spatial Scales of Soil Erosion and Transport in a Mountain Basin. *Italian Journal of Engineering Geology and Environment*, 2:17–30.

Longoni, L., Papini, M., Arosio, D., Zanzi, L., and Brambilla, D. (2014). A new geological model for Spriana landslide. *Bulletin of Engineering Geology and the Environment*, 73(4):959–970.

Longoni, L., Papini, M., Brambilla, D., Barazzetti, L., Roncoroni, F., Scaioni, M., and Ivanov, V. (2016b). Monitoring Riverbank Erosion in Mountain Catchments Using Terrestrial Laser Scanning. *Remote Sensing*, 8(3):241.

López-Tarazón, J. A., Batalla, R., Vericat, D., and Francke, T. (2009). Suspended sediment transport in a highly erodible catchment: the river isábena (southern pyrenees). *Geomorphology*, 109(3-4):210–221.

López-Tarazón, J., Batalla, R., Vericat, D., and Francke, T. (2012). The sediment budget of a highly dynamic mesoscale catchment: The River Isábena. *Geomorphology*, 138(1):15–28.

Malamud, B. D., Turcotte, D. L., Guzzetti, F., and Reichenbach, P. (2004). Landslides, earthquakes, and erosion. *Earth and Planetary Science Letters*, 229(1-2):45–59.

Malik, N., Bookhagen, B., Marwan, N., and Kurths, J. (2012). Analysis of spatial and temporal extreme monsoonal rainfall over South Asia using complex networks. *Climate Dynamics*, 39(3-4):971–987.

Malik, N., Bookhagen, B., and Mucha, P. J. (2016). Spatiotemporal patterns and trends of Indian monsoonal rainfall extremes: Spatiotemporal patterns and trends. *Geophysical Research Letters*, 43(4):1710–1717.

Malik, N., Marwan, N., and Kurths, J. (2010). Spatial structures and directionalities in Monsoonal precipitation over South Asia. *Nonlinear Processes in Geophysics*, 17(5):371–381.

Manda, A., Nakamura, H., Asano, N., Iizuka, S., Miyama, T., Moteki, Q., Yoshioka, M. K., Nishii, K., and Miyasaka, T. (2014). Impacts of a warming marginal sea on torrential rainfall organized under the Asian summer monsoon. *Scientific Reports*, 4.

Marc, O., Behling, R., Andermann, C., Turowski, J. M., Illien, L., Roessner, S., and Hovius, N. (2019). Long-term erosion of the nepal himalayas by bedrock landsliding: the role of monsoons, earthquakes and giant landslides. *Earth Surface Dynamics*, 7(1):107–128.

Marc, O., Hovius, N., Meunier, P., Gorum, T., and Uchida, T. (2016). A seismologically consistent expression for the total area and volume of earthquake-triggered landsliding. *Journal of Geophysical Research: Earth Surface*, 121(4):640–663.

Marc, O., Meunier, P., and Hovius, N. (2017). Prediction of the area affected by earthquake-induced landsliding based on seismological parameters. *Natural Hazards and Earth System Sciences*, 17(7):1159–1175.

Marchok, T. (2014). Summary of recent research related to rainfall. In *Third international workshop on tropical cyclones – Landfall processes*, WWRP - TCP, Republic of Korea.

Marra, F., Nikolopoulos, E., Creutin, J., and Borga, M. (2016). Space–time organization of debris flows-triggering rainfall and its effect on the identification of the rainfall threshold relationship. *Journal of Hydrology*, 541:246–255.

Martel, S. (2004). Mechanics of landslide initiation as a shear fracture phenomenon. *Marine Geology*, 203(3-4):319–339.

Martinotti, M. E., Pisano, L., Marchesini, I., Rossi, M., Peruccacci, S., Brunetti, M. T., Melillo, M., Amoruso, G., Loiacono, P., Vennari, C., Vessia, G., Trabace, M., Parise, M., and Guzzetti, F. (2017). Landslides, floods and sinkholes in a karst environment: the 1–6 September 2014 Gargano event, southern Italy. *Natural Hazards and Earth System Sciences*, 17(3):467–480.

Marwan, N. and Kurths, J. (2015). Complex network based techniques to identify extreme events and (sudden) transitions in spatio-temporal systems. *Chaos: An Interdisciplinary Journal of Nonlinear Science*, 25(9):097609.

Massa, M., Barani, S., and Lovati, S. (2014). Overview of topographic effects based on experimental observations: meaning, causes and possible interpretations. *Geophysical Journal International*, 197(3):1537–1550.

Massey, C., Townsend, D., Rathje, E., Allstadt, K. E., Lukovic, B., Kaneko, Y., Bradley, B., Wartman, J., Jibson, R. W., Petley, D. N., Horspool, N., Hamling, I., Carey, J., Cox, S., Davidson, J., Dellow, S., Godt, J. W., Holden, C., Jones, K., Kaiser, A., Little, M., Lyndsell, B., McColl, S., Morgenstern, R., Rengers, F. K., Rhoades, D., Rosser, B., Strong, D., Singeisen, C., and Villeneuve, M. (2018). Landslides Triggered by the 14 November 2016 Mw 7.8 Kaikoura Earthquake, New Zealand. *Bulletin of the Seismological Society of America*, 108(3B):1630–1648.

Matsumoto, J. (1989). Heavy rainfalls over East Asia. *International Journal of Climatology*, 9(4):407–423.

Matsushi, Y., Chigira, M., and Kosugi, K. (2014). Orographic rainfall, deep-seated catastrophic landslides, and landscape evolution: Geomorphic hazard assessment in active orogens. Technical report, INTERPRAEVENT.

Matsuura, S., Okamoto, T., Asano, S., Osawa, H., and Shibasaki, T. (2017). Influences of the snow cover on landslide displacement in winter period: a case study in a heavy snowfall area of Japan. *Environmental Earth Sciences*, 76(10).

Maufroy, E., Cruz-Atienza, V. M., and Gaffet, S. (2012). A Robust Method for Assessing 3-D Topographic Site Effects: A Case Study at the LSBB Underground Laboratory, France. *Earthquake Spectra*, 28(3):1097–1115.

Maufroy, E., Cruz-Atienza, V. M., Cotton, F., and Gaffet, S. (2015). Frequency-Scaled Curvature as a Proxy for Topographic Site-Effect Amplification and Ground-Motion Variability. *Bulletin of the Seismological Society of America*, 105(1):354–367.

McClung, D. M. (1981). Fracture mechanical models of dry slab avalanche release. *Journal of Geophysical Research: Solid Earth*, 86(B11):10783–10790.

McGuire, L. A., Rengers, F. K., Kean, J. W., Coe, J. A., Mirus, B. B., Baum, R. L., and Godt, J. W. (2016). Elucidating the role of vegetation in the initiation of rainfall-induced shallow landslides: Insights from an extreme rainfall event in the Colorado Front Range: Shallow Landslides. *Geophysical Research Letters*, 43(17):9084–9092.

Meunier, P., Hovius, N., and Haines, A. J. (2007). Regional patterns of earthquake-triggered landslides and their relation to ground motion. *Geophysical Research Letters*, 34(20).

Meunier, P., Hovius, N., and Haines, J. A. (2008). Topographic site effects and the location of earthquake induced landslides. *Earth and Planetary Science Letters*, 275(3-4):221–232.

Meunier, P., Uchida, T., and Hovius, N. (2013). Landslide patterns reveal the sources of large earthquakes. *Earth and Planetary Science Letters*, 363:27–33.

Meyer, N. K. (2014). *Debris flows - Initiation conditions and impact on functionality of Norwegian road network*. Dissertation, University of Oslo, Oslo.

Meza-Fajardo, K. C., Semblat, J., Chaillat, S., and Lenti, L. (2016). Seismic-Wave Amplification in 3d Alluvial Basins: 3d/1d Amplification Ratios from Fast Multipole BEM Simulations. *Bulletin of the Seismological Society of America*, 106(3):1267–1281.

Miles, S. B. and Keefer, D. K. (2009). Evaluation of CAMEL - comprehensive areal model of earthquake-induced landslides. *Engineering Geology*, 104(1-2):1–15.

Minder, J. R., Roe, G. H., and Montgomery, D. R. (2009). Spatial patterns of rainfall and shallow landslide susceptibility: Rainfall patterns and landslides. *Water Resources Research*, 45(4).

Mizuhashi, M., Towhata, I., Sato, J., and Tsujimura, T. (2006). Examination of Slope Hazard Assessment by Using Case Studies of Earthquake- and Rainfall-Induced Landslides. *Soils and Foundations*, 46(6):843–853.

Molnar, P. and Tapponnier, P. (1977). The Collision between India and Eurasia. *Scientific American*, 236(4):30–41.

Monaghan, A. J., Rife, D. L., Pinto, J. O., Davis, C. A., and Hannan, J. R. (2010). Global Precipitation Extremes Associated with Diurnally Varying Low-Level Jets. *Journal of Climate*, 23(19):5065–5084.

Moore, J. D. P., Yu, H., Tang, C.-H., Wang, T., Barbot, S., Peng, D., Masuti, S., Dauwels, J., Hsu, Y.-J., Lambert, V., Nanjundiah, P., Wei, S., Lindsey, E., Feng, L., and Shibazaki, B. (2017). Imaging the distribution of transient viscosity after the 2016 M w 7.1 Kumamoto earthquake. *Science*, 356(6334):163–167.

Morss, R. E., Mulder, K. J., Lazo, J. K., and Demuth, J. L. (2016). How do people perceive, understand, and anticipate responding to flash flood risks and warnings? Results from a public survey in Boulder, Colorado, USA. *Journal of Hydrology*, 541:649–664.

Mueller, E. N. and Pfister, A. (2011). Increasing occurrence of high-intensity rainstorm events relevant for the generation of soil erosion in a temperate lowland region in central europe. *Journal of hydrology*, 411(3-4):266–278.

Murakami, H., Wang, B., and Kitoh, A. (2011). Future Change of Western North Pacific Typhoons: Projections by a 20-km-Mesh Global Atmospheric Model*. *Journal of Climate*, 24(4):1154–1169.

Nadim, F., Kjekstad, O., Peduzzi, P., Herold, C., and Jaedicke, C. (2006). Global landslide and avalanche hotspots. *Landslides*, 3(2):159–173.

Nakazawa, T. (2006). Madden-Julian Oscillation Activity and Typhoon Landfall on Japan in 2004. *SOLA*, 2:136–139.

National Research Institute for Earth Science and Disaster Prevention (2014). Disaster Research Institute for Science and Technology Research Materials "1: 50,000 landslide topography map".

National Research Institute for Earth Science and Disaster Prevention (2016). Sediment movement distribution map by the Kumamoto earthquake (updated in 2016.6.27).

Newman, A. V. and Okal, E. A. (1998). Teleseismic estimates of radiated seismic energy: The E/M 0 discriminant for tsunami earthquakes. *Journal of Geophysical Research: Solid Earth*, 103(B11):26885–26898.

Newman, M. E. J. (2010). *Networks: an introduction*. Oxford University Press, Oxford ; New York. OCLC: ocn456837194.

Newmark, N. M. (1965). Effects of Earthquakes on Dams and Embankments. *Géotechnique*, 15(2):139–160.

Nikolopoulos, E. I., Crema, S., Marchi, L., Marra, F., Guzzetti, F., and Borga, M. (2014). Impact of uncertainty in rainfall estimation on the identification of rainfall thresholds for debris flow occurrence. *Geomorphology*, 221:286–297.

Nikolopoulos, E. I., Destro, E., Maggioni, V., Marra, F., and Borga, M. (2017). Satellite rainfall estimates for debris flow prediction: An evaluation based on rainfall accumulationduration thresholds. *Journal of Hydrometeorology*, 18(8):2207–2214.

Ninomiya, R. (1984). Characteristics of Baiu Front as a Predominant Subtropical Front in the Summer Northern Hemisphere. *Journal of the Meteorological Society of Japan*, 62(6):880–894.

Oguchi, T. (1996). Hillslope failure and sediment yield in Japanese regions with different storm intensity. Technical Report 28, University of Tokyo, Tokyo.

Ohba, M., Kadokura, S., Yoshida, Y., Nohara, D., and Toyoda, Y. (2015). Anomalous Weather Patterns in Relation to Heavy Precipitation Events in Japan during the Baiu Season. *Journal of Hydrometeorology*, 16(2):688–701.

Ohlmacher, G. C. (2007). Plan curvature and landslide probability in regions dominated by earth flows and earth slides. *Engineering Geology*, 91(2-4):117–134.

Okada, Y., Ochiai, H., Okamoto, T., Sassa, K., Fukuoka, H., and Igwe, O. (2007). A complex earth slide–earth flow induction by the heavy rainfall in July 2006, Okaya City, Nagano Prefecture, Japan. *Landslides*, 4(2):197–203.

Onnela, J.-P., Chakraborti, A., Kaski, K., Kertesz, J., and Kanto, A. (2003). Dynamics of market correlations: Taxonomy and portfolio analysis. *Physical Review E*, 68(5).

Onnela, J.-P., Kaski, K., and Kertesz, J. (2004). Clustering and information in correlation based financial networks. *The European Physical Journal B - Condensed Matter*, 38(2):353–362.

Osanai, N., Shimizu, T., Kuramoto, K., Kojima, S., and Noro, T. (2010). Japanese early-warning for debris flows and slope failures using rainfall indices with Radial Basis Function Network. *Landslides*, 7(3):325–338.

Palladino, M., Viero, A., Turconi, L., Brunetti, M., Peruccacci, S., Melillo, M., Luino, F., Deganutti, A., and Guzzetti, F. (2018). Rainfall thresholds for the activation of shallow landslides in the Italian Alps: the role of environmental conditioning factors. *Geomorphology*, 303:53–67.

Papalexiou, S. M., Koutsoyiannis, D., and Makropoulos, C. (2013). How extreme is extreme? An assessment of daily rainfall distribution tails. *Hydrology and Earth System Sciences*, 17(2):851–862.

Parise, M., Ravbar, N., Živanović, V., Mikszewski, A., Kresic, N., Mádl-Szőnyi, J., and Kukurić, N. (2015). Hazards in Karst and Managing Water Resources Quality. In Stevanović, Z., editor, *Karst Aquifers—Characterization and Engineering*, pages 601–687. Springer International Publishing, Cham.

Parker, R. N., Hancox, G. T., Petley, D. N., Massey, C. I., Densmore, A. L., and Rosser, N. J. (2015). Spatial distributions of earthquake-induced landslides and hillslope preconditioning in the northwest South Island, New Zealand. *Earth Surface Dynamics*, 3(4):501–525.

Paudel, P. P., Omura, H., Kubota, T., and Devkota, B. (2008). Characterization of terrain surface and mechanisms of shallow landsliding in upper Kurokawa watershed, Mt Aso, western Japan. *Bulletin of Engineering Geology and the Environment*, 67(1):87–95.

Pawluszek, K. and Borkowski, A. (2017). Impact of DEM-derived factors and analytical hierarchy process on landslide susceptibility mapping in the region of Rożnów Lake, Poland. *Natural Hazards*, 86(2):919–952.

Peruccacci, S., Brunetti, M. T., Gariano, S. L., Melillo, M., Rossi, M., and Guzzetti, F. (2017). Rainfall thresholds for possible landslide occurrence in Italy. *Geomorphology*, 290:39–57.

Petley, D. (2012). Global patterns of loss of life from landslides. *Geology*, 40(10):927–930.

Phillips, J. D., Schwanghart, W., and Heckmann, T. (2015). Graph theory in the geosciences. *Earth-Science Reviews*, 143:147–160.

Pike, R. J. and Sobieszczyk, S. (2008). Soil slip/debris flow localized by site attributes and wind-driven rain in the san francisco bay region storm of january 1982. *Geomorphology*, 94(3-4):290–313.

Piper, D., Kunz, M., Ehmele, F., Mohr, S., Mühr, B., Kron, A., and Daniell, J. (2016). Exceptional sequence of severe thunderstorms and related flash floods in May and June 2016 in Germany. Part I: Meteorological background. *Natural Hazards and Earth System Sciences Discussions*, pages 1–30.

Planchon, O. and Darboux, F. (2001). A fast, simple and versatile algorithm to fill the depressions of digital elevation models. *CATENA*, 46(2-3):159–176.

Pollen, N. and Simon, A. (2005). Estimating the mechanical effects of riparian vegetation on stream bank stability using a fiber bundle model: Modeling root reinforcement of stream banks. *Water Resources Research*, 41(7).

Ponziani, F., Pandolfo, C., Stelluti, M., Berni, N., Brocca, L., and Moramarco, T. (2012). Assessment of rainfall thresholds and soil moisture modeling for operational hydrogeological risk prevention in the Umbria region (central Italy). *Landslides*, 9(2):229–237.

Pradhan, A. M. S., Kang, H.-S., Lee, J.-S., and Kim, Y.-T. (2017). An ensemble landslide hazard model incorporating rainfall threshold for Mt. Umyeon, South Korea. *Bulletin of Engineering Geology and the Environment*.

Prein, A. F., Liu, C., Ikeda, K., Bullock, R., Rasmussen, R. M., Holland, G. J., and Clark, M. (2017). Simulating North American mesoscale convective systems with a convection-permitting climate model. *Climate Dynamics*.

Preisig, G., Eberhardt, E., Smithyman, M., Preh, A., and Bonzanigo, L. (2016). Hydromechanical Rock Mass Fatigue in Deep-Seated Landslides Accompanying Seasonal Variations in Pore Pressures. *Rock Mechanics and Rock Engineering*, 49(6):2333–2351.

Prinz, H. and Strauss, R. (2011). *Ingenieurgeologie*. Spektrum Akademischer Verlag, Heidelberg, Germany. OCLC: 785777024.

Quiroga, R. Q., Kreuz, T., and Grassberger, P. (2002). Event synchronization: A simple and fast method to measure synchronicity and time delay patterns. *Physical Review E*, 66(4).

Radice, A., Longoni, L., Papini, M., Brambilla, D., and Ivanov, V. (2016). Generation of a Design Flood-Event Scenario for a Mountain River with Intense Sediment Transport. *Water*, 8(12):597.

Radice, A., Malavasi, S., and Ballio, F. (2006). Solid transport measurements through image processing. *Experiments in Fluids*, 41(5):721–734.

Rahardjo, H., Li, X. W., Toll, D. G., and Leong, E. C. (2001). The effect of antecedent rainfall on slope stability. In Toll, D. G., editor, *Unsaturated Soil Concepts and Their Application in Geotechnical Practice*, pages 371–399. Springer Netherlands, Dordrecht.

Rasmussen, K. L. and Houze, R. A. (2012). A Flash-Flooding Storm at the Steep Edge of High Terrain: Disaster in the Himalayas. *Bulletin of the American Meteorological Society*, 93(11):1713–1724.

Revadekar, J. V., Varikoden, H., Preethi, B., and Mujumdar, M. (2016). Precipitation extremes during Indian summer monsoon: role of cyclonic disturbances. *Natural Hazards*, 81(3):1611–1625.

Rheinwalt, A., Boers, N., Marwan, N., Kurths, J., Hoffmann, P., Gerstengarbe, F.-W., and Werner, P. (2016). Non-linear time series analysis of precipitation events using regional climate networks for Germany. *Climate Dynamics*, 46(3-4):1065–1074.

Rheinwalt, A., Marwan, N., Kurths, J., Werner, P., and Gerstengarbe, F.-W. (2012). Boundary effects in network measures of spatially embedded networks. *EPL (Europhysics Letters)*, 100(2):28002.

Rickenmann, D., Badoux, A., and Hunzinger, L. (2016). Significance of sediment transport processes during piedmont floods: the 2005 flood events in Switzerland: The 2005 Flood Events in Switzerland. *Earth Surface Processes and Landforms*, 41(2):224–230.

Roback, K., Clark, M. K., West, A. J., Zekkos, D., Li, G., Gallen, S. F., Chamlagain, D., and Godt, J. W. (2018). The size, distribution, and mobility of landslides caused by the 2015 M w 7.8 Gorkha earthquake, Nepal. *Geomorphology*, 301:121–138.

Roering, J. J., Kirchner, J. W., and Dietrich, W. E. (2005). Characterizing structural and lithologic controls on deep-seated landsliding: Implications for topographic relief and landscape evolution in the Oregon Coast Range, USA. *Geological Society of America Bulletin*, 117(5):654.

Romeo, R. (2000). Seismically induced landslide displacements: A predictive model. *Engineering Geology*, 58(3-4):337–351.

Rotstein, Y. and Schaming, M. (2011). The Upper Rhine Graben (URG) revisited: Miocene transtension and transpression account for the observed first-order structures: Transpression in the Upper Rhine Graben. *Tectonics*, 30(3):n/a–n/a.

Roux, H., Labat, D., Garambois, P.-A., Maubourguet, M.-M., Chorda, J., and Dartus, D. (2011). A physically-based parsimonious hydrological model for flash floods in Mediterranean catchments. *Natural Hazards and Earth System Science*, 11(9):2567–2582.

Rozalis, S., Morin, E., Yair, Y., and Price, C. (2010). Flash flood prediction using an uncalibrated hydrological model and radar rainfall data in a Mediterranean watershed under changing hydrological conditions. *Journal of Hydrology*, 394(1-2):245–255.

Rudnicki, J. W. and Freund, L. B. (1981). On energy radiation from seismic sources. *Bulletin of the Seismological Society of America*, 71(3):583–595.

Rutkowska, A., Willems, P., and Niedzielski, T. (2017). Relation between design floods based on daily maxima and daily means: use of the Peak Over Threshold approach in the Upper Nysa Kłodzka Basin (SW Poland). *Geomatics, Natural Hazards and Risk*, 8(2):585–606.

Saba, S. B., van der Meijde, M., and van der Werff, H. (2010). Spatiotemporal landslide detection for the 2005 Kashmir earthquake region. *Geomorphology*, 124(1-2):17–25.

Saito, H., Korup, O., Uchida, T., Hayashi, S., and Oguchi, T. (2014). Rainfall conditions, typhoon frequency, and contemporary landslide erosion in Japan. *Geology*, 42(11):999–1002.

Saito, H., Nakayama, D., and Matsuyama, H. (2010). Relationship between the initiation of a shallow landslide and rainfall intensity—duration thresholds in Japan. *Geomorphology*, 118(1-2):167–175.

Salvati, P., Bianchi, C., Rossi, M., and Guzzetti, F. (2010). Societal landslide and flood risk in Italy. *Natural Hazards and Earth System Science*, 10(3):465–483.

Sampe, T. and Xie, S.-P. (2010). Large-Scale Dynamics of the Meiyu-Baiu Rainband: Environmental Forcing by the Westerly Jet*. *Journal of Climate*, 23(1):113–134.

Sato, N. and Takahashi, M. (2003). Interdecadal Variations of the Baiu Front and Summer Weather in Japan.

Sato, T. (2013). Mechanism of Orographic Precipitation around the Meghalaya Plateau Associated with Intraseasonal Oscillation and the Diurnal Cycle. *Monthly Weather Review*, 141(7):2451–2466.

Sato, T., Chigira, M., and Matsushi, Y. (2017). Topographic and Geological Features of Landslides Induced by the 2016 Kumamoto Earthquake in the Western Part of the Aso Caldera. *DPRI Annuals*, 60B:431–452.

Savage, J. C. (1966). Radiation from a realistic model of faulting. *Bulletin of the Seismological Society of America*, 56(2):577–592.

Scheevel, C. R., Baum, R. L., Mirus, B. B., and Smith, J. B. (2017). Precipitation thresholds for landslide occurrence near Seattle, Mukilteo, and Everett, Washington. Technical Report 2017-1039, US Geological Survey, Reston, VA.

Schmidt, K. M., Roering, J. J., Stock, J. D., Dietrich, W. E., Montgomery, D. R., and Schaub, T. (2001). The variability of root cohesion as an influence on shallow landslide susceptibility in the Oregon Coast Range. *Canadian Geotechnical Journal*, 38(5):995–1024.

Schnabel, P. B. and Bolton Seed, H. (1973). Accelerations in rock for earthquakes in the western United States. *Bulletin of the Seismological Society of America*, 63(2):501–516.

Schwanghart, W., Bernhardt, A., Stolle, A., Hoelzmann, P., Adhikari, B. R., Andermann, C., Tofelde, S., Merchel, S., Rugel, G., Fort, M., and Korup, O. (2016). Repeated catastrophic valley infill following medieval earthquakes in the Nepal Himalaya. *Science*, 351(6269):147–150.

Schwarz, G. (1978). Estimating the Dimension of a Model. *The Annals of Statistics*, 6(2):461–464.

Sedlar, F. (2016). Inundated Infrastructure: Jakarta's Failing Hydraulic Infrastructure. *Michigan Journal of Sustainability*, 4(20160901).

Semblat, J., Kham, M., Parara, E., Bard, P., Pitilakis, K., Makra, K., and Raptakis, D. (2005). Seismic wave amplification: Basin geometry vs soil layering. *Soil Dynamics and Earthquake Engineering*, 25(7-10):529–538.

Seneviratne, S. I., Nicholls, N., Easterling, D., Goodess, C. M., Kanae, S., Kossin, J., Luo, Y., Marengo, J., McInnes, K., Rahimi, M., Reichstein, M., Sorteberg, A., Vera, C., Zhang, X., Rusticucci, M., Semenov, V., Alexander, L. V., Allen, S., Benito, G., Cavazos, T., Clague, J., Conway, D., Della-Marta, P. M., Gerber, M., Gong, S., Goswami, B. N., Hemer, M., Huggel, C., van den Hurk, B., Kharin, V. V., Kitoh, A., Tank, A. M. K., Li, G., Mason, S., McGuire, W., van Oldenborgh, G. J., Orlowsky, B., Smith, S., Thiaw, W., Velegrakis, A., Yiou, P., Zhang, T., Zhou, T., and Zwiers, F. W. (2012). Changes in Climate Extremes and their Impacts on the Natural Physical Environment. In Field, C. B., Barros, V., Stocker, T. F., and Dahe, Q., editors, *Managing the Risks of Extreme Events and Disasters to Advance Climate Change Adaptation*, pages 109–230. Cambridge University Press, Cambridge.

Sethian, J. A. (1996). A fast marching level set method for monotonically advancing fronts. *Proceedings of the National Academy of Sciences*, 93(4):1591–1595.

Sethian, J. A. and Popovici, A. M. (1999). 3-D traveltime computation using the fast marching method. *Geophysics*, 64(2):516–523.

Shimazu, Y. (1998). Classification of Precipitation Systems in Mature and Early Weakening Stages of Typhoons around Japan. *Journal of the Meteorological Society of Japan. Ser. II*, 76(3):437–445.

Shinoda, M. and Miyata, Y. (2017). Regional landslide susceptibility following the Mid NIIGATA prefecture earthquake in 2004 with Newmars's sliding block analysis. *Landslides*, 14(6):1887–1899.

Shoja-taheri, B. Y. J. and Anderson, J. G. (1988). The 1978 Tabas, Iran, Earthquake: An Interpretation of the Strong Motion Records. *Bulletin of the Seismological Society of America*, 78(1):142–171.

Sidle, R. C. and Chigira, M. (2004). Landslides and debris flows strike Kyushu, Japan. *Eos, Transactions American Geophysical Union*, 85(15):145.

Sidle, R. C., Kim, K., Tsuboyama, Y., and Hosoda, I. (2011). Development and application of a simple hydrogeomorphic model for headwater catchments: Simple hydrological model for headwater catchments. *Water Resources Research*, 47(3).

Sim, D. (2016). Germany: Deadly flash floods leave Braunsbach buried under rocks, trees and car wrecks. *International Business Times*.

Simon, T. (1980). *Hydrogeologische Untersuchungen im Muschelkalk-Karst von Hohenlohe*. Ph.D., University of Stuttgart, Stuttgart, Germany.

Sivakumar, B. and Woldemeskel, F. M. (2014). Complex networks for streamflow dynamics. *Hydrology and Earth System Sciences*, 18(11):4565–4578.

Skempton, A. W. and Hutchinson, J. N. (1969). Stability of natural slopes and embankment foundations. In *Proceedings of the 7th International Conference on Soil Mechanics and Foundation Engineering, Held in Mexico City, 1969*, volume State of the Art volume, pages 291–340. Sociedad Mexicana de Mecanica.

Somerville, P., Irikura, K., Graves, R., Sawada, S., Wald, D., Abrahamson, N., Iwasaki, Y., Kagawa, T., Smith, N., and Kowada, A. (1999). Characterizing Crustal Earthquake Slip Models for the Prediction of Strong Ground Motion. *Seismological Research Letters*, 70(1):59–80.

Somerville, P. G., Smith, N. F., Graves, R. W., and Abrahamson, N. A. (1997). Modification of Empirical Strong Ground Motion Attenuation Relations to Include the Amplitude and Duration Effects of Rupture Directivity. *Seismological Research Letters*, 68(1):199–222.

Song, K., Wang, F., Dai, Z., Iio, A., Osaka, O., and Sakata, S. (2017). Geological characteristics of landslides triggered by the 2016 Kumamoto earthquake in Mt. Aso volcano, Japan. *Bulletin of Engineering Geology and the Environment*, pages 1–10.

Spudich, B. P., Chiou, B. S. J., Graves, R., Collins, N., and Somerville, P. (2004). A Formulation of Directivity for Earthquake Sources Using Isochrone Theory. *U.S. Geol. Surv. Open-File Rept. 2004-1268*, page 54.

Spudich, P., Bayless, J., Baker, J., Chiou, B. S. J., Rowshandel, B., Shahi, S., and Somerville, P. (2013). Final Report of the NGA-West2 Directivity Working Group. Technical Report Final, Pacific Earthquake Engineering Research Center.

Spudich, P. and Chiou, B. S. J. (2008). Directivity in NGA earthquake ground motions: Analysis using isochrone theory. *Earthquake Spectra*, 24(1):279–298.

Stanley, T. and Kirschbaum, D. B. (2017). A heuristic approach to global landslide susceptibility mapping. *Natural Hazards*, 87(1):145–164.

Stark, T. D., Baghdady, A. K., Hungr, O., and Aaron, J. (2017). Case Study: Oso, Washington, Landslide of March 22, 2014—Material Properties and Failure Mechanism. *Journal of Geotechnical and Geoenvironmental Engineering*, 143(5):05017001.

Steinhaeuser, K. and Tsonis, A. A. (2014). A climate model intercomparison at the dynamics level. *Climate Dynamics*, 42(5-6):1665–1670.

Stolbova, V., Martin, P., Bookhagen, B., Marwan, N., and Kurths, J. (2014). Topology and seasonal evolution of the network of extreme precipitation over the Indian subcontinent and Sri Lanka. *Nonlinear Processes in Geophysics*, 21(4):901–917.

Stolle, A., Bernhardt, A., Schwanghart, W., Hoelzmann, P., Adhikari, B. R., Fort, M., and Korup, O. (2017). Catastrophic valley fills record large Himalayan earthquakes, Pokhara, Nepal. *Quaternary Science Reviews*, 177:88–103.

Stolle, A., Langer, M., Blöthe, J. H., and Korup, O. (2015). On predicting debris flows in arid mountain belts. *Global and Planetary Change*, 126:1–13.

Strasser, A. (2009). *Rekonstruktion ehemaliger danubischer Landschaften und rheinische Abtragungsleistung im zeitraum von einer Million Jahren – eine Modellierung und Berechnung am Beispiel von zwei süddeutschen Flusssystemen*. Ph.D., Universität Stuttgart, Germany.

Strasser, F. O., Arango, M. C., and Bommer, J. J. (2010). Scaling of the Source Dimensions of Interface and Intraslab Subduction-zone Earthquakes with Moment Magnitude. *Seismological Research Letters*, 81(6):941–950.

Tacher, L. and Bonnard, C. (2007). Hydromechanical modelling of a large landslide considering climate change conditions. In *Landslides and Climate Change: Challenges and Solutions: Proceedings of the International Conference on Landslides and Climate Change, Ventnor, Isle of Wight, UK, 21–24 May 2007*. Taylor & Francis, 1 edition.

Tang, C., van Westen, C. J., Tanyas, H., and Jetten, V. G. (2016). Analysing post-earthquake landslide activity using multi-temporal landslide inventories near the epicentral area of the 2008 Wenchuan earthquake. *Natural Hazards and Earth System Sciences*, 16(12):2641–2655.

Tang, C., Zhu, J., Qi, X., and Ding, J. (2011). Landslides induced by the Wenchuan earthquake and the subsequent strong rainfall event: A case study in the Beichuan area of China. *Engineering Geology*, 122(1-2):22–33.

Tang, R., Fan, X., Scaringi, G., Xu, Q., van Westen, C. J., Ren, J., and Havenith, H.-B. (2018). Distinctive controls on the distribution of river-damming and non-damming landslides induced by the 2008 Wenchuan earthquake. *Bulletin of Engineering Geology and the Environment*.

Taniguchi, Y. (2008). Sediment Disasters Caused by Typhoon No.14, 2005, in Miyazaki Prefecture. *International Journal of Erosion Control Engineering*, 1(1):11–19.

Tanyaş, H., van Westen, C. J., Allstadt, K. E., Anna Nowicki Jessee, M., Görüm, T., Jibson, R. W., Godt, J. W., Sato, H. P., Schmitt, R. G., Marc, O., and Hovius, N. (2017). Presentation and Analysis of a Worldwide Database of Earthquake-Induced Landslide Inventories: Earthquake-Induced Landslide Inventories. *Journal of Geophysical Research: Earth Surface*, 122(10):1991–2015.

Tarantola, A. (2005). *Inverse problem theory and methods for model parameter estimation*. SIAM.

Taylor, S. R., Bonner, B. P., and Zandt, G. (1986). Attenuation and scattering of broadband P and S waves across North America. *Journal of Geophysical Research: Solid Earth*, 91(B7):7309–7325.

Thiombiano, A. N., El Adlouni, S., St-Hilaire, A., Ouarda, T. B., and El-Jabi, N. (2017). Nonstationary frequency analysis of extreme daily precipitation amounts in Southeastern Canada using a peaks-over-threshold approach. *Theoretical and Applied Climatology*, 129(1-2):413–426.

Tinti, E., Fukuyama, E., Piatanesi, A., and Cocco, M. (2005). A Kinematic Source-Time Function Compatible with Earthquake Dynamics. *Bulletin of the Seismological Society of America*, 95(4):1211–1223.

Torgoev, A. and Havenith, H. B. (2016). 2D dynamic studies combined with the surface curvature analysis to predict Arias Intensity amplification. *Journal of Seismology*, 20(3):711–731.

Travasarou, T., Bray, J. D., and Abrahamson, N. A. (2003). Empirical attenuation relationship for Arias Intensity. *Earthquake Engineering & Structural Dynamics*, 32(7):1133–1155.

Trigila, A., Iadanza, C., Esposito, C., and Scarascia-Mugnozza, G. (2015). Comparison of Logistic Regression and Random Forests techniques for shallow landslide susceptibility assessment in Giampilieri (NE Sicily, Italy). *Geomorphology*, 249:119–136.

Tsonis, A. and Roebber, P. (2004). The architecture of the climate network. *Physica A: Statistical Mechanics and its Applications*, 333:497–504.

Tsonis, A. A. and Swanson, K. L. (2008). Topology and Predictability of El Niño and La Niña Networks. *Physical Review Letters*, 100(22).

Tsonis, A. A. and Swanson, K. L. (2012). Review article "On the origins of decadal climate variability: a network perspective". *Nonlinear Processes in Geophysics*, 19(5):559–568.

Tsonis, A. A., Swanson, K. L., and Roebber, P. J. (2006). What Do Networks Have to Do with Climate? *Bulletin of the American Meteorological Society*, 87(5):585–595.

Turkington, T., Remaître, A., Ettema, J., Hussin, H., and van Westen, C. (2016). Assessing debris flow activity in a changing climate. *Climatic Change*, 137(1-2):293–305.

Uchide, T., Horikawa, H., Nakai, M., Matsushita, R., Shigematsu, N., Ando, R., and Imanishi, K. (2016). The 2016 Kumamoto–Oita earthquake sequence: aftershock seismicity gap and dynamic triggering in volcanic areas. *Earth, Planets and Space*, 68(1):180.

Ueda, H., Yasunari, T., and Kawamura, R. (1995). Abrupt Seasonal Change of Large-Scale Convective Activity over the Western Pacific in the Northern Summer. *Journal of the Meteorological Society of Japan*, 73(4):795–809.

USGS (2015). NDVI, the Foundation for Remote Sensing Phenology.

van Westen, C. (2016). National Scale Landslide Susceptibility Assessment for Dominica.

van Westen, C., van Asch, T., and Soeters, R. (2006). Landslide hazard and risk zonation—why is it still so difficult? *Bulletin of Engineering Geology and the Environment*, 65(2):167–184.

Vanham, D., Fleischhacker, E., and Rauch, W. (2008). Technical Note: Seasonality in alpine water resources management – a regional assessment. *Hydrology and Earth System Sciences*, 12(1):91–100.

Varnes, J. D. (1978). Slope movement types and processes. In *Landslides, analysis and control*, Special report - Transportation Research Board, National Research Council ; 176, pages 11–33. National Academy of Sciences, Washington, D.C.

Vogel, K., Ozturk, U., Riemer, A., Laudan, J., Sieg, T., Wendi, D., Agarwal, A., Rözer, V., Korup, O., and Thieken, A. H. (2017). Die Sturzflut von Braunsbach am 29. Mai 2016 - Entstehung, Ablauf und Schäden eines „Jahrhundertereignisses“. Teil 2: Geomorphologische Prozesse und Schadensanalyse. *HyWa*, 61(3):163–175.

Wallace, R. E. (1951). Geometry of shearing stress and relation to faulting. *The Journal of geology*, 59(2):118–130.

Wang, G. and Towhata, I. (2016). Global warming and landslide disaster: evidence from Japan. In Ho, K., Lacasse, S., and Picarelli, L., editors, *Slope Safety Preparedness for Impact of Climate Change*, pages 199–214. CRC Press, Taylor & Francis Group, 6000 Broken Sound Parkway NW, Suite 300, Boca Raton, FL 33487-2742.

Wang, R., Schurr, B., Milkereit, C., Shao, Z., and Jin, M. (2011). An Improved Automatic Scheme for Empirical Baseline Correction of Digital Strong-Motion Records. *Bulletin of the Seismological Society of America*, 101(5):2029–2044.

Weber, B. (2002). Tragwerksdynamik: Vorlesung, Sommersemester 2002. *ETH Zürich Research Collection*.

Webster, P. J. (2005). Changes in Tropical Cyclone Number, Duration, and Intensity in a Warming Environment. *Science*, 309(5742):1844–1846.

Wilde, M., Günther, A., Reichenbach, P., Malet, J.-P., and Hervás, J. (2018). Pan-European landslide susceptibility mapping: ELSUS Version 2. *Journal of Maps*, 14(2):97–104.

Willoughby, H. E., Marks, F. D., and Feinberg, R. J. (1984). Stationary and Moving Convective Bands in Hurricanes. *Journal of the Atmospheric Sciences*, 41(22):3189–3211.

Wilson, R. C. and Jayko, A. S. (1997). *Preliminary maps showing rainfall thresholds for debrisflow activity, San Francisco Bay Region, California*. Bibliogov. OCLC: 837560630.

Yagi, Y., Okuwaki, R., Enescu, B., Kasahara, A., Miyakawa, A., and Otsubo, M. (2016). Rupture process of the 2016 Kumamoto earthquake in relation to the thermal structure around Aso volcano. *Earth, Planets and Space*, 68(1):118.

Yamada, M., Heaton, T., and Beck, J. (2007). Real-Time Estimation of Fault Rupture Extent Using Near-Source versus Far-Source Classification. *Bulletin of the Seismological Society of America*, 97(6):1890–1910.

Yamada, M., Kumagai, H., Matsushi, Y., and Matsuzawa, T. (2013). Dynamic landslide processes revealed by broadband seismic records. *Geophysical Research Letters*, 40(12):2998–3002.

Yamada, M., Mangeney, A., Matsushi, Y., and Matsuzawa, T. (2018). Estimation of dynamic friction and movement history of large landslides. *Landslides*, d(April):1–12.

Yamada, M., Matsushi, Y., Chigira, M., and Mori, J. (2012). Seismic recordings of landslides caused by Typhoon Talas (2011), Japan: Seismic recordings of landslides. *Geophysical Research Letters*, 39(13):n/a–n/a.

Yamagishi, H. and Iwahashi, J. (2007). Comparison between the two triggered landslides in Mid-Niigata, Japan by July 13 heavy rainfall and October 23 intensive earthquakes in 2004. *Landslides*, 4(4):389–397.

Yamao, M., Sidle, R. C., Gomi, T., and Imaizumi, F. (2016). Characteristics of landslides in unwelded pyroclastic flow deposits, southern Kyushu, Japan. *Natural Hazards and Earth System Sciences*, 16(2):617–627.

Yamasaki, K., Gozolchiani, A., and Havlin, S. (2008). Climate Networks around the Globe are Significantly Affected by El Niño. *Physical Review Letters*, 100(22).

Yanites, B. J., Tucker, G. E., Mueller, K. J., and Chen, Y.-G. (2010). How rivers react to large earthquakes: Evidence from central Taiwan. *Geology*, 38(7):639–642.

Yoffe, E. H. (1951). LXXV. The moving griffith crack. *The London, Edinburgh, and Dublin Philosophical Magazine and Journal of Science*, 42(330):739–750.

Yoshida, K., Miyakoshi, K., Somei, K., and Irikura, K. (2017). Source process of the 2016 Kumamoto earthquake (Mj7.3) inferred from kinematic inversion of strong-motion records. *Earth, Planets and Space*, 69(1):64.

Youssef, A. M., Pradhan, B., and Sefry, S. A. (2016). Flash flood susceptibility assessment in Jeddah city (Kingdom of Saudi Arabia) using bivariate and multivariate statistical models. *Environmental Earth Sciences*, 75(12).

Yu, Z., Wang, Y., and Xu, H. (2015). Observed Rainfall Asymmetry in Tropical Cyclones Making Landfall over China. *Journal of Applied Meteorology and Climatology*, 54(1):117–136.

Yuan, R. M., Deng, Q. H., Cunningham, D., Xu, C., Xu, X. W., and Chang, C. P. a. (2013). Density distribution of landslides triggered by the 2008 wenchuan earthquake and their relationships to peak ground acceleration. *Bulletin of the Seismological Society of America*, 103:2344–2355.

Zevenbergen, L. W. and Thorne, C. R. (1987). Quantitative analysis of land surface topography. *Earth Surface Processes and Landforms*, 12(1):47–56.

Zhang, Q., Gu, X., Li, J., Shi, P., and Singh, V. P. (2018). The Impact of Tropical Cyclones on Extreme Precipitation over Coastal and Inland Areas of China and Its Association to ENSO. *Journal of Climate*, 31(5):1865–1880.

The photo on the front-cover page shows a landslide beside a waterfall by the southwestern wall of the Aso Caldera, whereas the photo on the end-cover page is the view of the Mount Aso from the western wall of the caldera. Both the photos are taken during a field trip between 21st and 24th October, 2016.